Dissertation
submitted to the
Combined Faculty of Mathematics, Engineering and Natural Sciences
of Heidelberg University, Germany
for the degree of
Doctor of Natural Sciences

Put forward by
Clara Escañuela Nieves
born in Cebreros, Spain
Oral examination: 27.04.2026

Improvements in Shower Reconstruction and Data Analysis Techniques for IACTs, and a Study of RX J1713.7–3946

Referees:
Prof. Dr. James A. Hinton
Prof. Dr. Andreas Quirrenbach

Candidate:
Clara Escañuela Nieves

ABSTRACT

Very-high-energy gamma rays (> 100 GeV) reveal fundamental insights into the particle composition, acceleration mechanisms, and particle escape from cosmic sources. Unlike charged cosmic rays deflected by magnetic fields, gamma rays travel in straight lines, tracing their origin directly. Ground-based telescope arrays study these gamma rays by collecting Cherenkov light from secondary particles produced when they interact with the atmosphere. Current instruments such as the High Energy Stereoscopic System (H.E.S.S.) have made significant advances in this field. The Cherenkov Telescope Array Observatory (CTAO) will achieve unprecedented sensitivity through two large arrays of telescopes equipped with high-performance Cherenkov cameras and advanced data analysis techniques.

The first part of this thesis presents and validates new methods for the CTAO data processing chain that improve the observatory's sensitivity and precision, with particular emphasis on reliability under suboptimal observation conditions. The study encompasses photoelectron extraction, image cleaning, and an alternative image parameterisation method. An online data volume reduction algorithm considerably reduces stored data while maintaining the observatory's performance. Simultaneously, a rapid online muon-tagging method identifies muon candidates for calibration. Together, these methods enhance the CTAO performance and reconstruction robustness.

Supernova remnants are theorised to be the primary sources of Galactic cosmic rays. RX J1713.7-3946 is among the brightest and most studied remnants at high energies. In the second part of this thesis, a new joint analysis of H.E.S.S. in conjunction with data from the Fermi Large Area Telescope (LAT) reveals significant gamma-ray emission outside the remnant. This provides strong evidence for protons escaping the acceleration site. Spectral differences within the remnant further indicate the acceleration of multiple particle types.

ZUSAMMENFASSUNG

Sehr hoch energetische Gammastrahlung (> 100 GeV) geben grundlegenden Einblick in Zusammensetzung, Beschleunigungsverfahren und Teilchenemission von kosmischen Quellen. Anders als geladene Teilchen, die von magnetischen Feldern abgelenkt werden, bewegen sich Gammastrahlen geradlinig, was es erlaubt ihre Quelle festzustellen. Erdgebundene Teleskopanordnungen untersuchen Gammastrahlung anhand von Tscherenkow Licht der Sekundärteilchen, die erzeugt werden wenn Gammastrahlen mit der Atmosphäre interagieren. Aktuelle Instrumente, wie das High Energy Stereoscopic System (H.E.S.S.) haben große Fortschritte gemacht. Das Cherenkov Telescope Array Observatory (CTAO) wird durch zwei große Teleskopfelder, mit hochperformanten Kameras und fortgeschrittenen Datenanalysetechniken, unerreichte Sensitivität liefern.

Der erste Teil dieser Dissertationsschrift zeigt und erprobt neue Methoden zur Verbesserung der Sensitivität und Präzision des Observatoriums, im Rahmen der CTAO Datenverarbeitungskette, mit einem besonderen Fokus auf Zuverlässigkeit bei nicht-optimalen Beobachtungsbedingungen. Diese Studie umfasst Photoelectronen-Extration, Bildreinigung und eine alternative Methode der Bild-Parametrisierung. Ein Echtzeit-Datenreduzierungsalgorithmus reduziert die zu speichernde Datenmenge deutlich und erhält dabei die Performance des Observatoriums. Gleichzeitig identifiziert eine Echtzeit-Myon-Erkennunsmethode Kandidaten für Kalibrierungen. Zusammen verbessern diese Methoden die Leistungsfähigkeit und Robustheit von CTAO.

Es wird angenommen, dass Supernovaüberreste die primäre Quelle von galaktischer kosmischer Strahlung sind. RX J1713.7-3946 ist unter den hellsten und besterforschten Supernovaüberresten im Hochenergie-Bereich. Im zweiten Teil dieser Dissertationsschrift zeigt eine neue, gemeinsame Analyse von H.E.S.S. und Daten des Fermi Large Area Telescope (LAT) signifikante Gammastrahlen-Emission von außerhalb des Supernovaüberrests, was starke Hinweise auf Protonen-Austritt am Beschleunigungsort gibt. Spektrale Unterschiede innerhalb des Supernovaüberrests deuten auf die Beschleunigung mehrerer Teilchentypen hin.

"Every great and deep difficulty bears in itself its own solution.
It forces us to change our thinking in order to find it"
– Niels Bohr

Table of contents

1

ORIGIN OF COSMIC RAYS AND EMISSION OF GAMMA RAYS

For several years before 1912, it was widely believed that ionising radiation originated on Earth and was emitted by rocks [1]. Victor Hess became intrigued by this radiation when multiple scientists reported observing unexpected discharge rates of electroscopes despite their high insulation. It was clear at the time that, if the ionising radiation were of terrestrial origin, it would decrease with altitude. In 1910, Theodore Wulf [2] measured the radiation at ground level and at the top of the Eiffel Tower. He detected more radiation at the altitude of the tower (around 300 m in altitude) than what was predicted if the radiation came solely from the Earth.

In 1911, Victor Hess [3] conducted his first balloon flight, reaching an altitude of ~ 1100 m and recording measurements of radiation with a sealed, pressure-tight electrometer. After several of these flights, he concluded that the radiation level decreased as he ascended, then rose rapidly once he exceeded a certain altitude. The radiation there was higher than that at the ground level. To confirm that the radiation was not coming from the Sun, he did a balloon flight during a total eclipse. The radiation measured during this flight was not lower than that in previous flights. The conclusion was clear: the origin of that radiation must be extraterrestrial, and the Sun is not its primary source. He named this radiation *Cosmic Rays* (CRs).

A series of subsequent experiments has indeed corroborated the extraterrestrial origin of cosmic rays. Other experiments were conducted several years after the discovery of cosmic rays. Some of these studies [4] [5] revealed the absorption of radiation in the atmosphere. The particles were confirmed to be charged particles after Jacob Clay [6] discovered that the cosmic ray flux was lower at the equator

due to deflections with the magnetic field. Furthermore, in 1938, W. Kolhörster [7] discovered that the measured radiation consisted of secondary particles produced by the interaction of cosmic rays high up in the atmosphere (more in [8]). These particles constitute the so-called *Extensive Air Showers* (EAS).
It is now known that cosmic rays are charged particles (electrons, positrons, protons, and heavier nuclei) accelerated in astrophysical accelerators, such as supernova remnants, to very high energies. These particles can have energies of more than EeV (10^{18} eV). The origin of cosmic rays in space cannot be directly determined from their detection. Due to their charge, they are continuously deflected by magnetic fields as they travel through space. However, the acceleration of these charged particles in astrophysical sources is often accompanied by gamma-ray emission that carries the properties of the injected cosmic-ray spectrum. Gamma rays are not deflected and point back to their origin. Therefore, gamma-ray detection provides information on the astrophysical accelerators of cosmic rays and their properties. This is the case for neutrinos, which can also be produced by cosmic rays. The field of gamma-ray astronomy has gained prominence, particularly with the development of modern detectors ([9], [10]) that enable detection of gamma rays across a wide range of energies.

1.1 Cosmic rays

Multiple modern instruments have measured the CR flux, covering a wide range of CR energies and particle types. The differential cosmic ray flux $J = \frac{dN}{dE}$ is multiplied by the square of the energy to get the energy density as seen in Fig. 1.1 as a function of the kinetic energy of the particle. It includes the distribution of charged particles, as well as gamma rays and neutrinos for comparison. The cosmic-ray spectrum is dominated by protons, followed by helium, then by heavier nuclei, and finally by electrons and positrons.
Measurements of the cosmic-ray spectrum, extending to very high energies, reveal that the energy of these cosmic rays cannot be explained by thermal emission and therefore does not depend on the source temperature. The hottest objects in the universe emit thermal radiation with a maximum energy of around 10 keV [11]. Consequently, particles with higher energies must be accelerated by non-thermal processes.

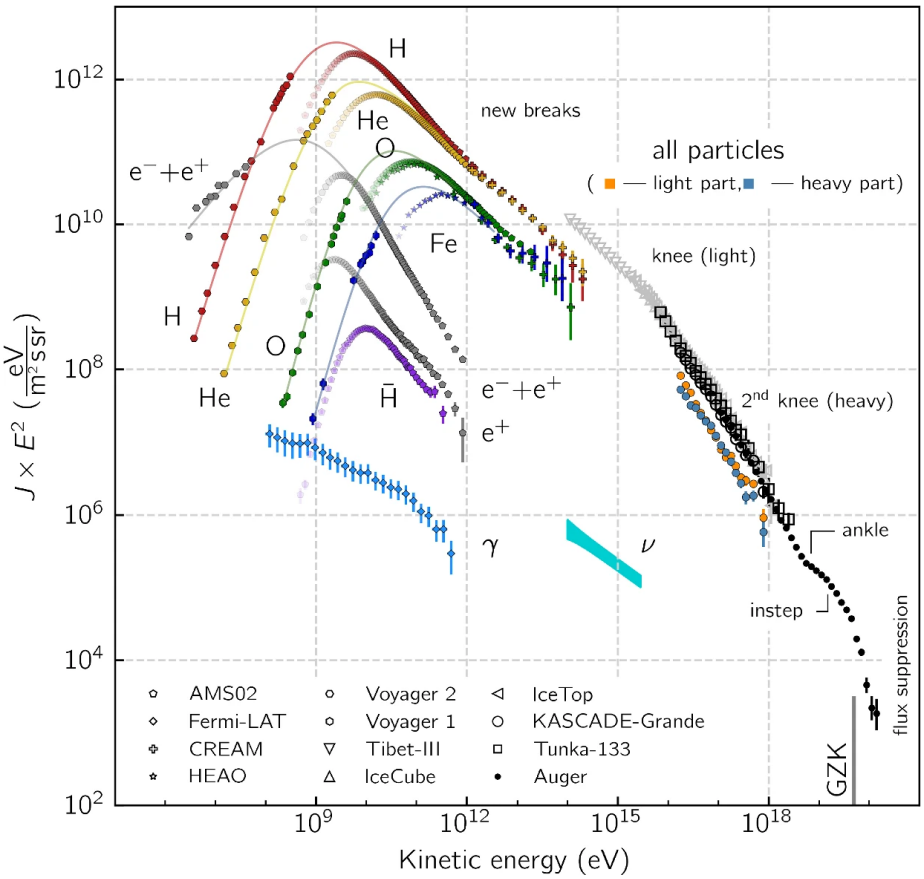

Figure 1.1: The cosmic ray spectrum measured by different experiments that cover a wide range of energies and particle types. The spectra of electrons, protons, heavy nuclei, neutrinos, and gamma rays are presented and show similar spectral features. In particular, the knee and ankle are highlighted in the plot. Taken from [12].

The spectral shape exhibits several properties that will be summarised in this section. A full description of the cosmic ray flux is provided by [12]. Below energies of the order of several GeV (the exact energy threshold depends on the nature of the charged particle), the spectrum follows a simple power law $\frac{dN}{dE} \propto E^{-\alpha}$, with α being near 0 as measured by the Voyager. The Voyager measures at the boundary beyond which the solar winds do not interact with cosmic rays (the Heliopause). However, inside the Heliopause, the drop in flux below ~ 1 GeV is drastic because the magnetic field of solar winds prevents most cosmic rays from reaching the inner solar system. The spectrum reaches its maximum at an energy of several GeV and then decays with a power law $\frac{dN}{dE} \propto E^{-2.7}$ until a break in the spectral index is observed at $\sim 3 \times 10^{15}$ eV. This energy is typically referred to as the "knee".

At the knee, the spectrum steepens, and the spectral index changes from the previous 2.7 to 3.1. Moreover, the contribution from heavier nuclei becomes increasingly significant. The characteristic power law up to the knee is commonly associated with cosmic rays being accelerated in supernova remnants (SNRs) via diffusive shock acceleration (more in Section 1.2.2). Acceleration of cosmic rays within SNRs predicts a spectral index between 2.0 – 2.2 from the acceleration mechanism, to which a value of 0.3 – 0.5 [13] is added by the diffuse particle propagation. Moreover, an energy cutoff is also predicted for cosmic rays accelerated by SNRs, around the knee [14] (see Section 1.4). Therefore, there is strong evidence for a Galactic origin of CRs before the knee, consistent with CR acceleration in SNRs. Observational evidence has not yet conclusively supported this theory.
The power law with index 3.1 extends up to an energy $\sim 10^{18}$ eV (the "ankle"), where another change in spectral index is observed. The transition from Galactic to extragalactic origin of the CRs is believed to occur at energies between the knee and the ankle. Above the ankle, cosmic rays are assumed to originate from extragalactic sources, as at such high energies, they are no longer confined within the Galaxy's magnetic field and can escape. And finally, at an energy of $\sim 10^{20}$ eV, the flux of particles drops rapidly. This may be due to interactions of particles with the Cosmic Microwave Background (CMB) (Greisen–Zatsepin–Kuzmin effect [15] [16]) or to an intrinsic cutoff in the spectra of cosmic rays.
The cosmic ray spectrum spans from an extensive range of energies, from 10^6 eV to very high energies 10^{20} eV. The spectrum can be explained only if mechanisms exist that accelerate particles to such high energies. Additionally, the smoothness of the spectrum across a wide range of energies could indicate standard features in particle acceleration processes.

1.2 Particle acceleration mechanisms

The acceleration of a particle in an electromagnetic field is generally given by the Lorentz force,

$$\frac{d}{dt}\vec{p} = q(\vec{E} + \vec{v} \times \vec{B}). \tag{1.2.1}$$

The change in momentum $\frac{d}{dt}\vec{p}$ is determined by the electric field $\vec{E}$ and the magnetic field $\vec{B}$ [17]. The velocity of the particle is $\vec{v}$ and its charge q. In

astrophysical environments, a static electric field cannot be sustained due to the high electrical conductivity of the ambient ionised gas. Instead, a non-static electric field is produced from a fluctuating magnetic field and plasma velocity $\overrightarrow{u}$, giving an electric field equivalent to $-\overrightarrow{u} \times \overrightarrow{B}$. The Lorentz force changes the particles' trajectories, while fluctuating fields cause them to interact with the plasma.
In a uniform magnetic field, the particle moves in a spiral along the magnetic field line, being accelerated perpendicular to both its velocity and the direction of the magnetic field, yet with no gain in energy. From Equation 1.2.1, a particle in the absence of an electric field moves perpendicular to the magnetic field with a Larmor frequency equivalent to,

$$w_L = \frac{|\overrightarrow{v}_\perp|}{R_L} = \frac{q|\overrightarrow{B}|}{\gamma m}, \tag{1.2.2}$$

with R_T being the Larmor [18] radius or gyroradius:

$$R_L \approx \frac{|p_\perp|}{q|B|}, \tag{1.2.3}$$

assuming perpendicular motion of the particle.
Multiple mechanisms have been proposed to explain the acceleration of cosmic rays to such high energies. Two processes are discussed in this thesis: second-order Fermi acceleration and first-order Fermi acceleration (diffusive shock acceleration). These mechanisms rely on interactions between cosmic-ray particles and gas clouds or moving shocks to increase their energy. The following discussion follows [17], and [19].

1.2.1 *Second order Fermi acceleration*

One of the first attempts to explain the spectrum of cosmic rays was done by Enrico Fermi in 1949 [20]. This first idea of cosmic-ray acceleration was named after him as second-order Fermi acceleration for reasons that will become clear shortly.
Its basic idea is that particles gain energy when interacting with magnetised clouds. Once a charged particle enters a magnetised, moving cloud, turbulent magnetic fields within the cloud deflect it, forcing it to perform a random walk and altering its trajectory until it eventually leaves the cloud. The particle then travels until its next interaction with another gas cloud. This is repeated multiple times. The

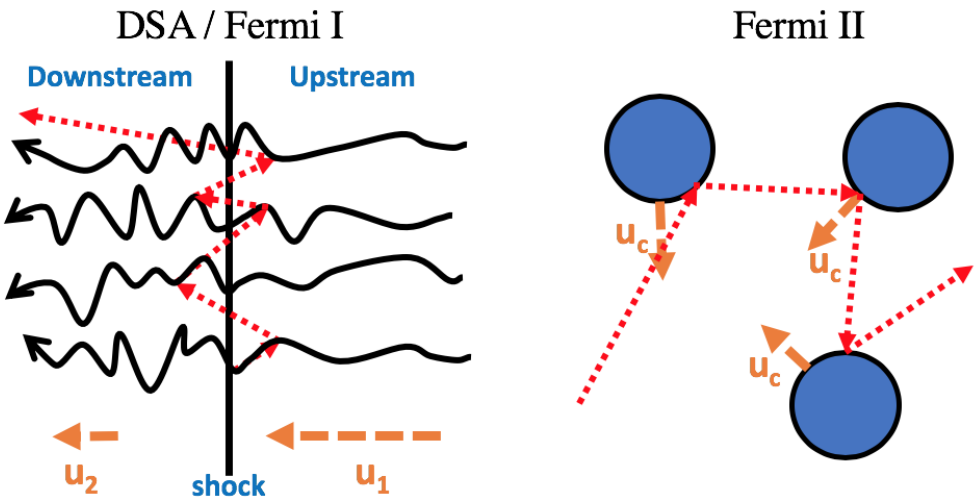

Figure 1.2: A sketch of the two particle acceleration processes described in the text: Diffuse shock acceleration (DSA / Fermi I) and second order Fermi acceleration (Fermi II). The velocities of the upstream and downstream media are shown as orange dashed lines, as well as the velocity of the magnetised clouds u_c. The particle trajectories are shown in red dashed. The magnetic field lines are in black. Taken from [21] with explicit permission.

particle gains energy in head-on collisions or loses part of it in tail-off interactions with the clouds. Head-on collisions are slightly more likely because the probability of a collision is proportional to the relative velocity of the particle and the cloud in that direction. The relative speed of head-on collisions is higher than in tail-off collisions.

The general principle of this method is illustrated in Fig. 1.2 (Fermi II). The particle in red undergoes a series of interactions with clouds that, for simplicity, are moving with the same speed u_c.

The average energy gain of a particle per collision is derived by considering multiple reference frames [17], and it is equivalent to,

$$\left\langle \frac{\Delta E}{E} \right\rangle = \frac{8}{3}\left(\frac{u_c}{c}\right)^2. \tag{1.2.4}$$

The particle's energy gain is proportional to the square of the cloud over particle (approximated to c) speeds, which limits the effectiveness of energy gain. This is why this acceleration mechanism is referred to as second-order. Furthermore, the timescale for the particle acceleration is given by,

$$t_{\text{acc}} = \frac{E}{\dot{E}} = \frac{E}{\Delta E} \times t_{\text{cycle}} = \frac{E}{\Delta E} \times \frac{\lambda}{c}, \tag{1.2.5}$$

where t_{cycle} is the mean time taken by a particle to complete one cycle of the acceleration process [22]. For this acceleration mechanism, this is the time between collisions. The time between collisions is provided by λ, the mean free path between interactions, and the particle's speed, which is approximately c. Moreover, the particle stays in the acceleration region for a time t_{esc} until it escapes. The escape time is equivalent to:

$$t_{\text{esc}} = \frac{t_{\text{cycle}}}{P_{\text{esc}}}, \tag{1.2.6}$$

where P_{esc} is the escape probability. The energy spectrum of particles ($N(E)$) is given by the diffusion-loss equation. The steady-state solution can be determined only by the acceleration and the escape timescales as,

$$\frac{d}{dE}\left(\frac{E}{t_{\text{acc}}}N\right) = -\frac{N}{t_{\text{esc}}}. \tag{1.2.7}$$

The equation can be solved with the solution $N(E) \propto E^{-q}$, with q being,

$$q = 1 + \frac{t_{\text{acc}}}{t_{\text{esc}}}. \tag{1.2.8}$$

The particle spectrum can therefore be expressed as a power-law, consistent with the measured cosmic-ray spectrum. Despite obtaining a power-law spectrum, a spectral index between 2 and 3 does not arise naturally. Only under very special circumstances can such spectral indices be derived. Furthermore, the magnetised clouds have relatively low speeds, which are insufficient to accelerate incoming particles efficiently. The collisions of particles with clouds are unlikely and of second order. Therefore, this acceleration mechanism cannot account for most of the cosmic-ray spectrum, particularly at the highest energies.

1.2.2 *First-order Fermi acceleration*

For diffusive shock acceleration (DSA) [22] or first-order Fermi acceleration, particles get accelerated by shock waves. A shock is a discontinuity in the properties (pressure, density, etc) of a medium that is propagating in space faster than the speed of sound. For the following derivations, it is assumed that the shock travels

at a non-relativistic speed. The shock is not an infinitely thin boundary; it has finite thickness. However, for this purpose, one can safely assume the shock to be effectively a discontinuity. The particles under discussion (protons and electrons) have a gyroradius (see Equation 1.2.3) for oblique and perpendicular shocks, and a mean free path in the case of parallel shocks, both of which exceed the shock's thickness. Consequently, they can move freely between the upstream and downstream media. Fig. 1.2 (DSA/Fermi I) illustrates the general concept of shock acceleration. A shock divides two regions—the upstream and downstream media—shown here in the shock's reference frame. The downstream region consists of medium that has already been swept up by the shock, while the upstream region lies ahead of the shock front. Both media are moving relative to the shock. A particle in the upstream region is scattered by fluctuations in the magnetic field in the form of Alfvén waves [23]. The particle undergoes scattering until it eventually crosses the shock. Once downstream, it is scattered again and eventually recrosses the shock. This cycle repeats until the particle escapes the acceleration region.
The energy gain can be calculated by considering the different reference frames. The upstream is moving towards the shock in the shock's reference frame with velocity u_1, and after crossing the shock, the downstream gas moves at a velocity of u_2 such that the continuity equation is held:

$$\rho_u \times u_1 = \rho_d \times u_2, \tag{1.2.9}$$

with ρ_u and ρ_d being the respective densities. The ratio of densities is equivalent to $r = \frac{u_1}{u_2} = \frac{\rho_d}{\rho_u} = \frac{\Gamma+1}{\Gamma-1}$ for a strong shock. Γ is the adiabatic index of the gas, which equals $\Gamma = \frac{5}{3}$ for a fully ionised gas. This yields $r = 4$ [24], meaning that $u_2 = \frac{1}{4}u_1$. In the upstream rest frame, the shock moves towards the upstream at speed u_1 and the downstream medium with speed $\frac{3}{4}u_1$. In the downstream reference frame, the shock moves away at $\frac{1}{4}u_1$ and the upstream wave approaches at speed $\frac{3}{4}u_1$.
Therefore, in any case, when a particle crosses the shock, it gains energy as the particles of the medium that are crossing are always moving towards the particle with a speed of $\frac{3}{4}u_1$. Once across the shock, the particle is scattered by magnetic field fluctuations in the medium until it eventually moves with the medium's speed plus its initial speed. Eventually, the particle crosses the shock again. On the opposite side, it repeats the process: scattering on the magnetic field, reaching an isotropic velocity distribution with the medium, and gaining energy. After several

such cycles, the particle leaves the shock region. The mean energy gain per cycle for a particle moving at relativistic speed is:

$$\left\langle \frac{\Delta E}{E} \right\rangle = \frac{4}{3}\frac{u_1 - u_2}{c}. \tag{1.2.10}$$

The probability of a particle escaping at each crossing step is equivalent to:

$$P_{\text{esc}} = \frac{4u_2}{c}. \tag{1.2.11}$$

The time to complete one cycle—from when the particle enters the downstream region, returns upstream, and then returns downstream again—is expressed as:

$$t_{\text{cycle}} = \frac{4}{c}\left(\frac{D_1}{u_1} + \frac{D_2}{u_2}\right), \tag{1.2.12}$$

where D_1 and D_2 are the diffusion coefficients in the upstream and downstream medium, respectively. Using Equation 1.2.6, the escape probability and cycle time are combined to achieve the escape time of:

$$t_{\text{esc}} = \frac{1}{u_2} \times \left(\frac{D_1}{u_1} + \frac{D_2}{u_2}\right). \tag{1.2.13}$$

The acceleration timescale is then equivalent to [25]:

$$t_{\text{acc}} = \frac{E}{\Delta E} \times t_{\text{cycle}} = \frac{3}{u_1 - u_2}\left(\frac{D_1}{u_1} + \frac{D_2}{u_2}\right), \tag{1.2.14}$$

The escape and acceleration timescales can be combined following Equation 1.2.8 to obtain a power law spectrum with a spectral index q of $1 + \frac{3}{r-1} = \frac{r+2}{r-1}$. It has been shown that, for a fully ionised gas, $r = 4$, the spectral index is 2, close to the observed value. The predicted spectral index is further discussed in Section 1.4. The theory of the first-order Fermi acceleration mechanism has the advantage of naturally explaining the cosmic ray spectral index, unlike the previous method. There are other mechanisms for particle acceleration which are not discussed here—for example, shear acceleration [26].

1.3 Production processes of high-energy gamma-rays

Little can be said about the origin of charged cosmic rays, as their trajectories are deflected by magnetic fields. However, cosmic rays, travelling at relativistic speeds, interact with the ambient medium, producing very energetic gamma rays that travel in straight lines, allowing their origin to be inferred. Additionally, neutrinos emitted during these interactions can provide further information about the production site.
Gamma rays are produced through interactions of protons or electrons with the surrounding medium—matter, magnetic fields, or photon fields [27]. Depending on the type of interaction, multiple gamma-ray production mechanisms are possible. Electrons can undergo multiple processes of energy loss. The two main leptonic mechanisms for producing high- and very-high-energy gamma rays are inverse Compton scattering (interaction with photon fields) and, at lower energies, synchrotron emission (interaction with magnetic fields). The hadronic emission is dominated by pion decay (interaction with matter). Detailed descriptions of each mechanism are found in the following paragraphs and are described in detail in [28] and [27].

1.3.1 *Synchrotron emission*

Charged particles moving at relativistic speeds in a magnetic field experience acceleration perpendicular to their direction of motion. This produces a spiral motion along the magnetic field lines, leading to energy losses through photon emission. The average power of emitted synchrotron radiation by a particle of mass m and energy E is given by [29],

$$\langle P_{\text{syn}} \rangle = -\frac{dE}{dt} = \frac{4}{3}\sigma_T c U_B \gamma^2 \beta^2 \propto \frac{1}{m^2}, \tag{1.3.1}$$

where σ_T is the Thomson cross section which is equivalent to $\sigma_T = \frac{8\pi}{3} r_e^2$ with r_e being the classical radius of the electron. U_B is the magnetic field energy density which is equivalent to $\frac{B^2}{2\mu_0}$ with B being the magnetic field of the medium and μ_0 the magnetic permeability of vacuum. γ is the Lorentz factor and $\beta = \frac{v}{c}$ is the particle's speed. The energy loss due to synchrotron radiation is inversely proportional to

the mass of the charged particle. Lighter particles lose more energy through this process, making the mechanism less effective for protons.
Furthermore, the cooling time of electrons due to synchrotron emission is equivalent to [29],

$$t_{\text{syn}} = \frac{E}{\dot{E}} = \frac{E}{\langle P_{\text{syn}} \rangle} \propto \frac{1}{B^2 \gamma} \text{yr}, \tag{1.3.2}$$

when $\beta \simeq 1$. More energetic electrons and stronger magnetic fields result in faster cooling.
As described in Section 1.2.1, the electron population after acceleration can be described as a power-law distribution $\frac{dN}{dE} \propto E^{-\alpha_e}$ in this example, although the injection electron spectrum also exhibits an energy cutoff at high energy. The energy spectrum of the resulting synchrotron radiation from these electrons also follows a power-law with index $\alpha_\gamma = \frac{\alpha_e+1}{2}$. Fig. 1.3 shows an example of an energy spectrum for an electron population following a power law with index $\alpha_e = 2$. However, energy losses through synchrotron and inverse-Compton radiation produce a break in the electron spectrum, changing the power-law index from α_e to $\alpha_e + 1 = 3$. The energy of the break depends on the magnetic field and age of the source, as can be seen in Fig. 1.3 when comparing the synchrotron spectra at 100 µG and 3 µG. The associated synchrotron spectrum also shows an energy break, with the spectral index changing from 1.5 to 2.0.

1.3.2 *Inverse Compton emission*

The name of this effect refers to its similarity to the Compton effect, but with the roles of the incident and scattered particles reversed. Inverse Compton (IC) [30] emission occurs when a sufficiently energetic electron scatters on a photon from a radiation field, transferring part of its energy to the photon. There are two regimes depending on the energy of the target photons:

- Thomson scattering when the energy of the photon $h\nu$ is much lower than the energy of the electron at rest $h\nu \ll m_e c^2$. The scatter in this case is almost elastic, with small energy transfer.
- Klein-Nishina regime [31] when $h\nu \gtrsim m_e c^2$; the scattering is inelastic.

The corresponding energy loss due to IC in the Thomson regime is [17],

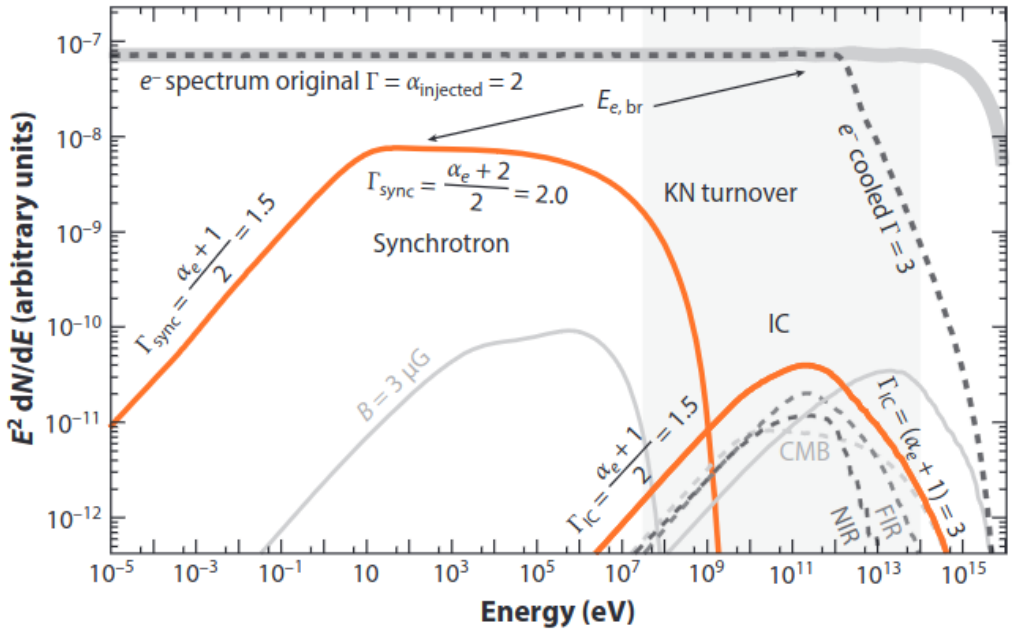

Figure 1.3: Energy spectrum of electrons injected with a power law index of 2 in grey and including energy losses in the grey dashed line. The corresponding synchrotron and inverse Compton spectra are shown, with their spectral indices highlighted. The orange line shows the case of a magnetic field of 100 μG. The gamma-ray spectrum is also shown at magnetic field 3 μG. The emission components of IC scattering are shown for three photon fields: far-infrared (FIR), near-infrared (NIR), and cosmic microwave background (CMB). Taken from [28] with explicit permission.

$$\langle P_{\mathrm{IC}} \rangle = \frac{4}{3} \sigma_T c U_R \gamma^2 \beta^2. \tag{1.3.3}$$

U_R is the energy density of the radiation field. The Thomson cross section, σ_T, was defined in the previous section and is constant. With Equation 1.3.3, one can derive the cooling time of electrons due to IC energy loss as,

$$t_{\mathrm{IC}} = \frac{E}{\langle P_{\mathrm{IC}} \rangle} \approx \frac{3 m_e c^2}{4 \sigma_T c \gamma U_R}. \tag{1.3.4}$$

Therefore, higher electron energies and radiation densities lead to shorter cooling times. This concerns the Thomson regime. The Klein-Nishina regime has a different cross-section, computed from quantum electrodynamics. The cross-section is smaller than Thomson's, and it weakly depends on the electron energy as follows:

$$\sigma_{\mathrm{KN}} \simeq \frac{3}{8} \frac{\sigma_T}{x} \left[\ln(2x) + \frac{1}{2} \right], \tag{1.3.5}$$

with $x = \frac{h\nu}{m_e c^2}$.
Assuming, as for synchrotron radiation, that the energy spectrum of the injected electrons follows a power law with spectral index α_e, the IC spectral shape also follows a power law. The index of the IC in the Thomson regime is the same as for synchrotron radiation, $\frac{\alpha_e+1}{2}$, and in the Klein-Nishima regime, the spectral index at higher energies is $\alpha_e + 1$. Therefore, even in the absence of a cooling break from the injected electron spectrum, the IC spectrum would experience a change in spectral index. The IC spectrum is also shown in Fig. 1.3 for the two regimes and three components after the interaction of electrons with different photon fields: far-infrared (FIR), near-infrared (NIR), and cosmic microwave background (CMB). It is also important to highlight the apparent similarities between the IC emission in the Thomson regime and the synchrotron emission. The ratio of the energy losses is given by,

$$\frac{P_{\rm syn}}{P_{\rm IC}} = \frac{U_B}{U_R}. \tag{1.3.6}$$

It is simply the ratio of the magnetic field to the radiation energy densities of the medium. Therefore, synchrotron and IC radiation are closely related processes. When electrons are present in the medium with a magnetic field, they typically emit gamma rays through both of these processes. Electrons undergoing synchrotron radiation populate the region with more photons. Those are then Compton scattered by the same electrons at high energies, leading to the so-called Synchrotron Self-Compton effect [29].

1.3.3 *Emission in π^0 decays*

Relativistic protons produce high-energy gamma rays through inelastic interactions with matter. Proton scatterings in matter lead to the production of neutral (π^0) and charged pions ($\pi^\pm$). Charged pions decay into muons ($\mu^\pm$), electrons and positrons ($e^\pm$), and neutrinos ($\overset{(-)}{\nu}$) [27]:

$$\begin{aligned} pp &\rightarrow \pi^\pm \rightarrow \mu^\pm + \overset{(-)}{\nu}_\mu \\ pp &\rightarrow \pi^\pm \rightarrow e^\pm + \nu_\mu + \bar{\nu}_\mu + \overset{(-)}{\nu}_e \end{aligned} \tag{1.3.7}$$

Neutral pions dominate the emission of gamma rays as they quickly decay into two gammas:

$$pp \rightarrow \pi^0 \rightarrow \gamma\gamma \tag{1.3.8}$$

About half of the energy of the primary proton is carried away by the leading nucleon (proton). The remaining half is given to the pion. The probability of producing each species of pion is equal. Therefore, the energy from the primary proton that is used for the production of gamma rays is 1/6 [32]. The energy of each gamma ray is ~ 0.1 of the energy of the proton. The minimum energy of protons for the production of pions is given by [27] as ~ 280 MeV. Furthermore, the cooling time of protons can be fully expressed in terms of the target number density n as,

$$t_{\rm pp} \simeq 3 \times 10^7 \left(\frac{n}{1\,{\rm cm}^{-3}}\right)^{-1} {\rm yr}. \tag{1.3.9}$$

The cooling time due to pp interactions is almost independent of energy and only depends on the density of target nucleons. As density increases, more interactions occur, and protons cool more rapidly. For a typical Galactic density of 1 cm^{-3}, the cooling time is of the order of 10^7 yr [28].
The spectrum of protons after acceleration can be described with a power law with an exponential cutoff at an energy $E_{c,\rm p}$:

$$\frac{dN_p}{dE_{\rm p}} \propto E_{\rm p}^{-\alpha} \exp\left(-\left(\frac{E_{\rm p}}{E_{c,\rm p}}\right)^{\beta}\right). \tag{1.3.10}$$

The spectrum of the gamma rays follows the same shape but with indices α' and β', and the energy cutoff at $E_{c,\gamma} \simeq 0.1 E_{c,\rm p}$. The index β' and β are related as described by [33]. For $\alpha = 2$ and $\beta = 1$, $\beta^{'}$ is around 0.5. Therefore, the cutoff is less sharp in the gamma-ray spectrum. The gamma-ray spectra from hadronic interactions with matter and IC are very similar. However, the gamma spectrum from pp interactions exhibits a distinctive feature known as the pion bump [34]. The pion bump is a low energy cutoff observed in the gamma-ray spectrum because the gamma rays from the decay of the neutral pion should at least carry with them half of the pion rest mass energy $E_{\rm min,\gamma} = m_\pi c^2/2 \simeq 67.5$ MeV. This is independent of the pion's energy spectrum. The detection of the bump could indicate proton production. Fig. 1.4 shows an example of a gamma-ray spectrum from the decay of pions, considering

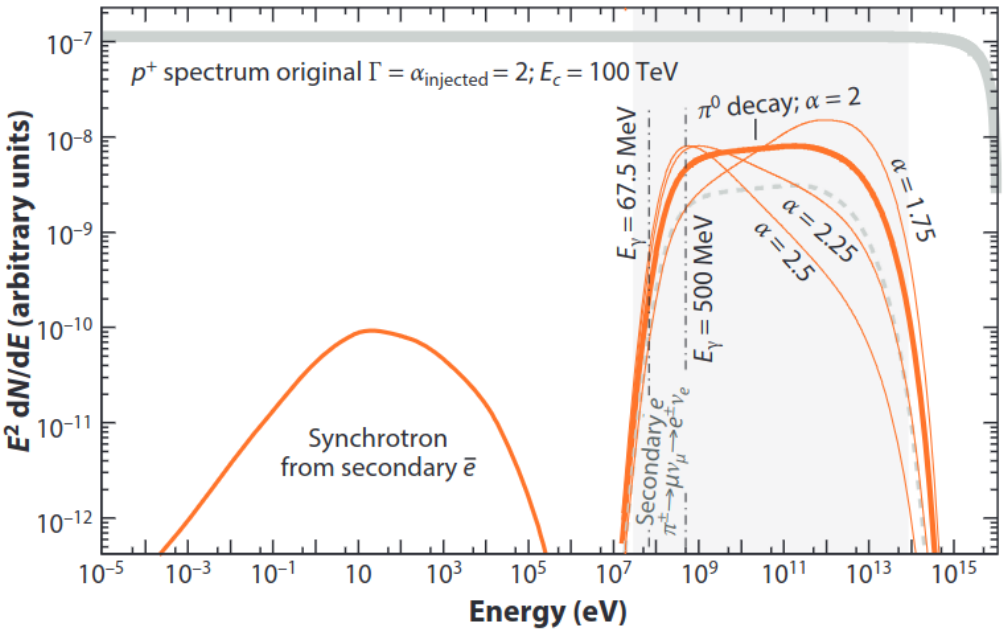

Figure 1.4: Energy spectrum of protons injected with a power law index of 2 in grey with a cutoff at energy 100 TeV. The corresponding spectra of the neutral and charged pions are shown, with their spectral indices highlighted. The orange line at high energies shows the gamma-ray spectrum resulting from π^0 decay. The effect of multiple injected power law indices is reflected in the thin orange lines. The dashed grey line shows the gamma-ray spectrum from secondary electrons produced by charged pion decays. The thin orange line on the left side of the plot shows the synchrotron emission spectrum of secondary electrons produced in hadronic interactions, assuming a magnetic field of 30 µG and a source age of 1000 yrs. Taken from [28] with explicit permission.

an injected flux of protons with a power law of index $\alpha = 2$ and energy cutoff $E_{c,\mathrm{p}} = 100$ TeV.

1.4 The origin of Galactic cosmic rays

The field of cosmic rays has seen significant advances over the years, yet much remains to be learned about these charged particles. One fundamental question remains open: what is the origin of cosmic rays? Current evidence suggests that the spectrum below 100 PeV has a Galactic origin.

Galactic cosmic rays are produced through particle acceleration, followed by diffusion through the Galaxy's magnetic field. Multiple detectors have measured the energy density of Galactic CRs to be $\sim 1\,\mathrm{eVcm}^{-3}$ [27]. As these accelerated

charged particles diffuse through the interstellar medium, the mean amount of matter traversed (grammage) is described as [27]:

$$\bar{x} = \tau_{\rm esc} m_{\rm p} n c, \tag{1.4.1}$$

where $\tau_{\rm esc}$ is the time it takes for a particle to escape the Galaxy, $m_{\rm p}$ is the proton mass, and n is the mean gas density inside the Galaxy. The grammage can be determined from the secondary particles produced by the interactions of primary CRs with the interstellar medium. Carbon is accelerated at sources and, as it travels through the medium, can produce boron, which, unlike carbon, is not significantly present at the acceleration sites. The carbon-to-boron ratio determines the grammage. From this, the escape time of CRs outside the Galaxy is estimated to be $\sim 10^7$ yr [27]. The escape time is approximately three orders of magnitude higher than it would be if the particles moved straight out. This provides strong evidence for diffuse motion driven by magnetic-field turbulence in the Galaxy before escape. The diffusion coefficient is energy-dependent with an index δ,

$$D(E) \propto E^{\delta}. \tag{1.4.2}$$

Therefore, the escape time is equivalent to [13],

$$\tau_{\rm esc} \propto \frac{1}{D(E)} \propto E^{-\delta}. \tag{1.4.3}$$

The index δ can be determined by fitting the measured Boron-to-Carbon ratio as a function of energy. Current measurements estimate δ to be $\sim 0.3-0.5$ [35] [36] [37]. Supernova remnants are commonly believed to be the main source population of CRs in the Galaxy. Numerous theoretical predictions support this conclusion, as does observational evidence. The spectral index of CRs below the knee is observed to be 2.7. In SNRs, particles are accelerated through diffusive shock acceleration, which leads to a power law spectrum of accelerated particles $\propto E^{-\Lambda}$, with Λ being ~ 2.0 [38] [39]. The spectrum becomes softer due to particle diffusion through the interstellar medium, as described earlier. This yields a spectral index of $\Lambda + \delta \approx 2.3-2.5$ that is independent of the shock properties. The DSA prediction is fairly close to what is needed to explain the CR spectrum, though a slight discrepancy remains unexplained. Nonlinear DSA [40] predicts $\Lambda \approx 2.3$, succesfully explaining the cosmic-ray flux.

For SNRs to be considered the primary source of Galactic CRs, they must efficiently accelerate charged particles. Sustaining the observed cosmic ray population requires 10% of the total mechanical energy from supernova shocks to be converted into non-thermal particle acceleration. This reasonable efficiency requirement provides a second line of evidence supporting supernova remnants as cosmic-ray sources.

One key challenge with SNRs as the main cosmic-ray sources is understanding how shocks can accelerate particles to energies reaching the knee [41]. For a particle with charge Z, its maximum energy is given by [41]:

$$E_{\max} = 6 \times 10^{13} Z \left(\frac{u}{3000 \text{ kms}^{-1}} \right) \frac{t}{300 \text{ yr}} \frac{B}{\mu\text{G}} \text{eV}, \tag{1.4.4}$$

where t is the time spent in the free-expansion phase, B is the magnetic field upstream of the shock, and u is the shock front speed. Whilst the maximum energy is achieved during the free-expansion phase, this phase has insufficient duration to explain the observed CR spectrum. For SNRs to accelerate particles to the knee, the magnetic field must exceed predicted values from interstellar magnetic field compression ($\sim$5 μG) [42]. Observations have revealed higher-than-expected magnetic fields in the downstream medium [43] [44], suggesting an amplification mechanism operates in the upstream medium.

Accelerated CRs excite Alfvén waves in SNR shocks, which result in a strong amplification of magnetic fields. The amplified field in turn enables those particles to scatter and gain even more energy—a self-generated acceleration environment. According to the Bell instability theory [45], the magnetic field can be amplified by several orders of magnitude, enhancing the overall process. Assuming efficient Bell instability, a maximum proton energy of approximately 1 PeV can be predicted [14]. Heavier elements reach proportionally higher energies—for instance, iron (Z=26) can reach $\sim$ 100 PeV. This transition to heavier species explains the steepening at the knee and is consistent with observations showing compositional changes between 1 and 100 PeV.

Theoretical predictions must be validated by observational data. If SNRs account for the Galactic CR flux, high-energy gamma rays should be emitted from π^0 decay if there is sufficient target material around. Therefore, detecting hadronic gamma-ray emission from SNRs is crucial to confirming that they are indeed the primary sources of Galactic CRs. Very-high-energy gamma rays from some SNRs

have been detected, but in all cases, both hadronic and leptonic acceleration can explain the observed energy spectra [46] [47] [48]. Moreover, IC 443 and W44 [49] have been detected up to GeV energies and clearly exhibit hadronic emission, as evidenced by the detection of the pion bump. This demonstrates that protons are indeed accelerated in SNRs.

1.5 Supernova remnants

Supernova explosions can result from two processes (core-collapse [50] and type Ia [51] supernovae). When a high-mass star ($> 8\,M_\odot$) reaches the end of its life, iron fusion in the core ceases to generate energy once the core mass falls below $1.4\,M_\odot$ (the Chandrasekhar limit). The star cannot generate sufficient pressure to counteract gravity, and the core collapses into a neutron star, accompanied by a shock wave propagating outward into the infalling outer core. An explosion of the outer layers is driven by the large number of high-energy neutrinos emitted by the core [52].
Alternatively, a supernova explosion can also occur in a binary system in which one star is a white dwarf. The white dwarf accretes mass from a binary companion, and when the mass of the white dwarf exceeds the Chandrasekhar limit, it explodes in a type Ia supernova.
The supernova expels several solar masses of ejecta into the interstellar medium at speeds of several thousand km/s [53], releasing approximately 10^{51} erg of energy [54]. Over its $\sim 10^5$ yr lifetime [55], the supernova remnant undergoes multiple evolutionary phases as the ejecta expands into and interacts with the interstellar medium until it finally dissolves into it. The evolutionary phases are: free-expansion, Sedov-Taylor, radiative, and finally dissipation into the medium.
The ejecta first undergoes a phase of free expansion of the shock, with the shock front propagating at speeds exceeding the speed of sound. This occurs when the ejecta mass is larger than the mass of the swept-by material. During this phase, the shock radius R expands linearly with time $R \propto t$ [56]. The gas cools down adiabatically as the shock expands. This phase lasts from several 10^2 to several 10^3 years until the swept-up mass becomes larger than the ejecta mass. When this occurs, the Sedov-Taylor phase starts.
In the Sedov-Taylor phase, the shock starts to decelerate, and the expansion of the radius of the shock expands adiabatically [57] at a lower rate $R \propto t^{2/5}$. A reverse

shock, which moves in the opposite direction to the shock expansion, becomes relevant and heats the gas within the remnant. This phase lasts for several tens of thousands of years.
As the shock decelerates, the timescale for radiative cooling becomes comparable or smaller than the remnant age. In the radiative phase, the shock wave is low of a few hundred km/s, and the gas inside the remnant cools down by radiative losses. After $\sim 10^5$ yrs, the shell dissipates into the interstellar medium.

1.5.1 *The case of the supernova remnant RX J1713.7-3946*

One of the brightest sources of gamma-ray emission detected so far is the supernova remnant RX J1713.7-3946. This SNR has been studied in detail for many years, with observations spanning multiple wavelengths. Despite the efforts, the nature of the high-energy emission remains unclear. There is some evidence for hadronic emission, but there are no precise observations that have proven the decay of π^0 inside the remnant. The discoveries related to RX J1713.7-3946 are highlighted and summarised in this section.
RX J1713.7-3946 (also known as G347.3-0.5) was first detected in 1996 by the ROSAT X-ray all-sky survey [58] in the constellation Scorpius. It was found to have an elliptical shape of diameter $\sim 70'$. The high X-ray flux detected by ROSAT confirmed that this SNR is one of the brightest in the Galaxy. Since 1997, and subsequently observed in the X-ray band, the emission has been confirmed to be dominantly non-thermal [59], with little thermal emission [60]. Since the early study of this source, it has been known that the dominant non-thermal X-ray emission arises from synchrotron radiation. Therefore, electrons must be accelerated to high energies within the remnant.
The object 1WGA J1713.4-3949 [61], roughly at the centre of the remnant, has been detected in X-rays. The detected X-ray emission from this source has not been accompanied by optical or radio detections, and no evidence for X-ray pulsation has been observed. This, together with the properties of the X-ray emission, agrees with the description of a compact central object [62], typically found in SNRs. 1WGA J1713.4-3949 is most likely a young neutron star that was formed by the supernova explosion. The presence of this object strongly suggests the remnant is the result of a core-collapse supernova explosion.

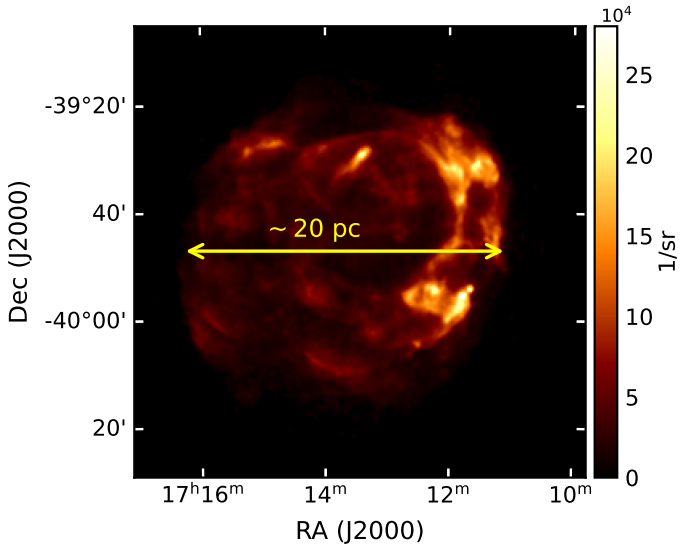

Figure 1.5: X-ray intensity map of RX J1713.7-3946 at the energy band 1-6 keV as detected by the XMM-Newton satellite. Fabio Acero provided the FITS file, from which the author produced the map.

The distance to the remnant has been estimated on multiple occasions, with a general consensus of approximately 1 kpc. This value was first estimated following the initial detection [59] and remains reasonable [63]. The age of the remnant remains a subject of debate. Historical documents indicate that Chinese astronomers observed a supernova at the site of the current remnant in AD 393. This earlier discovery is consistent with more recent studies of the remnant's age, which estimate it to be between $\sim 1000 - 2000$ yr [64] [65]. This implies that the remnant was in its free-expansion phase not long ago, possibly in the transition from free expansion to the Sedov phase. This is further justified by the detection of strong non-thermal emission, faint thermal emission, and the fast shock moving speed (3500–4500 km/s) [64] [65].

Multi-wavelength morphology

The SNR RX J1713.7-3946 is a shell-type supernova remnant. The XMM-Newton satellite has recently updated the X-ray map in the 1-6 keV energy range, revealing the complexity and inhomogeneity of the X-ray emission across the remnant (Fig. 1.5 in right ascension (RA) and declination (Dec) coordinates). Significant brightness variations are observed across the remnant. The western region (right side in Fig. 1.5) is the brightest and exhibits complex filamentary structures [66],

including two narrow parallel rims running from north to south. In contrast, the centre of the remnant is much fainter and smoother.

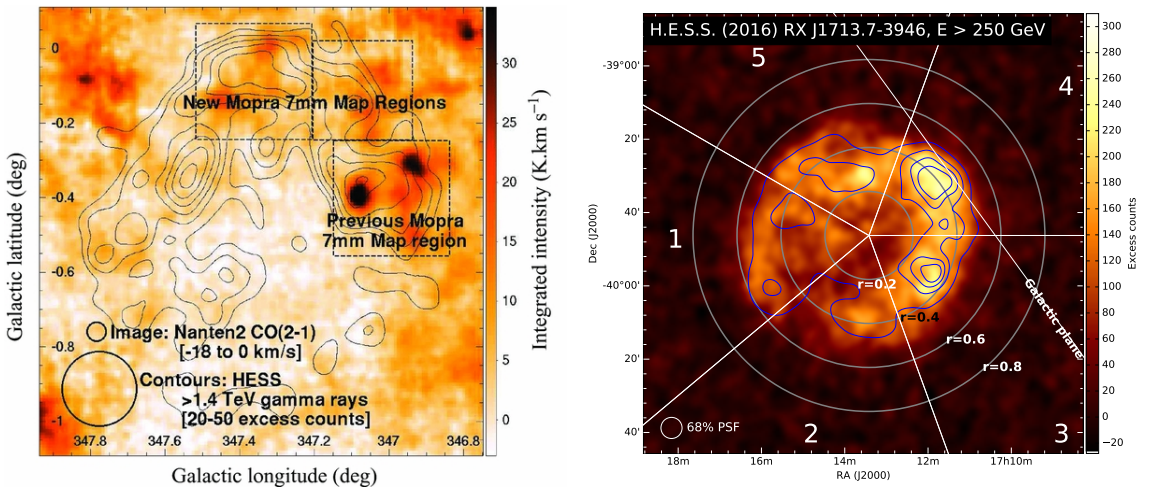

(a) CO map with H.E.S.S. contours **(b)** H.E.S.S. map with X-ray contours

Figure 1.6: Morphology of RX J1713.7-3946 as revealed by X-ray, gamma-ray, and CO emission. The left plot shows the Nanten2 CO(2-1) map superimposed by H.E.S.S. contour lines [67] from the contour map of the right. The intensity is derived by integrating the CO(2-1) spectra from −18 to 0 km s^{-1} (taken from [68]). The right plot shows the H.E.S.S. excess-counts map at energies > 250 GeV, overlaid with XMM-Newton X-ray contours. The map is divided into five regions (taken from [67]).

The X-ray emission from RX J1713.7-3946 is dominated by non-thermal synchrotron radiation and can generally be described by a power-law spectrum across the remnant. Spatial variations in the observed spectral indices are reported, particularly between the western and central regions. These variations may partly be influenced by differences in interstellar absorption, as the hydrogen column density is known to be higher toward the western part of the remnant due to foreground molecular material [66]. However, intrinsic variations in the electron population and magnetic field strength are also likely to contribute to the observed spectral differences.

Furthermore, the remnant has been detected by γ-ray experiments, including H.E.S.S., with high significance. A detailed study of the first observations of RX J1713.7-3946 with H.E.S.S. is provided by [11]. The gamma-ray map of H.E.S.S. is shown in Fig. 1.6b and the X-ray contours are superimposed on the map. The gamma- and X-ray emissions exhibit very similar morphologies but are not identical [69]. There are still apparent differences: a slight displacement of intensity

peaks within the remnant, and, in particular, gamma-ray emission outside the X-ray contours, which can be interpreted as particles escaping the shock front [67]. Moreover, Fig. 1.6a shows the H.E.S.S. contours of Fig. 1.6b superimposed on the CO emission. There is a correlation between the gamma and CO emission in the western side of the remnant [70] [68] [71], with the densest molecular clouds being around the locations of the brightest gamma ray emission. From these results, it can be argued that the presence of dense molecular clouds in the western region can lead to interactions between the remnant and molecular clouds, potentially resulting in *pp* interactions. The presence of electrons accelerated in the remnant has been confirmed on multiple occasions; however, the energy spectrum can be fitted to either a leptonic or a hadronic model. The latest H.E.S.S. results on RX J1713.7-3946 do not provide any clear conclusions as they cannot rule out purely leptonic or hadronic scenarios, or quantify the mixture fraction between them.
A reanalysis of the supernova remnant RX J1713.7-3946 using H.E.S.S. data will be performed in Chapter 6 and a joint analysis using Fermi-LAT and H.E.S.S. will be shown in Chapter 7.

2

DETECTION OF VERY-HIGH-ENERGY GAMMA-RAYS

Multiple approaches exist for the detection of gamma rays. Very-high-energy gamma rays can be detected using two principal types of instruments: ground-based and space-based gamma-ray detectors. Two main categories of ground-based detectors are employed for gamma-ray detection: arrays of ground-based telescopes and arrays of water tanks.

Despite apparent differences in the designs of ground- and space-based detectors, the underlying principle of gamma-ray detection remains similar. Gamma rays cannot be directly detected due to their short wavelength relative to atomic dimensions. However, the interaction of gamma rays either with the atmosphere (ground-based telescope arrays) or with conversion materials (space-based detectors) produces secondary particles that propagate at relativistic speeds. These secondary particles lose energy as they traverse the detection medium. Ground-based telescope arrays equipped with fast-recording cameras detect the Cherenkov light emitted by relativistic charged particles as they propagate through the atmosphere. Alternatively, water tank arrays positioned at high elevations detect Cherenkov light emitted by charged particles within the water medium. In space-based detectors, a calorimeter composed of dense material measures the energy deposited by these secondary particles.

One of the principal limiting factors of space-based gamma-ray detectors is the collection area. The physical constraints on detector size in space impose an upper limit on the maximum detectable gamma-ray energy. Ground-based detectors are not subject to such size constraints, enabling the deployment of large-scale arrays of telescopes or water tanks for detecting low-rate, high-energy events. Furthermore, the atmosphere functions as an extensive calorimeter that permits the complete

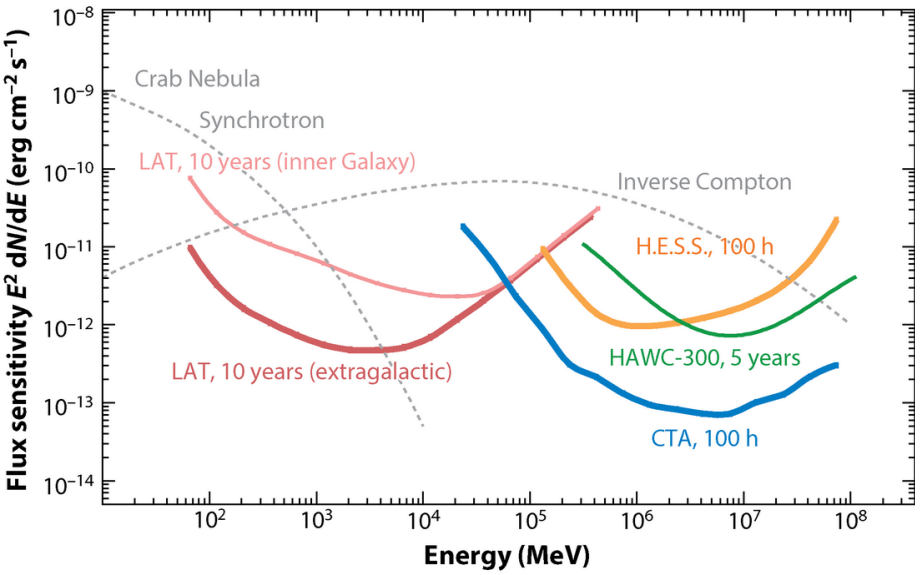

Figure 2.1: Sensitivities of multiple gamma-ray detectors to point-like sources. The sensitivity of Fermi-LAT is shown after 10 yrs of exposure. H.E.S.S. and the future CTAO are compared under the assumption of the same observation time of 100 h. A water tank array, HAWC, is also shown after 5 yrs of exposure. Taken from [28] with explicit permission.

development of particle showers, in contrast to the limited calorimeter volumes available in space-based detectors.

A summary plot of the sensitivities of current and future detectors is presented in Fig. 2.1. As the Cherenkov Telescope Array Observatory (CTAO) has not yet been built, the instrument's sensitivity is still subject to change. The LAT (Large Area Telescope) (see Section 2.7.1) aboard the Fermi satellite operates above the atmosphere in Earth orbit. It exhibits higher sensitivity at lower energies compared to other detector systems. The High Energy Stereoscopic System (H.E.S.S.) (see Section 2.2) and the CTAO (Section 2.3) represent current and future telescope arrays situated at high-altitude ground-based sites. The CTAO demonstrates superior sensitivity compared to existing detectors of its type, covering a wider energy range. HAWC, a water tank array, is also represented in Fig. 2.1 at high energies.

This section presents a detailed discussion of ground-based gamma-ray astronomy, as this thesis focuses on the analysis of data acquired with Imaging Atmospheric Cherenkov Telescopes (IACTs). The development of extensive air showers in the atmosphere is explained, together with the subsequent Cherenkov emission from secondary particles. The Imaging Atmospheric Cherenkov Technique is intro-

duced, along with the standard analysis chain for the CTAO, including reference to H.E.S.S.. Finally, a brief description of the Fermi-LAT instrument is provided.

2.1 Ground-based gamma-ray astronomy

2.1.1 *Extensive air showers*

Cosmic and gamma rays constantly reach the Earth's atmosphere. Because the atmosphere is opaque to these particles, they eventually interact with nuclei. When a particle enters the atmosphere at energies above a few GeV, the interaction generates a cascade of secondary particles travelling at relativistic speeds [72]. This particle cascade is referred to as an Extensive Air Shower (EAS) [73]. The type of secondary particles and the shape and extent of the air shower depend on the primary particle that undergoes the first interaction. This allows gamma rays to be distinguished from cosmic rays. A detailed description of EAS is provided for two distinct types of primary particles: gamma rays, which produce electromagnetic showers, and hadrons, which produce hadronic showers.

Electromagnetic showers

The Heitler model [74] can well describe electromagnetic (EM) showers. This simple model reproduces the key features of EM cascades. EM showers have two main particle production processes: electron-positron pair production and bremsstrahlung [75]. When a photon interacts with a nucleus, an electron-positron pair is produced. Each of these particles is decelerated by the atmosphere, resulting in bremsstrahlung gamma rays. Pair production and bremsstrahlung continue until the particle energy losses are dominated by ionisation rather than by radiative losses.
The Heitler model is represented in Fig. 2.2. This model assumes each particle decays into two secondary particles at fixed interaction lengths of $d = \lambda_e \ln(2)$. λ_e is the radiation length for air. Each particle produces two secondaries in every interaction, and each secondary particle carries half the energy of the primary particle $E = E_0/2$. Therefore, after k interactions, $N = 2^k$ particles are produced, each with an energy $E = E_0/2^k$. The critical energy is $E_c = 86\,\mathrm{MeV}$ [76]. At this energy, the ionisation loss equals the Bremsstrahlung loss, and the cascade begins

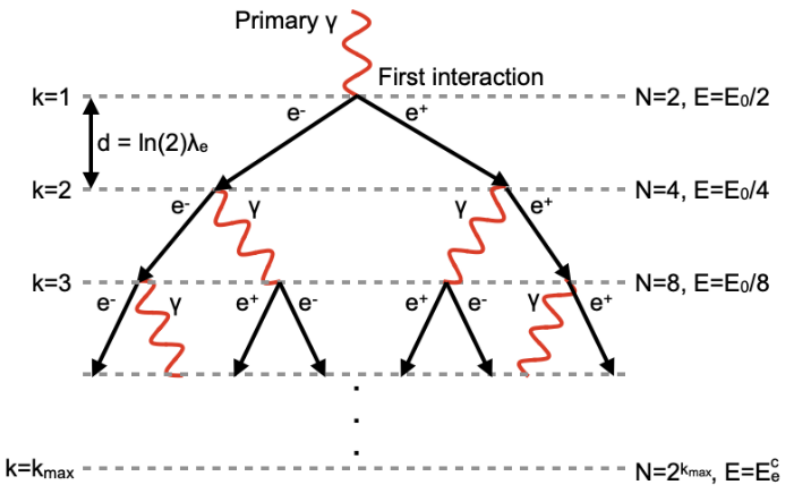

Figure 2.2: Schematic of an electromagnetic shower development in the atmosphere. The primary particle (γ) strikes a nucleus in the air and undergoes pair production. At each step k, the number of particles is doubled, and the energy is split by two until it reaches the critical energy when the shower stops developing. Taken from [78] with explicit permission of the author.

to die. The critical energy is reached at a penetration depth $X_{\max} = \lambda_e \ln\left(\frac{E_0}{E_c}\right)$ [77], where the shower reaches its maximum development.

Hadronic showers

Hadrons interact with nuclei in the atmosphere via the strong force. The first interaction produces predominantly neutral (π^0) and charged ($\pi^{\pm}$) pions as well as, to a lesser extent, fragments of the target nucleus (N), protons (p), and neutrons (n). Fig. 2.3 shows a simplified schematic of the particle production in the cascade. Neutral pions immediately decay into two gammas, and an electromagnetic sub-shower develops within the hadronic shower. The charged pions, however, interact with other nuclei of the atmosphere until a critical energy is reached [77]. Charged pions decay into muons $\mu^{\pm}$ and muon neutrinos $\overset{(-)}{\nu}_{\mu}$.
There are apparent differences between the shower developments of each primary particle. Hadronic showers produce a large number of muons from the decay of charged pions. Muons rarely accompany electromagnetic showers. Therefore, muon detection could be a good indicator of a proton-initiated shower. Moreover, the interaction depth of pions is greater than that of particles in EM cascades, so hadronic showers tend to penetrate deeper into the atmosphere. Lastly, EM showers are almost symmetric and very regular, whereas hadronic showers show wider

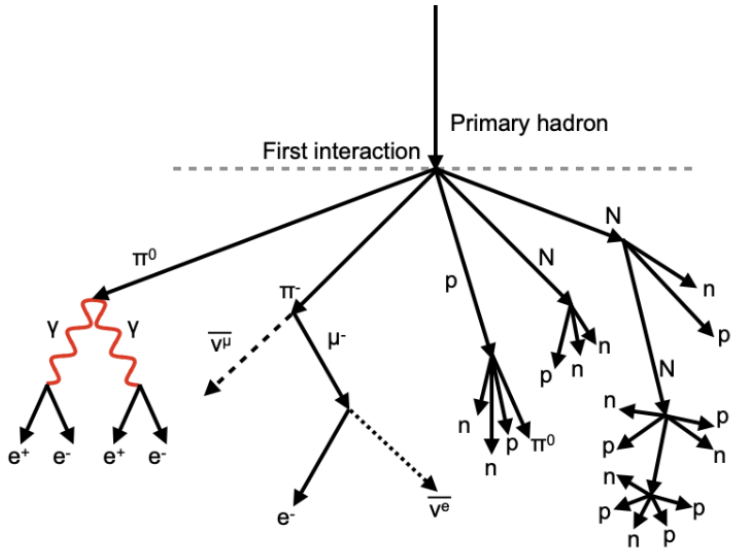

Figure 2.3: Schematic of the development of a hadronic shower in the atmosphere after a primary hadron interacts inelastically with a nucleus. The result is the production of several subshowers, some electromagnetic and others undergoing additional hadronic interactions. In hadronic showers, muons are released. Taken from [78] with explicit permission of the author.

spreads and very irregular shapes. Simulated EM and hadronic particle cascades are shown in Fig. 2.4 in the upper layer from a 300 GeV gamma and a 1 TeV proton, respectively. Gammas show a much cleaner, more regular shape, whereas proton interactions produce a messy particle cascade with multiple sub-showers. These differences in shower content and appearance are used in gamma-ray astronomy to distinguish gamma rays from protons.

2.1.2 *Cherenkov emission*

A charged particle that travels through a dielectric medium with refractive index n at a speed $v > c/n$ emits light known as Cherenkov light [80]. When a charged particle moves through a dielectric medium, it induces a dipole moment in the atoms, which then relaxes, emitting electromagnetic radiation. When the particle that traverses the medium does not travel faster than the speed of light in that medium, the radiation interferes destructively, and the resulting field is null at a certain distance. However, at relativistic speeds, the electromagnetic radiation field lines are coherent and emit light in a cone around the particle track as shown in Fig. 2.5. The angle of emission of Cherenkov light is,

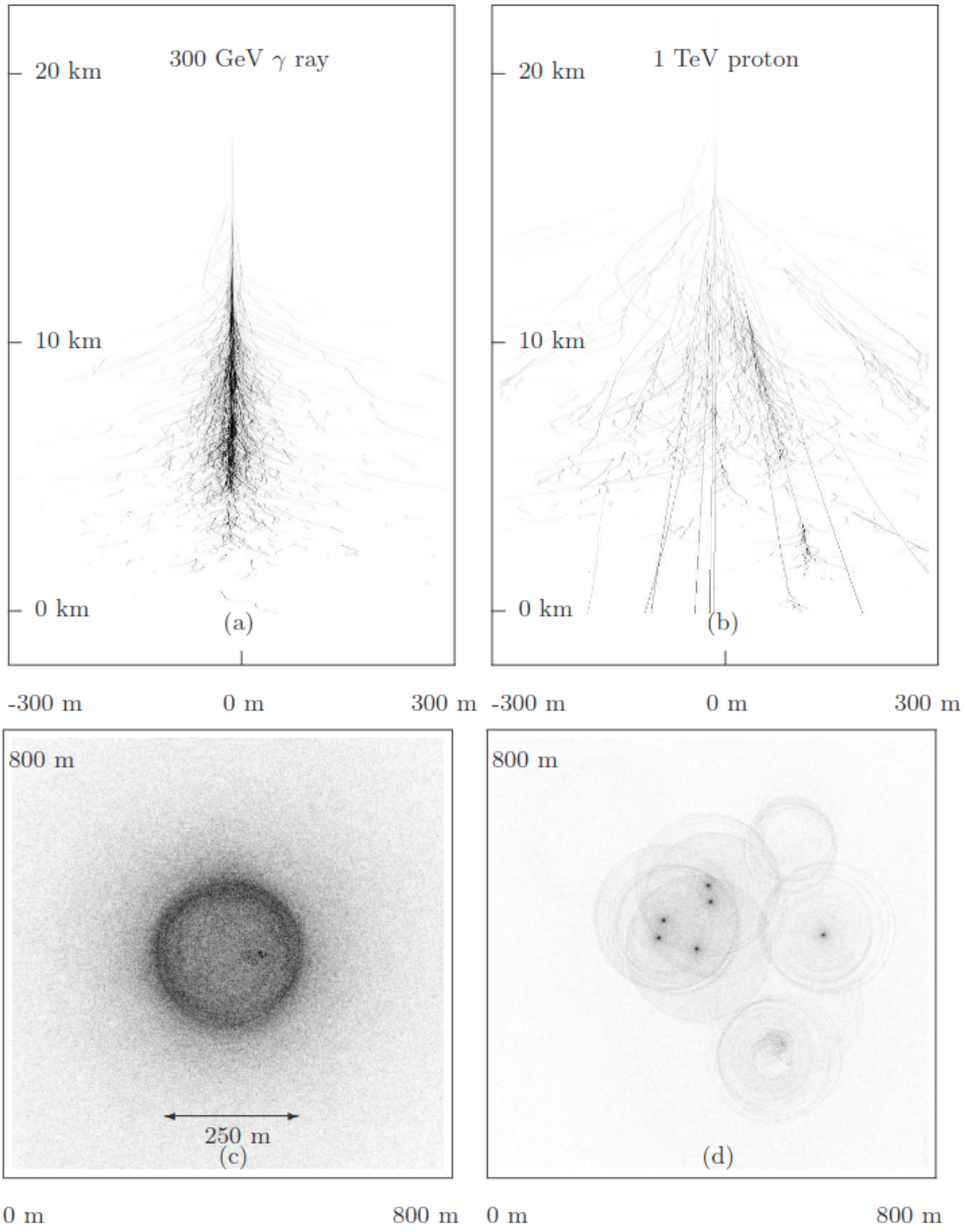

Figure 2.4: Simulation of two air showers. The left plots depict a gamma ray at 300 GeV, and the right plots show a proton at 1 TeV. The upper panel shows the longitudinal development of each shower as viewed from the side. The lower panel shows the projected Cherenkov light emitted by each secondary particle on the ground. Taken from [79] with explicit consent from the author.

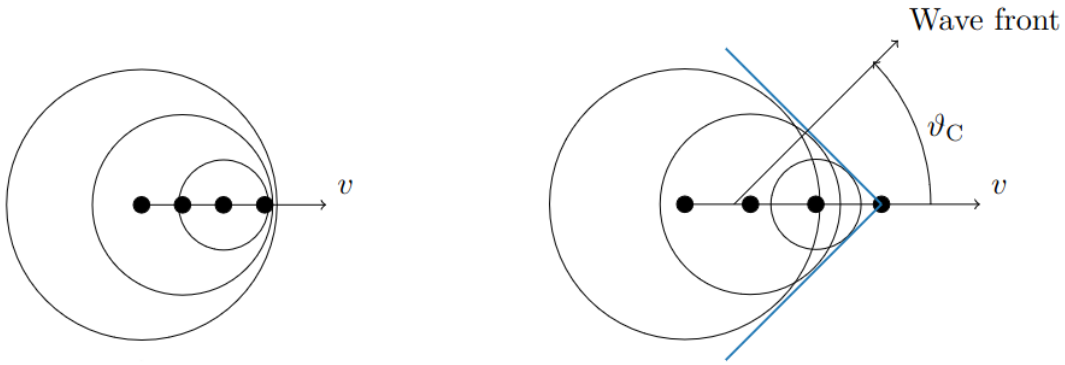

(a) $v < v_c$ **(b)** $v > v_c$

Figure 2.5: A charged particle moving through a dielectric medium when it travels lower (a) and faster (b) than the speed of light. In the first case, the electromagnetic waves interfere destructively, and no Cherenkov light is emitted. In the second case, the waves interact constructively, emitting light at an angle θ_c along the blue cone. Taken from [81] with explicit permission from the author.

$$\cos\theta_c = \frac{1}{\beta n}, \tag{2.1.1}$$

with $\beta = v/c$. θ_c typically lies between 1° and 2°, leading to a light pool on the ground of diameter $\sim 250\,\mathrm{m}$. The angle of emission depends on the refractive index of the medium; therefore, it increases with atmospheric depth. The light pool on the ground of Cherenkov light emitted by all the relativistic secondary particles with large enough energies is shown in Fig. 2.4 on the bottom panels. The simulated electromagnetic shower is more symmetric and regular, and the particles emit Cherenkov light in a constrained region. Hadronic showers are irregular and have more subcomponents. Therefore, the emission of Cherenkov light projected onto the ground indicates the spread of Cherenkov light from multiple particles in the shower. The minimum energy for a charged particle in a medium to cause the emission of Cherenkov light is:

$$E_{\mathrm{min}} = \gamma_{\mathrm{min}} m_0 c^2. \tag{2.1.2}$$

γ_{min} is the Lorentz factor and m_0 is the mass of the charged particle. The minimum speed of the particle is when $\beta = v/c = 1/n$. Therefore, the minimum energy of emission is,

$$E_{\text{min}} = \frac{m_0 c^2}{\sqrt{1 - n^{-2}}}. \tag{2.1.3}$$

For $n = 1.00029$ in air, the energy threshold for an electron is ~ 21 MeV, for a muon is ~ 4.4 GeV, and a proton emits when an energy ~ 39 GeV is exceeded. Below these energies, they do not emit Cherenkov light. The number of photons emitted per path length l and wavelength λ is given by the Frank-Tamm equation [82]:

$$\frac{dN}{d\lambda dl} = 2\pi\alpha Z^2 \lambda^{-2} \left(1 - (\beta n(\lambda))^{-2}\right), \tag{2.1.4}$$

α is the fine structure, Z is the particle charge. From this equation, it follows that Cherenkov light peaks in the ultraviolet. In the atmosphere, light at short wavelengths is scattered, and ultraviolet light below 300 nm is absorbed by ozone. This shifts the peak emission wavelength detectable at ground level to 300-350 nm in the blue region of the visible spectrum [83] [84].

2.1.3 *Imaging atmospheric Cherenkov telescopes*

Cherenkov light produced by EAS can be detected at ground level using IACTs. The emission of Cherenkov light by the particle shower reaches its peak between ~8-10 km of altitude. Therefore, the IACTs are placed on the ground at high altitudes of the order of 2,000 m to maximise the light yield captured. When multiple telescopes form an array, they are spaced so that each telescope lies within the same light pool for a single shower. This way, a single shower is more likely to be detected by multiple telescopes, leading to a more accurate reconstruction (see Section 2.4.4).

Telescopes use large mirrors > 4 m in diameter to collect the faint Cherenkov light. Cherenkov light is not only faint, but very fast. Therefore, the large mirrors collect and reflect the light onto a camera that must be fast enough to capture the shower and the differences in arrival times of light from each part of the air shower. The camera also needs to be sensitive to the blue waveband, as the Cherenkov spectrum peaks at ~300-350 nm. Photomultiplier tubes (PMTs) have historically been used in Cherenkov cameras; although other photon detectors are starting to gain relevance (for example, silicon photomultiplier in SST-Cam [85]). IACTs have limited operation times. They can record data only at night, because Cherenkov light is too faint to be detected when there is bright light. The photon detectors

can also be damaged by large light intensity and are protected during the daytime. Observations during a full moon are sometimes possible but require additional considerations and more sophisticated analysis techniques. Furthermore, the atmosphere plays a crucial role in the quality of a detection. The presence of clouds can considerably block Cherenkov light.

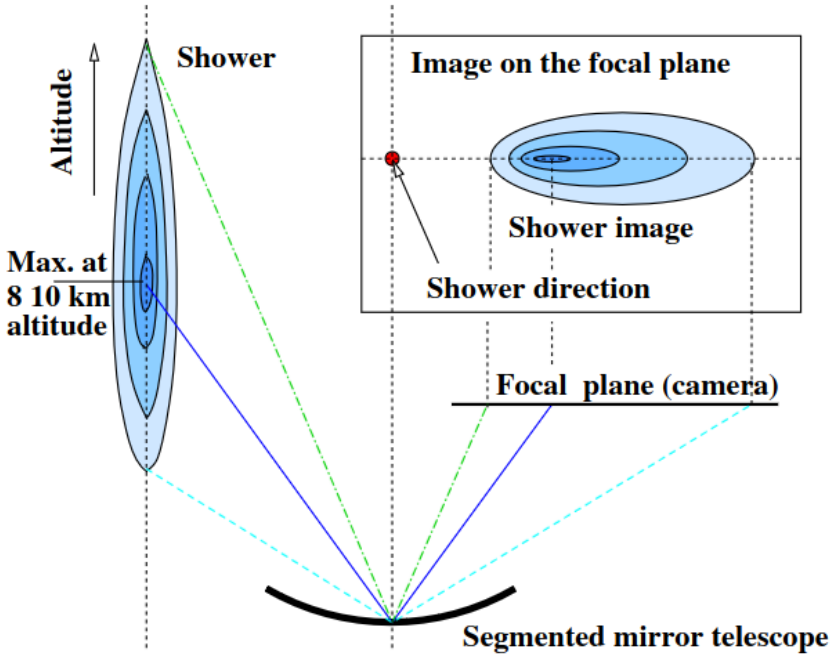

Figure 2.6: Sketch of the working principle of IACTs. An air shower with maximum development at an altitude of $\sim 8-10$ km emits Cherenkov light that is collected by the telescope mirror and reflected into a camera. The properties of the shower image are related to the original shower. The orientation of the image is used to extract the actual shower direction. Taken from Konrad Berhlöhr [86].

Showers appear as ellipses on the camera, representing the projection of the three-dimensional shower ellipsoid. The IACT principle is shown in Fig. 2.6. Light from different parts of the shower is focused into different pixels of the camera at the same angle as the angle of incidence. The resulting ellipse preserves the shower properties. The major axis indicates the shower direction, with the original shower located along it, either to the left or right of the centre. Shower asymmetry provides directional information, enabling reconstruction of the primary particle's direction and impact point from the imaged shower. These geometrical considerations show that faint, low-energy showers may be missed by the telescope at large impact distances. At large impact distances, the image becomes more elongated, and eventually part of the shower light may fall outside the telescope's FoV.

When multiple telescopes are placed within the light pool, the air shower is detected by multiple telescopes and imaged from different perspectives. These images can be combined to achieve a more accurate reconstruction or to reduce the rate of false positive triggers caused by the Night Sky Background (NSB), especially when the background is not homogeneous across the camera or when bright stars are detected.
Additionally, for any IACT, telescopes will require additional components for proper operation. Calibration devices are a key part. Inhomogeneities in camera pixels are detected by uniformly illuminating the camera at a known intensity. This is called flat-fielding. The flat-field unit is placed at the centre of the mirror, at a distance from the camera centre equal to the telescope focal length [87]. It consists of LEDs with programmable signal amplitude that provide illumination near the Cherenkov wavelength.

The technology of Cherenkov cameras

This thesis examines image reconstruction in Cherenkov cameras in detail. Specifically, in the case of the FlashCam. As this camera uses PMTs, these light detectors are the main focus of this chapter. More on FlashCam in Chapter 4.
The light reflected by the telescope mirror reaches the camera and is detected by photon detectors. The working principle of a PMT is described here.
A sketch of the multiple components of a PMT is shown in Fig. 2.7. Many types of PMTs exist for different use cases. They can have different shapes and sizes, be constructed from various materials, and be sensitive to different wavelengths. This makes PMTs adequate photon detectors for a wide range of applications. However, each PMTs contains a photocathode, a focusing chamber or electrode, a series of dynodes, and an anode.
A photon enters the PMT through the faceplate and impinges upon the photocathode. It transfers its energy to one electron in the material, which is subsequently ejected from the photocathode as a photoelectron (PE) via the photoelectric effect [88]. The PE is accelerated by an electric field generated by a voltage gradient between the photocathode and the first dynode, and it is focused in the focusing chamber. At the first dynode multiple electrons are ejected from one PE towards the second dynode. Electrons are multiplied at each dynode until they reach the anode, where they are collected. At the anode, an analogue voltage signal, also called a

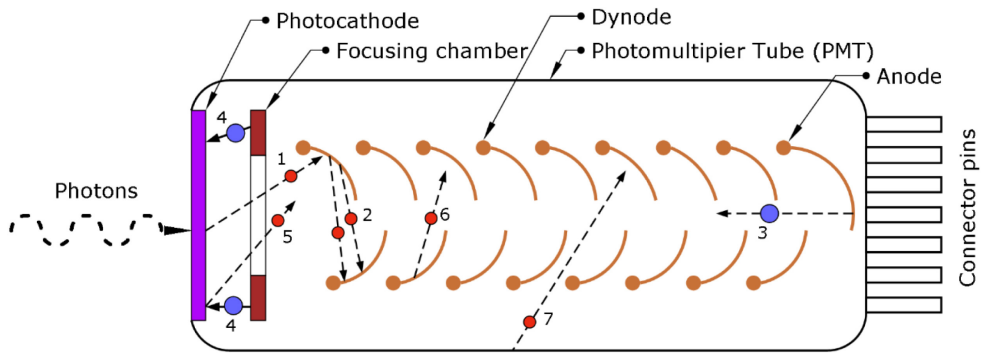

Figure 2.7: Sketch of the components of a PMT and the different paths an electron could undergo inside it. The main components are the photocathode, focusing chamber, dynodes, and anode. All these components are inside a vacuum chamber. It also reflects on the possible production of ions and their effects. Explanations for all cases are provided in the text below. Taken from [89] with explicit permission.

waveform, is produced. The signal is then digitalised using an Analogue-to-Digital Converter (ADC) to get a **trace**.

Specific parameters are particularly important for the characterisation and description of PMTs.

- **Quantum efficiency** The probability that a photoelectron is produced by an incident photon is expressed as the quantum efficiency, which depends on the photon wavelength. The quantum efficiency is the ratio of photoelectrons emitted by the photocathode to the number of incident photons [90].
- **Collection efficiency** The electrons get multiplied at every dynode stage until they reach the anode. However, some electrons may deviate from that trajectory and thus not contribute to amplification. The collection efficiency measures the fraction of PEs contributing to a signal at the anode. The total **detection efficiency** [90] of a PMT is then equivalent to the product of quantum efficiency and collection efficiency.
- **Transit time**

  The transit time of a PMT is the time it takes for a photoelectron to travel from the cathode to the anode. The transit time is not identical across PMTs, as it varies due to small geometric variations in the photoelectron interactions within them. The transit time spread (TTS) of a given pixel is quantified as the Full Width Half Maximum (FWHM) of the transit time distribution characteristic of the PMT.
- **Gain**

There are two types of gains. The first gain is relevant for traces. This gain is defined as the number of ADC counts recorded after signal digitisation per photoelectron that reaches the photocathode. The gain is computed from the peak height distribution of single PE pulses within one pixel.
The other gain is dimensionless and has a value upwards of $\sim 10^4$. This gain G of a PMT is determined entirely by the individual gains at each dynode. It is defined as the number of recorded electrons at the anode for each photoelectron.

- **Excess noise factor**
  At each dynode stage, the number of incoming electrons is multiplied by a factor known as the dynode gain. The number of electrons released (n_i) at every dynode is equivalent to the number of incoming electrons (n_{i-1}) times the gain factor of that dynode g_i. Even for an ideal PMT, the number of electrons after each stage of amplification can be known with a precision limited by Poisson statistics. The standard deviation of the number of electrons after dynode amplification is equivalent to:

$$\sigma_i = \sqrt{n_i}, \tag{2.1.5}$$

according to Poisson statistics. Therefore, the relative error at every stage is

$$\sigma_{i,r} = \frac{\sqrt{n_i}}{n_i}. \tag{2.1.6}$$

The total Poisson error in the final number of electrons that reach the anode is the quadratic sum of all the individual relative errors. Furthermore, the total number of electrons at the anode is given by:

$$n_t = n_0 \times G, \tag{2.1.7}$$

where n_0 is the initial number of photoelectrons and G is the total gain of the PMT, which is equivalent to the multiplication of all the individual gains of each dynode.
However, the total uncertainty exceeds the Poisson deviations alone. This is because a PMT is not a perfect device; among other things, electrons sometimes deviate from their trajectories and are not detected. The total noise of a PMT is referred to as the Excess Noise Factor (ENF). The ENF can be calculated from the peak height distribution. The peak height of the single

PE trace of each pixel is computed over many events, and the mean (μ) and standard deviation (σ) of the resulting peak height distribution are found. This way the ENF can be computed,

$$\mathrm{ENF} = 1 + \frac{\sigma^2}{\mu^2}. \tag{2.1.8}$$

More on the ENF and PMT-related variables in [91].

- **Afterpulses**
  Afterpulses are pulses with charges between 1 and several tens of photoelectrons that follow the signal. Different mechanisms cause them; however, the dominant afterpulse production arises from the ionisation of residual gas between the photocathode and the first dynode following interactions of photoelectrons [91]. The positively charged ions are attracted to the photocathode and interact with it, releasing several PEs that are delayed relative to the signal. The additional PEs also traverse the amplification process. The delay of these afterpulses is given by the transit time of the ions to reach the photocathode, which depends on the ion's mass-to-charge ratio. The afterpulse might appear several hundred nanoseconds (ns) after the signal. An afterpulsing probability curve with increasing afterpulse intensity is shown in Fig. 2.8.
  Fig. 2.7 shows the different paths of an electron or an ion inside the PMT. Electrons and photoelectrons are shown in red and ions in blue. Each number represents a different path an electron or ion could take. 1 is a photoelectron that is produced after the absorption of one photon in the photocathode. Photoelectron 1 reaches the first dynode from which multiple secondary electrons (case 2) are released towards the next amplification stage. 3 is an ion at the anode that travels back to the photocathode. Similarly, ions 4 drift from the focusing chamber to the photocathode. When an ion interacts with the photocathode, an electron or multiple electrons may be released (see electron 5). Finally, electrons may be spontaneously emitted from a dynode (6) or from the glass of the vacuum chamber (7). Between 3 and 7, afterpulses occur later than the signal.
  Other mechanisms for afterpulses are possible, such as photoelectrons scattering back at the first dynode [83]. However, the delay would be only a few nanoseconds, and the production mechanism is secondary.

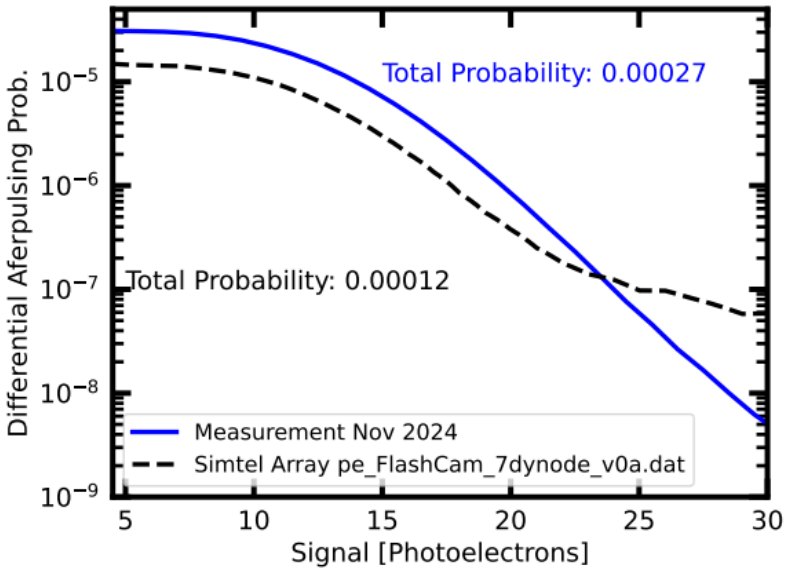

Figure 2.8: Probability of finding an afterpulse of a given intensity in photoelectrons in one pixel. The blue line shows the afterpulsing probability measured in the laboratory for a FlashCam camera. The black-dashed line shows the probability curve used in sim_telarray simulations of the camera. Provided by Simon Steinmassl.

2.2 The High Energy Stereoscopic System

H.E.S.S. is an array of five telescopes, designed to explore the gamma-ray universe. Fig. 2.9 shows the current layout of the telescope array. H.E.S.S. is located in Namibia at an altitude 1800 m above the sea level. It began operation in 2002 with its first telescope and started to take observations with four telescopes in 2004. The current H.E.S.S. array continues to observe the sky and plans to continue until 2028, but further discussions will be held as the date approaches.

Stereoscopic observations are possible with H.E.S.S., as it has multiple telescopes. H.E.S.S. has gone through multiple phases [92] [93]. Initially, H.E.S.S. consisted of only four telescopes (referred to as CT1-4) each with a mirror diameter of 12 m forming a square of edge length 120 m [94]. The telescopes follow a Davies-Cotton design [95] with a focal distance of 15 m. Each consists of 960 pixels with a size on the sky of 0.16°, which leads to a telescope field-of-view (FoV) of 5°. In 2016, the CT1-4 cameras were upgraded with new electronics.

In 2012, a fifth, larger telescope (CT5) was introduced in the middle of the square, with a mirror area of 600 m^2, equivalent to a mirror diameter of 28 m, and a camera with 2048 pixels. This additional telescope extends H.E.S.S.'s energy range and

Figure 2.9: Photograph of the layout of the H.E.S.S. telescope array. The four small CT1-4 telescopes are shown forming a square of diameter 120 m with CT5 in the middle of it. A building is visible in the foreground. This building houses the array operation site, the data acquisition system, and the trigger. Credits: Christian Föhr.

enabled detection at lower energies. The camera is mounted at a focal length of 36 m. The CT5 camera was replaced in 2019 with a FlashCam [87], which is also employed in the MSTs of the CTAO. A detailed description of this camera is provided in Chapter 4. The five telescopes lead to a detectable energy from ~ 30 GeV to ~ 100 TeV. Fig. 2.9 shows a photograph of the H.E.S.S. array after the incorporation of FlashCam in CT5. A summary of the H.E.S.S. phases and the most relevant updates is presented in Table 2.1.

Phase	Starting from	Main changes
H.E.S.S. I	2003	Initial array with four telescopes
H.E.S.S. II	2012	Addition of a fifth telescope
H.E.S.S. IU	2016	CT1-4 cameras are upgraded
FlashCam era	2019	CT5 is upgraded, installation of FlashCam

Table 2.1: Phases of the H.E.S.S. telescope array, year of the upgrade, and main changes between phases.

With the introduction of CT5 in 2012, the H.E.S.S. array introduced three trigger modes. The stereoscopic (or stereo) mode, used only in CT1-4, is configured to

trigger when two or more of the small telescopes fire within a short coincidence time window. CT5 triggers on monoscopic (mono) events; therefore, events are recorded whenever the camera is triggered. There is also a hybrid mode that includes all telescopes in the trigger scheme. In the latter mode, the array triggers when only one small telescope triggers, provided that CT5 also triggers.
Data runs are recorded for a duration of ~ 28 min to ensure homogeneity of the atmospheric conditions and stability of the instrument within each run. Calibration runs are conducted regularly to ensure accurate calibration of the observations. Furthermore, muons are continuously detected and used as a powerful calibration tool. More details on H.E.S.S. validation in Chapter 5.

2.3 The Cherenkov Telescope Array Observatory

The experience and successes of H.E.S.S., the Major Atmospheric Gamma Imaging Cherenkov (MAGIC) telescopes, and the Very Energetic Radiation Imaging Telescope Array System (VERITAS) were instrumental in establishing the field of ground-based, high-angular-resolution gamma-ray astronomy. These advancements paved the way for collaborative efforts to build a next-generation gamma-ray observatory. A large international consortium is now realising this ambitious project.
The CTAO [96] [97] is an array of multiple-sized telescopes developed by an international collaboration of scientists. It is an open observatory that will provide public access to high-level science data, unlike other on-ground gamma-ray arrays. Given the planned size of the observatory, it will achieve unprecedented resolution and sensitivity [98]. It will also provide a wider energy range, spanning from 20 GeV to 300 TeV. This will allow for the detection of approximately 1,000 additional emitting sources in the sky [96], and the Galactic plane survey is expected to detect about six times the number of sources of the H.E.S.S. survey [99]. Given that the observatory will comprise two sites in the two hemispheres, the CTAO will provide full-sky coverage.
The currently approved telescope layout is referred to as the alpha configuration. The Northern array is being built in the Roque de los Muchachos Observatory in Spain. It will consist of 4 Large-Sized Telescopes (LST) and 9 Medium-Sized Telescopes (MST) that will cover an area of $\sim 0.25\,\mathrm{km}^2$ and is located at an altitude of 2200 metres. As of the writing of this thesis, there is already one large telescope

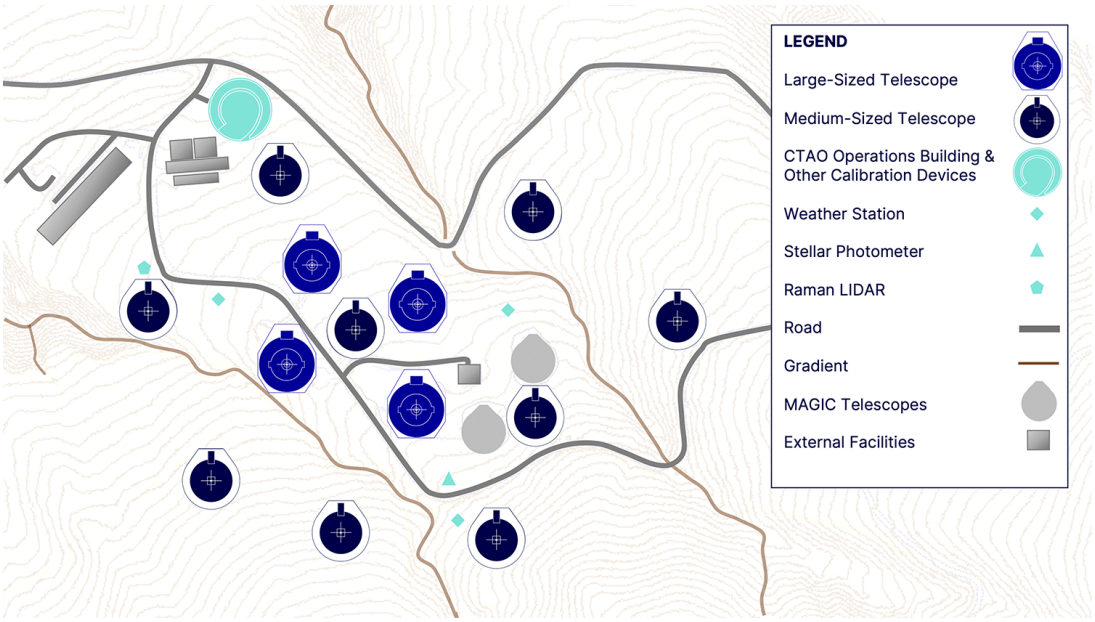

Figure 2.10: Planned telescope layout in the alpha configuration of the CTAO in the Northern array in La Palma. It consists of four LSTs and 9 MSTs. The array is located close to the two MAGIC telescopes. The telescopes are located near the observatory's operational facilities. Taken from [100].

fully operational [101] in the North and three more LSTs under construction. The Northern array planned telescope layout is shown in Fig. 2.10.
The Northern array will be limited to the low- to mid-energy range due to size constraints, whereas the Southern array, with a larger extension, will focus on higher energies. The Southern Hemisphere Array is being built at the Paranal Observatory in Chile. It will consists on 14 MSTs and 37 Small-Sized Telescopes (SST) extended over an area of $\sim 3\,\mathrm{km}^2$. The collaboration also plans to enhance the Southern array with four LSTs and three additional SSTs. Fig. 2.11 shows the alpha configuration of telescopes in the Southern array.
The LST [102] has a parabolic mirror with a diameter of 23 m and an effective mirror area of $370\,\mathrm{m}^2$. It comprises a PMT-based camera with 1855 pixels, each with a FoV of 0.1 deg, yielding a telescope FoV of 4.3 deg. The LST is designed to detect low-energy events because its larger collecting area increases the likelihood that they are captured.
The SST employs a dual-mirror Schwarzschild-Couder telescope design with a primary mirror of 4.3 m and a secondary mirror of 1.8 m in diameter [103]. The SSTs have a total telescope FoV of 8.8 deg.

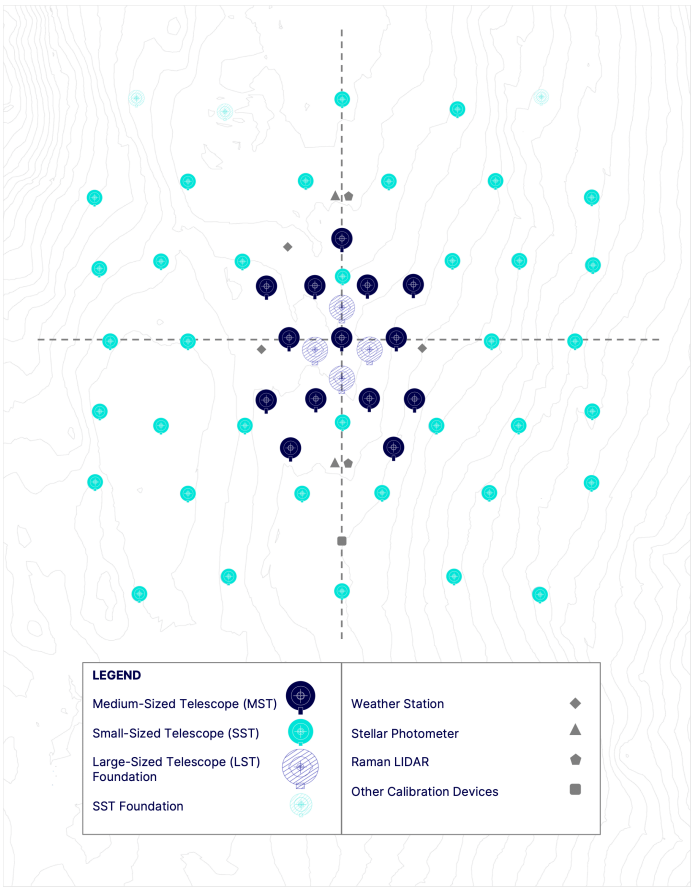

Figure 2.11: The CTAO planned telescope layout in the alpha configuration in the Southern array at the Paranal Observatory in Chile. It will consist of 14 MSTs and 37 SSTs. The enhancement of the array with four LSTs and more SSTs at the centre of the array is considered. The telescopes are located near the weather station and other calibration devices. Taken from [100].

On the other side, the MSTs have a modified Davis-Cotton mirror design with a diameter of 11.5 and an effective area of 88 m^2 [103]. Two different cameras will be installed in such telescopes, FlashCam [104] in the South and NectarCAM [105] in the North. Both cameras are composed of PMTs and have 1758 and 1855 pixels, respectively. The pixel FoV is 0.17 deg for both cameras, resulting in telescope FoV values of ~7.5 deg and ~7.7 deg, respectively. The technical specifications of each telescope are described on the CTAO website [103]. The three telescope types are shown in Fig. 2.12.

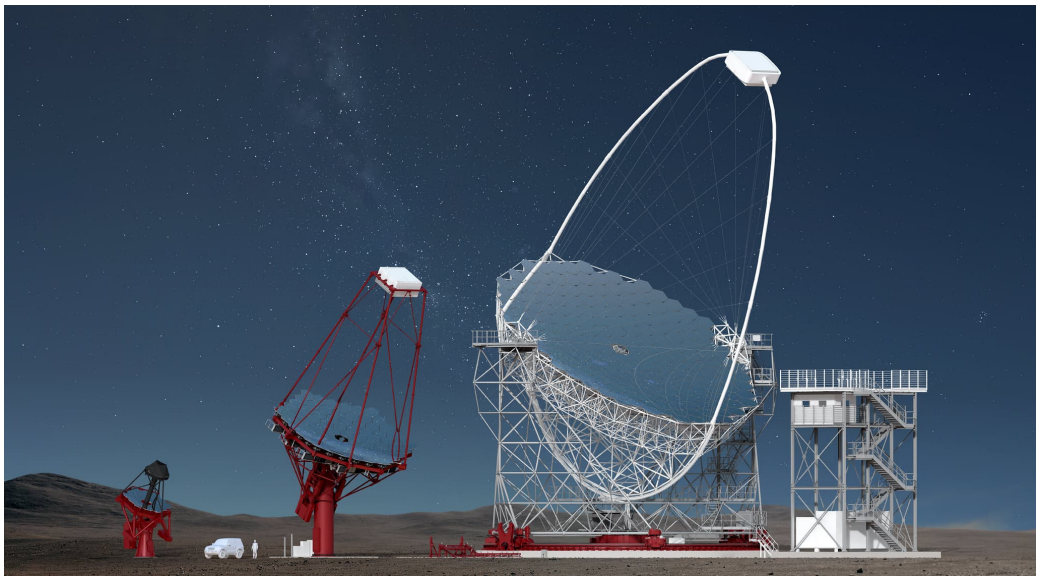

Figure 2.12: The three approved telescope designs of the CTAO [106]. From right to left, the large-, medium-, and small-sized telescopes are shown. Credit: Gabriel Pérez Díaz (IAC).

2.3.1 *Data calibration*

The description of the data chain and calibration will be provided as needed for the FlashCam Cherenkov camera.
The output of each pixel of each camera of the CTAO is an electric pulse in units of ADC counts or least significant bit (LSB) as a function of time. The ADC counts are converted into number of photoelectrons N_{PE} collected at the photocathode after applying the following calibration [107],

$$N_{\mathrm{PE}} = \frac{\mathrm{ADC} - \mathrm{Pedestal}}{G}. \tag{2.3.1}$$

The pedestal level (baseline) of each pixel is already calculated by FlashCam in the front-end electronics and transmitted to the camera server. The trace amplitudes are divided by the gain (LSB/PE) and converted to the number of PEs. The time offsets between pixels are adjusted in hardware in nanosecond (ns) steps, so that all pixels peak at the same time.
Additionally, flat-field runs will be measured regularly before observation begins to account for pixel-to-pixel gain variations. The PMTs are gain matched by adjusting their operational voltage to a precision of ±0.5%. Lastly, broken pixels will be flagged. Raw (or R0) traces received by the camera server are converted into the

so-called R1 traces following this precalibration procedure. Similar calibration is undergone for H.E.S.S. [108].
An offline, more detailed calibration will complement the previous online calibration routine once the data are stored. Pedestal and flat-field runs are recorded and stored by the observatory for subsequent calibration improvements. The pixel baseline is corrected if necessary, and the traces are multiplied by a flat-field coefficient that accounts for intensity differences among pixels under the same illumination. The peaks of the trigger traces are realigned, now using time corrections to achieve a maximum inhomogeneity in trigger time of ±500 ps for a flatfield run with an average intensity of ~ 50 PEs.
Furthermore, the telescope's optical throughput must be calibrated to accurately reconstruct the primary particle's energy. There are multiple components in a telescope that could lead to a degradation in light detection, such as the mirror reflectivity, the light cones, the quantum efficiencies of the photon detectors, etc [109]. The entire optical throughput of the telescope can be calibrated using the detection of full muon rings on the camera (see Section 4.2.1 and Section 5.1.3), as their light yield can be accurately predicted and compared with the detected light content.
ctapipe [110] is the prototype analysis software for the CTAO. It includes analysis techniques from R1 (pre-Data Volume Reduction) through DL2.

2.3.2 *The CTAO data chain*

A schematic representation of the CTAO data chain is shown in Fig. 2.13. The data path begins with the telescopes on-site. The observatory schedules data recording for these telescopes. At the camera level, the lowest data level is the R0 raw traces. These are uncalibrated traces. The traces undergo a basic precalibration process as explained in the previous section. The result is precalibrated R1 traces. The R1 data level also includes trigger time stamps and event type flags that classify each event as a Cherenkov shower, flatfield event, muon, or other calibration event. The following steps in the data chain require various software systems within the CTAO. Each is responsible for different stages of the data evolution. Some important software systems are [103] [111]:

- the Array Control and Data Acquisition (ACADA)
- the Data Processing and Preservation System (DPPS)
- the Science User Support System (SUSS)

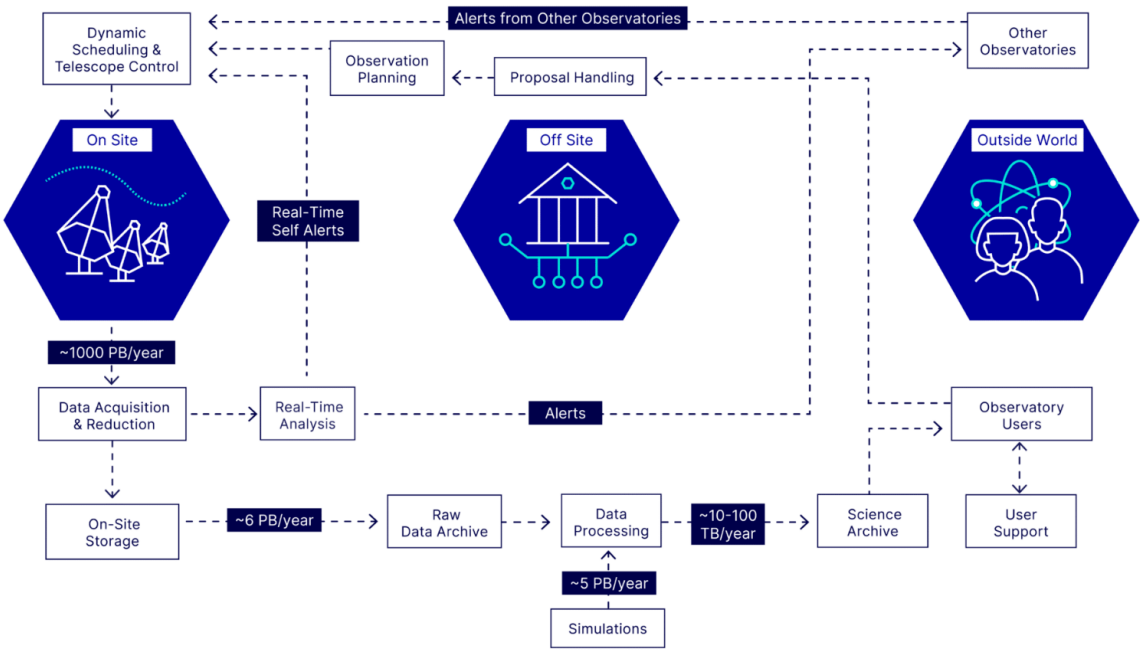

Figure 2.13: The CTAO data chain from observation proposal requests, through observation, data reduction, and storage, to final data processing supported by simulations. Taken from [106].

ACADA [112] comprises multiple subsystems. ACADA is responsible for controlling each telescope in the array and executing observations in accordance with previously determined time allocations and observation schedules. ACADA also determines when calibration runs should be performed for each telescope. The Array Data Handler (ADH) [113] within ACADA includes the Software Array Trigger (SWAT) instance, which identifies temporal coincidences among the triggers of each telescope. An event is considered to have triggered on the array when a coincidence trigger is detected. When the telescope array triggers, the R1 traces are sent from the camera servers to ACADA.

Events that pass the multiplicity trigger condition then undergo Data Volume Reduction (DVR). This is a key step in the CTAO data chain. The trigger rates of the observatory are too high to be efficiently stored by the observatory in the long term. This holds especially true because the CTAO, unlike other current IACT detectors, will store traces rather than only the charge and time of each pixel, as explained in the next section. Considering the number of telescopes, pixels, and time samples that must be stored, the resulting data volume is excessive. DVR will perform a rapid reconstruction of the image recorded by each telescope and,

from it, reduce the data volume by sending only pixels that appear to contain a Cherenkov signal and only a selection of signal samples within each trace to the DPPS. DVR will reduce data volume by a factor of 50. After DVR, lossless compression is applied, reducing the data volume to ~ 10 Petabytes (PB)/year [111], compared with the hundreds of PB/year before DVR (Fig. 2.13). The result is a subset of R1 traces, each cropped, which are referred to as DL0.
The ADH will also send DL0 data and calibration runs to the Science Alert Generation (SAG) [114] system, which will issue alerts to the astrophysical community if a transient phenomenon occurs. The SAG system is required to perform a fast, real-time analysis of the data [115] and to send science alerts within 20 seconds of receiving the data. During those 20 s, SAG reconstructs DL0 to DL3 with at least half the sensitivity of the offline analysis.
The raw DL0 output from ACADA is processed offline to reach final science-ready products by DPPS. DPPS is responsible for recalibrating the DL0 traces using calibration runs and muons. Then, the data undergoes multiple analytical techniques until scientific products are produced; details are provided in the next section. The analysis techniques employed by DPPS require a sufficient number of simulations [116]. Therefore, DPPS also includes the Simulation Production Pipeline system. DPPS will be able to reprocess the data when updated techniques become available, and for cross-checking. The science products are finally sent to SUSS. This system, together with the Science Operations Support System (SOSS), manages observation proposals, delivers data to users, and provides software tools for mid- and long-term observation scheduling.

2.4 IACTs offline reconstruction pipeline

In this section, a description of the data levels and standard analysis techniques employed in gamma-ray astronomy is provided. The discussed reconstruction pipeline is generally employed by IACTs, with specific details for CTAO and H.E.S.S. highlighted throughout the chapter.
After on-site data acquisition, the data is stored and analysed. There are multiple steps towards the final scientific output (Fig. 2.14). In the CTAO, the reduced traces of each pixel that passes the on-site Data Volume Reduction (DVR) will be stored. The DL0 data level is the raw output of the Array Data Handler and the lowest level permanently stored by the observatory. DL0 traces have some

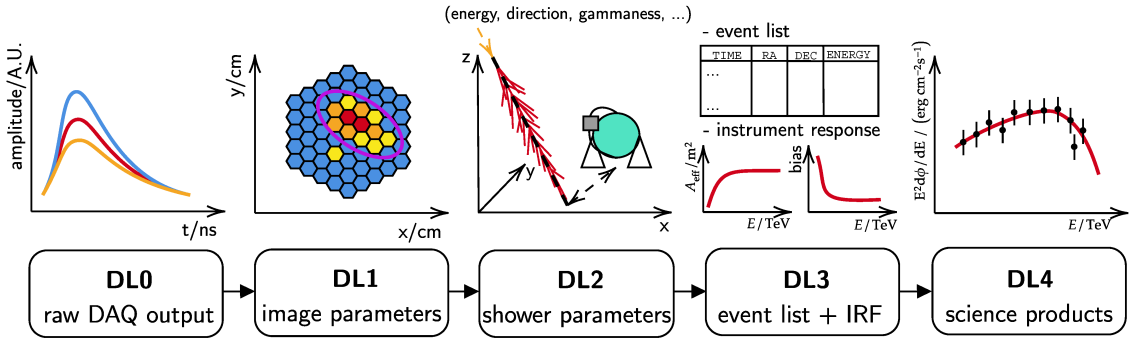

Figure 2.14: Schematic of the data levels and their products. This sketch, made for the H.E.S.S. data levels, remains valid for the CTAO. The raw data after precalibration and data reduction (DL0) form an image, which is cleaned and parameterised as DL1. The shower parameters are reconstructed (DL2), and the instrument response functions and event lists are computed (DL3) to produce the final science products. Taken from [118].

precalibration applied, but are recalibrated off-site and with higher precision. Then, the charge and time of photoelectrons are extracted, forming images on the camera. The image in charge units is reduced to a set of parameters, yielding DL1. Unlike CTAO, H.E.S.S. stores only the number of PEs and the time of arrival per pixel over the long term, rather than full traces. Furthermore, no DVR is required as the number of telescopes and the data rates are much lower. The parameter set is used as input to the shower reconstruction algorithms, which compute the energy, direction, and particle type, collectively referred to as DL2. The accuracy of these parameter reconstructions is evaluated using simulations, yielding DL3 output-quality plots. Finally, the science products are extracted (DL4). A detailed explanation of the multiple data levels can be found in [117].

2.4.1 *Monte Carlo simulations*

Shower analysis techniques aimed at reconstructing the energy and direction of the initiating particle require simulations that accurately model both the shower development and the Cherenkov light emission, as well as the instrument's response to this light. These simulations are also essential for precise detector calibration. The simulation process involves two main steps: first, modelling the development of air showers and the emission of Cherenkov light from secondary particles; second, implementing a detailed representation of the instrument and its response to

Cherenkov light. The first step of the simulation is performed by CORSIKA (COsmic Ray SImulations for KAscade) [119] and the second by sim_telarray [120].
The CORSIKA package can initiate showers with multiple primary particles: gamma rays, protons, electrons, muons, or heavy nuclei. Primary particles can be simulated with different initial energies and emission angles. CORSIKA simulates the development of EAS with different hadronic interaction models; the QGSJET-II [121] model is commonly used. Additionally, CORSIKA also simulates the emission of Cherenkov light from the secondary particles. With the IACT package of CORSIKA, the telescopes can be simulated in arrays at positions defined in three dimensions by (x_i, y_i, z_i). CORSIKA requires large CPU times to run. Therefore, each shower can be reused multiple times with the telescope array at different displacements with respect to its simulated position.
The CORSIKA output is piped into sim_telarray, which simulates atmospheric extinction and instrument response. sim_telarray [122] is highly flexible for simulating a wide range of instruments and telescope layouts. Many configuration parameters govern the detector's properties, including optical efficiency, trigger settings, mirror reflectivity, and so on. The transmission of Cherenkov light through the atmosphere is modelled with detailed atmospheric transmission tables. The simulations can be run with different NSB levels, either homogeneous or inhomogeneous, by inputting files that capture the actual appearance of the night sky. The output of sim_telarray is pulse shapes for each pixel of the camera. Pulses are generated by accounting for the telescope's reference pulse shape, provided by the telescope teams, the NSB level, optical ray tracing, PMTs' collection efficiencies, digitalisation, and so on. Furthermore, the output simulation file also contains the simulated "true" parameters. The simulations include the actual number of photoelectrons reaching each pixel, which can be compared with the reconstructed charge extracted from the pulse shape. Simulations are used to generate look-up tables for reconstructing the properties of primary particles.
These simulations are used for both H.E.S.S. and the CTAO and are highly accurate. They provide a valuable tool for validating the analysis chain, from trace calibration to final shower reconstruction. sim_telarray also helps in understanding the instrument and its components. Different telescope array configurations can be tested, and the best option identified through simulations.

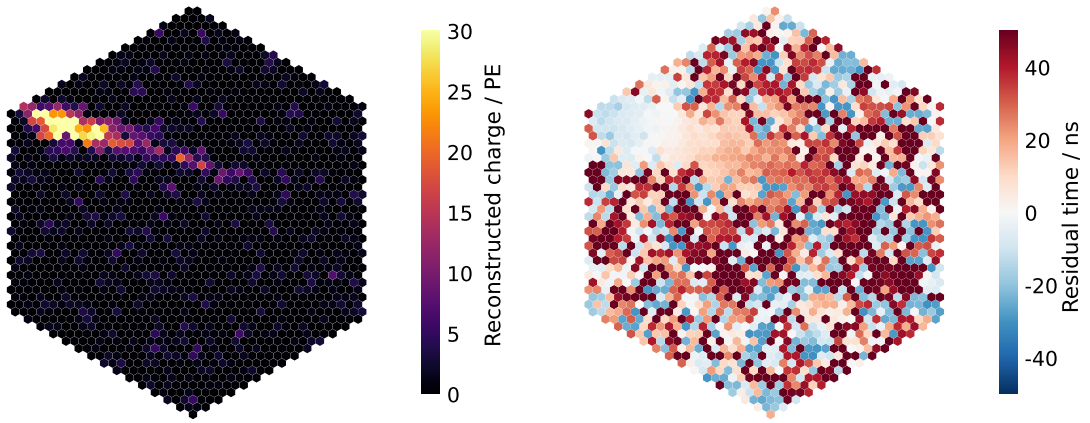

(a) Reconstructed charge

(b) Reconstructed time

Figure 2.15: A camera plane showing the reconstructed number of PEs (left) and the average arrival time per pixel (right). The arrival time is shown after subtracting the charge-weighted average time across all pixels.

2.4.2 *Image extraction and cleaning*

DL0 traces are recalibrated and then reconstructed into the total number of PEs released by the photocathode and the average arrival time of these photoelectrons. Charge reconstruction is typically performed by integrating the traces from each pixel within a window. Since the arrival time at which each photon hits a given PMT cannot be directly extracted, the average arrival time of all photoelectrons within a pixel is calculated instead, typically using the centre of gravity of the pulse within the window. This step yields the integrated charge and average arrival time for each pixel. Fig. 2.15 shows a simulated 1 TeV proton shower as observed by the FlashCam camera after charge and time reconstruction. Fig 2.15a shows the reconstructed charge of each pixel in the camera plane, whilst the corresponding image in units of reconstructed time is shown in Fig. 2.15b. The colour bar of Fig. 2.15b represents the difference between the reconstructed time and the charge-weighted average time across the camera, demonstrating that photoelectrons arrive within a narrow temporal window, forming a time cluster with a characteristic time gradient. No DVR step is applied before signal extraction for making Fig. 2.15. However, because the online DVR step is quite loose to avoid discarding signal pixels, the image still contains pixels with only noise, and after image extraction, their intensities follow a distribution with mean zero and variance proportional

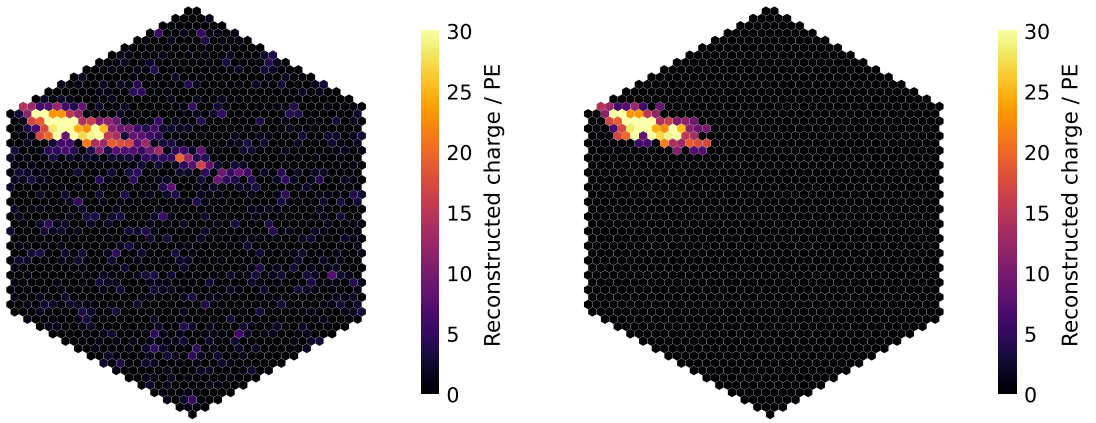

(a) Before cleaning **(b)** After cleaning

Figure 2.16: A shower image before and after image cleaning with Tailcuts. The left plot shows the reconstructed charge for each pixel, whilst the right plot shows only pixels that pass the cleaning criteria. Tailcuts is applied with the cuts (9 PEs, 5 PEs, 2) on the picture, boundary threshold and number of neighbouring pixels, respectively.

to the NSB rate. Furthermore, noise pixels arrive randomly and exhibit no pixel-to-pixel time correlations, unlike the signal. Pixels with only noise can lead to inaccurate estimates of shower parameters. Therefore, the image is cleaned to significantly reduce the number of noise-only pixels. The most common image cleaning approach applies multiple intensity thresholds to individual pixels. For example, the Tailcuts [123] algorithm is amongst the most well-known methods. In Tailcuts, two thresholds are defined: the picture threshold and the boundary threshold. All pixels above the picture threshold pass the cleaning. Additionally, pixels with intensity higher than the boundary threshold pass if they have more than N neighbouring pixels that pass the picture threshold. The result is an image that closely resembles an elongated ellipse with a shortened tail (see Fig. 2.16b), reflecting the "tail cutting" that gives the method its name.
After cleaning, the reconstructed times within the ellipse in Fig. 2.15b are shown in Fig. 2.17 along the longitudinal (major) axis of the shower. This axis corresponds to the direction of the shower's motion. The data points exhibit a clear linear relationship, demonstrating a temporal gradient along the major axis of the elliptical image. This gradient arises from travel-time differences: light from different parts of the shower travels different distances to reach the telescope dish.

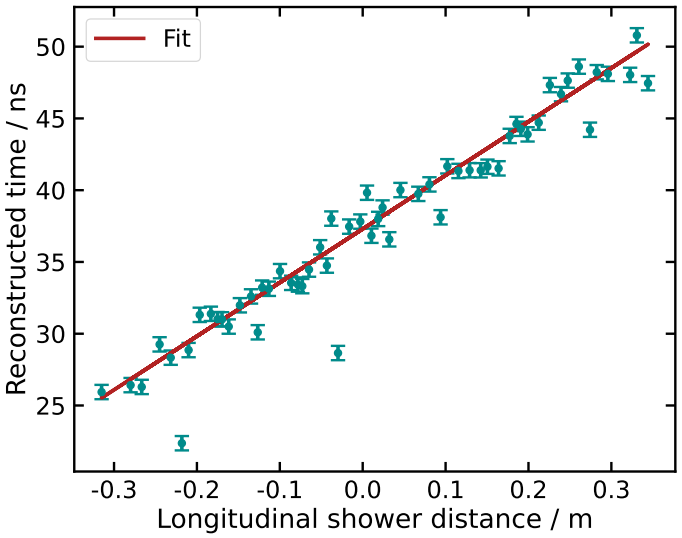

Figure 2.17: The reconstructed time of each pixel as a function of its longitudinal distance with respect to the centre of gravity of the shower. The values are obtained from Fig. 2.15b for pixels passing the cleaning seen in Fig. 2.16b. The red line shows the linear fit through the points.

2.4.3 *Image parameterisation*

The cleaned images can be reduced to a set of parameters that characterise their shape. gamma and proton-initiated showers have a different development in the atmosphere, as discussed in Section 2.1.1. The various shower developments are imaged on the camera plane, exhibiting distinct characteristics. Therefore, this set of parameters that resumes every image should be able to capture the differences in the shapes of these two types. In particular, gamma-ray showers are imaged as more elliptical and regular on the camera. The Hillas parameters [124] use moment analysis to compute the image parameters. A detailed explanation of Hillas parameters, on which this section is based, is given in [125].
The Hillas parameters are calculated from the DL1 cleaned image, assuming the shower image is elliptical. Some of these parameters are sketched in Fig. 2.18. An additional parameter is the image size, defined as the sum of the intensities of each pixel after cleaning. The location of the image in the camera is given by the image's centre of gravity (COG) (C in the diagram). The COG is at a distance (*dist*) from the camera centre [126]. The shower orientation is given by the *miss* parameter, which is the perpendicular distance between the major axis and the camera centre. α also indicates the image orientation. It is defined as the angle between the major

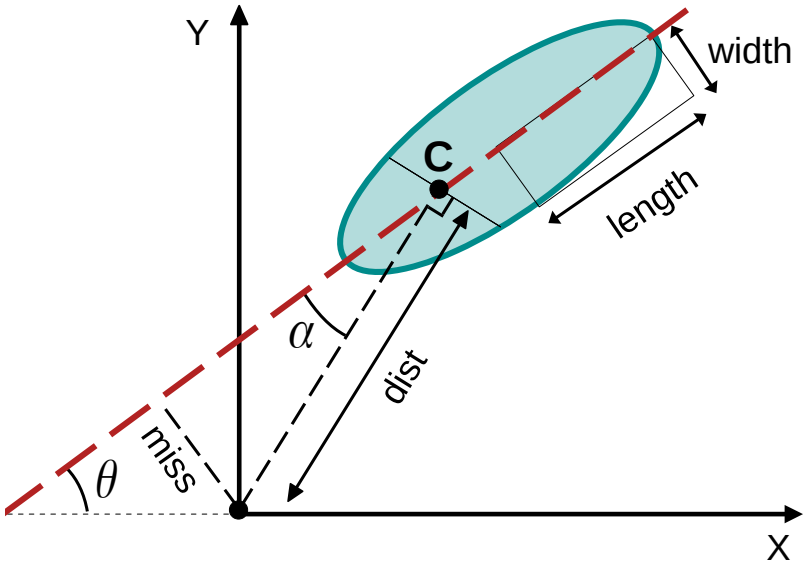

Figure 2.18: Schematic view of the Hillas parameters of an imaged shower with respect to the camera coordinates (x, y). The image is simplified to an ellipse, with the centre slightly asymmetric. Some important Hillas parameters are highlighted in the sketch. The imaged shower extension and direction resemble the shape of the original shower.

axis and the line that goes through the camera centre and the image centroid. Furthermore, the shower extension is given by the image's *length* and *width*, which are the root-mean-square (RMS) values of the charge content along the major and minor axes, respectively. One can also compute the *azwidth*, which provides a measure of the image extension and is equivalent to the RMS of the charge spread perpendicular to the line connecting the centroid to the camera centre.
Another important parameter for subsequent analysis is the *leakage*. The *leakage* is the fraction of the signal after cleaning that is located in the outer two rows of pixels. Furthermore, higher-order moments are required to better characterise the image's shape. The *skewness* provides a measure of image asymmetry, which can be used in gamma-hadron separation. Moreover, *kurtosis* provides an estimate of the distribution's tail heaviness. Some of the parameters described here can be used to distinguish between protons and gammas, as their distributions differ. Hadronic air showers exhibit significantly larger *skewness* and *kurtosis* than electromagnetic showers, reflecting their greater asymmetry and heavier tails. Moreover, these parameters can be used as inputs to energy reconstruction algorithms, as described in the next section.

2.4.4 *Shower reconstruction*

The CTAO will store events only when triggered by at least two telescopes, known as stereoscopic (or stereo) events. Monoscopic (mono) events, which trigger on only one telescope, will not be included in the reconstruction, unlike the H.E.S.S. telescope array, which operates in multiple modes, triggering on mono events with CT5 and on stereo with CT1-4. Monoscopic reconstruction is used in H.E.S.S. to trigger on lower-energy events, but it is less accurate for reconstruction. The stereoscopic condition provides a much more accurate derivation of the shower characteristics. In this section, only the reconstruction of stereo events is presented, as monoscopic reconstruction is not considered in the thesis.

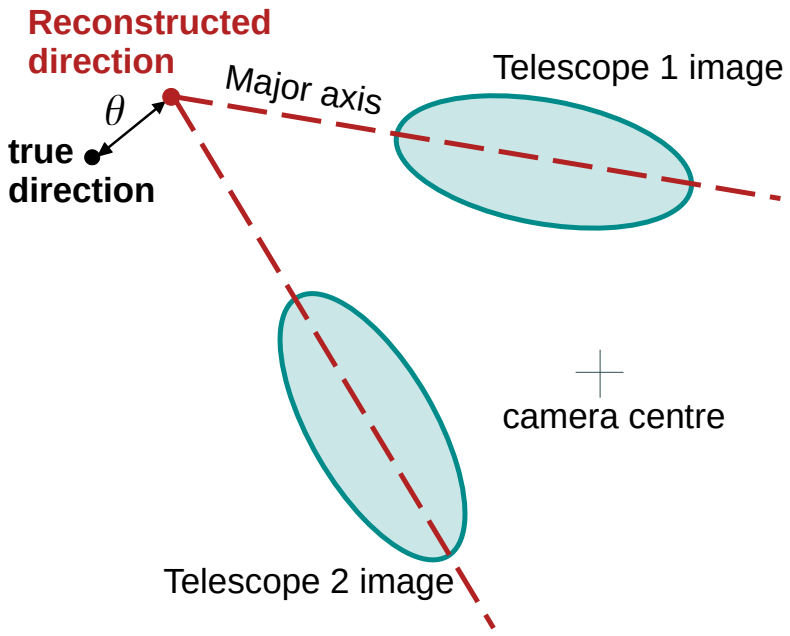

Figure 2.19: Schematic of the reconstruction of a primary particle direction. The shower event is recorded by two telescopes and imaged by their cameras. The two images are combined into a single frame. The direction of the primary particle is the intersection of the two major axes. This reconstructed direction deviates from the true direction by θ.

The reconstruction of stereo events is described in more detail in [127]. Hillas parameterisation yields several basic shower parameters, including the image's major axis, which points towards the shower's major axis. For stereo reconstruction, a single event is recorded and imaged by multiple telescopes. All unique image

pairs from the event are constructed, and the intersection of the major axes of each of these pairs is computed. The final intersection of the event is the average of the pairwise intersections, weighted by different weighting schemes. Commonly, each image is weighted with the Hillas intensity times the ratio of the Hillas length over Hillas width. The final weight of the telescope pair is the product of the two individual weights. The core position of the shower is then computed as the weighted average of these intersections.

The shower direction is similarly computed as the intersection of the camera planes for each pair (see Fig. 2.19), using the same weights [95]. Similarly, the height at which Cherenkov emission peaks can also be determined in a similar way. Note that energy and direction reconstruction are performed only on images that exceed a certain size and intensity thresholds. Typically, a cut is made in the total number of photoelectrons detected by the camera and in the total number of surviving pixels after cleaning. This way, the reconstruction accuracy is not affected by low-signal images that lack substantial information.

The energy is reconstructed using a random forest regressor. The regressor is trained on simulations that provide input parameters encoding image properties; in the cases of CTAO and H.E.S.S., the Hillas parameters, among others, are used. Then, using simulations, the regressor is trained on a subset of events and is then used to predict the energy of the remaining test events from their image parameters. For stereo events, the energy predictions from each telescope that trigger on the event are combined to yield a per-event energy estimate. This is done by simply averaging, occasionally with a weighting factor similar to that described previously. It is important to note that the number of photoelectrons detected by each camera depends not only on the primary particle's energy but also on the shower's geometry relative to the telescope. For example, the telescope's pointing direction is a crucial factor to consider in reconstruction. At large zenith angles, the air shower traverses more atmosphere, spreading over a larger region, also resulting in fainter illumination for each telescope. Therefore, the regressor is trained on simulations of different zenith angles. Furthermore, the shower core's impact distance relative to the telescope also plays a role. The regressor is also typically trained on the reconstructed impact distances.

Template-based reconstruction

Previous reconstruction methods are limited to using only image parameters that describe certain aspects of the image, rather than fully capturing it. More sophisticated methods instead use the entire image and perform a fitting routine on it to a set of template images from simulations. With this approach, all the available information from the cleaned image is used for reconstruction. One of these methods is the Image Pixel-wise fit for Atmospheric Cherenkov Telescopes (ImPACT) [128]. Gamma-induced showers are simulated together with the IACT array, as described in Section 2.4.1. Template gamma-ray images are built from these simulations. The detected images are fitted to the template images using a maximum-likelihood method. The method uses the outputs of previous Hillas-based reconstruction methods as seeds. As a result, the recorded image is associated with one of the template images, and the energy and directions are reconstructed. This leads to a significant improvement in the shower reconstruction.

Gamma-hadron separation

The final step toward the DL2 data level is classifying showers as initiated by gamma particles or hadrons. This is a crucial step, as the vast majority of events detected by telescopes are protons. Particle classification is performed by comparing image properties of the two particle types that initiate showers. The first generation of IACTs employed a gamma classification based on simple cuts in image parameters [129], mainly from the DL1 data levels. Currently, more complex and sophisticated methods use machine learning algorithms, such as neural networks [130] and boosted decision trees [131].
Machine learning algorithms are trained on specific image features extracted from shower simulations of known ground-truth classification. Training data are either gamma-ray simulations or so-called off-events. These off-events typically are background events recorded by telescopes when pointed away from any gamma-ray source, so that only protons are detected. Proton simulations are generally avoided due to substantial uncertainty in hadronic models. As explained earlier, the model is trained only on sufficiently large images; therefore, image-size cuts are performed. The training is performed independently for each zenith and azimuth angle as before.

For each event and telescope, the images are associated with a single particle-classification score, or *gammaness*. This is a measure of how closely the image resembles a gamma shower, as determined by prior training. Then, each telescope that triggers on a given event has a gammaness score for the same shower. The scores from each telescope are combined into a single *gammaness* probability by averaging across telescopes, with weights assigned based on image size, reconstruction quality, or related factors. A cut on the *gammaness* is applied, and events with values below the cut are rejected.

2.4.5 *Instrument Response Functions*

The Instrument Response Functions (IRFs), and the reconstructed event lists constitute the DL3 data level. The IRFs store the probabilistic response of the instrument and analysis chain to events with their given properties. The IRFs store the information on how accurately the shower properties are reconstructed for simulated events. This includes the precision of energy and direction reconstruction relative to the simulated true values, as well as the residual background rate after gamma-hadron separation. It also includes the array's collection area. The IRF is, therefore, given by the following equation,

$$R(\overrightarrow{p}_{\text{reco}}, E_{\text{reco}} | \overrightarrow{p}_{\text{true}, E_{\text{true}}}) = \text{Aeff}(\overrightarrow{p}_{\text{true}}, E_{\text{true}}) \times \text{PSF}(\overrightarrow{p}_{\text{reco}} | \overrightarrow{p}_{\text{true}}, E_{\text{true}}) \times E_{\text{disp}}(E_{\text{reco}} | \overrightarrow{p}_{\text{true}}, E_{\text{true}}) \tag{2.4.1}$$

where $\overrightarrow{p}_{\text{reco}}$ and $\overrightarrow{p}_{\text{true}}$ are the reconstructed and true positions of a gamma ray in the sky, respectively. E_{reco} and E_{true} are the reconstructed and true energies of the particle, respectively. Furthermore, Aeff is the effective area, PSF is the point spread function, and E_{disp} is the energy dispersion.

Effective area

The effective area, or collection area, is the total ground area over which the array is sensitive to gamma rays. The effective area depends on the shower energy, the telescope zenith angle, the azimuth angle, and the offset angle between the shower and the telescope pointing direction, since telescopes do not always detect on-axis showers completely. The effective area can be calculated from gamma-ray

simulations as the ratio of the number of gamma events that trigger on the array and pass quality cuts to the total number of simulated events, multiplied by the array's area over which all gamma-ray showers are simulated. The effective area is typically expressed in units of m^2 and is shown as a function of the simulated true energy. `pyirf` has been studied as a tool to provide IRFs to the CTAO [132].

Energy dispersion

The energy dispersion is the probability that a gamma ray with true energy E_{true} is reconstructed with an energy E_{reco}. The precision with which energy is reconstructed is sometimes quantified by the energy resolution. The energy resolution can be described as the Root Mean Square (RMS) of the reconstructed energy distribution for a given true energy bin.

Point Spread Function

The PSF is a measure of the accuracy of the direction reconstruction of a gamma-ray shower. The PSF is typically expressed as the angular distance from the direction of the source that contains a given fraction of the events. The 68% containment is usually used. As before, the angular resolution depends on the offset and zenith angles, as well as the true energy of the primary particle.

Background rate

This is the rate of background events that survived the particle classification. These are protons that appear gamma-like and, therefore, survived the gamma-hadron separation step. At lower energies (below ~1 TeV), there is also an electron contribution. Unlike the previous quantities, the background rate is computed from proton simulations, or, more precisely, from off-run real events.

2.5 High level analysis

The high-level analysis is performed by *gammapy* [133], which takes the DL3 as input and produces science products. *gammapy* can be applied to data from different gamma-ray detectors, from Cherenkov telescope arrays (such as H.E.S.S. and CTAO), water tanks (HAWC) or space detectors (Fermi-LAT). This can be done with a standard DL3 data format, GADF [118]. The DL3 data consist of

the previously described IRFs and lists of events with a high probability of being gamma rays, including reconstructed direction and energy, and the event time, defined as the observation time for each event. Event classes are also supported. Each event class has its own IRF, sensitivity, and quality cuts.
gammapy has recently become the primary scientific tool for analysing gamma-ray sources across multiple detectors, such as H.E.S.S. ([134], [135]), and it will be the standard science analysis tool for the CTAO ([136], [137]).

2.5.1 *Data reduction*

Events from DL3 are binned into a 3D sky map: longitude, latitude, and energy. Celestial coordinates are projected onto a spherical sky map, which is then converted into a pixelated image with adjustable pixel size. The IRFs are also projected into a sky map with a binning adapted to their resolution. The data are stored in a core DL4 container (datasets), which is subsequently used to extract the significance, spectral shape, and flux points. Furthermore, datasets also contain a background model that estimates the number of background counts in the map.
A good background estimation is crucial for deriving significance maps and performing spectral fitting. All commonly used methods require defining an exclusion region that masks the signal in the map to avoid biasing the background estimate. A detailed description of these methods is found in [138]. The DL4 container includes the following: the number of detected gamma rays per pixel, the background model, the IRFs, and a safe mask that excludes regions with high systematics.

2.5.2 *Observation significance*

The significance of a gamma-ray signal is evaluated with hypothesis testing. Two hypotheses are possible. First, the null hypothesis ($\mathcal{H}_0$) that no source is present and only background is seen in that region. Second, there is an excess signal, and it cannot be explained solely by background, $\mathcal{H}_1$. The likelihood of each of these hypotheses is $\mathcal{L}$. For the Poisson statistic with a known background, the log-likelihood is expressed as [139]:

$$\ln \mathcal{L} = -N_{\text{pred}} + N_{\text{obs}} \ln(N_{\text{pred}}), \tag{2.5.1}$$

where N_{pred} and N_{obs} are the expected and observed counts, respectively. The test statistic (TS) [140] is equivalent to,

$$\text{TS} = -2\left(\ln \mathcal{L}(\mathcal{H}_0) - \ln \mathcal{L}(\mathcal{H}_1)\right). \tag{2.5.2}$$

The TS measures the extent to which the source hypothesis is favoured over the null hypothesis. When there is only one degree of freedom, then the significance (σ) is defined as $\sqrt{TS}$ or for negative excess counts, $-\sqrt{TS}$. Generally, the minimum significance to claim that a gamma-ray source is detected is of 5σ.
There are two ways to determine the significance of a gamma-ray emission in a constrained region. These are achieved by either comparing the excess count to the expected background or by fitting a model.

Significance based on excess

In this case, the significance of a region in a sky map is given by the number of excess counts. The number of counts is compared to the predicted number of background counts in the absence of a signal. This method is also referred to as backward folding.
The background is computed, as mentioned earlier, on regions of the sky map where no signal is suspected to influence the background model. Therefore, no background model can be extracted directly in the region of interest where an excess is observed. The background in this region is calculated by extrapolating the number of background counts outside the exclusion region into the excluded region. The likelihood test and significance estimation using excess counts are derived in [141].

Significance based on a model

With this approach, also known as forward folding, excess counts are estimated using a model and then compared with the measured counts. The model is formed by combining a background model with a source model, and can include parameters to apply spatial and spectral corrections to the background template. The model includes representations of the source's spatial morphology and spectral shape. The models are fitted to the real data using maximum likelihood. In this case, significance depends on the chosen model.

The predicted signal counts N_{pred} for a source at a given position $\overrightarrow{p}_{\text{reco}}$ in sky and with energy E_{reco} are,

$$N_{\text{pred}}(\overrightarrow{p}_{\text{reco}}, E_{\text{reco}}) = N_{\text{pred,bkg}}(\overrightarrow{p}_{\text{reco}}, E_{\text{reco}}) + t_{\text{obs}} \int d\overrightarrow{p}_{\text{true}} \int dE_{\text{true}}\, R(\overrightarrow{p}_{\text{reco}}, E_{\text{reco}} | \overrightarrow{p}_{\text{true}}, E_{\text{true}})\, \phi(\overrightarrow{p}_{\text{true}}, E_{\text{true}}). \tag{2.5.3}$$

$\phi(\overrightarrow{p}_{\text{true}}, E_{\text{true}})$ is the source flux model and $R(\overrightarrow{p}_{\text{reco}}, E_{\text{reco}} | \overrightarrow{p}_{\text{true}}, E_{\text{true}})$ is the instrument response function as described in Equation 2.4.1. $N_{\text{pred,bkg}}(\overrightarrow{p}_{\text{reco}}, E_{\text{reco}})$ is the predicted background counts at position $\overrightarrow{p}_{\text{reco}}$ from the background model.

Significance maps

The significance map is obtained by computing significance, as explained above, not for a region but for each pixel in the sky map. This provides a means of identifying significant areas on a map. It is also a valuable way to assess whether the background model exhibits systematic errors. The residuals of the significance map should follow a Gaussian distribution with mean 0 and unit variance, if enough events are detected.

2.5.3 *Source modelling*

When a significant excess is detected, the morphology and spectrum of the significant region are fitted with a sky model. The spatial and spectral models are fitted to the data by maximising the likelihood. Spectral models describe the flux of gamma rays as a function of energy $\phi(E) = \frac{dN}{dE}$. Multiple spectral models are included in *gammapy*[1] to describe the gamma-ray spectral shapes arising from different acceleration processes (see Section 1.3).
Important spectral models for this thesis include the exponential cutoff power law, the log-parabola, and a simple power law. The simple power law is expressed as:

$$\phi = \phi_0 \left(\frac{E}{E_0} \right)^{-\Gamma}, \tag{2.5.4}$$

[1] https://docs.gammapy.org/1.0/user-guide/model-gallery/index.html

where E_0 is the reference energy, typically set to 1 TeV for H.E.S.S., ϕ_0 is the amplitude in units of 1/(TeV s cm^2), and Γ is the index. The exponential cutoff power-law model introduces an energy cutoff $E_{\text{cut}} = \frac{1}{\lambda}$:

$$\phi = \phi_0 \left(\frac{E}{E_0} \right)^{-\Gamma} \exp\left(-\left(\frac{E}{E_{\text{cut}}} \right)^{\alpha} \right). \tag{2.5.5}$$

The log parabola model is given by,

$$\phi = \phi_0 \left(\frac{E}{E_0} \right)^{-\alpha - \beta \log \frac{E}{E_0}}. \tag{2.5.6}$$

Spatial models are not always necessary. Some sources are modelled using an energy-dependent spectral model independent of spatial coordinates, assuming that most of the emission along the line of sight comes from a single source. This is, to a very high accuracy, the case of the Crab Nebula [142]. The background model in this case is also assumed to be spatially independent. However, in most cases, a spatial model is needed to account for spectral variations along extended sources or to describe complex regions along the Galactic plane where multiple sources can overlap.

2.5.4 *Flux points*

Flux points are computed in *gammapy* by refitting only the amplitude of the best-fit spectral model to the excess counts in each energy bin. The amplitude is refitted by introducing a normalisation factor at each bin. The flux is therefore computed separately for each reconstructed energy bin. It detects fluctuations around the reference spectral model. A difference in spectral shape compared to the reference model implies that another spectral model should be used and the flux points recomputed (as they depend on the reference model). When the detection significance in an energy bin is below a given threshold, an upper limit is usually given instead of a flux point. The upper limit indicates the largest flux consistent with the source remaining undetected at a chosen confidence level. In *gammapy*, an upper limit is drawn when the detection significance in that bin is lower than 2σ.

2.6 The H.E.S.S. event reconstruction

The offline H.E.S.S. analysis is similar to that of the CTAO. One of the main differences is that H.E.S.S. does not store full or partial traces for offline integration. In H.E.S.S., only the integrated charge and average arrival time are stored. No data volume reduction is performed online because the number of telescopes is much smaller than in the planned CTAO arrays, and the extracted charge and time occupy much less space than traces, each of which contains tens of time samples. On the other hand, the lack of a complete trace means that no additional charge or time extraction is performed offline, which could limit the reconstruction's performance.
The data is then cleaned using either Tailcuts or a time-based clustering method (Section 5.2). The Hillas parameters calculated from the cleaned images are used to reconstruct the shower properties. The Hillas-based shower reconstruction methods are used as seeds for ImPACT, which provides the final reconstructed parameters in stereoscopic observations. *gammapy* is used for the high-level analysis.

2.7 Gamma-ray space detectors

2.7.1 *Fermi Large Area Telescope*

The Fermi Gamma-ray Space Telescope, formerly known as the Gamma-ray Large Area Space Telescope (GLAST) [143], is a space-based detector designed to study gamma rays across a wide range of energies, from 8 keV to more than 300 MeV. Fermi was launched on June 11, 2008, and has since provided sky maps in the gamma-ray regime, yielding significant results [144]. Fermi is equipped with two instruments: the Large Area Telescope (LAT) and the Gamma-ray Burst Monitor (GBM). Fermi-LAT is sensitive to the highest energies from 20 MeV to more than 300 GeV, while Fermi-GBM detects energies from 8 keV to $\sim$ 30 MeV. Fermi primarily operates, unlike IACTs, in an all-sky survey (*scanning*) mode [145]. It continuously sweeps the sky by alternating the pointing directly from 50° north in one orbit to 50° south in the next orbit. Given the large field-of-view of the detector, which covers around 20% of the sky, the sky is fully covered with uniform exposure after only $\sim$ 3 hours (2 complete orbits) of data taking.

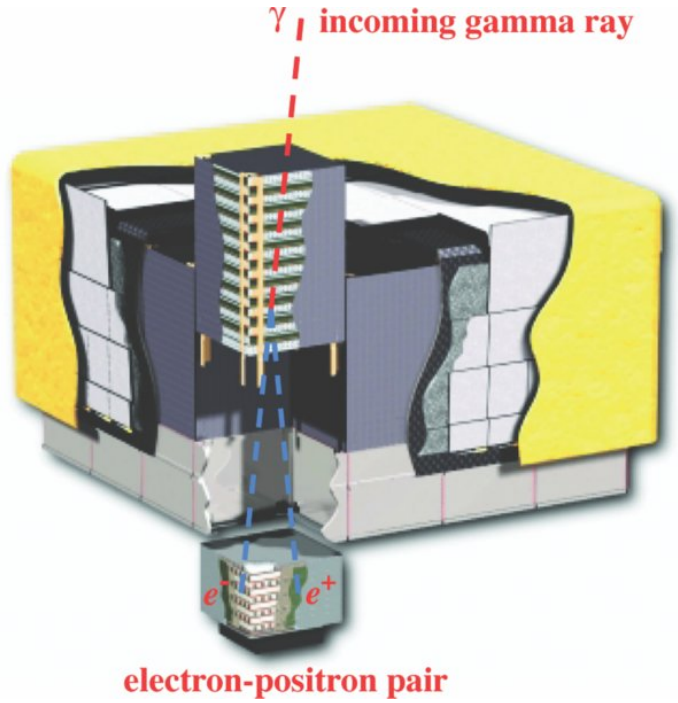

Figure 2.20: Schematic layout of Fermi-LAT, showing the distinct parts of the detector. The interior of one of the 4×4 towers is shown, with the tracker layers and the calorimeter. In the tracker, an incoming gamma-ray undergoes pair production into an electron and a positron. The particle pair deposits energy into the calorimeter. An anti-coincidence detector (shown in yellow) surrounds the tracker. Taken from [145] with explicit permission.

Fermi-LAT [145] employs detection principles similar to those used in ground-based gamma-ray detection. An electromagnetic shower is induced by the pair production of an electron and a positron following the interaction of a gamma ray within the detector. The detector comprises a calorimeter and an anti-coincidence detector (ACD) surrounding a particle tracker. Charged particle tracks are reconstructed in the tracker, while the shower develops and deposits energy in the calorimeter. Fermi-LAT has dimensions of 1.8 m × 1.8 m × 0.72 m and is composed of 4×4 towers [146], each containing a calorimeter and a tracker (see Fig. 2.20).

- **Tracker**. The tracker comprises layers of silicon strip detectors interleaved with conversion planes of high-Z tungsten material. A gamma particle undergoes pair production in the conversion planes, and an electron and a positron are emitted. The silicon layers record the track of the secondary charged particles. As the direction of the e^+e^- pair travels nearly in the same direction as the primary gamma particle, the direction of the incoming gamma ray can be computed. The trackers are used for direction reconstruction. Furthermore,

they provide essential information for triggering an event. If two tracks are identified as originating from a common point, it is likely a gamma event.

- **Calorimeter**. The calorimeter sits below the tracker, and it is composed of a thick enough material (CsI). The calorimeter measures the energy deposition of the e^+e^- from the resulting electromagnetic showers, providing information on the primary gamma's energy. Moreover, another trigger step occurs here. The shower profiles are used to further discriminate between gammas and charged particles, as described in Section 2.1.1.
- **Anti-coincidence detector**. The ACD [147] surrounds the tracker layers. The ACD is an important component of LAT for rejecting charged particles, which are more likely to trigger than gamma rays. The ACD is expected to tag charged particles with a 0.9997 efficiency. The detector consists of scintillator tiles and scintillator fibres that release a signal when charged particles interact with them. PMTs detect this signal.
- **Trigger**. The previously described trigger steps are partially applied on-site to limit the amount of data transmitted to Earth. LAT sends ~ 400 Hz from the original 10 kHz [148].

More information on the technical design of Fermi-LAT in [145].

2.7.2 *Event reconstruction in Fermi-LAT*

Several updates have been developed since the beginning of operation. The most recent data release used the latest version of the event reconstruction software, Pass 8 [149]. This latest version also introduces additional critical changes to the chain, resulting in a significant improvement in the reconstruction quality. A detailed description of the event reconstruction chain of Pass 8 for Fermi-LAT is given in [150], [151], [152], and [149]. A brief overview of the reconstruction and event types is provided in this section.

The final event reconstruction provides information on the incoming particle's direction, energy, and classification, from which IRFs are built. The reconstruction is performed by combining signals from the detector's three subsystems: the tracker, the calorimeter, and the ACD. In Pass 8, unlike previous releases, the track direction is reconstructed mainly in the tracker and does not rely on the calorimeter. The direction of the incoming particle is reconstructed by combining the reconstructed track directions of the electron and positron. In many cases, the

secondary particles do not form clean single tracks, but instead branch and initiate small electromagnetic showers within the tracker. The branches are linked together into a tree structure, and the particle track is obtained with a fitting procedure. The energy is reconstructed at the calorimeter from the energy deposition of the shower secondary particles. Furthermore, event classification is performed using information from the three subsystems, as described earlier.
As part of the event reconstruction, quality cuts are applied to the data. This step yields multiple event types and classes. Event classes differ from each other by the selection cut on the probability that the incoming particle is a photon (earlier referred to as *gammaness*). In each event class, events are grouped according to the quality of the direction reconstruction (Event types) [153]. Each event class is designed for a scientific purpose.

Event classes

The different event classes depend on the photon-probability cuts. The TRANSIENT event class has the loosest cut and admits a higher rate of background events. This is the selected class typically for short-duration events. An intermediate selection cut is applied in the event class SOURCE, which is favourable for the analysis of extended sources. The tightest cut is applied to the event class ULTRACLEANVETO, which has a reduced effective area and background rate relative to the previous classes.

Event types

Each event class contains other subgroups (event types). They can either be divided into a FRONT and END event type, depending on the tracker layer where the gamma was converted into a e^+e^- pair. The conversion in earlier layers yields improved angular resolution. The events can be further divided into quartiles of angular direction reconstruction quality. The quartiles are denoted PSF0, PSF1, PSF2, and PSF3, in order of increasing quality.
Event lists after selection cuts, along with the corresponding IRFs from the previous reconstruction and selection, are stored in Flexible Image Transport System (FITS) [154] files that can be read into *gammapy*. The data are then reduced to DL4 datasets and analysed as explained earlier. These datasets can be combined with datasets from other instruments to do a joint fit.

3

IMPROVEMENTS TO THE CTAO DATA ANALYSIS CHAIN

This chapter and the next provide detailed validation of new methods for the standard CTAO data analysis chain. Fig. 3.1 summarises the developments presented in this thesis, with references to the corresponding sections where they are discussed. From R0 to R1, raw traces are precalibrated, and events are flagged as Cherenkov or calibration runs. Muon tagging (next chapter, Section 4.2.3) identifies muon candidates usable for muon calibration. The precalibrated traces undergo online Data Volume Reduction (DVR) (Section 3.2). This reduces the amount of data before storage, as the observatory cannot store the vast volume of the raw data. The most critical step in DVR is the removal of noise pixels from the image. This step is thoroughly studied in this chapter, using a time-based clustering algorithm followed by a charge-based second step that leverages all image information. The method was implemented, optimised, and tested by the author. The description in this thesis builds upon the author's previous paper [155]. After DVR, the traces that survive the cleaning are stored for offline analysis.

DL0 traces are recalibrated and reconstructed offline into a single charge-time tuple for each pixel. Typically, charge is extracted by summing over a subset of time samples and time by determining the trace's centre of gravity or rising edge. This section examines modifications to the traditional scheme by applying trace preprocessing. This method is intended for use with one of the FlashCam cameras (see Chapter 4), but it can be applied to the traces of any Cherenkov camera. The signal extraction method was integrated into *ctapipe* [110] by Felix Werner and the author of this thesis [156] [157]. In this section, charge extraction is performed only in the linear regime, where the trace maximum height increases linearly with injected charge. This regime is optimised and tested by the author using

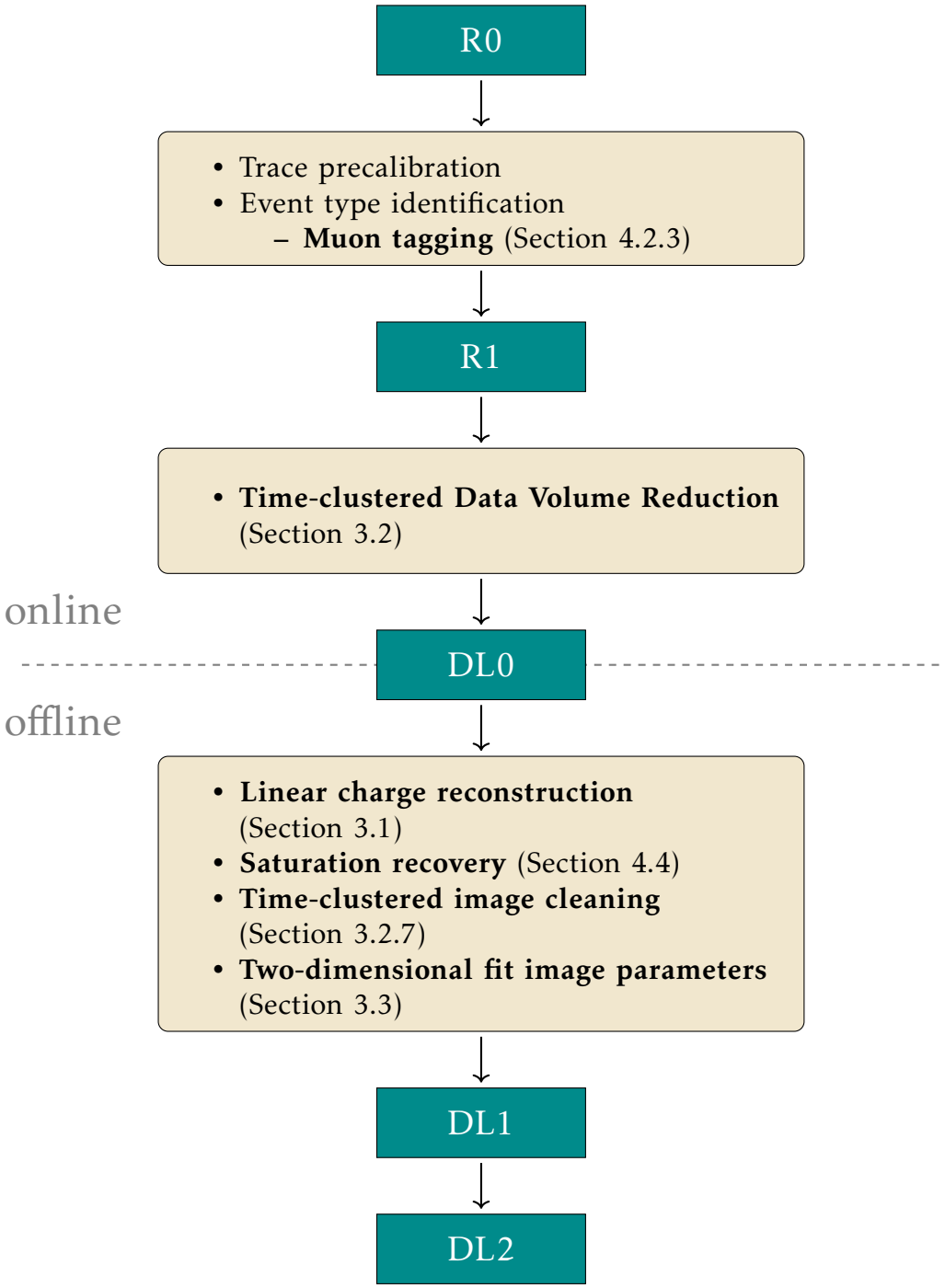

Figure 3.1: Workflow of the CTAO data processing steps. The contribution of this thesis to the conversion from each data level to the next is highlighted, and the relevant sections are indicated. This thesis's contributions to the CTAO are: muon tagging, data volume reduction, charge reconstruction (linear and saturation regimes), image cleaning, and parameterisation.

simulations. The saturation regime, tests on flatfield data runs, and simulation-data consistency are explored in Section 4.4.
DVR performs the same function as an image cleaning algorithm, but operates online with loose cuts. This ensures that signal pixels are preserved and offline reconstruction methods like ImPACT (Section 2.4.4) remain applicable. Therefore, noise-only pixels are still detected and further rejected in the offline analysis. Further tests on IRF performance are shown in Section 3.2.7 to show the implications of this method in the precision of shower reconstruction when applied to image cleaning inside the offline data chain.
The cleaned images are then parameterised. This involves computing a set of image parameters that are fed into event reconstruction algorithms to reconstruct the energy, direction, and particle type. The standard method for this step is Hillas parameterisation. The author implemented a preliminary two-dimensional ellipse-fitting procedure (Section 3.3) to improve parameter extraction, particularly for cropped images with a large fraction of the shower outside the camera's physical limits. The performance is fully tested by the author.

3.1 Signal extraction

When a photon strikes a PMT, a photoelectron is released from the photocathode with a certain quantum efficiency and amplified into multiple electrons with a collection efficiency (see Section 2.1.3). The FlashCam PMTs are very quick with typically $\sim 2.6\,\mathrm{ns}$ signal rise time and $< 3.5\,\mathrm{ns}$ FWHM. The FlashCam electronics shape the signal using a low-pass filter to make it compatible with 4 ns sampling. In the linear regime, the height and integrated charge of the electric pulse are proportional to the number of photoelectrons released by the cathode and, therefore, to the number of photons that initially got into the pixel.
Cherenkov light is detected on only a subset of camera pixels. Consequently, many pixels do not detect any signal but only noise from the NSB and the PMT electronics. In noise-only pixels, the reconstructed arrival times are essentially random, and the charge follows a Poissonian distribution centred at the integration window times the NSB rate. After baseline subtraction, the distribution is centred around zero. The variance of this distribution increases linearly with NSB. Charge and time are the fundamental parameters for discriminating the imaged shower

from noise, which in turn is essential for reconstructing the properties of the air shower.
Given the importance of signal reconstruction, extensive studies have been conducted, and numerous techniques have been developed [158] [159]. A common approach is to define an integration window and integrate the trace within it. The integration window must be positioned to capture a significant fraction of the pulse while minimising the contribution of noise-dominated samples. Integrating the trace provides an estimate of the number of PEs that is less affected by factors such as time jitter and phase (the relative alignment between the analogue pulse and the ADC sampling clock) than other techniques, such as peak height.
A good approach to defining the window position is to consider the traces of neighbouring pixels. For a neighbour-based integration window, the sum of the traces of all nearest neighbours of a given pixel is computed. The closest neighbours are those that directly touch the pixel in question. The position of the maximum of the neighbour-summed trace is defined as the peak of the trace (*neighbour_peak*) under evaluation. Then, the pixel is integrated from the start of the window defined as (*neighbour_peak - window_shift*), with *window_shift* being an integer number of time samples, to the end of the window (start + *window_width*), with *window_width* being the number of samples to be integrated. Therefore, the integral gives the charge, and the centre of gravity within the window provides the arrival time. This is one of the standard extraction algorithms used in *ctapipe* [110], called Neighbour Peak Window Sum (NPWS).
The method has two crucial free parameters that affect the reconstruction: the *window_width* and *window_shift*. The *window_shift* can be defined such that the window is not symmetric about the neighbouring peak. This can be relevant for traces with long pulse tails. The *window_width* is chosen to be neither too short to miss a large fraction of the trace nor too long to integrate excessive noise. This method is unbiased and relatively robust to noise-induced miscalculations of the window position. Nevertheless, it may result in random peak positions in low-signal regions of the camera.

3.1.1 *Criteria for reconstruction validation*

The bias and resolution between the reconstructed charge Q_{reco} and the true charge Q_{true} are the two basic performance tests for a given charge-extraction method.

The true charge is obtained from simulations and corresponds to the true number of photoelectrons before any noise is added. When the true charge is low, the individual photoelectrons sometimes arrive with a significant spread, so that not all PEs fall within the integration window.
The charge bias is the average conversion factor between the reconstructed and true charges, defined in this thesis as the ratio of the two:

$$B = \left\langle \frac{Q_{\text{reco}}}{Q_{\text{true}}} \right\rangle \tag{3.1.1}$$

A bias-free reconstruction would lead to a bias of 1.0. The deviation of Q_{reco} with respect to Q_{true} is:

$$D = Q_{\text{reco}} - Q_{\text{true}}. \tag{3.1.2}$$

The RMS error is given by,

$$RMSE = \sqrt{\langle D^2 \rangle} \tag{3.1.3}$$

The resolution or quality of the charge extraction is defined as the relative RMS error:

$$R = \frac{RMSE}{\langle Q_{\text{true}} \rangle} \tag{3.1.4}$$

The resolution and bias are used to optimise the extractor's free parameters and to compare different extraction schemes.

3.1.2 *The FlashCam extractor*

Implementing certain modifications to the standard NPWS method is necessary to adapt it to the characteristics of FlashCam traces, and these modifications may also be applicable to the remaining Cherenkov cameras. This new extractor is referred to as *the FlashCam extractor* [157].
The charge extraction in this section is tested using sim_telarray and CORSIKA simulations of on-axis gamma-initiating showers. The events are simulated at a zenith angle of 20° and offset of 0°. Only one MST is simulated from the Southern array with a FlashCam installed in it, and ~17,000 events are triggered. Trace saturation has not yet been simulated; therefore, its effect is not shown in any

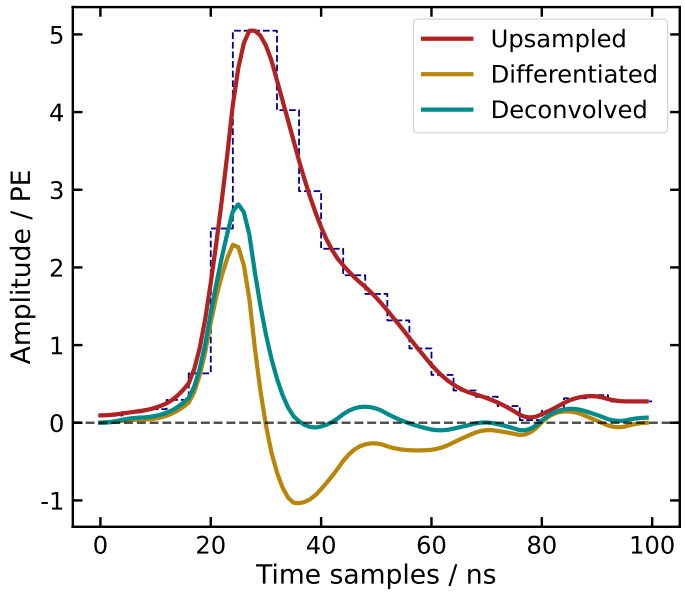

Figure 3.2: The four representations of a simulated FlashCam trace after going through different steps of processing. The original calibrated trace (dashed dark blue line) is in steps of a FlashCam sample of 4 ns width. The corresponding upsampled, differentiated, and deconvolved traces are superimposed on the original.

of the plots. The impact of saturation and the reconstruction approach in the saturation regime will be explored in Section 4.4, where FlashCam specifications will be discussed in more detail.

The FlashCam traces require special preprocessing due to their relatively slow sampling rate of 250 MHz [160], which is significantly lower than the ~1 GHz rates used by other cameras. To achieve nanosecond-level sampling resolution, the traces are upsampled by repeating each sample four times, followed by a linear moving-average filter applied twice—once forward and once backwards—to ensure zero-phase distortion. This is done with a version of `scipy.signal.filtfilt` [161] from the SciPy library [162] optimised for computational speed. The upsampled trace is shown in Fig. 3.2 superimposed on the original trace after baseline subtraction.

The peak of the differentiated pulse (see Fig. 3.2) provides an amplitude-independent pulse time. The differentiated trace is obtained by differentiating the original trace and then upsampling it; it does not require baseline subtraction.

Moreover, the FlashCam preamplifier (more on amplification scheme in Chapter 4) behaves as a first-order low-pass filter, attenuating the signal's high-frequency components. This introduces an unwanted convolution, manifesting as an ex-

ponentially decaying tail in the pulse trace. Differentiating the pulse reveals a prominent Gaussian-like peak followed by a pole, corresponding to a frequency at which the system response increases sharply—a frequency that ideally should have been zero.

Pole-zero (pz) deconvolution [163] reverses the effect of the detector by applying the preamplifier response (or filter) in the inverse [164]. The camera's reference pulse shape is used to determine the pole-zero parameters by characterising the rate of decay of the pulse edge. The trace is deconvolved and then upsampled, leading to Fig. 3.2 (deconvolved). Each instance of the original calibrated trace: upsampled, differentiated, and deconvolved traces, is used during the signal extraction scheme. The charge is extracted by summing the amplitudes of the deconvolved trace, instead of the original calibrated trace, inside a window defined as for NPWS. However, unlike in NPWS, the traces of the nearest neighbours are soft-clipped before being summed. This clipping step reduces the influence of large-amplitude afterpulses in the sum, which can otherwise shift the signal peak by several samples. The probability of finding an afterpulse in one pixel of FlashCam (see Fig. 2.8) is small. However, given the number of pixels and events a Cherenkov camera must process, it is not unreasonable to observe a significant afterpulse. The intensity of afterpulses can be comparable to or exceed that of signal pulses, thereby shifting the window location considerably.

In the original NPWS method, the reconstructed time is defined as the weighted average of the samples. In this algorithm, the reconstructed time is determined as the weighted average of the differentiated trace samples within a region where the differentiated trace exceeds 5% of its peak amplitude.

Deconvolution leads to charge loss, which is corrected by dividing the sum by a deconvolution gain-loss factor (G_{pz}), which depends on the integration window. It is computed with the reference pulse shape as follows:

$$G_{\mathrm{pz}} = \frac{\sum_{\mathrm{n}_0}^{\mathrm{n}_0+w} R_{\mathrm{pz}}}{\sum_{0}^{\mathrm{N}} R_{\mathrm{rt}}} \tag{3.1.5}$$

where n_0 is the starting sample of the integration window, w is the *window_width*, and N is the last sample of the trace. The deconvolved reference pulse is denoted, R_{pz} and the original reference pulse is R_{rt}. The integral of a deconvolved trace (A_{pz}) is corrected to get the actual reconstructed charge (Q_{rec}) as follows:

$$Q_{\text{rec}} = \frac{A_{\text{pz}}}{G_{\text{pz}}} \tag{3.1.6}$$

However, the gain loss correction still cannot correct for a small bias in charge reconstruction as can be seen in Fig. 3.3b at 0 ns. This is because the curve does not account for the arrival-time difference between photons within each pixel. There is typically a spread of a few nanoseconds in the Cherenkov time profile that is not captured by the reference pulse shape computed from flat-field runs. The bias is fully corrected by convolving the reference pulse shape with a Gaussian of a standard deviation equivalent to the average time spread within a pixel.
The standard deviation of the Gaussian is optimised with the charge bias and resolution of simulated events at nominal NSB (216 MHz). The resolution and bias are defined as described earlier in Section 3.1.1. Fig. 3.3b shows how the bias is reduced significantly for σ equal to 1.5 ns. And the charge resolution is visibly improved, especially at large amplitudes, as seen in Fig. 3.3a. The dashed black line shows the best achievable charge resolution, which corresponds to Poisson fluctuations multiplied by the average ENF of 1.1 (see FlashCam parameters in Chapter 4). These plots are made with a *window_width* of 8 ns and a *window_shift* of 3 ns.

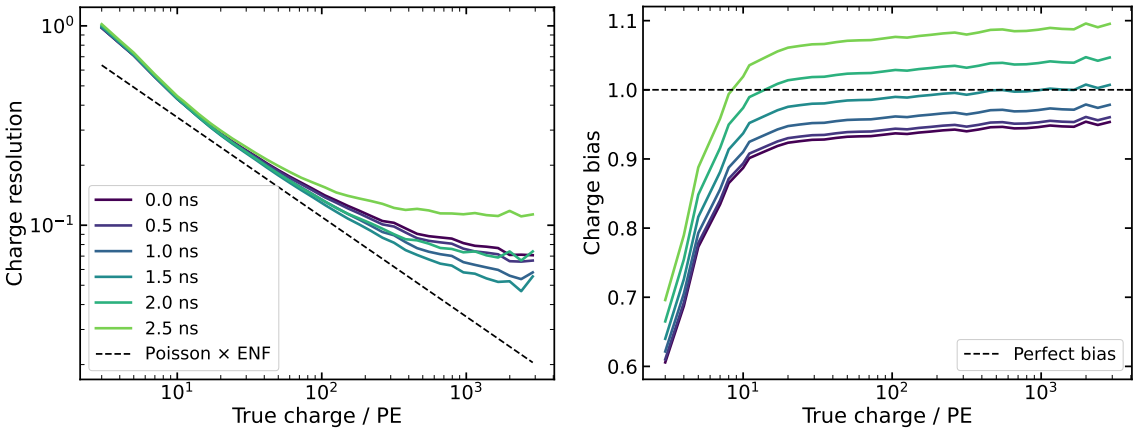

(a) Charge resolution

(b) Charge bias

Figure 3.3: Charge resolution (left panel) and bias (right panel) averaged over all pixels in the camera and events, using simulations of gamma-ray initiated showers under nominal NSB of 216 MHz. The charge is reconstructed with the FlashCam extractor. The *window_width* and *window_shift* are set to 8 ns and 3 ns, respectively. Each line corresponds to a different value of the standard deviation of the Cherenkov time profile.

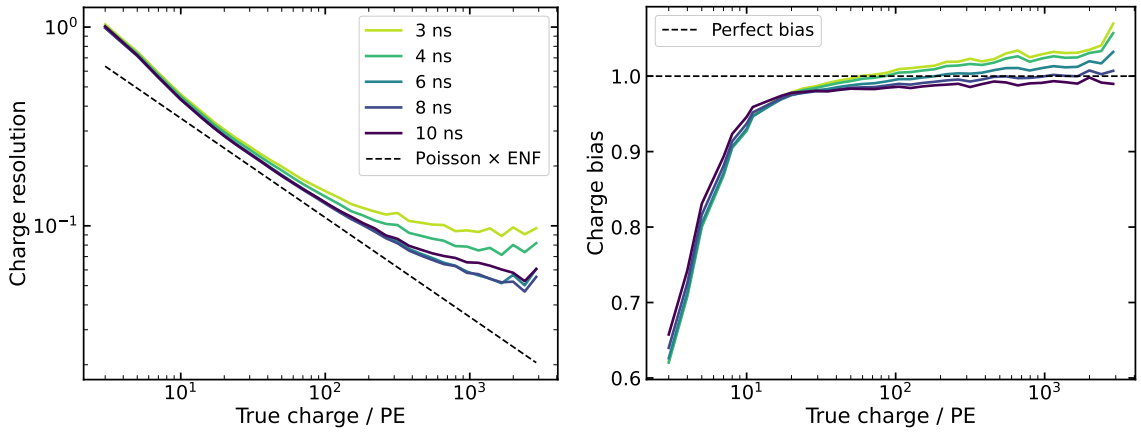

(a) Charge resolution **(b)** Charge bias

Figure 3.4: Charge resolution (left panel) and bias (right panel) averaged over all pixels in the camera and events, using simulations of gamma-ray initiated showers under nominal NSB of 216 MHz. The charge is reconstructed with the FlashCam extractor. The *window_shift* and Cherenkov time profile standard deviation are set to 3 ns and 1.5 ns, respectively. Each line corresponds to a different value of the *window_width*.

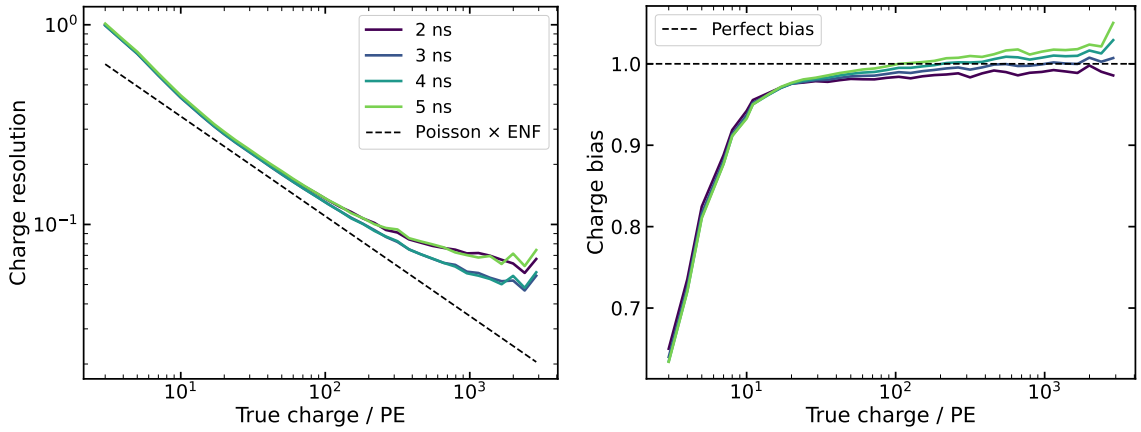

(a) Charge resolution **(b)** Charge bias

Figure 3.5: Charge resolution (left panel) and bias (right panel) averaged over all pixels in the camera and events, using simulations of gamma-ray showers under nominal NSB of 216 MHz. The charge is reconstructed with the FlashCam extractor. The *window_width* and Cherenkov time profile standard deviation are set to 8 ns and 1.5 ns, respectively. Each line corresponds to a different value of the *window_shift*.

Additionally, when a broken pixel is present in the camera, the reconstructed charge and time of that pixel are equal to the average of those of its nearest neighbouring pixels. When no neighbour pixel is available, the pixel is filled with zeros [165].

	window_width	*window_shift*	Time spread
FlashCam extractor	7.0 ns	3.0 ns	1.5 ns
NPWS extractor	7.0 samples	3.0 samples	–

Table 3.1: Optimised parameters for the FlashCam extractor and NPWS used in the comparative plots throughout this section.

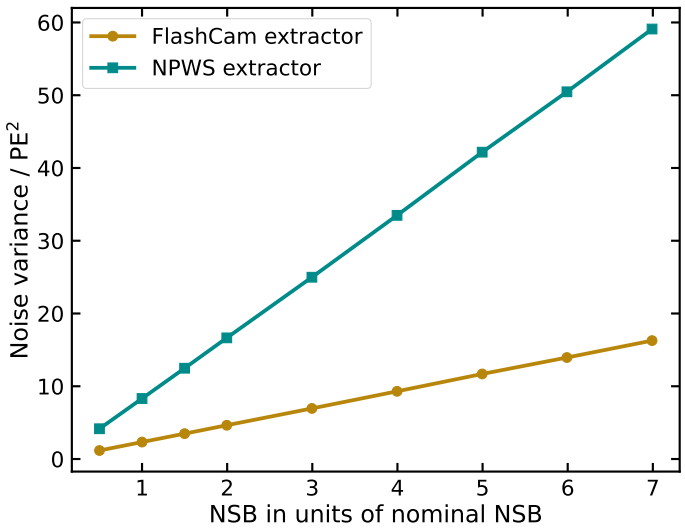

Figure 3.6: Variance of the reconstructed charge distribution for noise pixels as a function of NSB in units of nominal NSB (216 MHz) using the FlashCam extractor and NPWS. Since the distribution widens with increasing background, the variance is computed separately at each NSB level.

The *window_width* is also optimised by comparing the charge bias and resolution. The *window_width* is tested by setting the *window_shift* to 3 ns and the standard deviation to 1.5 ns. Fig. 3.4 shows that the optimised width is between 6 and 8 ns as it gives the best charge resolution and bias at nominal NSB. The *window_shift* is optimised similarly, as seen in Fig 3.5, by freezing the *window_width* to 8 ns and the standard deviation to 1.5 ns. A symmetric integration window is appropriate in this case, as the deconvolved trace is no longer asymmetric. The values used for the remaining plots are listed in Table 3.1 for the FlashCam extractor and NPWS. The variance of the noise distribution is shown in Fig 3.6 as NSB increases when the FlashCam extractor and the NPWS are applied to the same simulated events. Noise pixels are those with no signal detected, i.e., when 0 PE of true charge is injected into the pixel during simulation. At nominal NSB, the noise variance is significantly higher for NPWS than for the FlashCam extractor. Moreover, the

difference in variance increases more markedly with NSB when using NPWS. As no upsampling is performed for NPWS, the samples are 4 ns long, and the tail of the pulse extends for several samples. The trace needs to be integrated over a large-enough window of 7 samples (28 ns), including a significant fraction of noise, which becomes problematic especially at significant NSB rates.
The charge resolution is compared in Fig. 3.7 using the two extraction methods. The FlashCam extractor performs substantially better across the entire charge range and at nominal and high (five times the nominal) NSB rates.

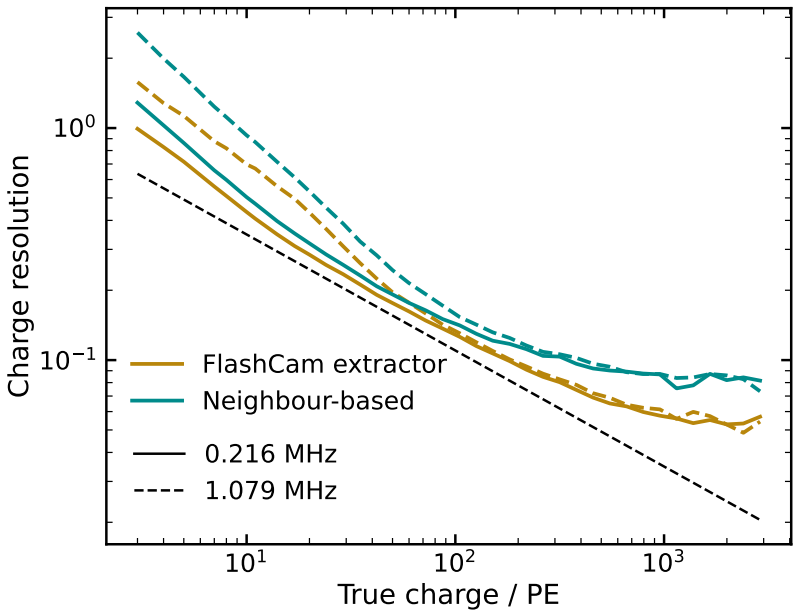

Figure 3.7: Charge resolution of simulated gamma-ray initiated showers using the FlashCam extractor and NPWS at two NSB levels: 216 MHz and 1079 MHz. The dashed black line shows the best possible performance, equivalent to Poisson resolution times the ENF.

3.1.3 *Image extraction with a time gradient*

One potential issue with neighbour-based extraction methods is that the integration window position is sometimes miscalculated. This can occur due to high-intensity afterpulses or neighbouring pixels with low signal amplitudes comparable to noise fluctuations. The previously evaluated extractor method can be extended by adding a step to correct the peak positions via a time-gradient adjustment [166] [167]. The method procedure is based on the *ctapipe* `TwoPassWindowSum` algorithm and follows these steps:

1. The number of PEs and average arrival time are extracted for each pixel with a neighbour-based method.
2. The image is cleaned with Tailcuts as described in Section 2.4.2.
3. The centre of gravity and major and minor axes of the image are computed, following the Hillas scheme (compare Section 2.4.3). The longitudinal and transverse distances of each pixel are computed.
4. The linear relation between time and distance of a pixel from the centre of gravity of the image along the longitudinal axis is obtained (see Fig. 2.17 in Section 2.4.2).
5. The trace is reintegrated into a window with the *neighbour_peak* being the new predicted time.

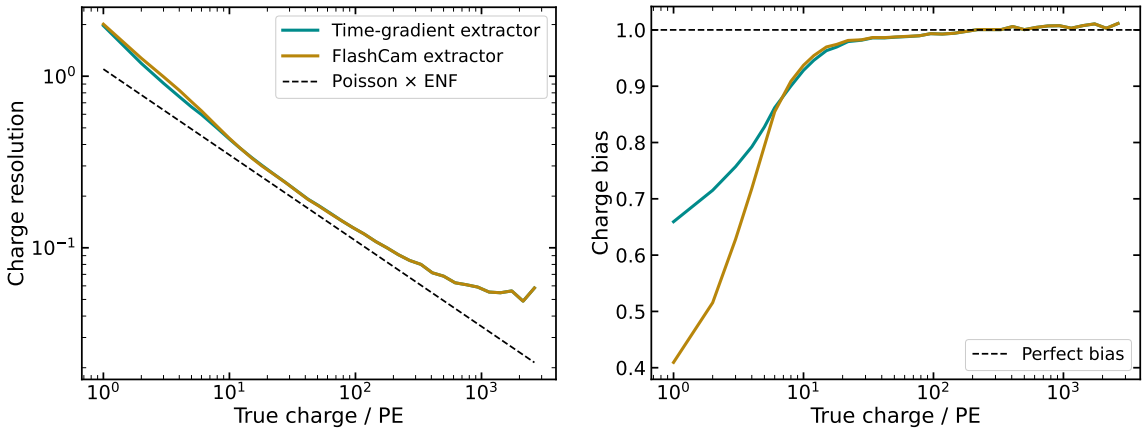

(a) Charge resolution **(b)** Charge bias

Figure 3.8: Charge resolution (left panel) and bias (right panel) are averaged over all pixels and events using simulations of gamma-ray showers. Two extraction methods are compared: the default FlashCam extractor and an updated version that uses a time-gradient peak correction. The dashed black lines show the best achievable resolution (left) and bias (right).

The verification of this method is performed using the following details. For step 1, the FlashCam extractor is used to conduct an initial evaluation of the per-pixel charge and time. The results of this step are cleaned using the Tailcuts cleaning algorithm with a picture threshold of 9 PE, a boundary threshold of 5 PE, and a minimum of 2 neighbouring pixels. The cleaned image undergoes the standard Hillas parameter calculation, from which the longitudinal distance of each pixel is computed. A linear fit between the reconstructed time and the longitudinal distance is used to determine the peak position for each pixel, which is then used to redefine the integration window position. Each deconvolved trace is again

integrated (with the same values as in Table 3.1) to get the final reconstructed charge.
The signal extracted after a time gradient correction may omit temporal features, such as those from muon rings. This could be improved by applying a temporal gradient to clusters identified by a clustering algorithm (Section 3.2). This time-gradient correction is also slower, as the image cleaning and parameterisation must be run twice: once before the final charge and time extraction, and once after.
The reconstructed charge shows a significantly improved charge bias (see Fig. 3.8b) and slightly better charge resolution (Fig. 3.8a) at low charge. This new step is designed to correct for misplaced window positions at low charge and shows promising results, though further investigation is warranted. While it is less computationally efficient than the previous method and therefore unsuitable for real-time analysis, it is a promising option for offline processing.

3.2 Studies on Data Volume Reduction

The CTAO will consist of two observation sites, each hosting numerous telescopes, substantially more than any other current observatory of its kind. The Southern array, with more than 50 telescopes planned [100], will be particularly extensive. Each of these telescopes will be equipped with a high-performance Cherenkov camera capable of imaging fast, faint flashes of Cherenkov light using about two thousand highly sensitive photon detectors.
Unlike the H.E.S.S. array, the CTAO will store traces for each detected pixel, each at least several tens of nanoseconds long, rather than the average arrival time and total signal intensity. Storing full or partial traces for each pixel and camera enables more sophisticated offline reconstruction methods, particularly image-extraction algorithms. Nevertheless, this translates into a very high data rate of hundreds of PB per year at each observatory site [111].
The expected data rate would exceed the observatory's storage capacity, making DVR a necessary solution. To guarantee effective data handling, a considerable reduction in data volume is required—ideally to approximately 10 PB/year (see Section 2.3.2). This yields a reduction factor, defined as the ratio of the data rate before and after DVR, ranging from 10 (at the beginning of operation) to 50 once the method is thoroughly tested and functional. An additional factor of 2 can be achieved through lossless data compression.
DVR is split into two steps:

- **Pixel selection**. The data volume can be reduced by significantly rejecting noise pixels that do not contain shower information. Camera images consist of two types of pixels: those containing only night-sky background and noise (noise pixels), and those containing Cherenkov light from air showers (signal pixels).
- **Shortening of traces**. Waveforms are digitised for a preset number of samples. However, the signal is present in only a subset of these samples. By shortening the digitised traces to exclude noise-only samples, considerable storage space can be saved.

This section is based on the paper [155] by the author of this thesis. Some of the plots shown in [155] were slightly modified. First, the DVR method for pixel selection is reviewed and described. This method is then optimised and tested

against Tailcuts (introduced in Section 2.4.2). Finally, new perspectives for this method are explored.

3.2.1 *Time-based clustering*

The Density-Based Spatial Clustering of Applications with Noise (DBSCAN) [168] is an unsupervised density-based clustering method. It identifies clusters as regions of high density in an N-dimensional space, separated by areas of lower density. DBSCAN is a well-established algorithm that offers several advantages. Unlike other methods, it does not require specifying the number of clusters—a particularly important feature for detecting subcomponents of hadronic showers. The algorithm can also handle arbitrary cluster shapes, and not all input points need to be assigned to a cluster; some may be classified as noise. However, DBSCAN cannot effectively group data with significantly different densities because its free parameters are too restrictive [169].

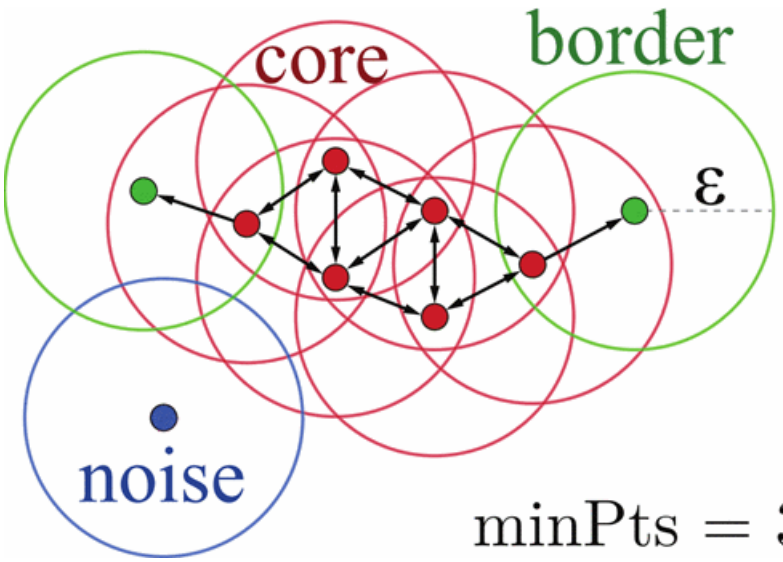

Figure 3.9: Illustration of the DBSCAN mechanism. The core points appear in red surrounded by a circle of radius ε. The green points are the border points, which are located at a distance ε from any core point. The remaining blue point is noise. Taken from [170].

The two basic free parameters in DBSCAN are the minimum number of points to consider a dense region (*minPts*) and the minimum distance to form a neighbourhood (ε). Each data point in DBSCAN can be classified as a core, border, or noise point. Core points are those that have at least *minPts* in a distance ε. The points within a ε distance to a core point are defined as border points. The rest

constitutes the noise. Each core and border point is assigned to a cluster that is reachable in density. Each point can only be assigned to one cluster ID. Fig. 3.9 shows this principle. All red points are identified as core because there are more than *minPts* (in this case *minPts*=3) within ε. The green points are within ε of one red point. The blue point is noise because it is too far away from the dense region. The bottom layer of Fig. 3.10 shows the reconstructed time distribution across the camera plane after subtracting the intensity-weighted average time for three events. The corresponding reconstructed charge distribution is shown in the top layer. Pixels that detect Cherenkov light form a distinct region in the camera. Even when pixel intensity is low, the time is similar to that of neighbouring pixels, thereby forming a distinct region. This pattern on the reconstructed time is ideal for DBSCAN.

However, two considerations must be addressed. Firstly, some spurious and small clusters in time are artificially generated by the choice of the signal extraction method. That is because, as discussed in Section 3.1.2, the arrival time of each pixel is extracted with a neighbour-based algorithm. A pre-cut in pixel intensity (hereafter referred to as the *noise cut*) is applied before clustering to reduce the likelihood of keeping spurious time clusters. The intensity cut is defined with respect to the noise level.

Secondly, the reconstructed pixel time and the camera coordinates are on significantly different scales. The time values range from 0 to 100 ns, and the camera's spatial coordinates from approximately -1.2 to 1.2 m. DBSCAN cannot correctly handle such differences, and no clusters are found. The time dimension and the x and y dimensions are scaled, therefore, such that ε is equal to 1 and can be excluded as a free parameter. The timescale parameter is defined as *tscale* and the spatial scale is *dscale*. The spatial scale is identical for both the x and y axes. This first part of the DVR method follows the image cleaning algorithm in [109].

This method could lead to highly charged pixels being removed if their reconstructed times differ from those of neighbouring pixels due to miscalculations in the time extraction. Therefore, a second step is added after performing DBSCAN. Pixels that do not pass the clustering algorithm but have significant intensity (above a so-called *tailcuts threshold*) are added if they have at least one other significant pixel neighbour that exceeds the same threshold. Ultimately, this method combines clustering with a Tailcuts-based algorithm to account for intensity information.

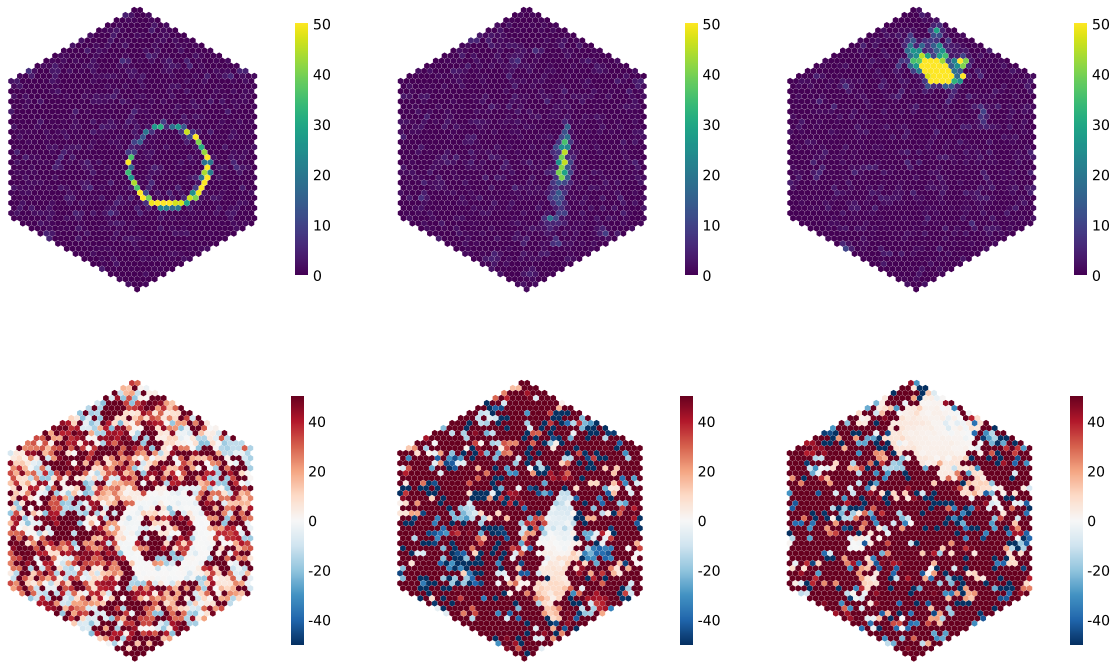

Figure 3.10: Three example images recorded by a FlashCam using simulations. The top layer shows the reconstructed charge, and the bottom one the corresponding reconstructed time minus the intensity-weighted average reconstructed time.

Lastly, rows of neighbouring pixels (*dilated rows*) could be added after selecting the pixels that pass DVR, further enhancing, if necessary, the detection of pixels. In this section, this method is evaluated as a DVR algorithm for detecting the maximum number of signal pixels, which also entails significant data volume loss. The performance of the time-based clustering is compared with Tailcuts. Tailcuts, as explained in Section 2.4.2, have four free parameters. Two charge-dependent thresholds, the picture and boundary thresholds, the minimum number of neighbours that exceed the picture threshold, picture neighbours, and the number of dilated rows. All pixels above the picture threshold and all pixels above the boundary threshold are stored if they have at least a given number of picture neighbours. Then rows of pixels can be added around the resulting image.

3.2.2 *Verification on a simulated FlashCam*

The following verification is performed on proton- and gamma-induced simulations using CORSIKA and sim_telarray, at a zenith angle of 20°, simulating one

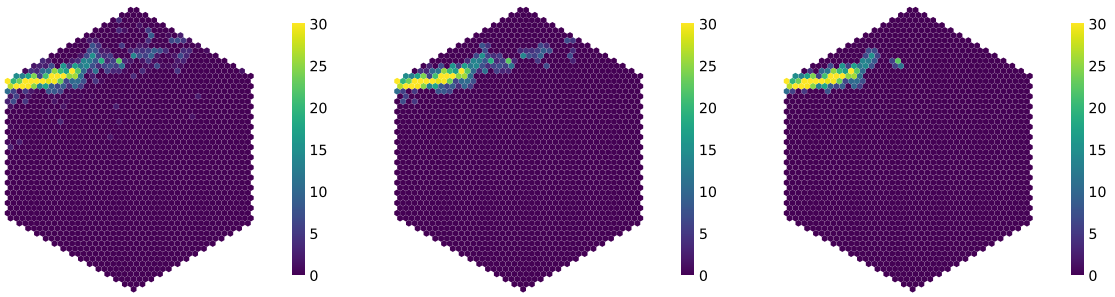

(a) Perfect selection **(b)** Time-based clustering **(c)** Tailcuts

Figure 3.11: Example of a simulated proton shower as seen in the camera plane after charge reconstruction for pixels surviving DVR. The left panel shows only pixels that contain true charge, as obtained by simulations. The middle and right panels show the image after time-based clustering and Tailcuts, respectively.

MST with a FlashCam. Gammas are simulated on axis, while protons are simulated with a viewcone around the simulated telescope direction with a solid angle of 10°. The signal is extracted using the neighbour-based FlashCam extractor introduced in the previous section.

Fig. 3.11 shows an example of a simulated proton-initiated shower. The left figure shows the reconstructed image from a simulated FlashCam when a perfect DVR method is applied—that is, when all pixels with true charge pass the reduction process, and all noise pixels are excluded. The reconstructed image is shown in the middle figure after applying the time-based clustering algorithm, and the effect of Tailcuts is shown in the right panel. The tailcuts method removes many low-intensity pixels from the shower's tail. This algorithm, therefore, tends to oversimplify showers, resulting in shapes that resemble ellipses. At the high level, this is less problematic than data volume reduction; however, degradation in energy resolution and gamma-hadron separation still occurs. Time-based clustering also detects low-intensity pixels from the image tail that belong to the time cluster.

A good way to determine which DVR algorithm is best for the CTAO is to examine the number of detected signal and noise pixels. Signal pixels will have multiple definitions along this section. However, they can be described as pixels with at least a number Q of true PEs. As the methods are tested with sim_telarray simulations, the true charge that was injected into each pixel is known. Noise pixels are those with 0 PE of injected true charge.

The signal efficiency and total DVR factor are obtained for all possible combinations of free parameters. Table 3.2 shows all the values that each parameter of the time-

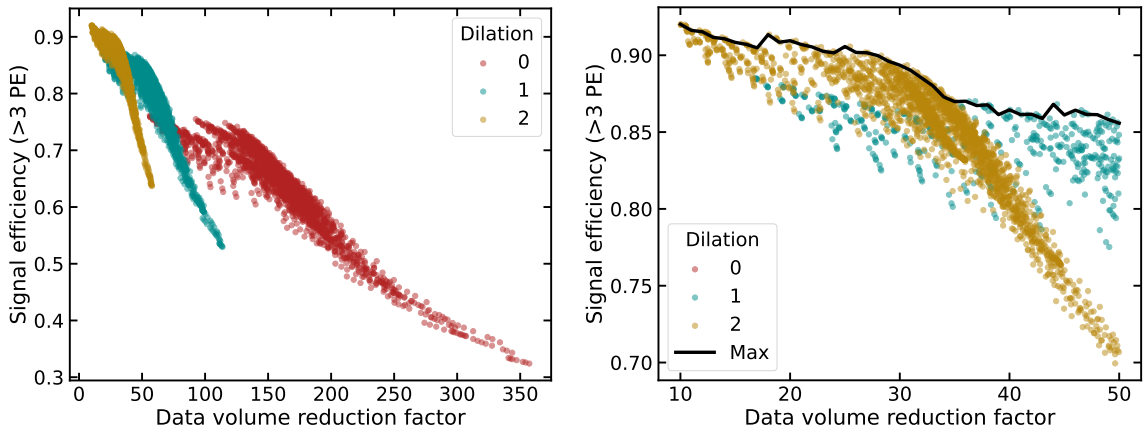

(a) Full range of reduction factors

(b) DVR factor from 10 to 50

Figure 3.12: Signal efficiency at detecting pixels with > 3 true PEs as a function of data volume reduction factor for multiple parameter combinations using time-based clustering. Computed on proton simulations at NSB 216 MHz. All values tested for each free parameter are shown in Table 3.2. (a) shows the evolution of the signal efficiency across all DVR factors and (b) only from 10 to 50 (defined by the CTAO). The black solid line shows the best signal efficiency. The three values for the number of dilated rows are indicated with different colours.

Parameter	Values	DVR 30	DVR 40
noise cut (PE)	2.3, 2.5, 2.7, 3.0, 3.5, 3.7, 4.0	2.3	2.5
dscale (m)	0.075, 0.1, 0.125, 0.15, 0.175	0.175	0.175
tscale (ns)	3, 4, 5	5	4
tailcuts threshold (PE)	6, 8, 10	8	6
minPts	3, 4, 5, 6, 7	6	4
dilated rows	0, 1, 2	2	1

Table 3.2: Values used in the optimisation process for each free parameter of time-based clustering, and the resulting optimised values at DVR factors 30 and 40.

Parameter	Values	DVR 30	DVR 40
picture threshold (PE)	From 4.0 to 15.0, steps of 1.0	4.0	6.0
boundary threshold (PE)	From 2.0 to 11.0, steps of 1.0	5.0	4.0
picture neighbours	0, 1, 2	2	2
dilated rows	0, 1, 2	2	2

Table 3.3: Values used in the optimisation process for each free parameter of Tailcuts, and the resulting optimised values at DVR factors 30 and 40.

based clustering can take. Table 3.3 shows the same for Tailcuts. After looping through all these values and computing all possible combinations, Fig 3.12 is

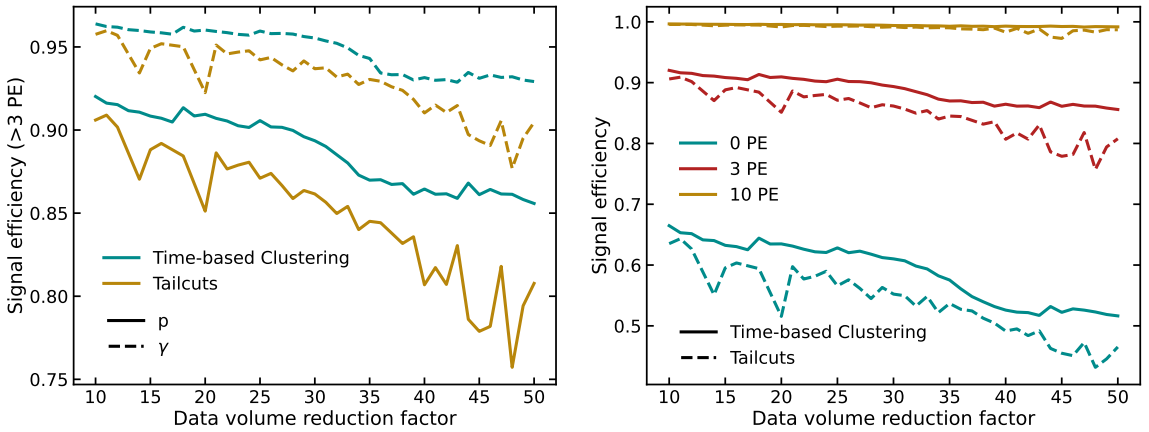

(a) Signal efficiency > 3 PEs with increasing DVR factor for the two DVR algorithms using gamma and proton simulations.

(b) Protons-only signal efficiency of detecting pixels with > 0 PEs, > 3 PEs and > 10 PEs of true signal as a function of DVR factor.

Figure 3.13: Fraction of signal pixels detected by time-based clustering or Tailcuts as a function of the DVR factor for FlashCam, using proton and gamma-ray simulations. Computed using the optimised set of free parameters at each DVR factor.

obtained. Fig. 3.12a shows the total fraction of signal pixels (defined as pixels with more than 3 PEs) detected as a function of the DVR factor. It is computed using proton shower simulations at an NSB rate of 216 MHz. Each point represents a different parameter set, with signal efficiency and DVR computed from the same set of simulated events. The different colours indicate the number of dilated rows that are added. Fig. 3.12b shows a subset of these points for DVR factor ≥ 10 and ≤ 50. The black line represents the maximum signal efficiency achieved for each DVR factor. For each DVR factor bin (of size 1), the parameter set achieving the highest signal efficiency is considered optimal for that level of data reduction. The same procedure is applied to Tailcuts.

The result of the above investigation is shown in Fig. 3.13a, which depicts the highest signal efficiency achieved by the time-based clustering and Tailcuts algorithms as the DVR factor increases from 10 to 50. The signal efficiency is calculated for both methods using the same gamma-ray (dashed lines) and proton (solid lines) simulations. Fig. 3.13b shows the signal efficiency when a signal pixel is defined as having more than 0, 3, and 10 PEs of true intensity, always tested on proton showers.

The CTAO will first apply data volume reduction with a low DVR factor of 10, which will then increase progressively to 50. It is observed that the time-based clustering method consistently detects more signal pixels than Tailcuts, using both

gamma and proton showers, at the same DVR factors. Therefore, with the time-based clustering method, more signal and less noise are always detected, achieving the same reduction factor. At DVR factors of 30 and 40, the best parameter combination for Tailcuts and time-based clustering are found in Table 3.3 and 3.2, respectively.

3.2.3 *Robustness of the methods*

The methods are tested against changes in the instrument and the sky that can affect the DVR algorithm's performance. Robustness is crucial, as DVR must perform well under all conditions. The following scenarios are tested:

- Increasing NSB rate
- Increasing number of broken pixels in the camera
- Increasing uncertainty in calibration

The optimal parameters for the two DVR factors, 30 and 40, are used in the following performance plots.

Night sky background rate

The algorithms are tested at different NSB levels by simulating a FlashCam exposed only to the NSB sky, with no showers. The nominal NSB is set to 0.216 PEs/ns. Multiple simulations are performed at different overall NSB rates, ranging from half of the nominal NSB rate and up to 4.0 times the nominal NSB. The DVR methods are applied to this data, with the charge-dependent parameters of each technique, Tailcuts, and time-based clustering, defined not in absolute PE but as percentiles of the charge distribution. The percentile is chosen such that at nominal NSB, the charge-dependent parameters at DVR factors of 30 and 40 lead to the values shown in Table 3.2 and 3.3.
For each simulated NSB level, the number of events with at least one noise cluster that wrongly pass the DVR election is determined and plotted in Figure 3.14, normalised to the number of events at the nominal NSB rate, as a function of increasing NSB. The rate of events containing noise decreases with NSB because, in the neighbour-based charge reconstruction, the probability to encounter a pair of unusually large noise pulses (i.e., exceeding the percentile of the individual pixel charge distribution) in adjacent pixels diminishes with increasing NSB [155]. This effect is reflected in both the Tailcuts and time-based clustering methods.

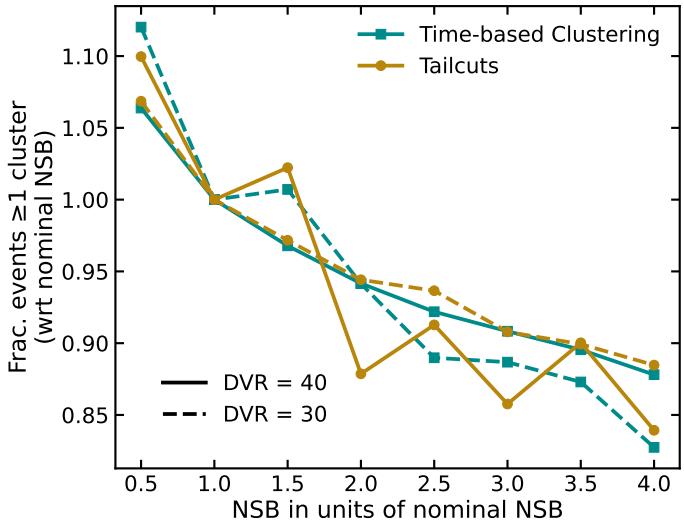

Figure 3.14: Fraction of noise-only events that contain at least one noise cluster after DVR, i.e. that survive, over the fraction at nominal NSB as a function of increasing NSB from 0.5 to 4.0 of the nominal NSB. The two DVR methods are compared at two reduction levels of 30 and 40. Events do not include any CHerenkov signal; only noise and NSB.

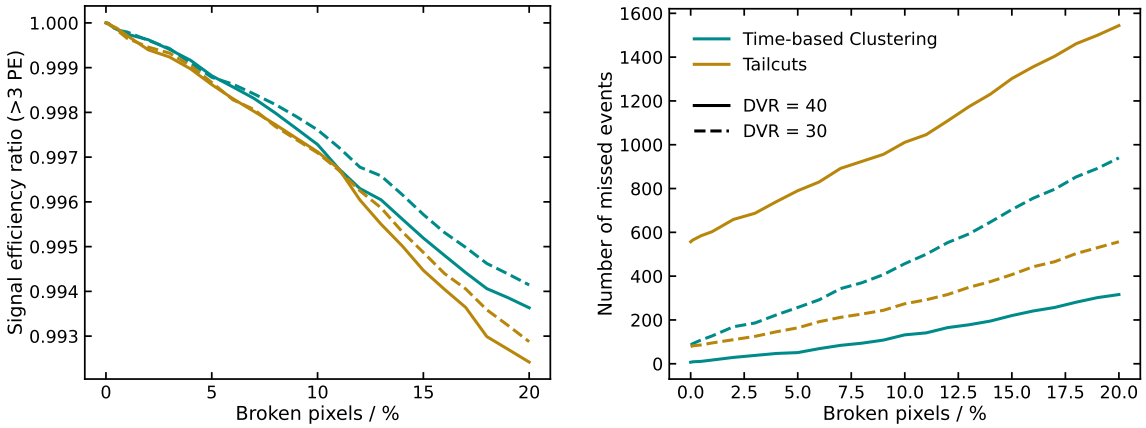

(a) Ratio of the signal efficiency (> 3 PEs) at a given percentage of broken pixels and at 0%.

(b) Number of missed events as the fraction of broken pixels (in %) increases.

Figure 3.15: Effect of increasing the percentage of broken pixels in the camera on signal detection after time-based clustering method and Tailcuts are applied at two different DVR levels of 30 and 40. Computed using gamma-ray shower simulations.

Broken pixels

Some pixels may malfunction for various reasons. It could be a localised problem in only one pixel, or, for example, a bright star that causes the deactivation of two or three pixels as a protection measure. The performance of the two DVR methods

with broken pixels is evaluated by inducing multiple pixel malfunctions in the simulations.

Fig. 3.15a shows the ratio of signal efficiency (> 3 PEs) at a given percentage of broken pixels to that at 0%, as a function of increasing fraction of broken pixels in the camera, using gamma-ray shower simulations at 216 MHz NSB rate. The broken pixel fraction ranges from 0% (i.e., only the six inherently broken pixels in FlashCam, Chapter 4) to 20% of the total camera pixels. Even at 20%, the signal efficiency remains above 99% of the original signal detection rate.

Fig. 3.15b shows the evolution of the number of missed events as the fraction of broken pixels in the camera increases. The figure is made from more than 20,000 simulated gamma events. Tailcuts show a substantial difference in the number of missed events for DVR factors 30 and 40, attributable to a higher picture threshold. The time-based clustering method, however, detects nearly all events at DVR 40 but misses a higher number of events at DVR 30 due to a higher Tailcuts threshold and a higher *minPts* value.

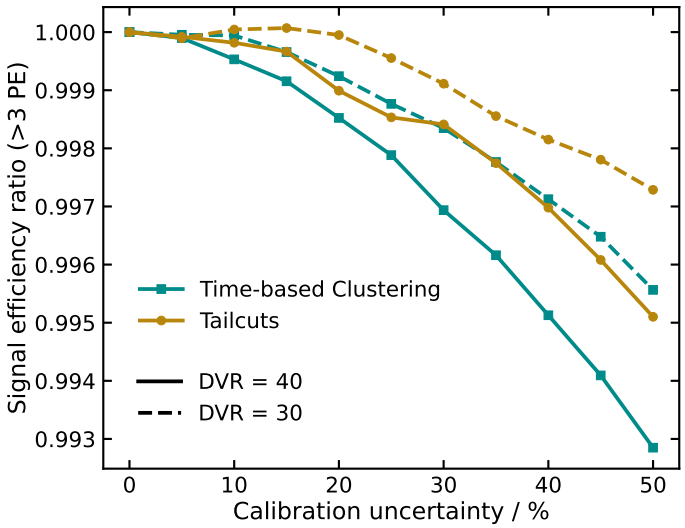

Figure 3.16: Ratio of the signal efficiency (> 3 PEs) with increasing gain calibration uncertainty over the signal efficiency at 0%. Two DVR factors, 30 and 40, are evaluated for each method: Tailcuts and time-based clustering, using gamma-ray shower simulations at NSB of 216 MHz.

Calibration uncertainty

The effect of gain calibration uncertainties on the DVR methods is evaluated. The calibration uncertainty is simulated by multiplying each pixel's charge by

a Gaussian random variable with mean 1.0 and standard deviation equal to the calibration uncertainty.
Fig. 3.16 shows the signal efficiency ratio relative to calibration uncertainties, ranging from 0% to 50%. The ratio is consistently > 0.99 for both DVR algorithms and DVR factors, showing significant robustness. The Clustering method is slightly more affected by the calibration uncertainty, but the difference is not significant. Overall, both methods demonstrate robustness to increasing night-sky background levels, the number of broken pixels, and calibration uncertainty.

3.2.4 *Verification on other CTAO cameras*

So far, the methods have been verified only on simulated FlashCam data. DVR must be applicable to all other CTAO cameras and universal across different camera types. In this part, the other CTAO cameras are tested. These are the cameras for SST [85] and LST [171], and NectarCAM [105] for MST. The images are reconstructed with the standard neighbour-based extractor (NPWS).

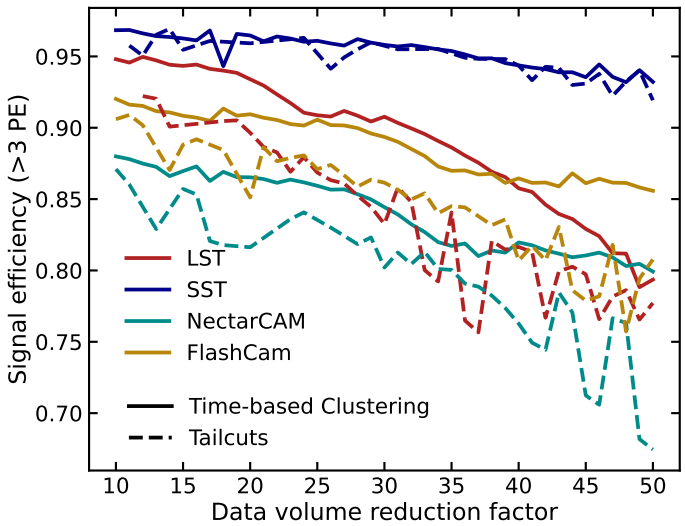

Figure 3.17: Signal efficiency at detecting pixels with > 3 PEs for all four CTAO cameras (SST-Camera, LST-Camera, MST-NectarCAM, and MST-FlashCam) and the two DVR algorithms (Tailcuts and time-based clustering) as a function of increasing DVR factor. Using proton shower simulations.

A set of values for each free parameter is looped over, and the signal efficiency and DVR factor are computed for each parameter combination, as was done with FlashCam. It is worth noting that the range of values differs from telescope to

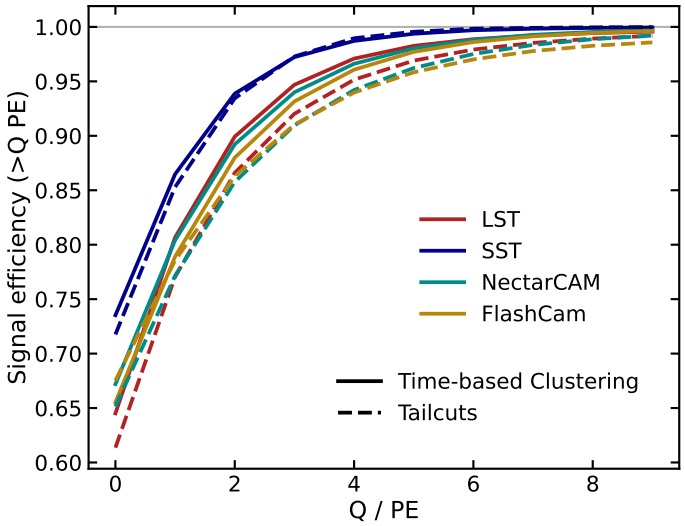

Figure 3.18: Efficiency of detecting pixels with true signal > Q PEs as Q increases. The free parameters for time-based clustering and Tailcuts are selected to achieve a DVR factor of 40. Four CTAO cameras are compared: SST-Camera, LST-Camera, MST-NectarCAM, and MST-FlashCam. The solid line shows the performance of time-based clustering, while the dashed line shows the performance of Tailcuts.

telescope. The SST camera, for instance, has smaller pixel spacings which result in smaller *dscale* values. The parameter set that yields the highest signal efficiency for each DVR factor is plotted in Fig. 3.17 and is tested on proton simulations. For all cameras except SST-Cam, time-based clustering outperforms Tailcuts in detecting signal while achieving the same level of data reduction. The SST camera detects the most signal, and both methods perform similarly in this case.
Fig. 3.18 shows the fraction of signal pixels with true charge > Q PEs that are correctly identified by both DVR methods as Q increases from 0 PEs to 9 PEs. This figure is made using gamma-initiated simulations at nominal NSB. The default nominal NSB differs across cameras in sim_telarray. The signal efficiency is computed for a set of free parameters that lead to a DVR factor of 40. The time-based clustering method achieves perfect efficiency for every camera at around $Q \approx 8$ PEs, whereas Tailcuts consistently performs worse.

3.2.5 *Alternative methods*

Some modifications to the basic method described earlier are examined in this section. Four alternatives are considered:

- Change in the charge extraction method
- Charge-dependent weights for each input point in DBSCAN
- Addition of an extra fourth dimension
- Alternatives to DBSCAN as the cluster algorithm

Multi-Peak clustering

A Cherenkov shower produces an image on the ground that illuminates the camera—and many of its pixels—within a short time window. The photons reach a given pixel nearly simultaneously, although not precisely. There is always a small time spread between them. This spread is usually negligible, but in some cases it can produce multiple intensity peaks rather than a single, clean pulse. A neighbour-based image extractor does not account for this complexity in the pulse shape and returns an average arrival time.
A second complication arises from afterpulses, which are detected at significant rates in all PMT-based cameras. These can appear hundreds of nanoseconds after the main signal pulse. Afterpulses may produce significant signals within a readout window, thereby skewing the search windows of neighbouring pixels.

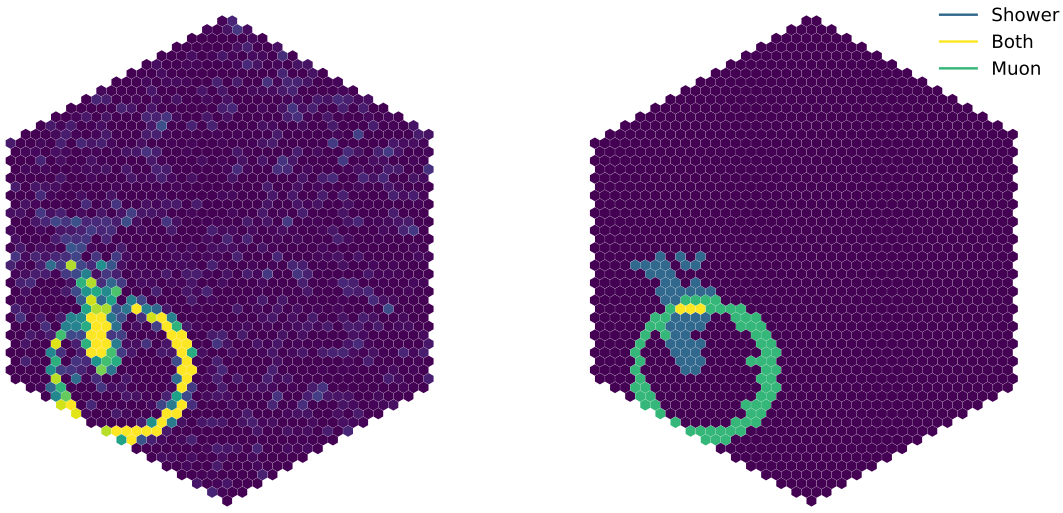

Figure 3.19: Multi-peak clustering capability demonstrated on a simulated muon ring and shower in the FlashCam camera plane. Left panel: reconstructed image in PE before DVR. Right panel: groups of pixels identified by the multi-peak clustering. The yellow pixels are part of both clusters.

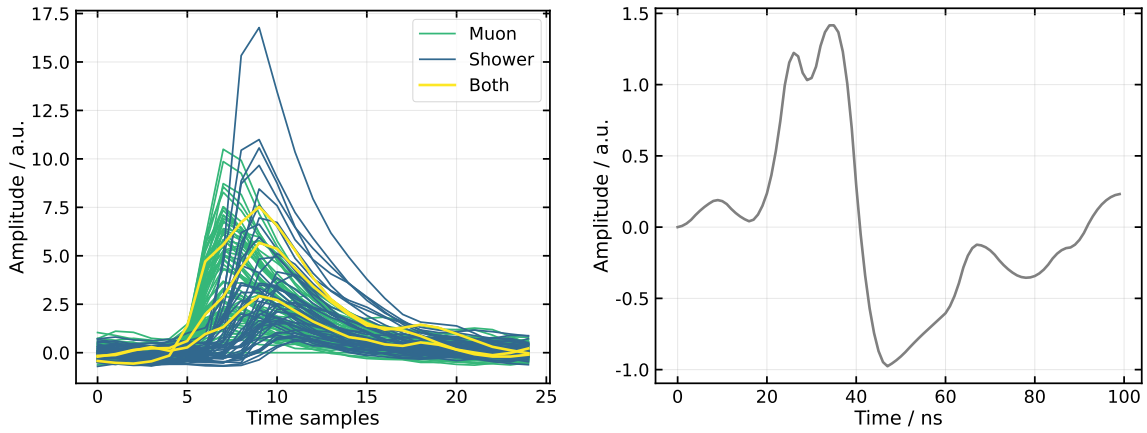

Figure 3.20: Left panel: calibrated traces from pixels within each cluster, with colours indicating the cluster ID in Fig. 3.19. The muon reaches the camera before the shower, and its traces are shifted to the left. Three pixels detect light from the shower and muon, and are clustered into both groups. Right panel: Differentiated and upsampled trace from one of the yellow pixels that belongs to two clusters.

Beyond timing spread and afterpulses, a third challenge emerges when Cherenkov cameras record images containing two separate clusters associated with different showers. This is especially common for hadronic events, which often produce accompanying muons. As a result, a single image can include light from multiple Cherenkov showers, and some pixels may receive photons from more than one of them. Their traces can therefore show two or more distinct intensity peaks. Identifying these clusters separately is important for gamma–hadron separation.
To address these three challenges—timing spread, afterpulses, and multiple shower clusters—a robust solution involves detecting every significant local maximum in each trace rather than selecting a single peak based on neighbouring pixels. This approach improves the construction of time clusters when multiple peaks are present. Each significant peak is treated as an independent time measurement and passed to DBSCAN, provided that its intensity exceeds a threshold relative to the pixel's noise level. After clustering, any pixel with a substantial signal-to-noise ratio that the time-clustering step might have excluded is also added. The signal is simply the peak value.
Fig. 3.19 shows the result of clustering every local peak in each trace for one target event. The left panel displays a PE image in which a muon ring is clearly distinguished from a shower, with both overlapping in multiple pixels. The right panel presents the clustering results: two distinct clusters corresponding to the muon and shower images, with three pixels detecting Cherenkov signals from

both sources and, therefore, assigned to both clusters. This method allows pixels to belong to multiple clusters when multiple signals with different arrival times overlap.
Fig. 3.20 shows the traces of pixels in each cluster. The left panel displays all pixels passing the clustering step, coloured by cluster ID as in Fig. 3.19. The muon arrives first, indicated by traces shifted to the left on the time axis, while the shower follows shortly thereafter. The three pixels belonging to both clusters appear as yellow traces with two peaks. The right panel shows the differentiated and upsampled trace for a single yellow pixel. The trace clearly exhibits two peaks. Standard clustering would capture only the latest, slightly more prominent peak, leaving part of the pixel's information unaccounted for. This algorithm successfully discriminates between the two main components of the trace.
This revised method for reconstructing pixel charge and time also avoids introducing artificial time correlations among noise pixels. Figure 3.21 shows the signal-efficiency versus DVR factor curve for the Multi-Peak method alongside the previously described methods. While it outperforms Tailcuts, it does not surpass the standard time-based clustering approach for signal detection. However, it warrants further discussion and study as a promising candidate for both offline image cleaning and online DVR, as the signal-to-noise ratio calculation is independent of calibration and thus unaffected by calibration uncertainty.

Weighted DBSCAN

The time-clustering method is effective at detecting temporal patterns within an image. However, the absence of charge information in the clustering of the data is a limitation of this method. Ideally, one would like to combine charge and time information to improve cluster identification and avoid removing significant-intensity pixels. This is why, for the standard DVR method described earlier, a second step has been applied that includes pixels not selected by DBSCAN but with a very high significant charge.
A more integrated solution is to incorporate charge information directly into the clustering process, rather than via an additional post-processing step. DBSCAN supports a per-point weight factor, allowing greater weight to be assigned to time measurements based on their charge significance. Instead of counting the number of points within an ε radius neighbourhood and comparing it to *minPts*, the weights

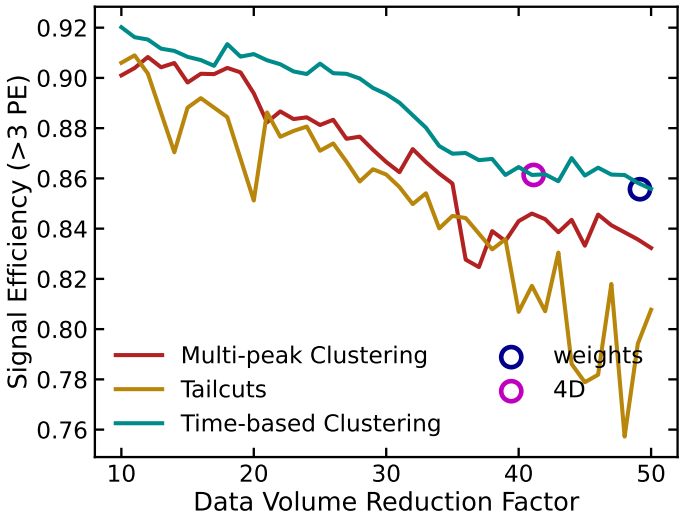

Figure 3.21: Signal efficiency of detecting pixels with a true signal of > 3 PEs as a function of the DVR factor for the standard time-based clustering, Tailcuts, and the multi-peak clustering. The weighted and 4D clustering methods are compared to the other algorithms using the free parameters shown in Figure 3.21 at DVR factor 40.

of the points within that region are summed. Since the weights must satisfy ≤ 1.0, a smaller *minPts* value is typically needed to be compared to the unweighted case. The charge-dependent weighting factor is defined as,

$$\frac{1}{1+\exp\frac{-(Q\,(\mathrm{PE})+A)}{B}} \tag{3.2.1}$$

where A and B are two free parameters, and Q is the charge in PE. Other expressions for the weighting can be analysed. The weighting factor is also used to improve the detection of small clusters that standard DBSCAN would otherwise miss. This method will also be explored later on H.E.S.S. FlashCam (Section 5.2). In Fig 3.21, the total signal efficiency and DVR factor after using this method are seen as a dark blue circle with free parameters set to the ones at DVR 40 for the standard procedure. It clearly shows that, with this method, it is harder to achieve the same *minPts* as without weights. Signal efficiency decreases, and the DVR factor increases. But still, the result lies on the time-based clustering line.

Extra dimension in DBSCAN

Another way to account for the intensity of each pixel within the cluster is to add a fourth charge-dependent dimension to DBSCAN. The charge-dependent extra

dimension cannot be the charge itself, as the cluster is formed based on value proximity and similar density. The additional dimension is added as follows,

$$\log_{10}\left(\frac{Q\,(\mathrm{PE})}{Q_{\max}\,(\mathrm{PE})}\right) \tag{3.2.2}$$

The magenta circle in Fig. 3.21 shows the total signal efficiency and DVR factor when using a time-based clustering method with an extra charge dimension using the parameters of time-based clustering at a DVR factor of 40. Adding an extra dimension does not seem to increase the ability to detect more signal pixels.

Other clustering algorithms

In addition to the previously described clustering algorithm, another method can be used instead of DBSCAN. Starting with Hierarchical DBSCAN (HDBSCAN) [172], it completely misidentifies clusters and cannot handle the data points.
The major drawback of DBSCAN is that it is not designed to handle data of varying density. In proton-induced showers, small clusters of subcomponents with multiple densities are expected. Therefore, the OPTICS (Ordering points to identify the clustering structure) [173] algorithm is also explored, as it is designed to handle data of varying densities.

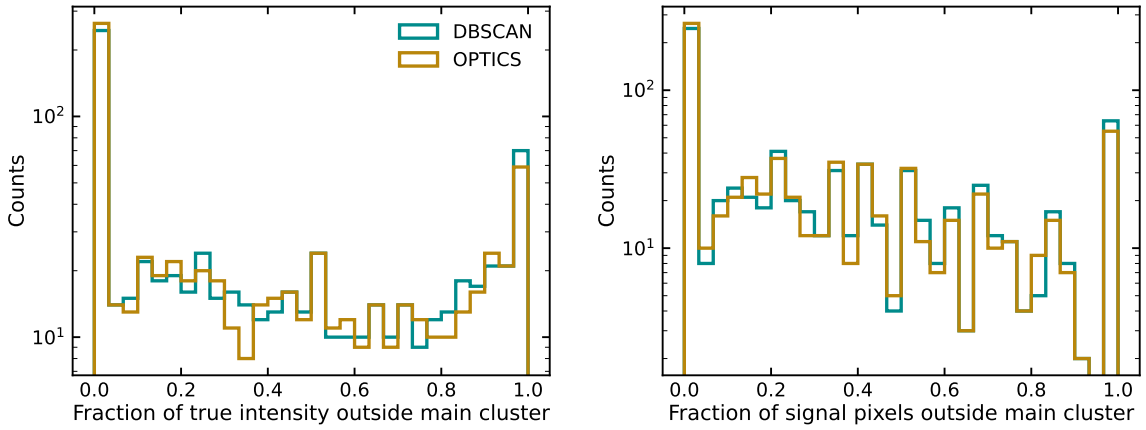

(a) Fraction of detected true intensity outside the main cluster

(b) Fraction of detected pixels outside the main cluster.

Figure 3.22: Detection comparison between DBSCAN and OPTICS of signal correctly identified outside the main cluster. Left panel: Distribution of the fraction of the total true intensity outside the main cluster detected by each method. Right panel: Distribution of the fraction of signal pixels outside the main cluster identified by each method.

Fig. 3.22 shows the capability of both methods in detecting pixels that are located outside the main cluster. These tests are performed on proton simulations. The two clustering algorithms are compared under the same parameter settings. On the left, the distribution of the fraction of detected true intensity (the true intensity here is the sum of all pixels' true charge only if they exceed 3 PEs) by DBSCAN and OPTICS outside the main cluster. On the right plot, the same is shown, but instead of intensity, the fraction of detected pixels with > 3 PEs.
Both algorithms similarly detect pixels that are not part of the main shower component. There is no clear evidence that either method performs significantly better; therefore, DBSCAN remains the best choice given its superior computational speed.

3.2.6 *Computational time*

As discussed in [155], the algorithms have not yet been optimised for speed and have been tested only in Python [174] [175] so far. Therefore, these tests on computational performance are very preliminary. Initial benchmarks show that the Clustering and Tailcuts approaches have comparable processing times. On a single CPU core, each method can process roughly 200–300 events per second, which would require about 20 cores to satisfy the CTAO requirements.

3.2.7 *Array-level performance*

The Tailcuts and time-based clustering methods described above also serve as image-cleaning algorithms in offline analysis. Each technique's image-cleaning performance is evaluated by comparing the angular and energy reconstruction in simulated gamma-induced showers.
The IRFs are computed using gamma-ray simulations at 20° zenith angle and 0° offset between the telescope axis and the shower core. The simulated array of telescopes consists of 14 MSTs in the Southern array equipped with FlashCam cameras. The configuration and geometry of the MSTs is discussed in Appendix B. Two sets of free parameters for Tailcuts and time-based clustering are selected to achieve the same DVR factors corresponding to 195 and 200. For image cleaning, the data reduction factor is set considerably higher than for DVR, since image cleaning requires tighter cuts and lower false positive rates to maintain performance. Selecting parameters based on signal efficiency and DVR factor is suboptimal for image

cleaning. Each method should instead be optimised by selecting parameters that maximise gamma-hadron separation performance, as described in [176]. However, this approach is computationally expensive and highly inefficient. This thesis focuses primarily on DVR and signal-pixel detection rather than image cleaning and resolution performance. Image cleaning is explored as a natural application of DVR methods, but remains secondary to the main objectives.

Charge and time are extracted from all pixels using the FlashCam extractor without applying a prior DVR step. Image cleaning is performed using either Tailcuts or the time-based clustering algorithm. Both methods are tested using free parameters that yield the same two DVR factors, 195 and 200. Then the Hillas parameters are calculated. From the Hillas parameters, the intersection of the major axes of each pair of images is used to reconstruct the direction of the shower, as described in Section 2.4.4. Energy is reconstructed using a random forest regressor. A multiplicity cut is applied, requiring at least three telescopes to trigger, thereby ensuring stereoscopic reconstruction. The following additional cuts are applied to ensure only good-quality images are included in the reconstruction:

- The total image intensity per camera must exceed 50 PEs after cleaning
- Hillas parameterisation must be valid, and Hillas *width* must be > 0 m
- The total number of pixels after cleaning must exceed 3
- The number of PEs at the borders of the camera (the outermost two rows of pixels) must be < 0.2 of the total intensity of the image after cleaning. This cut ensures that truncated images, which have a large fraction of their development outside the camera, are discarded, as they lead to large reconstruction uncertainties (more on the next section).

Furthermore, the IRFs are computed before any gamma-hadron separation cuts. Fig. 3.23 shows the angular resolution achieved using the two image cleaning methods. Across the two DVR factors considered here, both methods perform similarly, with no apparent improvement in either direction. The energy bias and resolution plots are shown in Fig. 3.24. Similar energy performance is also observed. However, the energy resolution shows a slight improvement with the clustering approach.

The weighted time-based clustering, explained in Section 3.2.5, is also compared with the standard clustering algorithm. Fig. 3.25 shows the angular and energy resolution achieved using the two methods at a DVR factor of 200. As the weighting makes it harder to reach *minPts*, *minPts* is lowered from 7 (used in the unweighted

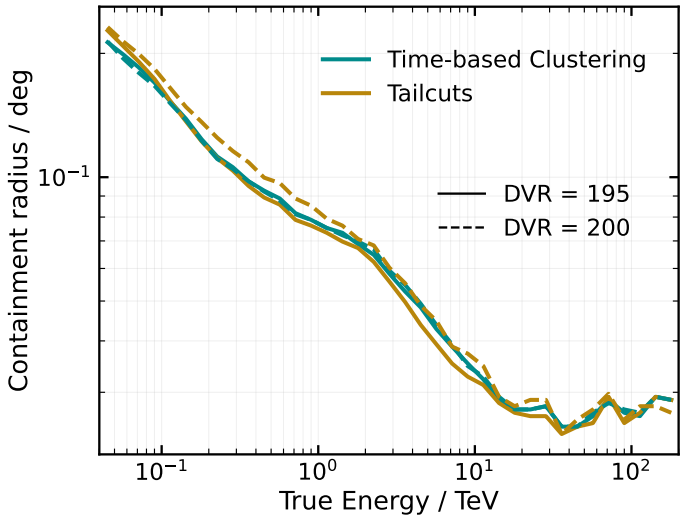

Figure 3.23: Angular resolution, defined as 68% containment radius, using Tailcuts and time-based clustering algorithms for image cleaning. The free parameters are defined so that both methods are compared at the same two DVR factors, 195 and 200. Results are based on simulated on-axis gamma-ray events at 20° zenith in an array of 14 MSTs at the Southern site.

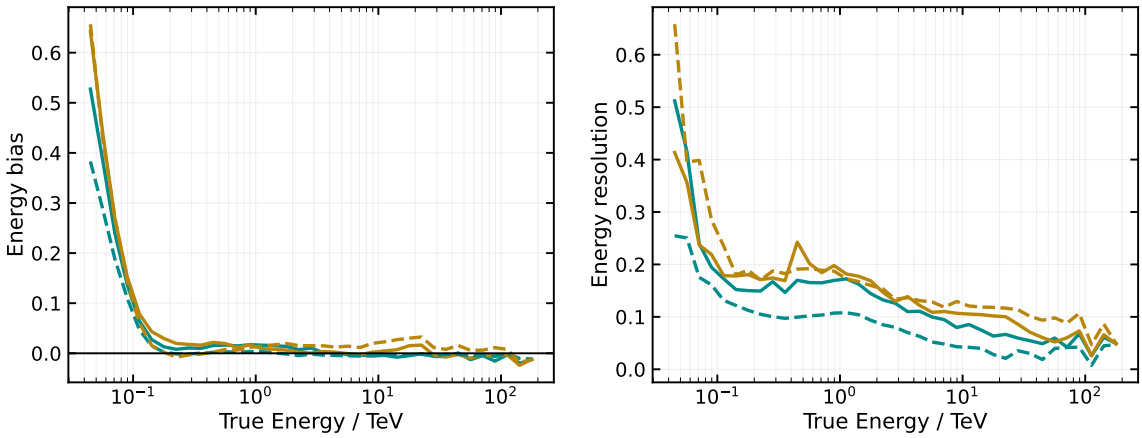

(a) Energy bias

(b) Energy resolution

Figure 3.24: Energy performance (bias and resolution) using Tailcuts and time-based clustering algorithms for image cleaning. The free parameters are defined so that both methods are compared at the same two DVR factors, 195 and 200. Results are based on simulated on-axis gamma-ray events at 20° zenith in an array of 14 MSTs.

case) to 5 (in the weighted case). The performance of both methods is nearly identical.

While this comparatively rough investigation of time-clustered cleaning only shows small improvements in energy resolution, others have shown that similar methods

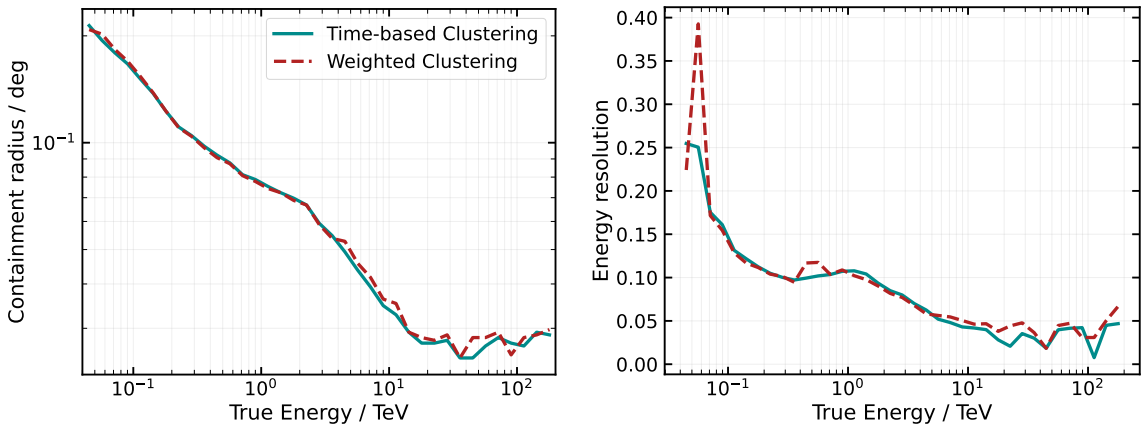

(a) Angular resolution

(b) Energy resolution

Figure 3.25: Comparison of angular and energy resolution performance between the standard and weighted time-based clustering methods. Both approaches use the same free parameters selected to achieve a DVR factor of 200, except *minPts*, which is reduced from 7 to 5 in the weighted case. Results are based on simulated on-axis gamma-ray events at 20° zenith in an array of 14 MSTs.

are more capable with more refined parameters (cf. [176]). Section 5.2 further shows the improvements of the weighting time-clustered image cleaning in terms of angular and energy resolution and sensitivity for H.E.S.S..

3.3 Image parameterisation

Typically, the cleaned shower images are processed by the computation of the Hillas parameters, as described in Section 2.4.3. These parameters are then used as an input to reconstruct the basic properties of the particle that initiated the air shower: energy, direction, and particle species.
The parameterisation of a shower image is generally well described by the Hillas parameters. However, two types of images are excluded from the shower parameter reconstruction to ensure reliable results. First, images that are too small are excluded. With only a few pixels, quantities such as the major axis and orientation cannot be accurately computed. Second, truncated images. These occur at large impact distances where elongated shower images are detected partially at the edge of the camera and extend beyond its physical limits. At such distances, only the most energetic events can be detected. The camera's physical boundaries constrain parameter estimation, preventing accurate computation of the Hillas parameters. This produces large uncertainties in the Hillas ellipse orientation and extension, thereby reducing angular reconstruction accuracy. To improve reconstruction accuracy, a truncation cut is applied to remove edge events. However, this approach limits the effective area and significantly reduces the number of high-energy events, thereby decreasing detector sensitivity at these energies.
The rejection of cropped or truncated images can either be performed by imposing a cut at the maximum distance of the Hillas COG to the camera centre, or by imposing a cut at the maximum fraction of signal collected in the outermost two rows of pixels in the camera, also referred to as *leakage*. The second cut is more precise because it directly measures the shower intensity at the camera edge. In contrast, the first cut may reject images that lack significant *leakage*.
Fig. 3.26 shows the signal *leakage* as a function of the simulated impact distance, using a single FlashCam installed in an MST and gamma-ray simulations. The line shows the average across many simulated events. The *leakage* clearly increases with impact distance. At large impact distances, only the most energetic events can reach the telescope and trigger the camera. Truncated images are rejected with a cut at $leakage \leq 0.1$.
As the impact distance increases and, therefore, a greater number of truncated images are observed, the Hillas reconstruction of these images degrades. The radial distance from the camera centre to the Hillas COG should, in principle, increase

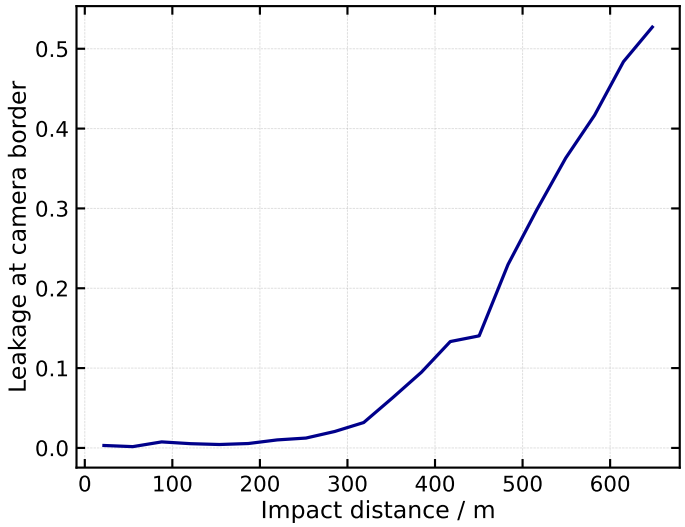

Figure 3.26: The *leakage* or fraction of signal pixels detected at the outermost two rows of the camera as a function of the simulated impact distance, averaged over all simulated gamma-ray events.

linearly with impact distance. However, the distance of the image as shown in Fig. 3.27a (Hillas) increases more slowly as the impact distance exceeds $\sim 400\,\mathrm{m}$. These effects are not physical but a consequence of the poor parameterisation of truncated images. Similarly, the Hillas *length* (see Fig. 3.27b) increases with impact distance until truncated images start to become relevant and the average Hillas length starts to decrease dramatically.

3.3.1 *Two-dimensional ellipse fitting*

VERITAS [177] first described a method for fitting a cleaned image with a two-dimensional Gaussian model to improve reconstruction of truncated images. This method has been tested multiple times [178]. A preliminary study of this method on the CTAO was done by Gaia Verna [179] [180] [181]. This section examines a modified version of the previous two studies. A preliminary version of this method is in the public pull request of *ctapipe* by the author of this thesis [182]. The method can be described with the following steps:

- Images are cleaned with Tailcuts
- The Hillas parameters are calculated on the cleaned images

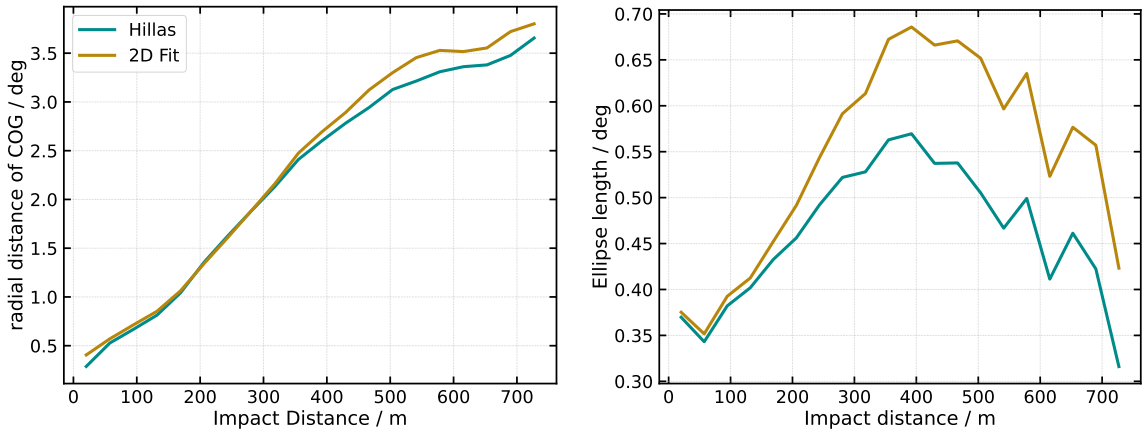

(a) Centre of gravity

(b) Length

Figure 3.27: Radial distance from the camera centre to the reconstructed ellipse COG (left panel) and ellipse *length* (right panel) of cleaned images as a function of the true value of the impact distance of the event to the telescope, averaged over all events. Two reconstruction methods are shown: Hillas and 2D ellipse fitting parameterisation. Using gamma-ray simulations.

- Tailcuts image cleaning is too restrictive, resulting in the loss of relevant features of the shower image. Therefore, two extra rows of pixels are added around the cleaned image.
- The extended image is fitted to a two-dimensional model that resembles the shower image. The model's seeds are the Hillas parameters. In this step, the negative log likelihood of each pixel is computed, and the sum over each pixel is minimised

A 2D model is fitted by performing a pixel-by-pixel comparison between expectations and observations and minimising the sum of the pixel negative log-likelihoods. The Hillas parameters are good seeds for the fit. Different models can be considered in the fitting. In previous analysis, a simple 2D Gaussian was investigated. However, showers exhibit longitudinal asymmetry. Therefore, rather than fitting the image with a 2D Gaussian, a skewed Gaussian is used on the longitudinal axis to account for the asymmetry. The image's *skewness* can be extracted directly from the fit. In the transverse direction, a Gaussian distribution provides an appropriate parametrisation for the shower profile.

The image can therefore be described by a Gaussian distribution in the transverse direction, multiplied by a skewed Gaussian distribution in the longitudinal direction. The normal distribution is given by:

$$\phi(x_i, y_i) = A \exp\left(-\frac{1}{2}\left(\frac{\text{trans}_i}{\sigma_{\text{width}}}\right)^2\right), \tag{3.3.1}$$

where A is the amplitude and σ_{width} is the *width* of the ellipse. trans_i is the transversal distance of each pixel to the centre of gravity of the image, and it is equivalent to:

$$\text{trans}_i = -(x_i - x_c)\sin(\theta) + (y_i - y_c)\cos(\theta) \tag{3.3.2}$$

Each pixel is located at a position within the camera of (x_i, y_i) and (x_c, y_c) is the position of the COG in the x and y-axis. θ is the rotation angle of the ellipse as described in Fig. 2.18. The skewed Gaussian distribution [183] is equivalent to:

$$P(x_i, y_i) = \frac{2}{w} \times \phi\left(\frac{\text{lon}_i - \varepsilon}{w}\right) \times \Phi\left(\alpha \frac{\text{lon}_i - \varepsilon}{w}\right), \tag{3.3.3}$$

where lon_i is the pixel longitudinal distance from the COG:

$$\text{lon}_i = (x_i - x_c)\cos(\theta) + (y_i - y_c)\sin(\theta). \tag{3.3.4}$$

The skewed Gaussian distribution is the normal distribution ϕ times the normal cumulative distribution Φ. α is the parameter that describes the shape of the distribution; $\alpha = 0$ leads to a normal distribution. It relates to the *skewness* (α_3) of the distribution as:

$$\alpha_3 = \frac{1}{2}(4 - \pi)\frac{\left(\frac{2}{\pi}\delta^2\right)^{2/3}}{\left(1 - \delta^2\frac{2}{\pi}\right)^{3/2}}, \tag{3.3.5}$$

with δ defined as,

$$\delta = \frac{\alpha}{\sqrt{1 + \alpha^2}}. \tag{3.3.6}$$

The scale parameter w is related to the *length* of the ellipse (σ_{length}) and δ as follows,

$$w = \frac{\sigma_{\text{length}}}{\sqrt{1 - \frac{2\delta^2}{\pi}}}. \tag{3.3.7}$$

Finally, the location parameter ε is related to δ as,

$$\varepsilon = -w\delta\sqrt{\frac{2}{\pi}}. \tag{3.3.8}$$

With a skewed normal distribution along the longitudinal axis and a normal distribution in the transverse direction, one can fit σ_{length}, σ_{width}, (x_c, y_c), and θ and derive the *skewness*. With these parameters, the *kurtosis* can be computed as described in [183]. More details on the skewed distribution can be found in [183], [184], and in the skewnorm package of SciPy [185]. By combining Equation 3.3.1 and Equation 3.3.3 and multiplying by the total number of PEs in the cleaned image, the predicted number of PEs in each pixel is extracted. The difference between the predicted and detected signals per pixel is then minimised.

Model likelihood

The likelihood to observe a signal s from n photoelectrons in a pixel given the expectation (predicted value) μ is the convolution of a Poisson distribution with the photomultiplier resolution [186]. The photomultiplier resolution is a Gaussian distribution of width $\sqrt{\sigma_p^2 + \sigma_\gamma^2}$, where σ_p is the pedestal width and σ_γ is the width of the single photoelectron peak. The likelihood of a pixel detecting a signal s is the sum over all possible numbers of PEs n [187],

$$P(s|\mu, \sigma_p, \sigma_\gamma) = \sum_n \frac{\mu^n e^{-\mu}}{n!\sqrt{2\pi(\sigma_p^2 + n\sigma_\gamma^2)}} \exp\left(\frac{-(s-n)^2}{2(\sigma_p^2 + n\sigma_\gamma^2)}\right). \tag{3.3.9}$$

Equation 3.3.9 can be further simplified when μ is high as,

$$P(s|\mu, \sigma_p, \sigma_\gamma) = \frac{1}{\sqrt{2\pi(\sigma_p^2 + \mu(1+\sigma_\gamma^2))}} \exp\left(\frac{-(s-\mu)^2}{2(\sigma_p^2 + \mu\sigma_\gamma^2)}\right). \tag{3.3.10}$$

The negative log-likelihood of pixel i is given by,

$$\ln\mathcal{L}_i = -2\ln P_i(s_i|\mu_i, \sigma_{pi}, \sigma_{\gamma i}). \tag{3.3.11}$$

The telescope negative log-likelihood [186] is the sum of the likelihood of each pixel in Equation 3.3.11 $\ln\mathcal{L} = -2\sum_{\text{pixel},\, i} \ln P_i(s_i|\mu_i, \sigma_{pi}, \sigma_{\gamma i})$. The telescope negative log-likelihood is minimised using MINUIT [188]. The Python [174] interface iminuit [189] to the MINUIT2 C++ package is used.

The fit also yields a goodness-of-fit measure that can serve as a key parameter for gamma-hadron separation. Goodness-of-fit (GoF) compares the model expectation with the observed image, quantifying how well a model based on gamma-ray showers describes the observations [178]. It is defined as,

$$\mathrm{GoF} = \frac{\sum_{pixel,\,i} (\ln\mathcal{L} - \langle \ln\mathcal{L} \rangle)}{\sqrt{2N_{dof}}}, \tag{3.3.12}$$

where N_{dof} is the number of degrees of freedom and $\langle \ln\mathcal{L} \rangle$ is the average value of the negative log-likelihood. The goodness-of-fit is stored for each event.

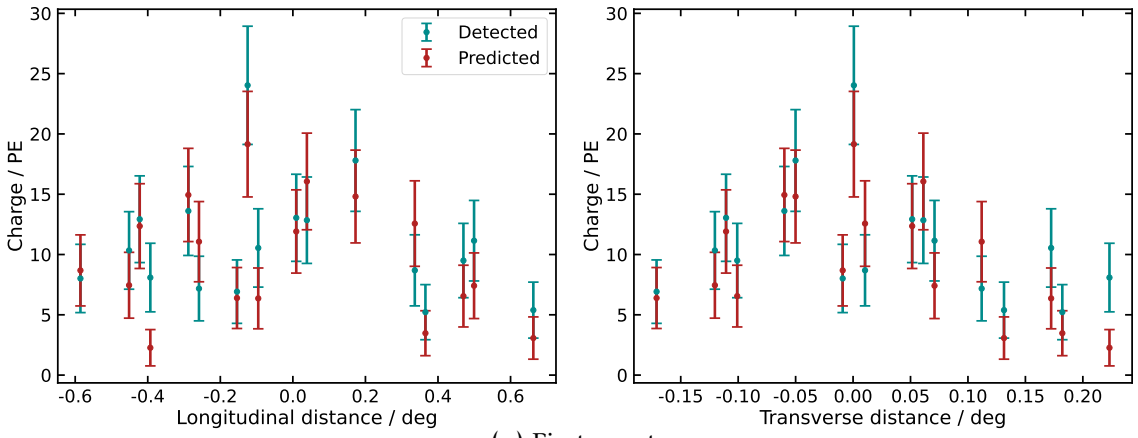

(a) First event

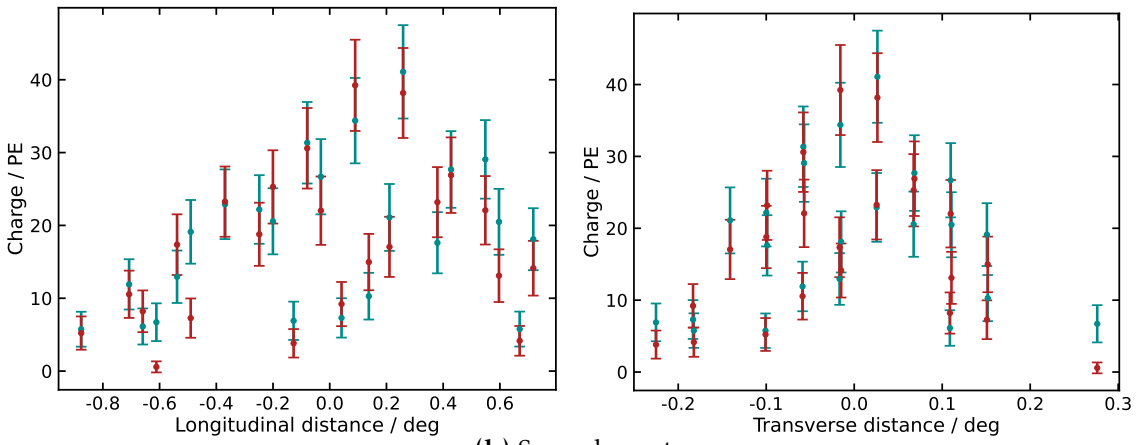

(b) Second event

Figure 3.28: The number of reconstructed PEs as a function of the longitudinal (left) and transverse (right) distance is shown together with the corresponding prediction in each pixel after image fitting with a 2D skewed Gaussian distribution. Two events are shown from gamma-ray simulations.

3.3.2 *Performance on simulations*

A 2D skewed Gaussian fit is performed, and the model-predicted signal is compared with the cleaned, reconstructed signal. Fig. 3.28 shows this comparison for each pixel in two simulated events. Fig. 3.28a presents the first simulated event, and Fig. 3.28b shows the second. For each event, the left figure shows pixel charge as a function of longitudinal distance, and the right figure shows charge as a function of transverse distance. Both examples demonstrate good agreement between the detected and predicted number of PEs.
Returning to Fig. 3.27, the ellipse parameters from the 2D fit are compared with the Hillas parameters as a function of increasing impact distance. Specifically, it shows the 2D-fitted *length* and radial distance of the COG, alongside the Hillas *length* and COG. At impact distances where image truncation becomes significant, the radial COG coordinates from the 2D fit increase more steeply with impact distance than those from Hillas parameterisation. Similarly, the fitted *length* exceeds the Hillas *length*, even for truncated images. Although the fitting method remains affected by truncation, its parameters are generally less sensitive to it. This results in a longer reconstructed *length* and a greater distance between the reconstructed image COG and the camera centre at high impact distances.

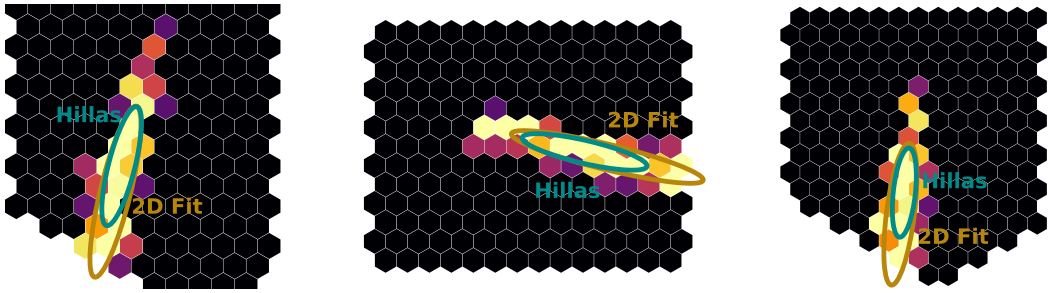

Figure 3.29: Three examples show simulated truncated images after extraction and cleaning, with reconstructed ellipses marked from Hillas parameterisation and 2D ellipse fitting.

Fig. 3.29 shows the reconstructed ellipse of three truncated images from gamma-ray simulations using both Hillas and 2D ellipse fitting. The Hillas ellipse is constrained within the camera limits, whereas the fitted ellipse extends beyond and more closely captures the actual extension of the shower image, though not fully.
The method is tested through angular direction reconstruction of simulated on-axis gamma-initiated showers. The simulation uses the full subarray of 14 MSTs

equipped with FlashCam cameras at a zenith angle of 20°, 0° offset, and an NSB rate of 216 MHz. Angular resolution performance is computed and compared for both Hillas and 2D-ellipse fitting parameters. The angular resolution is estimated only from images that meet the following criteria:

- A total amplitude of at least 50 PEs after cleaning
- At least 7 pixels retained after cleaning
- Valid Hillas or 2D-fitted parameters

A cut in truncated images is also examined. Two truncation cut scenarios are considered, distinguished by the maximum allowed *leakage*:

- No cut on *leakage* at the camera border
- A strict cut on truncation, < 0.1

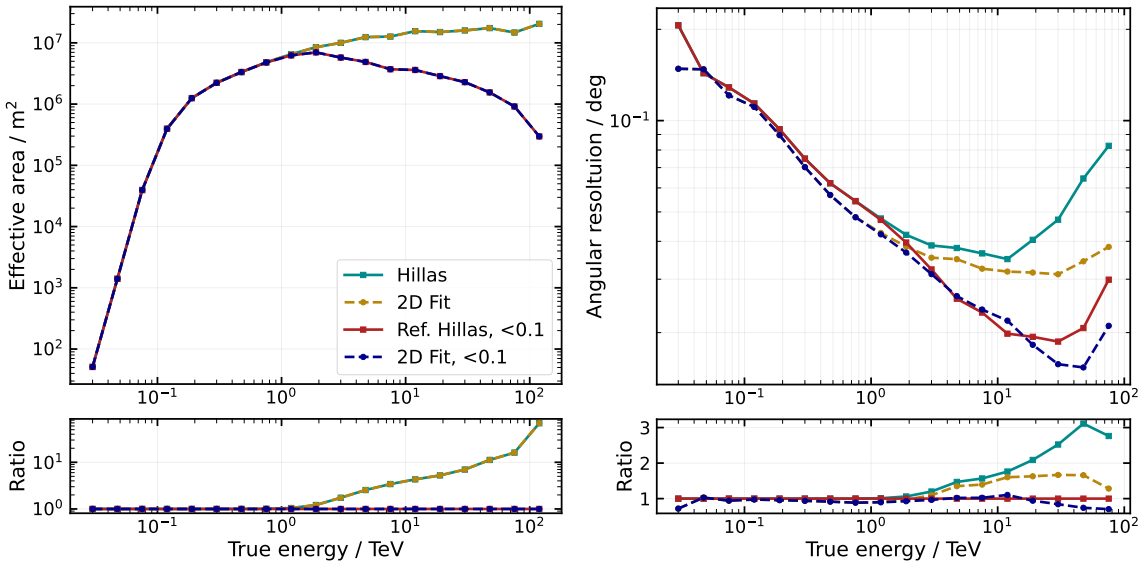

(a) Effective area

(b) 68% containment radius

Figure 3.30: Effective area and angular resolution using Hillas and 2D ellipse fitting algorithms for the computation of the image parameters. The performance is shown on simulations of 14 MSTs in the Southern array at nominal NSB. Two truncation cuts are examined. In the first case, a stringent threshold in the *leakage* is applied (< 0.1). In the second, no truncation cut is considered.

The angular resolution of both parameterisation methods is computed using a Tail-cuts cleaning algorithm with a picture threshold of 10 PEs, a boundary threshold of 5 PEs, and at least two neighbouring pixels. The parameters are then computed from the images that pass the quality cuts using both parameterisation methods. After parameterisation, a multiplicity cut is applied to the number of triggering telescopes. Only events that are detected by at least three telescopes after quality

cuts are included in the reconstruction. The direction of each event is reconstructed using the method described in Section 2.4.4 and the effective area is described in Section 2.4.5.

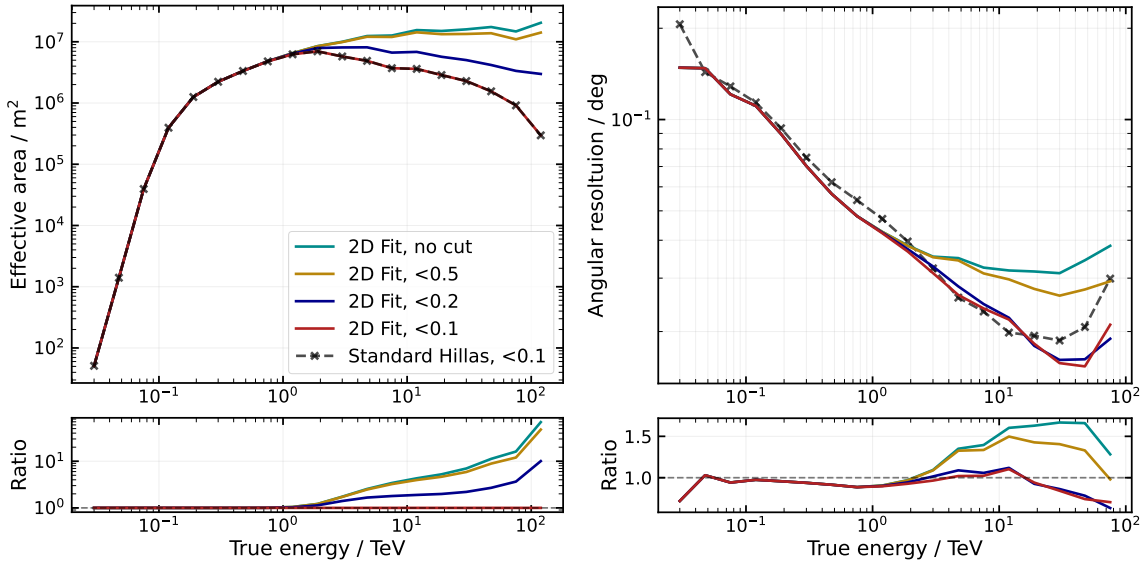

(a) Effective area **(b)** 68% containment radius

Figure 3.31: Effective area and angular resolution using the 2D ellipse fitting for image parameterisation on the same simulation set of 14 MSTs at nominal NSB. The performance of 2D ellipse fitting is shown for multiple truncation cuts at < 0.1, < 0.2, and < 0.5 of *leakage*, as well as for the case with no truncation cut. The performance curves are compared with the Hillas result when truncated images are excluded (< 0.1).

Fig. 3.30 shows the angular resolution and effective area using the two different methods for image parameterisation and the two cuts on truncated images. The effective area of the 2D ellipse fit and the Hillas parameterisation are identical within each quality cut. When truncated images are rejected, the effective area drops at 1 TeV. The inclusion of truncated images leads to a high uncertainty in the direction reconstruction at the same energy, as seen in Fig. 3.30b. This uncertainty is significantly improved when a 2D ellipse is fitted to the image. However, the performance remains substantially worse than without truncated images. When truncation images are excluded, direction reconstruction is clearly improved in both cases, and the fit slightly outperforms Hillas.

The effects of different truncation cuts are computed for the 2D ellipse fit and compared with the Hillas scenario with a cut at < 0.1 *leakage* in Fig. 3.31. Angular resolution and effective area are evaluated with truncation cuts at < 0.1, < 0.2, and < 0.5. Fig. 3.31b demonstrates that angular resolution degrades with increasing

leakage cut values. At < 0.5, direction reconstruction underperforms relative to Hillas at < 0.1. In contrast, the 2D fit at 0.1 and 0.2 outperforms the standard Hillas approach. At 0.2, the effective area (Fig. 3.31a) increases considerably compared to 0.1. Therefore, the 2D fit not only yields better angular resolution than standard Hillas but also a larger effective area, enabling looser truncation cuts that incorporate more high-energy events into the analysis.

3.4 Summary and outlook

Improved algorithms were presented for the following steps of the CTAO data processing chain: signal extraction of precalibrated traces, real-time data volume reduction, offline image cleaning, and image parameterisation.

A signal-extraction algorithm was implemented and tested using simulations of a FlashCam in the CTAO. The method performs trace preprocessing to address long-tailed pulses. The introduction of deconvolution and upsampling makes the pulse more compact and reduces the effect of phase jitter. It eliminates the long tail, thereby reducing the integration window from 7 samples (28 ns) to 7 ns. Therefore, preprocessing the traces before integration reduces the extractor's sensitivity to NSB rates. This extractor has been tested on FlashCam traces; in the future, the tests could be extended to other cameras within the CTAO. Saturation was not covered in this section. Signal extraction from saturated pulses is discussed in the next chapter.

DVR was discussed in detail. A DVR algorithm was presented as a candidate for the CTAO online analysis. This algorithm consists of a time-clustering first step followed by an intensity-based second step to use all available image information. Time-based clustering was compared with Tailcuts in terms of performance. Time-based clustering outperforms Tailcuts in discrimination power between signal and noise pixels. It continuously detects more signal and fewer noise pixels. The method was tested under high NSB conditions, a high number of broken pixels, and increasing calibration uncertainty. The algorithm was proven to be highly robust. Furthermore, the method was demonstrated to work for all CTAO cameras without requiring any modifications. A similar algorithm is being implemented in ACADA for its use on the LSTs in the Northern Hemisphere array. Several modifications to the standard clustering algorithm were investigated. Each alternative offers benefits for different applications. For example, multi-peak clustering improves time cluster identification and muon detection. However, none of these alternatives outperforms the standard method in terms of detection capabilities.

The DVR algorithms are also employed for image cleaning, as these tasks are closely linked. Both Tailcuts and time-based clustering achieve similar angular and energy resolutions. The standard time-based clustering algorithm was compared with

the weighted time-based clustering, yielding comparable performance. To enable a rigorous comparison between methods, future studies should optimise image cleaning algorithms based on IRF performance rather than detection, and each method should be evaluated with its optimal parameters.

Finally, the last step before event reconstruction is image parameterisation. The traditional cut performed by H.E.S.S. and, in the future, by the CTAO on truncated images improves the angular reconstruction of events while considerably minimising the effective area at high energies. This negatively affects the instruments' sensitivity to the low-rate, highest-energy events.
A more precise reconstruction of truncated images is possible using a 2D ellipse fitting scheme. The resulting increase in effective area, combined with slight improvements in angular resolution, could lead to enhanced sensitivities, particularly at high energies. Since achieving the highest sensitivities at the highest energies is crucial for detecting potential PeVatron candidates and understanding the origin of CRs [190], future studies of this method will focus on quantifying these improvements in sensitivity.
Furthermore, future studies should also include performance tests of gamma-hadron separation, incorporating goodness-of-fit as an additional parameter in the random forest regressor. The influence of NSB and broken pixels should also be evaluated. Lastly, the influence of this method on smaller telescope arrays, such as H.E.S.S., needs to be addressed. Smaller arrays should benefit most from this reconstruction scheme, as the number of events rejected by truncation cuts is higher, given that there are more telescopes at the array's border than those surrounded by others.

4

FLASHCAM

This chapter begins with a description of the FlashCam camera concept and its trigger system. The trigger system output is then used in an online muon tagging algorithm, which is introduced and tested. Finally, charge extraction at saturation is evaluated using flat-field laboratory data and compared with simulations. The charge extractor algorithm in the linear regime described in Section 3.1 is further investigated.
The contributions from the author of this thesis are the implementation, optimisation, and validation of the muon tagging method. For charge extraction, the author validated, implemented, and tested the charge reconstruction method at saturation, and conducted all subsequent performance tests in the linear regime.

4.1 FlashCam Architecture

FlashCam is a high-performance camera that has been installed in CT5 at H.E.S.S. since 2019 and will also be used in the MSTs of the CTAO Southern array. It features a novel, fully digital readout system divided into three subsystems: the photon-detector plane (PDP), the readout electronics system (ROS), and the data acquisition (DAQ) system. The PDP and ROS are housed within the mechanical camera body, whose walk-in architecture provides direct access to the PDP plane for easy component replacements. A detailed explanation of the FlashCam architecture is provided by Simon Sailer [83].
The FlashCam mechanics (see Fig. 4.1) consist of a camera housing that encloses all PDP and ROS components. Designed for telescope installation, the housing features aluminium foam walls for insulation. The PDP plane is covered with a transparent window that shields the PMTs from dust. In front of this window is

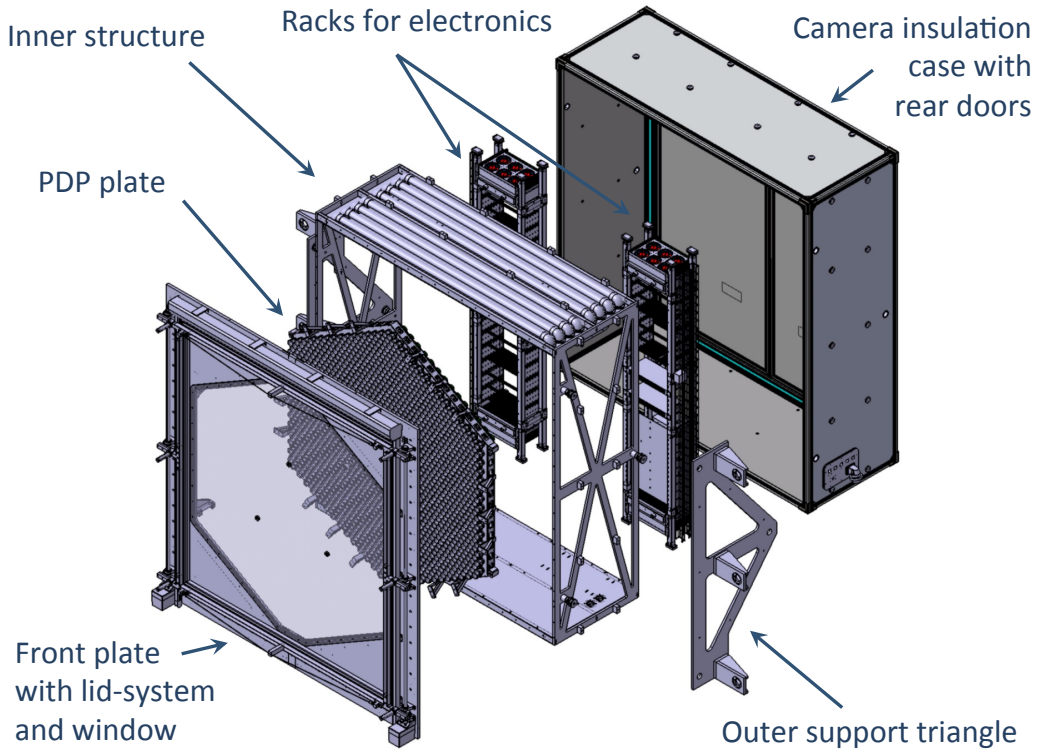

Figure 4.1: FlashCam camera mechanics components inside the camera case. The camera side pointing toward the telescope includes a window shield in front of the PDP plane. This is followed by the electronics enclosed in the inner structure and the camera case. The camera case includes doors on the opposite side that provide access to the ROS. Taken from [160].

a light-tight shutter that can be closed during the day. The housing includes a cooling system. The camera weighs ~ 2 tons and has dimensions of $3{\times}3{\times}1.1\ \mathrm{m}^3$. Furthermore, the rear of the camera, which incorporates the ROS, can be easily accessed using the rear doors.

The PDP sub-system consists of 1764 PMTs organised in 147 PDP-modules with 12 PMTs each (see Fig. 4.2). Each PMT has a size of 0.18° and contains 7 dynodes. The PMTs collect light with the help of Winston cones of 25 mm apertures which are placed in front of each pixel, except for three of them (see Section 4.3.1). The total field of view of the camera is between 7° and 7.7°.

A prototype FlashCam is located in a dark room at the Max Planck Institut für Kernphysik (MPIK) in Heidelberg. The camera can be seen in Fig. 4.3. Fig. 4.3a shows the camera front. The light cones are clearly visible, with a transparent protective window placed in front of the PMTs. Fig. 4.3b shows the rear of the camera with the rear doors open.

(a) Front

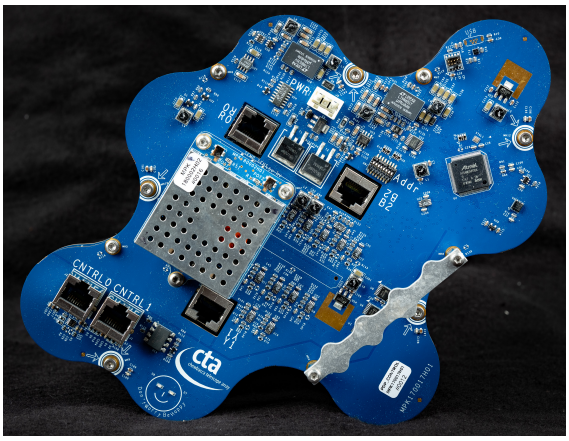

(b) Back

(c) Side

Figure 4.2: Photographs of the current PDP module (each containing 12 PMTs) used for the FlashCam in the MPIK laboratory. The PDPs are shown from the front, back, and side. Provided by Felix Werner, available in [191].

The different components of FlashCam and the signal path are explained in Fig. 4.4. The PDP plane contains the PMTs soldered to a printed circuit board, which also includes the preamplifiers, the high-voltage supply for the pixels, and the slow control. Preamplifiers are soldered to the same printed board so that the analogue signal is amplified close to the PMT. The signal is amplified linearly with the number of photoelectrons up to ~ 250 PEs. Once this limit is reached, the amplification exhibits a nonlinear dependence. At the predefined amplifier limit (typically 4095 LSB), the pulse height saturates while the pulse integral keeps growing logarithmically with input charge [192]. This amplification scheme eliminates the need for separate high- and low-gain channels. Furthermore, it provides the camera with a wide dynamic range, spanning from ~ 1 to 3000 PEs.

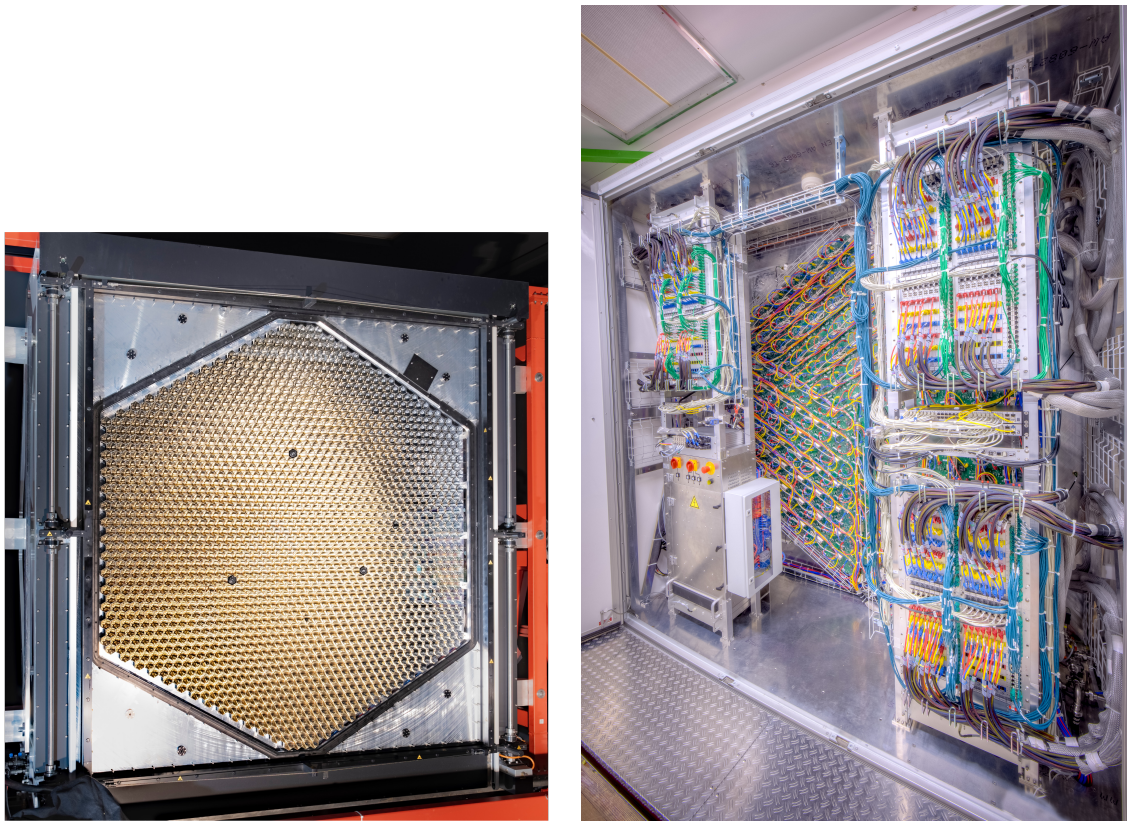

(a) FlashCam light cones. **(b)** rear of the camera house

Figure 4.3: View of FlashCam in the dark room in MPIK from the front (left) and the rear (right) when the rear doors are opened. Credit: Christian Föhr.

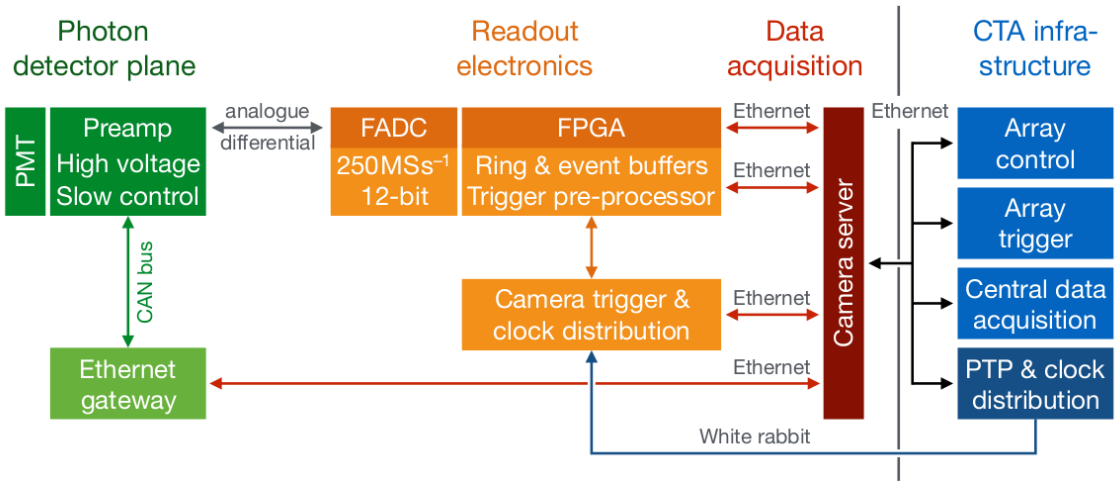

Figure 4.4: Schematic of the FlashCam sub-systems and their multiple components, as well as the connections between each of them. Taken from [192].

The amplified signal is transmitted to the ROS via CAT-6 cables. The analogue signals are digitised using 12-bit Flash Analogue-to-Digital Converters (FADCs) that sample at 250 million samples per second. The incoming samples are buffered and processed on the onboard Field-Programmable Gate Arrays (FPGAs) of the ROS. The digital trigger decision is continuously calculated in parallel from the same incoming samples.
The ROS is built with motherboards equipped with three types of daughter boards: trigger cards, ADC cards, and a master distribution board that distributes the trigger signal and provides a common clock. Two PDPs, each with 12 channels, send the amplified signals to a single ADC card. All the ADC cards send their trigger signals to a single trigger card. The trigger cards exchange trigger signals with neighbours to form a final trigger decision [83]. More on the trigger in Section 4.1.1. The trigger decision is transmitted to the master distribution board, where the telescope trigger is determined. When the camera triggers, a selected time slice of the signal is copied from the ring buffer into the event buffer and transmitted to the camera server over fibre cables.

4.1.1 *FlashCam Trigger System*

This section is based on the detailed explanation and validation of the FlashCam trigger system by Simon Sailer [83].
Cherenkov cameras are designed to detect the fast and faint Cherenkov signals emitted by EAS. Their trigger systems must detect even small shower images containing only a few pixels with significant intensity, as these images remain essential for shower reconstruction and directly determine the observatory's low-energy threshold. However, Cherenkov signals are continuously contaminated by background light from the night sky. Consequently, the trigger system must ensure highly efficient rejection of NSB-only events. The trigger is based on the combination of signals from neighbouring pixels, which is subsequently compared against a trigger threshold. The trigger system must operate reliably under moonlight conditions while maintaining a low rate of noise-induced triggers. Additionally, the multiplicity trigger condition of the CTAO will further reduce the number of false positive triggers.
Fig. 4.5 shows the trigger concept and the pathway of a trigger signal from the ADC cards to the master distribution card. FlashCam is conceptually divided into

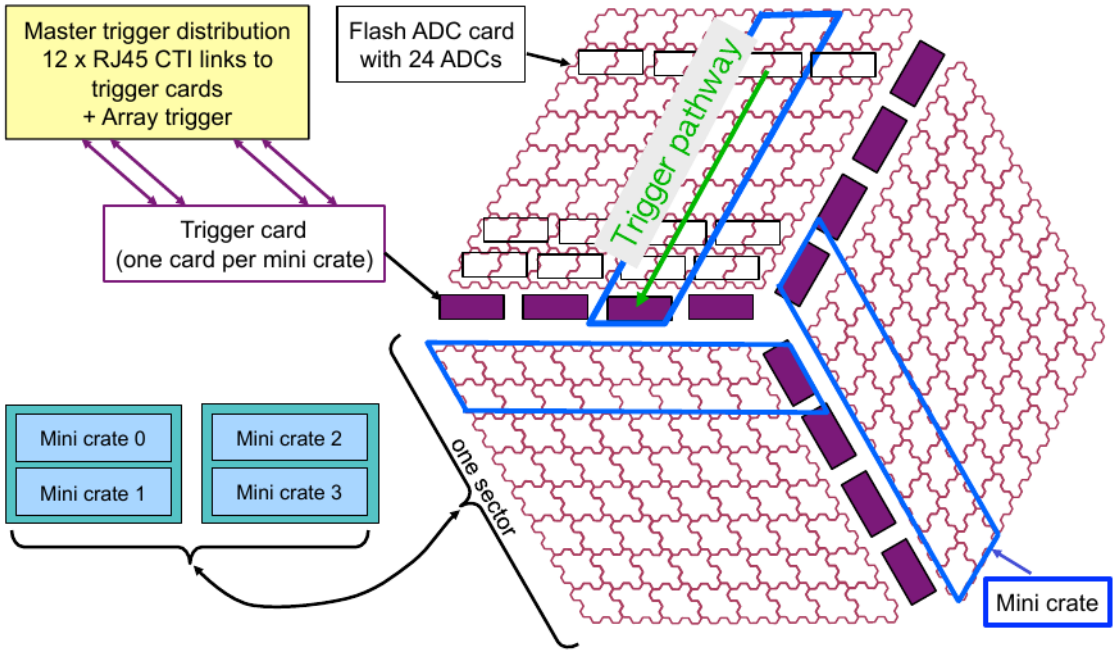

Figure 4.5: Schematic of the trigger signal distribution for the FlashCam. Each pair of PDP modules sends amplified signals to one ADC card (black rectangle). Each ADC card sends a trigger signal to its associated trigger card. All ADC cards within a given minicrate send signals to the same trigger card. The final trigger signal is encoded in 12-bits in the master trigger distribution. Taken from [83].

three sectors. Each sector consists of 4 so-called mini-crates. These mini-crates contain ADC cards. Each pair of PDP modules transmits amplified signals to one ADC card (black rectangles in Fig. 4.5). Each mini-crate sends the trigger signal of each ADC card in the mini-crate to a single trigger card (purple rectangles in Fig. 4.5). The final trigger signal is sent to the master trigger distribution card.
The trigger is implemented at three hardware levels: the ADC cards, the trigger cards, and the master distribution card. The first level takes place on the ADC cards. The signal passes through an integer-differentiation filter. The value is scaled down and clipped to limit the signal's dynamic range. The values of three neighbouring channels are summed up. Each sum is sent to the next hardware level, the trigger card. At the trigger card, each three-pixel sum is summed again with two neighbouring three-pixel sums to form a *patch* of 9 pixels. Throughout this thesis, a patch refers to the sum of 9 pixels. The camera contains 588 overlapping patch sums, with the overlap enabling homogeneous analysis of the camera response.
Finally, the patch sums are compared to a trigger threshold. Every trigger card encodes the result of this check in a 1-bit signal, which is then sent from the trigger

cards to the master distribution card. Consequently, the selected time slices are transferred from the continuous ring buffer to the event buffer. The signal is then sent to the camera server.
From this trigger logic, one can extract how many of the total 588 patches actually triggered for a given event. Likewise, it is known where those patches are located in the camera and which trigger card they send their trigger information to. The trigger cards containing any triggering patch are obtained from the master distribution card. The number of patches and cards that triggered is known, and this information will be used to develop a fast online muon-tagging algorithm.

4.2 Muon Tagging with FlashCam

The CTAO will require an exhaustive calibration strategy to achieve its performance goals. The energy resolution of the detector should be within 10-15% [193], and the transmission of Cherenkov photons through the detector and their subsequent conversion to photoelectrons need to be known with an uncertainty of no more than 5% [194]. Muons provide a unique tool to achieve these goals.
Muons travel through the atmosphere in nearly straight lines and can produce a characteristic ring-like image on the camera if they hit the telescope. More often, muons don't strike the mirror dish and only part of the ring is seen. Cherenkov light is emitted at a nearly constant angle relative to the muon's direction of motion. As a result, a single telescope can record most of the light emitted by the muon, although this depends strongly on the muon's production altitude.
The geometry of the imaged ring enables reconstruction of muon properties, such as its impact point and energy. From muon properties, one can simulate the expected light yield from this particle and, by comparing the simulated and observed intensities, calibrate the telescopes and estimate the detector's optical throughput. The optical throughput is defined as the fraction of the total emitted light that is recorded.
Furthermore, the optical throughput can be monitored in real time, including during observations, because muons are continuously detected, as they accompany hadronic showers. This provides a time-dependent calibration that enables accurate reconstruction even when abrupt changes in optical throughput are observed. As will be seen later with H.E.S.S. in Section 5.1, the muon efficiency can change significantly between observation runs.

The CTAO will include a multiplicity trigger condition to discard events with only one telescope trigger. A sizeable number of muons will therefore be discarded, as most muons trigger only one telescope. Given the role of muons in the observatory's final performance, every camera is required to tag muon candidates even if they only trigger one telescope. Unlike LSTs, which can detect a high rate of muons stereoscopically, the additional muon-tagging algorithm will be especially important for smaller telescopes.
The muon tagging algorithm must detect most muon rings produced in the camera while rejecting the vast majority of hadronic showers. The CTAO has established quantitative requirements for muon tagging:

- Every camera should be able to detect at least 90% of muon rings that have an energy $\geq 20\,\mathrm{GeV}$.
- The total rate introduced by all calibration methods together must not exceed 1400 Hz. This includes muon calibration, flat-field, and pedestal calibration runs.

In the first half of the chapter, the muon calibration is briefly introduced, followed by a discussion of the muon's geometry at the observation level. Finally, the contributions of this thesis, i.e., development, implementation, validation, and optimisation of the muon tagging method, are presented.

4.2.1 *Basics on system geometry and muon calibration*

The description of muon calibration is strongly based on [194] and [195].
Relativistic muons have a large penetration depth and travel in a straight line while emitting Cherenkov light at a constant angle θ_c if they exceed a minimum energy. The Cherenkov angle can be expressed in terms of the particle's speed $\beta = \frac{v}{c}$ and the refractive index $n(\lambda)$ of the atmosphere as follows:

$$\cos\theta_c = \frac{1}{\beta n(\lambda)}. \tag{4.2.1}$$

The refractive index depends on the wavelength of light. Cherenkov cameras are optimised to detect light in the 300-600 nm range [196]. The refractive index is nearly constant in this range. Since the refractive index of air and muon velocity can be assumed constant over the small track segment from which light is recorded, the Cherenkov angle is also constant. However, the angle varies with altitude due to energy losses and changes in the refractive index.
The geometry of the muon as it hits the camera dish is resumed in Fig. 4.6. The impact distance ρ is the distance from the point where the muon hits the mirror plane to the dish centre. A fully-contained muon ring is produced provided that the impact distance is small and the offset angle, v, between the muon direction (red arrow) and the telescope pointing direction is nearly aligned. The length of the chord, $D(\rho, \phi)$, is defined as the distance between the impact point of the muon and the edge of the dish. The length of the chord depends on the azimuth angle ϕ, defined with respect to the reference ϕ_0, which leads to the longest chord.

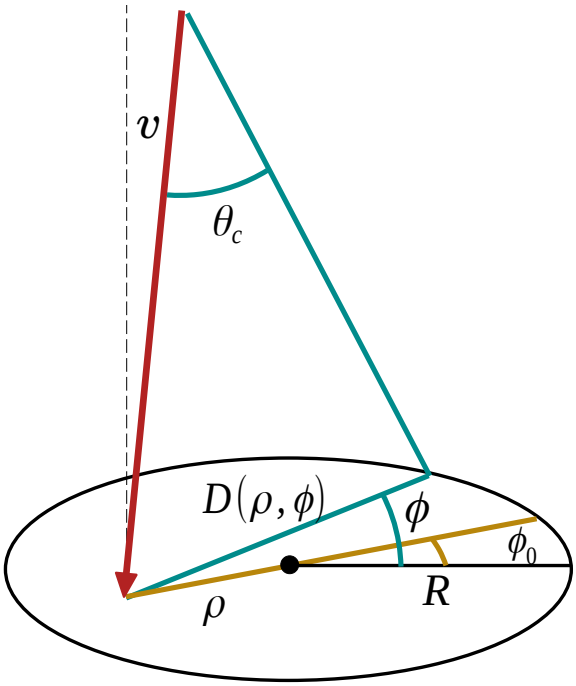

Figure 4.6: Schematic of the geometry of a muon after it hits the mirror dish. The muon trajectory is shown as a red arrow striking the telescope mirror of radius R at an impact point a distance ρ from the telescope's centre. The trajectory of the muon is inclined at an angle v with respect to the optical axis of the telescope. The muon generates Cherenkov light at an angle θ_c along the particle's trajectory.

Based on this geometry, a muon with sufficient energy generates a full ring in the camera if these two conditions are fulfilled:

- The muon hits the mirror dish, which occurs when the impact distance is $\leq$ R, being R the radius of the dish.
- The angle between the direction of the muon and the optical axis of the telescope follows $v + \theta_c \leq \text{FoV}/2$

An MST has a mirror dish diameter of 11.5 m [103]. Assuming it is circular, the maximum impact distance of the muon ρ_{max} should be ~5.75 m to form a full muon ring. Additionally, the field of view of FlashCam is between 7° and 7.7°. Therefore, v must be $\lesssim$2.6°. When the muon arrival direction is aligned with the telescope's optical axis, the centre of the muon ring coincides with the centre of the camera. As the offset between the telescope axis and the muon direction increases, the centre of the muon ring moves towards the edge of the camera.
When all Cherenkov light from the muon reaches the telescope dish, it is reflected towards the camera, forming a ring (see Fig. 4.7). Along each chord, light to the

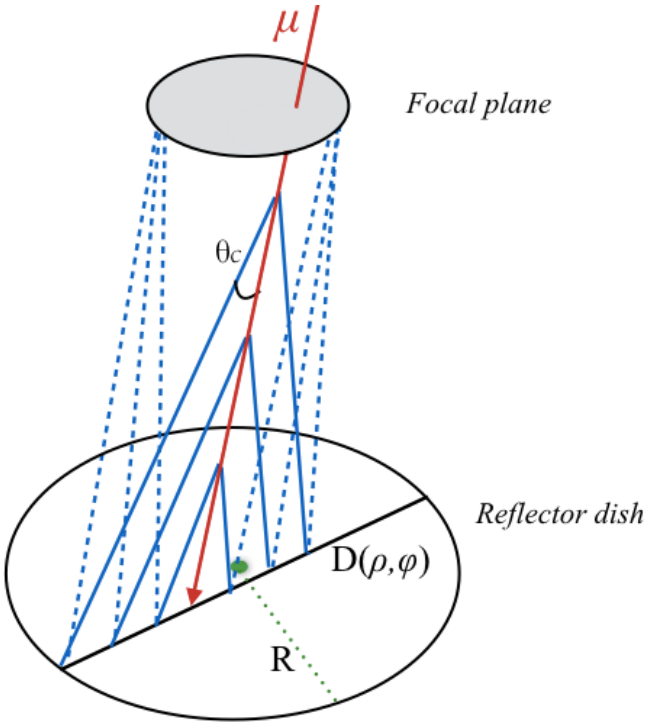

Figure 4.7: All Cherenkov light incident in the dish at the same angle with respect to the optical axis is reflected into the same camera pixel. The example sketch shows the concept for a given azimuth angle. This is the case at every azimuth, producing a muon ring in the camera. Taken from Alison Mitchell [195] with explicit permission from the author.

left of the muon's impact point on the mirror is reflected onto one pixel, while light to the right is reflected onto another pixel, both reflected at the same angle of incidence. If the muon does not hit the mirror dish but lands outside, only a partial arc of the ring is seen by the camera. The fraction of the ring seen by the camera decreases with increasing impact distance.
The number of Cherenkov photons emitted by a muon per unit path x and azimuth angle ϕ between a wavelength range (λ_1, λ_2) is described by [195]:

$$\frac{d^2N}{dxd\phi} = \alpha \int_{\lambda_1}^{\lambda_2} \frac{\psi(\lambda)}{\lambda^2}\left(1 - \frac{1}{\beta^2 n(\lambda)^2}\right) d\lambda, \tag{4.2.2}$$

where α is the fine structure constant and $\psi(\lambda)$ is the photon collection efficiency of the detector. By including Equation 4.2.1 into Equation 4.2.2, the λ dependent parameters can be isolated, by defining the total intensity as, $I = \int_{\lambda_1}^{\lambda_2} \frac{\psi(\lambda)}{\lambda^2} d\lambda$. Equation 4.2.2 can therefore be expressed as:

$$\frac{dN}{d\phi} = \frac{\alpha I}{2}\sin(2\theta_c)\int dx, \tag{4.2.3}$$

with $\int dx$ being the chord $D(\rho, \phi)$. The number of Cherenkov photons produced by a muon, as an approximation, depends only on the geometrical parameters and the Cherenkov angle of emission, which corresponds to the radius of the muon ring image in the camera. Therefore, the geometrical reconstruction of the muon image in the camera can determine the total number of photons emitted by the muon, which can be compared with the number of detected photoelectrons. And, therefore, the optical efficiency of the telescope may be obtained. As derived in Section 2.1.2, the minimum energy to emit Cherenkov light can also be derived to be $\sim 4.4\,\mathrm{GeV}$.

4.2.2 *True selection of muon rings in simulations*

Simulations are used to test the muon tagging algorithm. These simulations provide detailed information on the nature of particles that reach the observation level and, for muons, whether they would produce a fully contained muon ring. To achieve a true muon ring selection for comparison with the FlashCam muon tagging algorithm, the energy, direction, impact distance, and particle type of each particle reaching the observation level must be identified.
CORSIKA + sim_telarray (see Section 2.4.1) provide information on each particle that reaches the telescope, as well as information on the primary particle that hits the atmosphere. A random position offset is applied to the simulated telescope array to generate multiple instances of the detector system for a given shower, without incurring additional intensive CPU usage. The array offsets (x_{core}, y_{core}) are recorded in the output file. The initial simulated position of the telescope (x_{tel}, y_{tel}) is also stored.
Detailed information on each particle reaching the ground is stored, including the particle type given by CORSIKA, the impact position of the particle at the observation level (x_0, y_0, 0), the arrival time, the particle momentum, and the arrival direction in cosines (c_x, c_y). The cosine direction in the z axis is $c_z = -\sqrt{1 - {c_x}^2 - {c_y}^2}$. In IACT simulations, the telescope is modelled as a fiducial sphere containing the telescope components [120]. The position of arrival of the particle with respect to the centre of the fiducial sphere is,

$$
\begin{aligned}
x_{0,\mathrm{tel}} &= x_0 - x_\mathrm{a} - x_\mathrm{tel} \\
y_{0,\mathrm{tel}} &= y_0 - y_\mathrm{a} - y_\mathrm{tel} \\
z_{0,\mathrm{tel}} &= -h_\mathrm{tel}
\end{aligned}
\tag{4.2.4}
$$

where h_tel is the height of the telescope from the ground to the sphere centre, as shown in Fig. 4.8. $(x_\mathrm{a}, y_\mathrm{a})$ are defined as minus the array offsets $(-x_\mathrm{core}, -y_\mathrm{core})$. The latter is defined from the perspective of the telescope array, and the former is defined with respect to CORSIKA. Equation 4.2.4 expresses the position of the particle at the ground level with respect to the sphere centre. However, this centre is slightly offset from the mirror's centre. The offset is given by three parameters: a_0, a_1, and a_2. For an MST, $a_2 = 0\,\mathrm{m}$, $a_1 = 1.6\,\mathrm{m}$, and $a_0 = -1.78\,\mathrm{m}$. The mirror is assumed to have perfectly aligned mirror segments. The impact distance is computed assuming the mirror components are on the tangent plane of Fig. 4.8 instead of the curved mirror surface. This is considered to be a good approximation. In the sphere frame of reference, the optics reference point or mirror centre is located at:

$$
\begin{aligned}
x_m &= (a_1 - a_2\cos\theta - a_0\sin\theta)\cos\phi, \\
y_m &= -(a_1 - a_2\cos\theta - a_0\sin\theta)\sin\phi, \\
z_m &= a_2\sin\theta - a_0\cos\theta,
\end{aligned}
\tag{4.2.5}
$$

where θ is the zenith angle and ϕ is the azimuth angle towards which the telescope is pointing. The particle track is given by the reference point in Equation 4.2.4 and the cosine directions of the particle trajectory. The position of the mirror centre is given by Equation 4.2.5. The distance between the particle line and the mirror centre, also referred to as impact distance, is computed with the function `line_point_distance()` provided by hessio [197].
Similarly, the angle offset between the particle's direction of arrival and the telescope axis is given by the angular separation between the particle's longitudes and latitudes and the telescope's optical axis, both of which are extracted from the simulations. Several examples of Cherenkov images of muons are shown in Fig. 4.9, together with the particle's impact distance from the mirror centre, the particle's momentum at ground level, and the offset from the telescope axis.

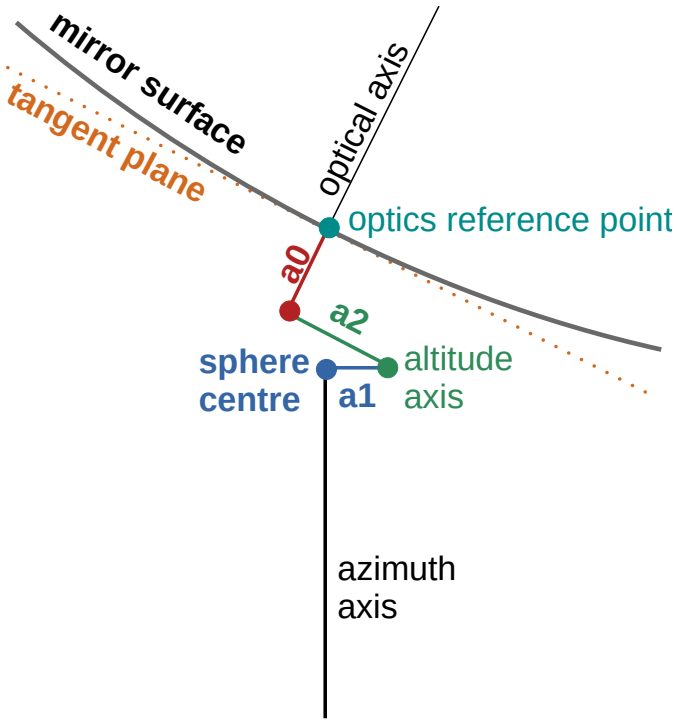

Figure 4.8: Schematic of the geometry of a simulated telescope in sim_telarray. The telescope is simulated as a fiducial sphere centred at the sphere's centre. The sphere centre is simulated at a distance from the ground: h_{tel}. The telescope moves along the azimuth and altitude axes. The sphere centre is displaced from the centre of the mirror by the distances a_0, a_1, and a_2. The sketch is of the author's own elaboration, strongly based on internal discussions with Konrad Bernlöhr.

4.2.3 *Muon ring detection with FlashCam*

In the CTAO, data streams from all telescopes in the array will be sent to the ADH, provided the events satisfy the SWAT condition [198], which requires that more than one telescope trigger in coincidence. Since muons usually trigger only one telescope, and muons that exhibit a fully contained ring shape have a low rate of appearance, it is essential also to store those monoscopic events that are suspected to be muon rings. Muon tagging algorithms have to loop over each event to find muons that could potentially generate a detectable ring. With data rates on the order of GBytes/s [199] for an MST, a high-speed method is required that can quickly check whether a muon ring is present. Otherwise, muon tagging could be computationally expensive, potentially leading to performance issues. This muon tagging algorithm was previously introduced by the author of this thesis in [200],

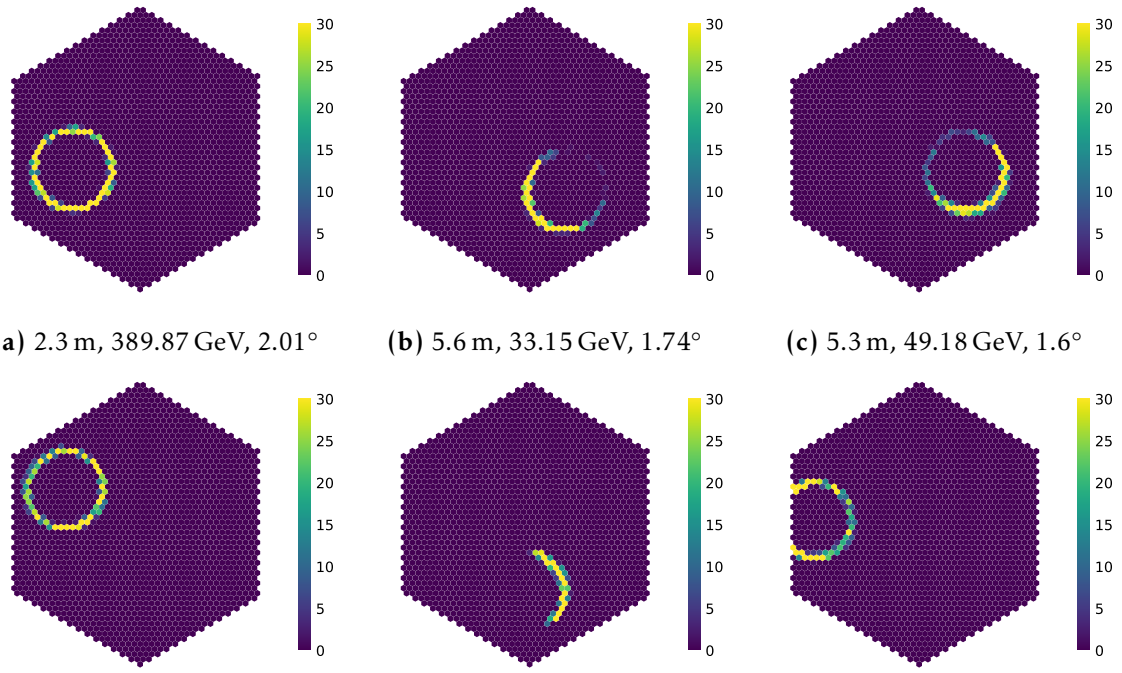

(a) 2.3 m, 389.87 GeV, 2.01° **(b)** 5.6 m, 33.15 GeV, 1.74° **(c)** 5.3 m, 49.18 GeV, 1.6°

(d) 1.4 m, 20.95 GeV, 2.37° **(e)** 6.5 m, 66.06 GeV, 2.04° **(f)** 3.3 m, 22.73 GeV, 2.99°

Figure 4.9: Simulated muon ring images at different impact distances, angle offsets to the optical axis of the telescope, and muon energies on the ground. The impact distance, energy, and offset of each muon that generates the image are printed beneath each subplot.

and this section follows closely what was published there. A proof of concept was shown in [198].

Fig. 4.9 shows examples of muon ring images with different energies, impact distances, and offsets. As the impact distance increases to around 5.5 m, partial muon rings start to appear. Similarly, at high offsets, close to 3.0°, the muon is partially formed outside the geometrical limits of the camera. At impact distances between 5.0 and 5.5 m, there is an apparent asymmetry in the intensity across the muon ring, but these are muon rings that should still be triggered on. Muon rings, as seen in Fig. 4.9, occupy a sizeable portion of the camera plane, extending over a large region.

The number of pixels that a muon ring triggers on is predicted to be approximately:

$$N_{\text{pix}} = \frac{2\pi\theta_c}{\theta_{\text{pix}}}, \tag{4.2.6}$$

assuming that only one row of pixels is illuminated. θ_{pix} is the pixel size of FlashCam, 0.18°. The Cherenkov angle is assumed to be around 1.2°. This results in between 40 and 50 triggered pixels.
Muon rings extend over a large region of the camera, triggering, on average, more patches and cards (see Section 4.1.1 on the trigger system of FlashCam) than the most common low-energy showers that dominate the trigger. The distribution of the number of patches (9 pixel sums, a total of 588 patches) and cards (a maximum of 12) that each event triggers on is extracted and seen in Fig. 4.10a. The left plot shows simulated protons, and the right plot shows simulated muons that produce a full muon ring on the camera, (i.e. that have impact distance $\leq 5.5\,\text{m}$ and offset $\leq 2.6°$). Muon rings generally trigger on more than 25 patches, unlike protons (left plot) that mostly trigger on only a few patches. However, many proton showers are still observed within the red-highlighted limits at 26 patches and 3 cards, coinciding with the locations of muon rings.
Further improvements on the rejection of proton showers can be done by introducing trigger times. Cherenkov light from muons illuminates the camera almost instantaneously. All pixels respond to Cherenkov light from muons at similar times, typically within 1 FlashCam readout sample (4 ns). Gamma- and, especially, proton-initiated showers exhibit a temporal gradient, and each pixel can trigger at significantly different time samples. Therefore, for better discrimination between proton showers and muon rings, the number of trigger patches and cards is computed within only one to two time samples. A one-sample window (see Fig. 4.10b) leads to a significant reduction in the number of patches and cards of muons as well as protons. This effect arises because, at times, light reaches the camera at the end of a time sample, and the subsequent light is recorded in the next sample, even though it arrived almost instantaneously. Therefore, the best discrimination is seen when using a 2-sample trigger window (Fig. 4.10c). In this case, the distributions of patches and cards for muon rings are almost identical to those in Fig. 4.10a; however, the distribution of protons moves towards the outer edge of the red limits.

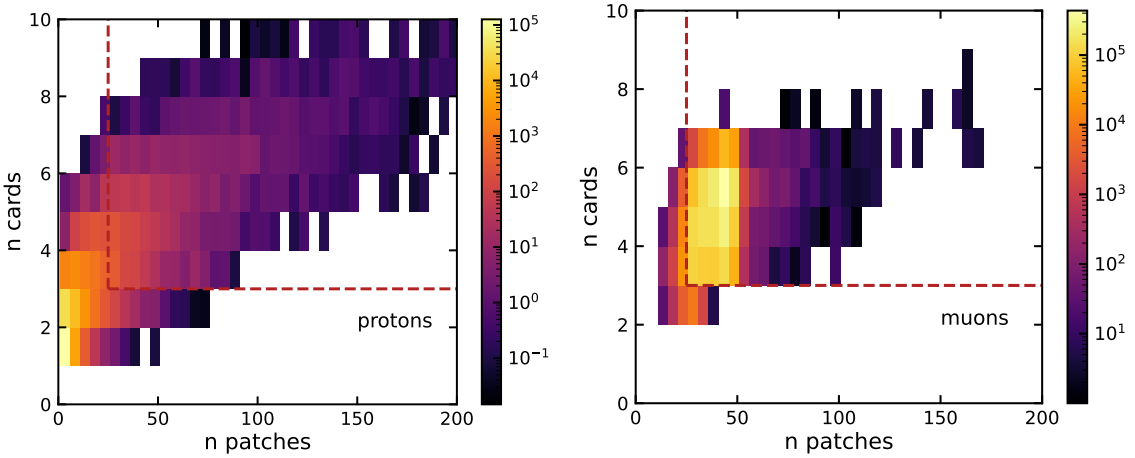

(a) Full trigger window

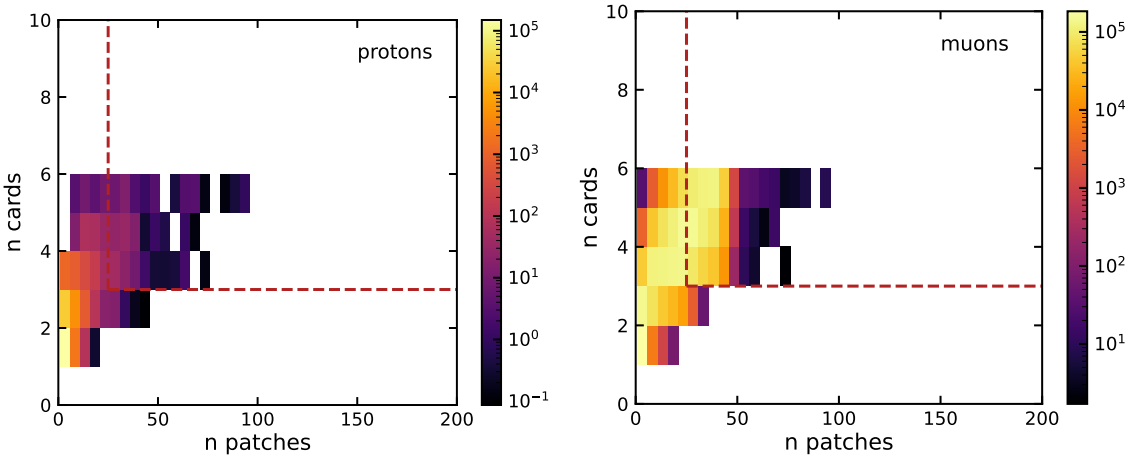

(b) Trigger sample only

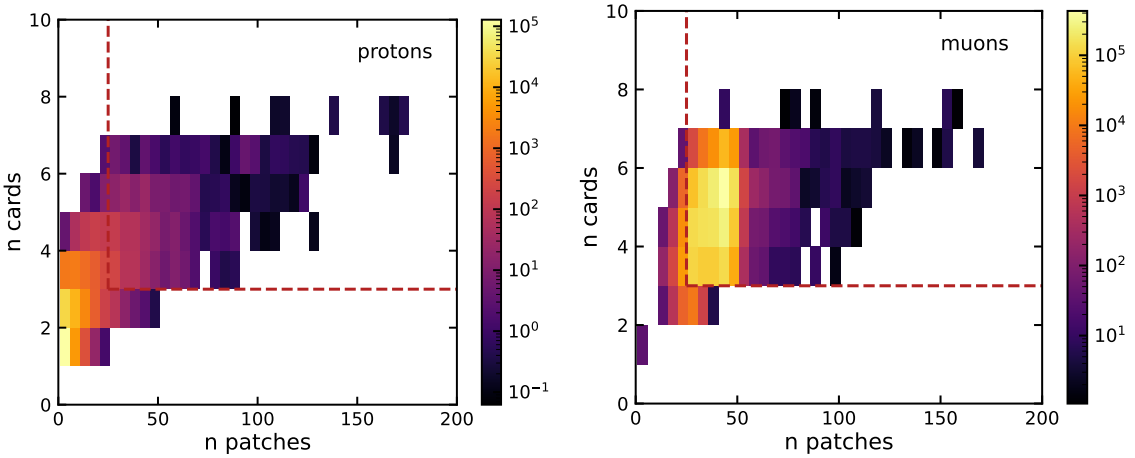

(c) 2 samples trigger

Figure 4.10: Distribution of proton showers (left) and only muon rings (right) according to the number of patches and cards that they trigger on. The red-dashed lines show the proposed cuts to patches and cards at 26 and 3, respectively. The distributions are shown for different trigger windows.

The importance of trigger times in the discrimination capability of the tagging algorithm can be further understood with Fig. A.1 in Appendix A. Fig. A.1 shows two example showers, one being a high-energy proton-initiated shower and the other producing a muon ring. The distribution of triggered patches in the camera is shown, with the positions of the pixels within each patch averaged. This is shown using the full time window and only two samples. The patches that trigger the muon ring are the same regardless of the time window. However, the imaged proton shower yields significantly fewer triggered patches when the time window is reduced.
Therefore, the previous results show that a cut in the minimum number of patches and cards triggered by a particle is a strong discriminator between protons and muon rings. The muon tagging method relies only on the trigger information of each event. For testing, the number of trigger patches and trigger times are read using pyeventio [201]. The associated trigger cards can be extracted from a file containing information on the trigger patches and their associated cards. In the field, the number of triggered patches will be obtained from the firmware, and the cards from the master distribution. This information will be sent to the camera server, where the two cuts will be applied. The method performs a fast software check: it compares two numbers (the number of triggered patches and cards) against two thresholds. This is the simplest and fastest approach.

4.2.4 *Validation and optimisation*

The method is tested on proton and muon simulations. Proton showers are being simulated at a zenith angle of 20°, and showers are coming from the North. The full array of 14 MSTs is simulated, and no stereo trigger condition is forced. Therefore, if only one telescope triggers, the full array also triggers. Protons are simulated as coming within a cone of radius 10° around the simulated fixed value for zenith and azimuth. The rate of full muon rings in proton-induced showers is low, and, therefore, the detection efficiency of muon rings by muon tagging is also tested on muon-only simulations to increase the number of events. Muons are simulated from the same zenith and azimuth, with a cone of 3°. The muons are simulated to start at an altitude 683 g/cm^2.
As shown earlier, a muon produces a ring on the camera when the impact distance is ≤ 5.5 m, and the offset is $\leq 2.6°$. Figure 4.11 shows the muon detection efficiency

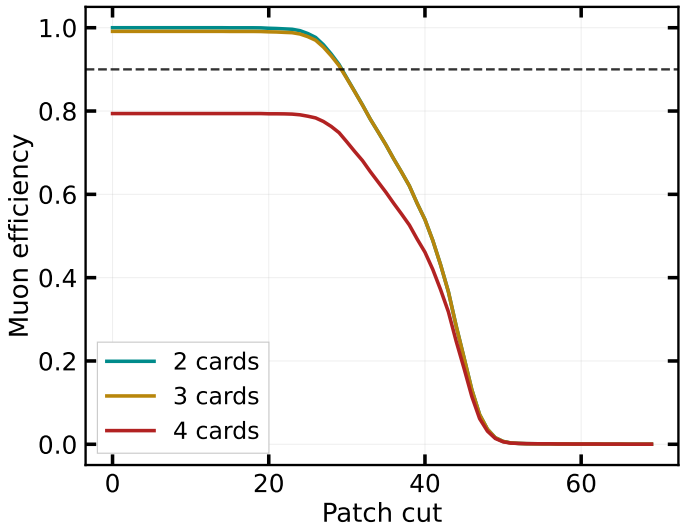

Figure 4.11: Detection efficiency of muon rings with energies ≥ 20 GeV at the ground over patch cut. Each line represents a different cut in the minimum number of cards, set at ≥ 2, ≥ 3, ≥ 4, for an event to be tagged. The black dashed line represents the CTAO requirement at 0.9.

for different trigger cuts, applied to muons with energies above 20 GeV. Three card cuts are illustrated, ranging from ≥ 2 to ≥ 4. The muon detection efficiency is reduced significantly when the card cut is ≥ 4. For this card cut, efficiency never reaches the 0.9 value required by the CTAO. Either cutting on at least 2 or 3 cards yields good, similar results. The following plots are performed with a card cut of ≥ 3.

The muon efficiency's dependency on the patch cut is evaluated for different cuts in muon impact distances of ≤ 5.0, ≤ 5.5, and ≤ 6.0 m (see Fig. 4.12a). For larger maximum impact distances, the muon efficiency falls below 0.9 at lower patch cuts. Consistent with Fig. 4.9b, muon arcs appear at 6.0 m, degrading the efficiency. However, below 5.5 m, fully-contained muon ring candidates are observed (Fig. 4.9c). Fig. 4.12a shows that even when the maximum impact distance cut increases from 5.0 m to 5.5 m, the efficiency decreases. Within this range, fully-contained muon rings are formed, but the light intensity is less symmetric along the ring, leaving regions of low intensity that may occasionally be missed by the trigger.

Similarly, in Fig. 4.12b, a two-dimensional distribution of muon efficiency is shown as a function of the geometry of the muon when it reaches the observation level. The muon efficiency is computed for a patch cut at ≥ 26 and muon energy ≥ 20 GeV. The

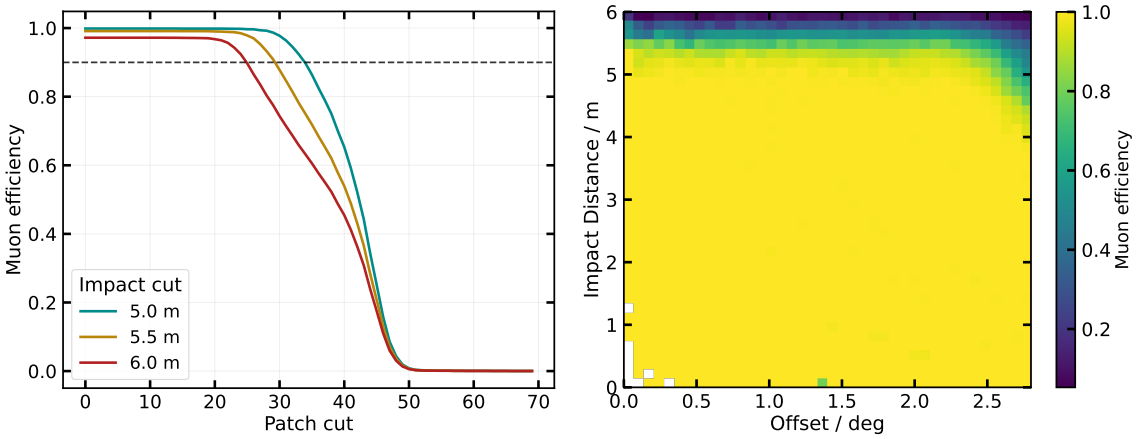

(a) Efficiency with patch cut for different cuts in impact distance

(b) Muon efficiency map as a function of offset and impact distance

Figure 4.12: Efficiency of detecting muon rings with impact distance and offset after a card cut of ≥ 3. The left plot shows the muon efficiency as a function of the patch cut for three cuts in the muon maximum impact distance, ≤ 5.0, ≤ 5.5, and ≤ 6.0 m. The offset of all muon events falls within ≤ 2.6°. The right plot shows the muon efficiency in bins of the muons' offset and impact distance after a patch cut at ≥ 26. The black dashed line shows the CTAO requirement at 0.9.

horizontal axis shows the offset between the particle's direction and the telescope axis. The vertical axis shows the impact distance to the mirror dish. Muon tagging detects muons even at larger offsets than 2.6°, which is the maximum angle at which the muon ring is fully contained. From impact distances of ≥ 5.5 m, the efficiency degrades markedly.

The efficiency at detecting any event from proton shower simulations is shown in Fig. 4.13a over patch cut. At ≥ 26 patches, 2% of all the events that trigger on one or more telescopes are accepted after muon tagging. However, among these, only mono events are considered extra events and are stored solely because the muon tagging algorithm selects them. Stereo events selected by muon tagging will already be stored. Therefore, only 0.16% of events are extra mono events that are added to the trigger rate.

Fig. 4.13b shows the number of proton showers before and after muon tagging as a function of simulated shower energy. The distributions are shown for mono-only events and for all events (including mono and stereo). The distribution is weighted to reach a spectral index of −2.7, as expected for CR showers. A significant reduction in the number of events is observed between the original distribution and the distribution after selecting only events that pass the trigger cuts.

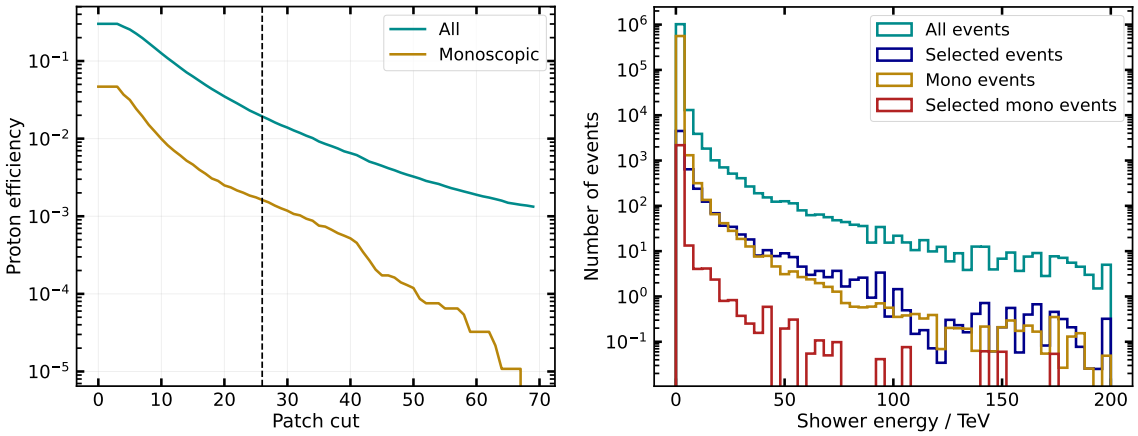

(a) Proton efficiency with increasing patch cut of mono and stereo and mono-only events

(b) Number of proton events before and after tagging as a function of energy

Figure 4.13: Proton detection efficiency for (a) increasing minimum patch cuts, shown for all events and monoscopic-only events. (b) shows the total event count as a function of shower energy for all events and mono-only events. The corresponding distributions after muon tagging selection are also shown for both trigger multiplicity conditions, with a patch cut of ≥ 26 and a card cut of ≥ 3.

The total event rate passing the muon tagging method cannot be directly extracted from simulations because there is no reference time. The extraction of trigger rates from simulations is explained in more detail later on in Section 5.1.5. The effective area of these simulations is computed as the ratio of triggered events on any telescope to the total number of simulated events, multiplied by the simulated area from which showers are generated. The effective area is folded with the cosmic-ray spectrum and then multiplied by a correction factor to account for the effects of heavier nuclei. The trigger rates are then multiplied by the proton efficiency after muon tagging, as a function of energy, resulting in a total rate of a few tens of Hz for the selected mono events. When considering all events that pass the tagging, also stereo, a rate of ~400 Hz is obtained. Therefore, the rate is fully in accordance with the CTAO requirements.

The purity of the method is defined as the number of true positives divided by the sum of true and false positives. From proton simulations, true positives are defined as muon particles within the impact distance and offset limits that form a ring. False positives include all proton showers (mono or stereo) and muons outside the range where they can form muon rings. Muon arcs are also a background in this case. The purity of this method is low, around 9%. This is due to the presence of a substantial background. However, this is totally sufficient given the resulting high

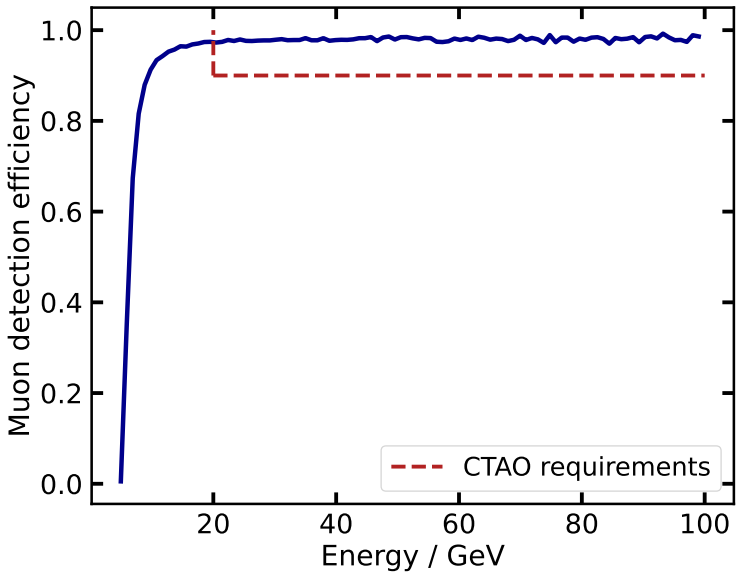

Figure 4.14: Detection efficiency of detecting muon rings as a function of the muon energy. The minimum muon energy for Cherenkov emission is 5 GeV. The cut is performed at ≥ 26 patches and ≥ 3 cards. The dashed red rectangle shows the CTAO requirements at 0.9 above 20 GeV.

muon efficiency and low background rate, especially when only mono events are selected.

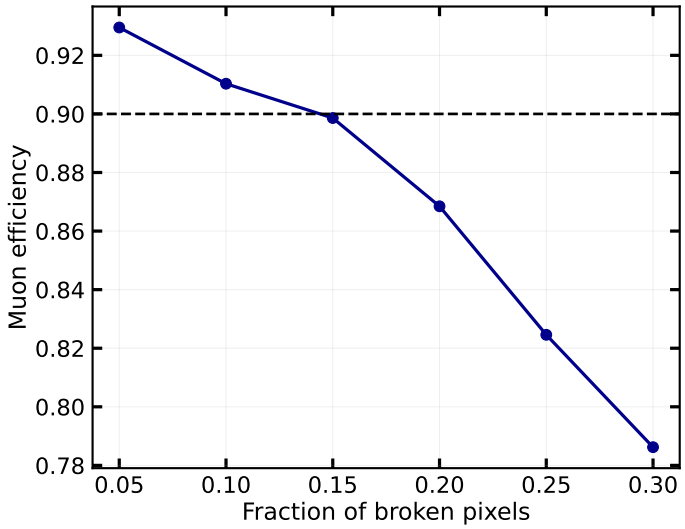

Figure 4.15: Efficiency of detecting muon rings (> 20 GeV), after cuts in ≥ 26 patches and ≥ 3 cards, as a function of increasing fraction of broken pixels in the camera. The CTAO requirement is shown with a horizontal dashed black line at 0.9.

The final muon efficiency, after cuts at ≥ 26 patches and ≥ 3 cards, as a function of the muon energy when it reaches the ground, is shown in Fig. 4.14. The CTAO requirements state that muons of energy ≥ 20 GeV must be detected with an efficiency of ≥ 0.9. This can be achieved using this algorithm, which already achieves those efficiencies at half the required energy. The requirements are highlighted in red in Fig. 4.14.

Finally, the method's robustness is evaluated as the number of deactivated pixels increases and across multiple NSB rates. Fig. 4.15 shows the evolution of the muon efficiency as the number of broken pixels in the camera increases. The muon detection efficiency falls below the 90% threshold when 15% of the camera pixels are deactivated. This is equivalent to more than 250 broken pixels in the camera. Therefore, efficiency remains stable and exceeds the CTAO requirements even when an excessively large number of pixels in the camera are defective. Furthermore, when the NSB rate is high (5 times the nominal NSB of simulations, being the nominal 216 MHz), the muon efficiency decreases significantly (see Fig. 4.16a). At high NSB, the amplitude threshold above which a patch sum results in a trigger is incremented to account for the higher NSB rates. This results in lower muon efficiencies, but also lower proton efficiencies (Fig. 4.16b). Therefore, reducing the cut in the number of patches yields results comparable to those for nominal NSB.

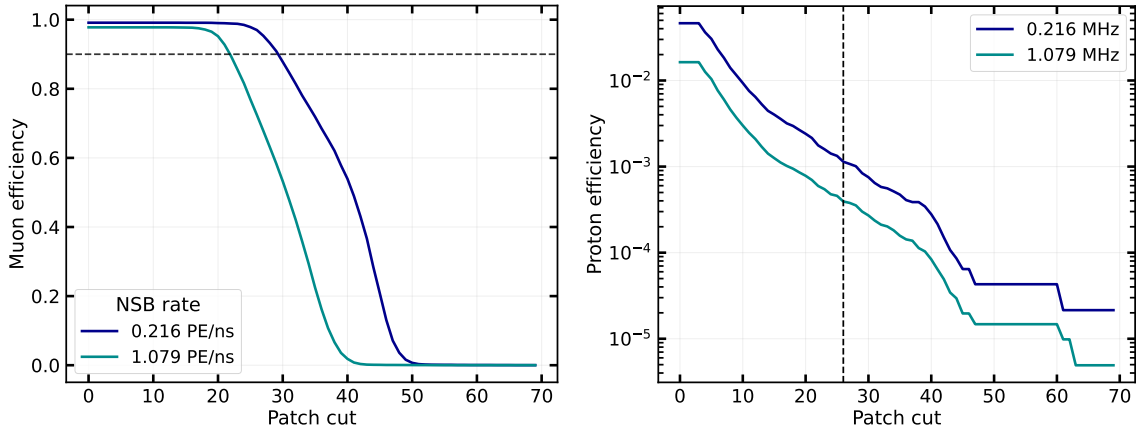

(a) Muon efficiency

(b) Proton efficiency

Figure 4.16: Fraction of detected events (muons with > 20 GeV on the left and all events on the right) at two NSB levels (216 and 1079 MHz) as a function of increasing cut in number of patches when the number of cards is set at ≥ 3. The CTAO requirement is shown with a horizontal dashed black line at 0.9 on the left plot. The vertical black dashed line in the right plot highlights the cut on the number of patches for the nominal NSB (at 26).

4.3 Characterisation of the camera response

4.3.1 *Laboratory measurements*

A copy of the FlashCam is located in the MPIK laboratory in Heidelberg. The camera is inside a dark room to prevent external light contamination. The darkbox is furthermore outfitted with a light source, which enables homogeneous illumination of varying intensity for flat-field data runs. The respective setup is shown in Fig. 4.17. It consists of a Q-switched laser of 355 nm wavelength. The laser intensity is stable within 1%, the timing has a FWHM of 300 ps [83]. A programmable Optical Density (OD) 4 filter wheel is placed in front of the laser to control light intensity. The light is spread homogeneously across the camera plane using a beam expander and diffuser located 4.6 m from the PMTs, emulating short-pulsed light flashes.
Additionally, homogeneous NSB is emulated with a diffused LED. The NSB levels range from 0 MHz to very high NSB rates of 2000 MHz.
In flat-fielding, all traces per pixel for different filter-wheel positions (or signal amplitudes) and readout windows are recorded. The FPGA continuously determines the baseline level of the traces and sends them to the camera server for analysis. Furthermore, the supply voltage of each PMT is recorded during a flat-fielding run, which allows for gain-matching before the actual measurement.

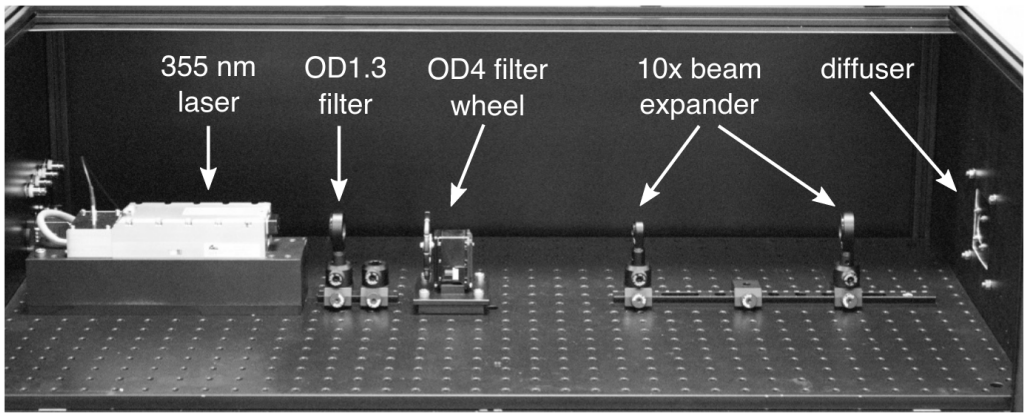

Figure 4.17: Laser setup for the homogeneous illumination of a FlashCam located in a dark room in MPIK. A laser of wavelength 355 nm is the light source. The intensity of the light emission is regulated with a filter wheel. The laser light is homogenised using a beam expander and a diffuser. Taken from [192].

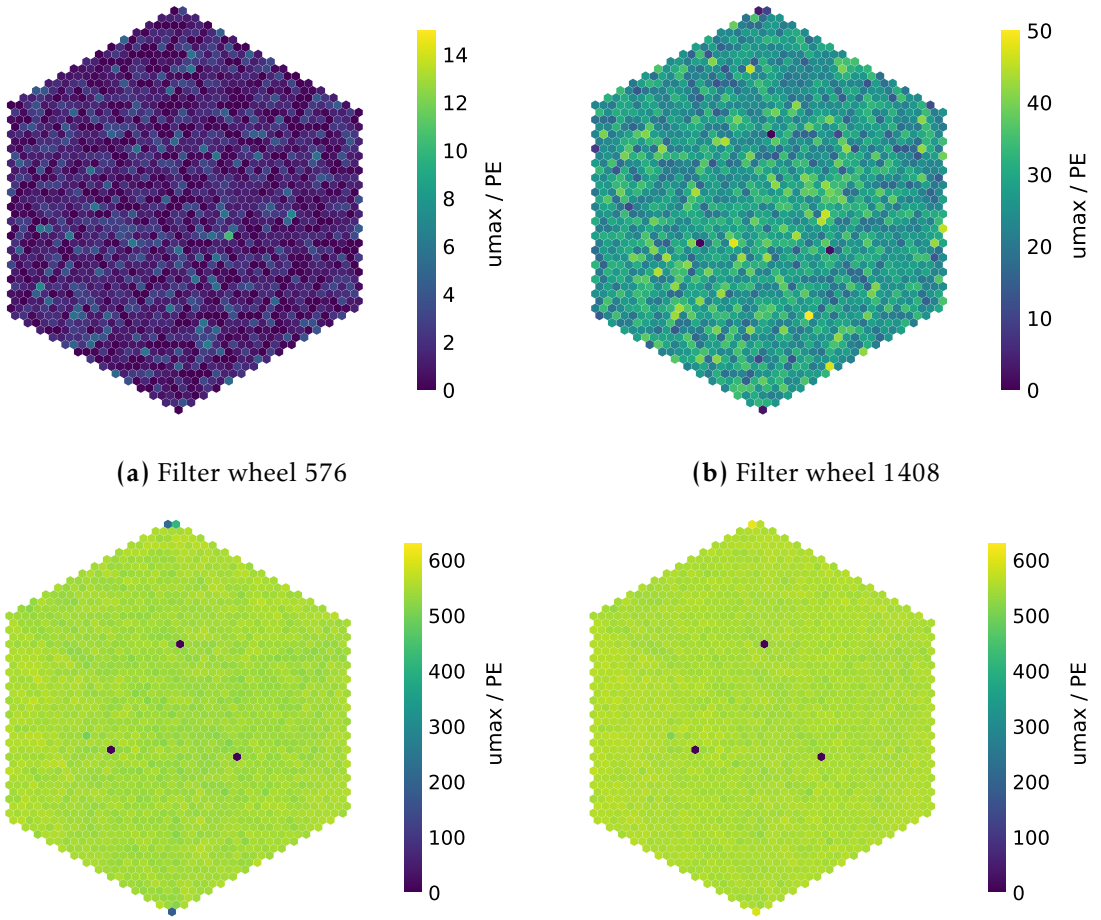

(a) Filter wheel 576

(b) Filter wheel 1408

(c) Filter wheel 2208

(d) Filter wheel 2688

Figure 4.18: Flat-field measurements in the laboratory after illuminating the FlashCam at four different filter wheel positions. The colorbar shows the maximum of the trace after upsampling (*umax*). As the filter wheel position is increased, *umax* increases until saturation is reached. Saturation is observed in the bottom figures, where *umax* at filter-wheel 2688 no longer increases, as compared with filter-wheel position 2208, despite being illuminated with more light. Filter wheel positions 576 and 1408 operate in the linear regime, with *umax* increasing monotonically with illumination.

Fig. 4.18 shows the camera plane with its 1764 pixels after being homogeneously illuminated in the darkroom with different filter wheel positions. The colorbar shows the maximum of the upsampled pulse at each pixel, denoted *umax*. *umax* increases with increasing filter-wheel position (as seen at filter-wheel positions 576 and 1408), reaching a saturated level already seen at filter-wheel position 2208. Deep saturation is seen at 2688. The plot also shows the illumination's homogeneity. Only small fluctuations in *umax* within an image are observed.

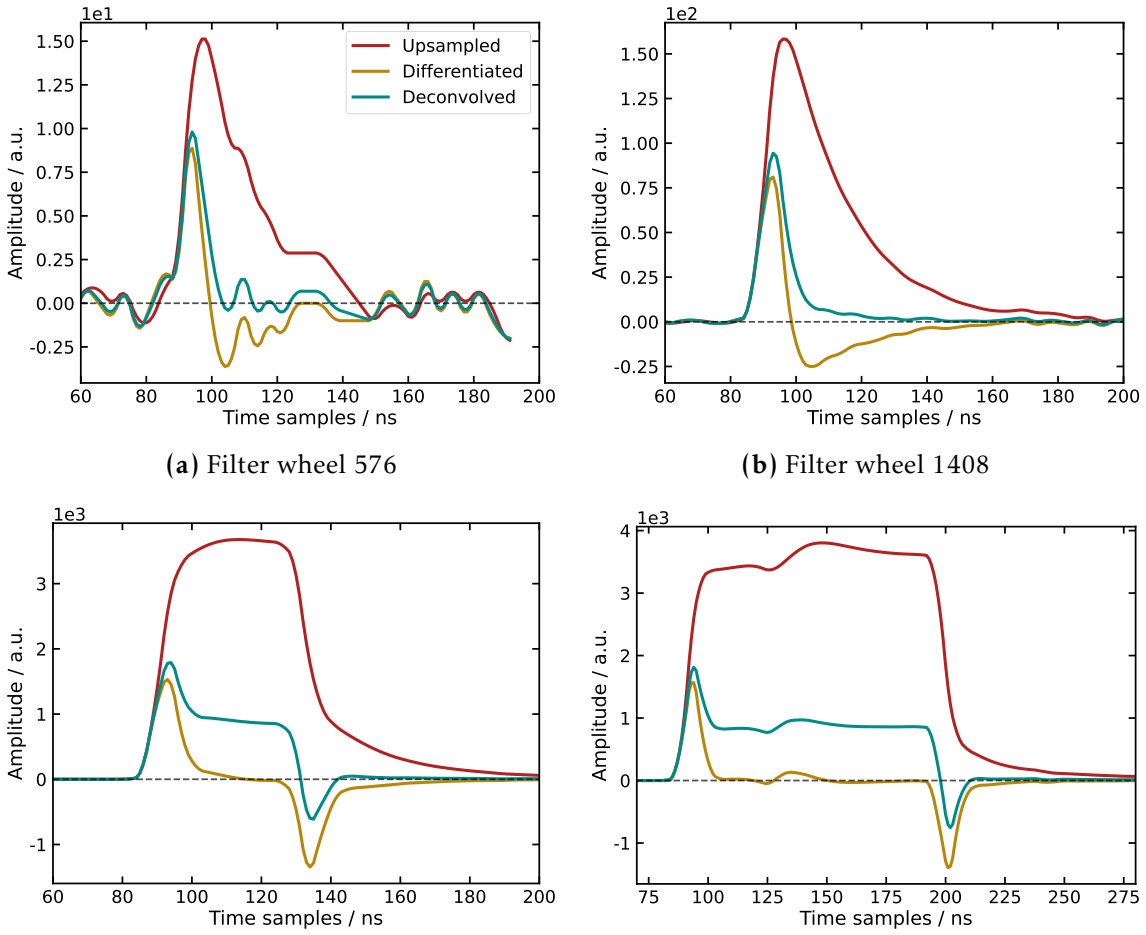

(a) Filter wheel 576

(b) Filter wheel 1408

(c) Filter wheel 2208

(d) Filter wheel 2688

Figure 4.19: Upsampled, differentiated, and pole-zero deconvolved traces at four filter-wheel positions from the linear regime to saturation regime: 576, 1408, 2208, and 2688. The traces are recorded in the laboratory.

Therefore, the four illumination levels in Fig. 4.18 reveal the two intensity regimes: linear and saturation. The linear regime, when the peak of the trace increases with signal amplitude and the saturation regime, when the peak of the trace no longer increases with the amplitude. Saturation starts at around 600 PEs.
Three pixels forming a triangle around the camera centre do not detect any signal. This is because at these positions three struts are used to hold the UV-transparent protective window [87]. Furthermore, there are three more pixels, two topmost and one bottommost, that are masked using three OD filters of different attenuation factors. The masked pixels are used to calibrate the camera at saturation, as will be discussed later.

Fig. 4.19 shows the evolution of the traces as the camera is illuminated in the laboratory at progressively higher light intensities with the same filter-wheel positions as in Fig. 4.18. Three traces are shown in each plot. The upsampled trace after interpolation to achieve ns sampling (explained in Section 3.1.2), the differentiated trace, obtained by differentiating the raw trace and then upsampling, and the pole-zero-deconvolved and upsampled trace. While Fig. 4.19a and 4.19b show a distinct signal pulse, Fig. 4.19c shows a trace in the saturated regime, and Fig 4.19d shows a deep saturated pulse. *umax* at saturation does not increase with intensity; however, the area of the pulse does.

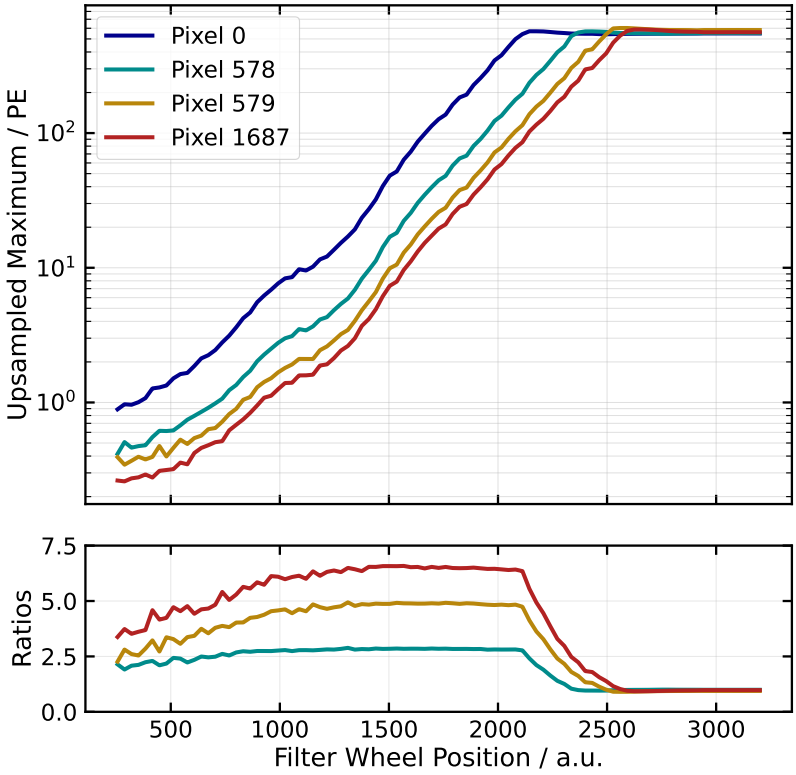

Figure 4.20: Evolution of *umax* with filter wheel position for pixel 0, which is one of the normal pixels, and the three masked pixels, pixels 578, 579, and 1687, using flat-field data from the laboratory at 300 MHz NSB. The bottom plot shows the ratio of pixel 0 to each masked pixel. This corresponds to the inverse of the masking ratio of each masked pixel.

Fig. 4.20 shows the relation of *umax* and the filter-wheel position in the top panel of the plot. The bottom panel shows the ratio of a standard pixel (pixel 0) to the masked pixels (pixels 578, 579, 1687). This plot is made with an NSB rate of 300 MHz. At low filter-wheel positions, noise has a more significant impact on the calculation of *umax*. As the filter-wheel position increases to approximately 2100,

a constant ratio of masked-to-standard pixels is observed, which is equal to the inverse of the ODs used for masking the respective PMT. Around a filter-wheel position of 2100, pulses saturate in the normal pixels, while the masked pixels saturate at higher filter-wheel positions, depending on their masking ratio.
A reference pulse shape in the linear regime is extracted for each pixel. The reference pulse shape is calculated as the median pulse shape across all events with the filter wheel set to position 1664 and without NSB background light, after gain matching all pixels via voltage adjustment. Figure 4.21 shows the individual pixel reference pulse shapes and the all-pixel average. These reference pulse shapes are subsequently employed for signal extraction in the linear regime to correct for gain loss and time shift induced by deconvolution, as discussed in Section 3.1.2.

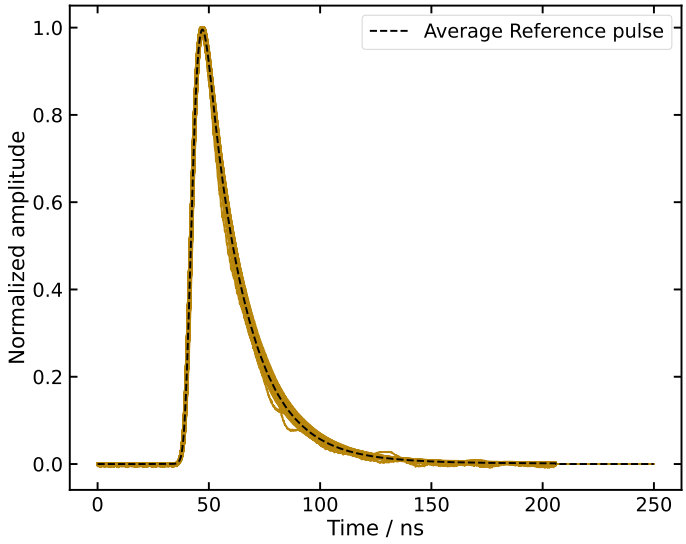

Figure 4.21: Reference pulse shapes of each pixel, calculated as the median over all flat-field events when the filter wheel position is set to 1664. The average reference pulse shape of all pixels is shown as a dashed black line.

Technical properties of the PMTs employed in this section are specified in Table 4.1, including the gain (defined as LSB/PE), excess noise factor, transit time spread, and afterpulsing probability. The table presents the values averaged over all pixels.

4.4 Charge extraction at saturation

Section 3.1.2 described the modifications made to the NPWS extractor of *ctapipe* to adapt it to the FlashCam trace characteristics. This method was tested and

Gain	~6.1 LSB/PE
ENF	~1.1
TTS	up to 2 ns
Afterpulsing	<0.02%

Table 4.1: Basic characteristics of the FlashCam PMTs. This includes the average end-to-end signal gain in the electronics, the average excess noise factor, transit time spread (defined as FWHM), and the probability of afterpulses with charge > 4 PEs. These parameters are described in Section 2.1.3. These quantities are also used in the simulations.

optimised in shower simulations without saturation implementation. It is further tested in this section using laboratory flat-field data runs, and its performance is compared with simulations of flat-field runs with the same laboratory setup.
This method only works in the linear regime. For the saturation regime, a new method is studied and tested on flat-field simulations, laboratory measurements, and shower simulations. The method's performance is compared to the CTAO requirements for charge resolution.
The CTAO charge resolution requirements are included in many of the following plots and are defined for illumination ≤ 4000 photons. These requirements are specified for simulated gamma-ray showers at low NSB of 266 MHz (including albedo) and high NSB, defined as five times the low NSB.

4.4.1 *Validation with flat-field data*

The charge resolution and bias are defined as in Section 3.1.1. However, the true charge for flat-field laboratory runs is unknown, precluding a direct comparison with the reconstructed charge.
For performance evaluation in flat-field runs, the "true charge" at each filter-wheel illumination level is defined as *umax*. While *umax* provides a reliable estimator in the linear regime, it saturates at ~ 600 PEs for normal pixels. The charge range over which *umax* remains valid is extended by employing the masked pixels to calibrate the flat-field device intensity at saturation. Following this calibration, the linear behaviour of *umax* extends up to filter-wheel position ~ 2500 (equivalent to ~ 4000 PEs), where the last masked pixel (pixel 1687) begins to saturate.

4.4.2 *Flat-field simulations*

Flat-field simulations are produced in sim_telarray by modelling a FlashCam and a laser positioned at the same distance from the camera as in the laboratory setup. The camera is then exposed only to flat-field events and varying NSB levels, matching the conditions in the data. Furthermore, the pixel-average transit time and gain match those of the real PMTs. The averaged characteristics of PMTs in FlashCam are summarised in Table 4.1.
sim_telarray does not include simulations of saturated pulses. In this Section, the FlashCam behaviour is simulated more realistically with a simple description for saturation. The resulting charge resolution from these simplified simulations of saturated pulses and from the measured laboratory data will be compared.
As a first approach, saturated pulses are simulated by hard-clipping the trace at the clipping level of 4095 LSB (before baseline subtraction). However, in this approach, the area of simulated traces does not increase with intensity, unlike that observed in the data (see Fig. 4.19). An easy way around this issue is simulating saturated pulses by still hard-clipping with the NumPy [202] function `clip` [203]. But, during the clipping, when a sample exceeds the preamplifier limit, the excess charge (the difference between the sample value and the clipping level) is propagated to subsequent samples. An overflow limit is imposed to prevent unrealistic charge accumulation. This approach, introduced by the author of this thesis, ensures that the pulse area increases with intensity, even at saturation, accurately reproducing the observed trace behaviour.

4.4.3 *Reconstruction method at saturation*

Saturated pulses are integrated over a fixed-length window of 90 ns, chosen to capture most signal samples from pulses produced by at least ~ 4000 photons or ~ 1100 PEs, the maximum signal required by the CTAO to be extracted within the requirements. The number of photons is obtained by multiplying *umax* by 0.277 PEs/photons, which is the specific conversion factor for the FlashCam. The window begins from the rising edge of the upsampled pulse minus 10 ns. The trace area of flat-field laboratory runs correlates with the estimated true charge based on the linearised *umax* as seen in Fig. 4.22b at two NSB levels of 300 MHz and

1500 MHz. The relationship between the area of traces in flat-field simulations and true charge is also shown in Fig. 4.22a.

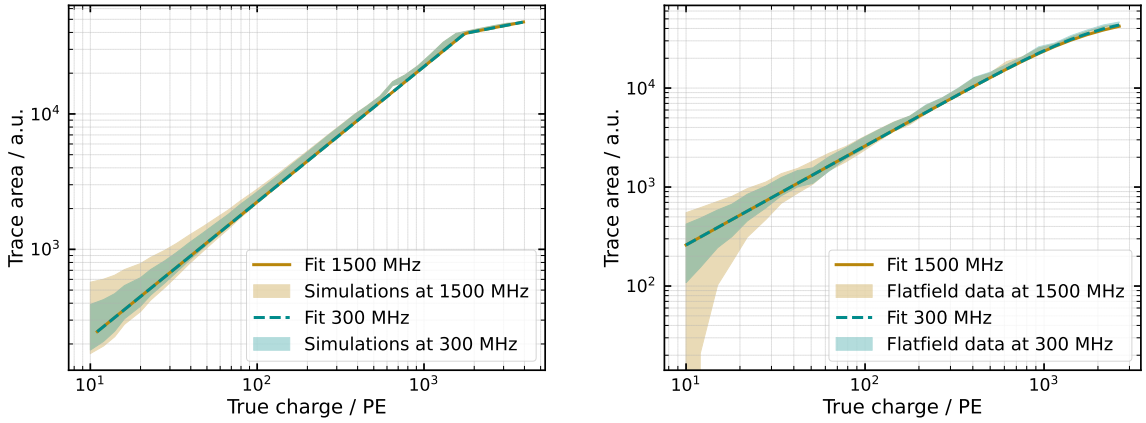

(a) Simulations **(b)** Laboratory data

Figure 4.22: Relation between the area under the trace within a window of size 90 ns and the true charge (when using simulations) and, for data, the estimated true charge based on the linearised *umax*. Computed on flat-field simulations (left) and laboratory runs (right). The shaded region represents the distribution of trace-area measurements across events for a single pixel.

While the relationship between trace area and true charge remains consistent for the two NSB conditions, the deviation from the fitted model across events is greater at high NSB levels, particularly in the low-true-charge regime. This dispersion is further amplified in flat-field laboratory data compared to simulations.
There is a clear break point (x_{break}) between 1000 PEs and 2000 PEs in both cases, even though more prominently in the simulated case. The break point marks a change in the power-law index. Because the post-break gradient is less steep in simulations, they exhibit a weaker response in this region. The range of possible true charge values for a given trace area is larger than when using the laboratory data, leading to poorer charge estimates above ~ 1700 PEs.
Both in simulations and data, the relationship between the trace area and the true charge is given by a smooth broken power law [204]:

$$F(x) = A \times \left(\frac{x}{x_0}\right)^{-\gamma_1} \times \left(1 + \left(\frac{x}{x_{\text{break}}}\right)^{\left(\frac{\gamma_2-\gamma_1}{\beta}\right)^{-\beta}}\right), \tag{4.4.1}$$

where $F(x)$ is the trace area and x is the true charge. The parameter x_0 can be fixed to 1. Similarly, γ_1 is also fixed to a value of -1, as well as γ_2, which is set to -0.25

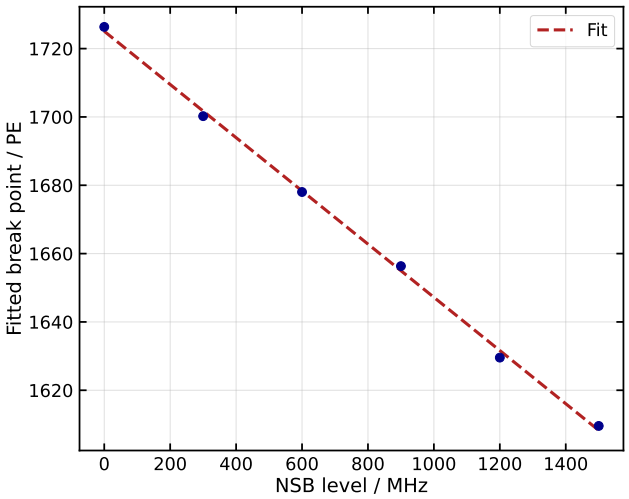

Figure 4.23: Linear relationship between the position of the break (x_{break}) and the NSB level. This is done on multiple lab flat-field data runs at different NSB rates after fitting the trace area and *umax* with Equation 4.4.1.

and β to 0.3, after fitting laboratory flat-field runs. The break is due to the fact that the 90 ns window length cannot capture traces above ~ 1700 PEs. Increasing the window length would eliminate this effect at high intensities. The effect is less significant using laboratory flat-field runs.
The previous parameters are independent of NSB and are constant across pixels. Therefore, only two parameters are left in the fit, the amplitude A and x_{break}. The amplitude is pixel-dependent and related to the pixel integral; therefore, it can be calibrated independently. Additionally, x_{break} is the same across pixels but varies with the NSB rate. The value for x_{break} relates linearly with the NSB rate, as shown in Fig. 4.23. All these parameters are found to be independent of the PDP modules' temperature.

4.4.4 *Performance tests*

The signal extraction algorithm is divided into two steps. The FlashCam extractor in Section 3.1.2 describes the linear response, and the trace area describes saturation. The charge is reconstructed using the linear and saturation methods, and the final charge resolution and bias are shown in Fig. 4.24 as a function of the average number of photons reaching the photocathode. The plots are calculated through laboratory flat-field runs across the full range of filter-wheel positions. The NSB rate is set to 300 MHz.

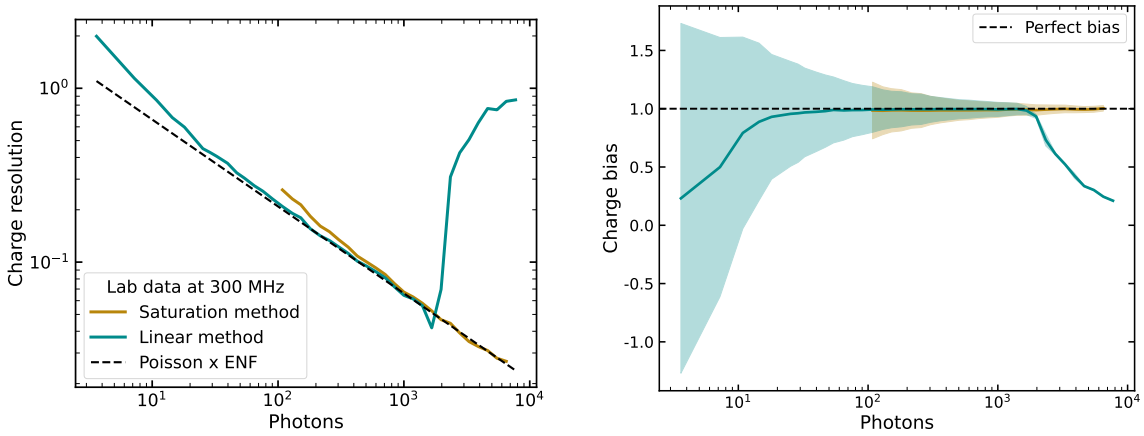

(a) Charge resolution **(b)** Charge bias

Figure 4.24: Charge resolution and bias when charge is reconstructed using the linear and saturation extraction methods (as described in the text) over the whole intensity range. The performance is shown for laboratory flat-field data runs at an NSB of 300 MHz. The best possible charge resolution and bias are shown as dashed black lines. The shaded area in panel (b) shows the bias distribution across events.

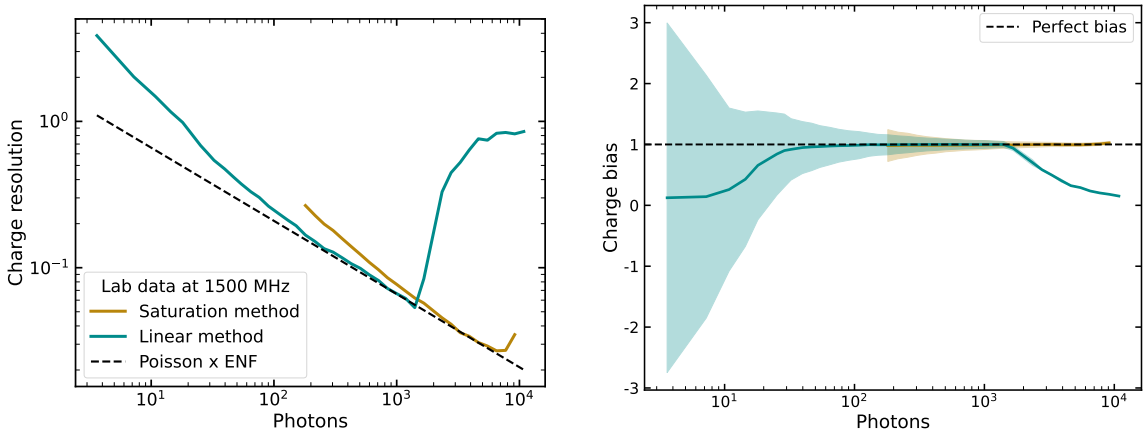

(a) Charge resolution **(b)** Charge bias

Figure 4.25: Charge resolution and bias when charge is reconstructed using the linear and saturation extraction methods (as described in the text) over the whole intensity range. The performance is shown for laboratory flat-field data runs at an NSB of 1500 MHz. The best possible charge resolution and bias are shown as dashed black lines. The shaded area in panel (b) shows the bias distribution across events.

Fig. 4.24a shows the charge resolution averaged across all events, whereas Fig. 4.24b displays the averaged charge bias, and the shaded region reflects the variation in bias across events. The performance curves are shown only for one pixel. The charge resolution curve obtained by the linear method yields completely incorrect

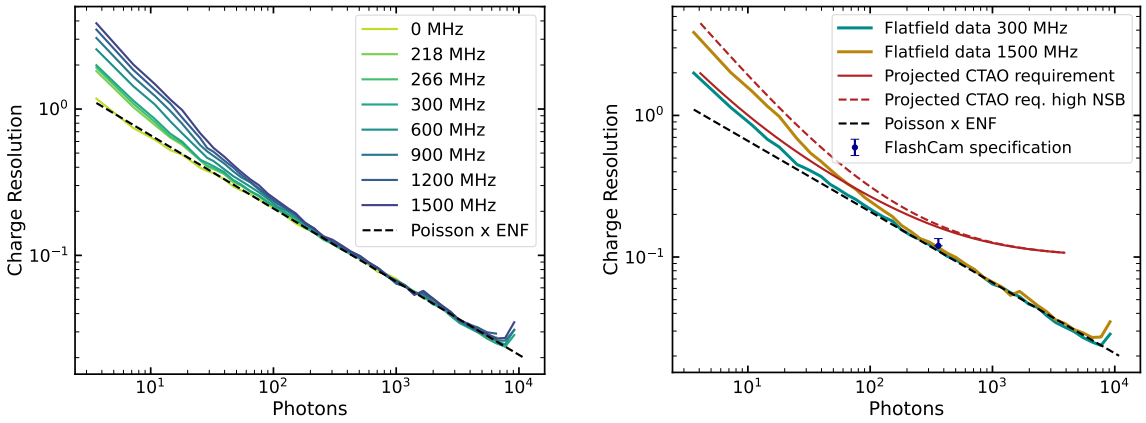

(a) Multiple NSB rates

(b) Requirements comparison

Figure 4.26: Charge resolution using laboratory flat-field measurements at multiple NSB rates for one pixel. The left figure shows all NSB rates from 0 MHz to 1500 MHz. The right figure shows the curves at 300 MHz and 1500 MHz together with the projected CTAO requirements at low (solid line) and high (dashed line) NSB, defined at an NSB of 266 MHz and five times that, respectively. The FlashCam specification is also included.

reconstructions above 1000 photons. The charge resolution obtained using the saturation-regime method yields low reconstruction uncertainties, approaching the best possible performance at high illumination. The charge bias obtained with the linear- and saturation-regime methods lies near the line of perfect bias, with large spreads and strong bias at low true charge.

The charge resolution and bias are shown in Fig. 4.25 with the same conditions as before, but at an NSB of 1500 MHz. The performance of the linear method is worse at low illumination levels and higher NSB rates, as expected, because the signal is more easily confused with NSB. The saturation method also performs slightly worse near the point of coincidence between the two regimes, due to a poorer fit. However, the resolution still almost aligns with the Poisson × ENF curve at > 2000 photons. The charge bias gets worse at low charge.

At reconstructed charge < 400 PEs, the charge is extracted from each pixel with the linear-regime FlashCam extractor. At charge > 480 PEs, intensity is obtained from the trace area and Equation 4.4.1. Between 400 PEs, and 480 PEs, both reconstruction methods are applied, and two values for the reconstructed charge are obtained. The final charge in this range is received by a moving weighted average. The final charge resolution after merging the two methods is shown in Fig. 4.26a for one pixel at multiple NSB levels. The charge resolution is shown as a function of the number of incoming photons. Increases in NSB lead to a worse

charge reconstruction performance at low charge. The resolution at the intersection of the linear and saturation regimes close to 2000 photons degrades slightly but not significantly.

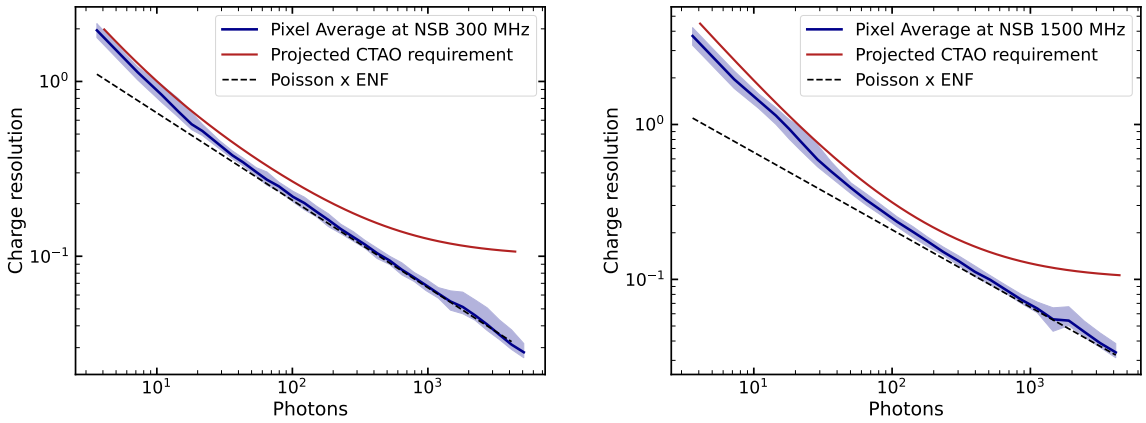

(a) 300 MHz **(b)** 1500 MHz

Figure 4.27: Charge resolution using laboratory flat-field measurements for all pixels at 300 MHz (left) and 1500 MHz (right). The solid blue line shows the average across all pixels, and the shaded areas indicate the regions that encompass the resolution curves for all pixels. The CTAO requirements at low (left) and high (right) NSB are also projected.

Similarly, Fig. 4.26b shows the charge resolution curves at 300 MHz and 1500 MHz NSB for one pixel. The dark blue upper error limit in the plot represents the FlashCam specification. The specification estimates that at 100 PEs (equivalent to ∼360 photons), the charge resolution is 12%, with an upper error bar of up to 15%. The red solid and dashed lines show the CTAO requirements ($\leq$ 4000 photons) at low and high NSB, respectively. Low NSB is defined as 266 MHz, including albedo, and high NSB is five times the nominal NSB. Even at higher NSB rates, the charge resolution exceeds the projected CTAO requirement, with considerable improvement at high intensities.

The previous charge-resolution curves show only the performance of a single pixel. Fig. 4.27 shows the resolution of all pixels. The pixel average is shown as a solid line, and the surrounding shaded area indicates the region in which all pixel resolution curves lie. The consistency of all pixels under both low and high NSB conditions and across the full intensity range is evident. As mentioned earlier, the amplitude parameter in Equation 4.4.1 is pixel-dependent and is obtained separately for each pixel.

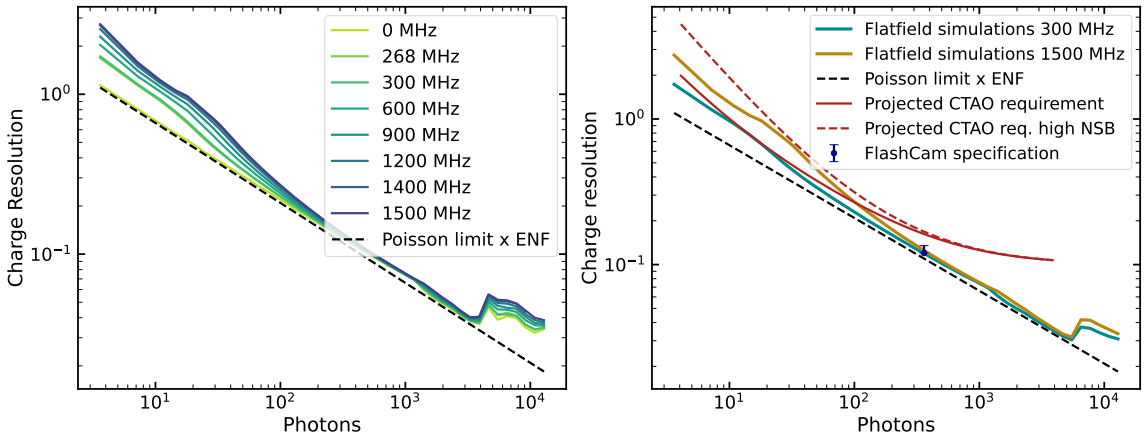

(a) Multiple NSB rates

(b) Requirements comparison

Figure 4.28: Charge resolution of simulated flat-field events at multiple NSB rates. The left plot shows resolution curves from 0 MHz to 1500 MHz. The right plot shows the resolution at 300 MHz and 1500 MHz NSB rates, along with the projected CTAO requirements at low and high NSB and the FlashCam specification.

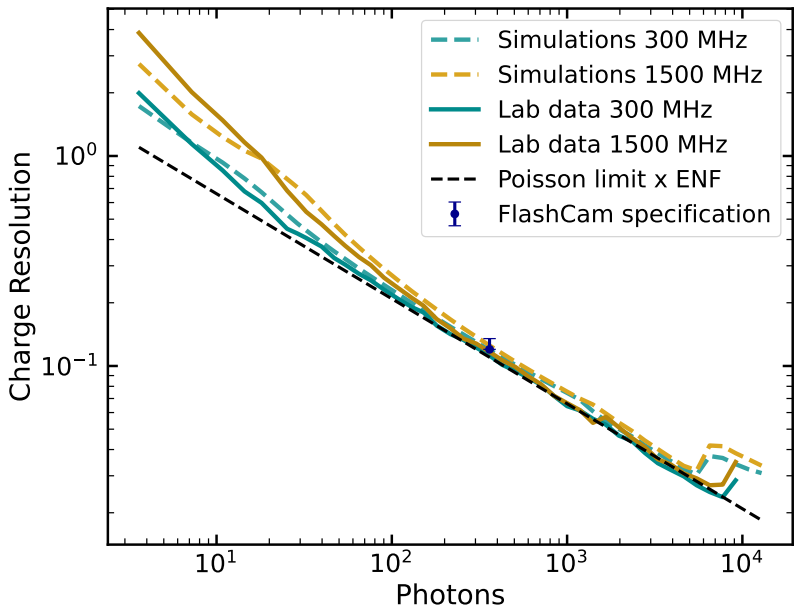

Figure 4.29: Comparison of the charge resolution curves obtained from flat-field events in the laboratory and with simulations at two NSB values: 300 MHz and 1500 MHz. The resolution from the data is computed for a single pixel, and the simulated resolution is averaged across pixels. This is shown alongside the limit on the best resolution and the FlashCam specification.

The method is furthermore tested against simulations. Fig. 4.28 shows the same as Fig. 4.26, but using sim_telarray simulations of flat-field events under the same

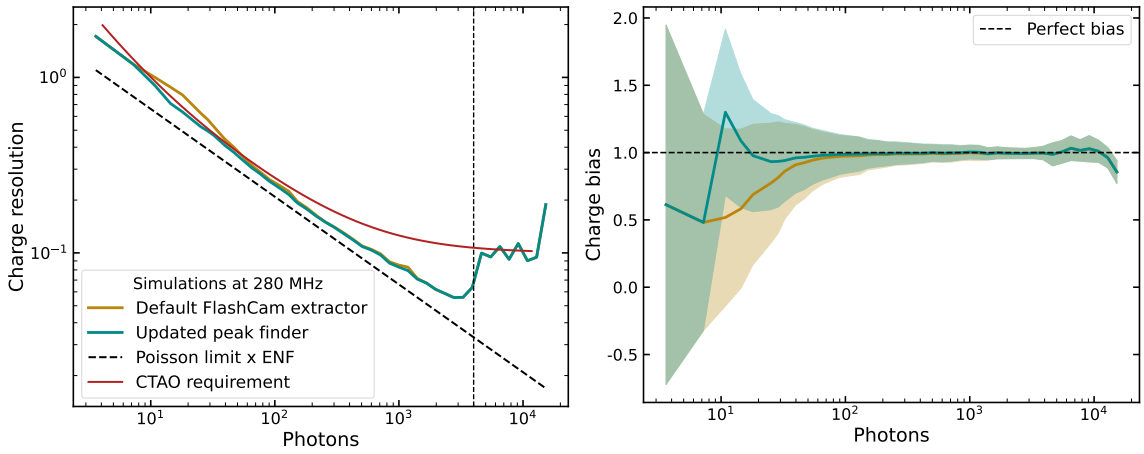

(a) Charge resolution

(b) Charge bias

Figure 4.30: Charge resolution and bias computed on gamma-ray shower simulations using the default FlashCam extractor in the linear regime and the updated version with a new peak finder for illumination higher than 10 photons. The charge resolution is plotted alongside the CTAO requirement at low NSB, with a line indicating the maximum photon count at which the CTAO requirement must be met.

conditions. Above ~4000 photons, the resolution degrades relative to laboratory data. This is due to both the simplification of saturated-pulse simulation and a too-short integration window, which causes the effect shown in Fig. 4.22 and, in turn, degrades the reconstruction. The resolution at low intensity is better than using laboratory runs. The resolution degrades with NSB at both low (< 100 photons) and high (> 4000 photons) illumination levels. Fig. 4.28b shows that the charge resolution is better than the CTAO requirements even at higher-than-specified NSB rates.

The charge resolution curves at 300 and 1500 MHz, obtained from flat-field data and simulation events, are compared in Fig. 4.29. The curves match reasonably well at intermediate intensities, from a few tens of photons to 4000 photons. At low illumination, especially with high NSB, the resolution of laboratory runs is slightly worse, likely because the simulated noise is somewhat underestimated. The resolution mismatch at > 4000 photons is due to the overly simplistic saturation simulation model.

This demonstrates overall good consistency between the data and the simulations for flat-field events. The method is now evaluated in shower simulations across the full CTAO illumination range, up to 4000 photons, using gamma-ray showers. Simulations of on-axis gamma-ray showers for an MST-FlashCam are performed

with zenith angle 20°. Two NSB rates are simulated for comparison with the CTAO performance: 280 MHz and 1400 MHz.
By examining the charge reconstruction on showers, a bump between ∼ 10 and ∼ 70 photons is observed that exceeds the CTAO requirements, as shown in Fig. 4.30a (Default FlashCam extractor). This is corrected for by adding a step to the linear reconstruction that identifies the peak of the traces not by examining neighbouring pixels, but simply as the maximum of the local trace (see Fig. 4.30a (Updated peak finder)). This is introduced in the method and done only when the pixel intensity is > 10 photons. The transition depends on NSB. This step improves resolution at the bump but is not applied at the lowest intensities, as the neighbour-based method outperforms at low intensities due to its lower noise sensitivity. At low charge, the local peak of the trace can easily be mistaken for a noise pulse. The charge bias is shown in Fig. 4.30b, and displays a slightly better bias with the updated peak finder. The bump at those low charges can be due to the lack of smoothing of the FlashCam traces after upsampling. Without smoothing, additional jitter in the neighbour-sum peak position results in slightly misaligned integration windows. As a future update of the algorithm, one can explore the effect of smoothing.

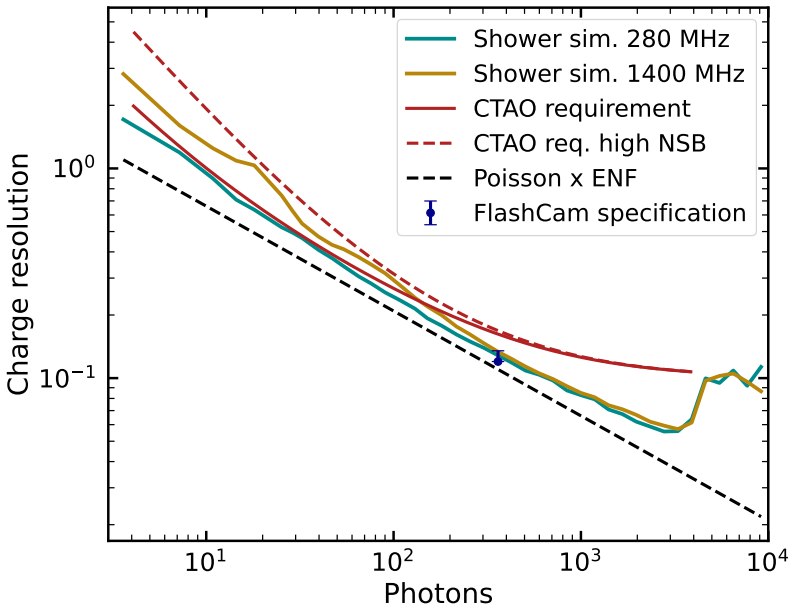

Figure 4.31: Charge resolution, averaged over all pixels, of simulated gamma-initiated showers as a function of the number of photons reaching the photocathode. A MST-FlashCam is simulated. The CTAO requirements are highlighted in red at low (solid line) and high (dashed line) NSB.

Fig. 4.31 shows the final charge resolution for gamma-ray shower simulations of one MST in the South. The red lines show the CTAO requirements on shower simulations, defined up to 4000 photons. The NSB rate in the simulations exceeds the specified requirement, yet the requirements are still fully met. At illumination levels above the CTAO limit, the method's performance degrades significantly. It is expected to see a significant lower degradation when using real observations.

4.5 Time reconstruction

The time reconstruction was verified and developed by Anne Timmermans [205]; the results are presented in this section for completeness. The time reconstruction of the FlashCam PMT pulses can be summarised with the following steps:

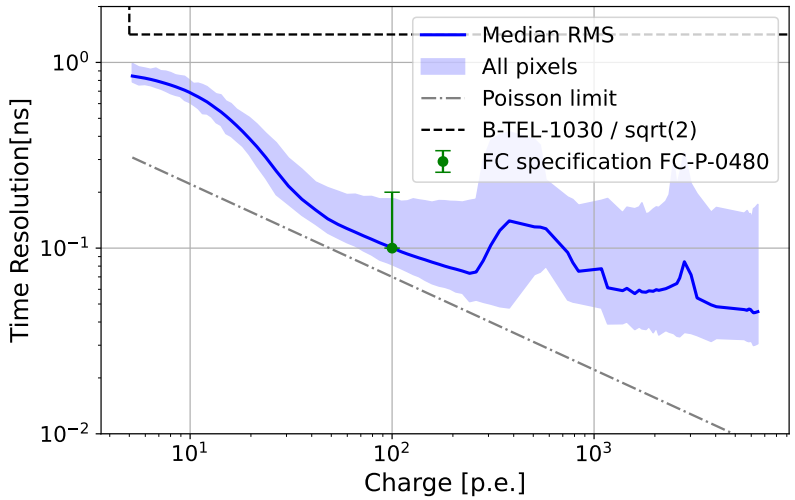

Figure 4.32: Time resolution at an NSB of 125 MHz as a function of charge. This is computed from flat-field laboratory data. The filled area encompasses the curve of each PMT. The darker blue solid line shows the median of all pixels, and the green line shows the FlashCam specification. The dashed box at the top of the plot is the CTAO requirement. Provided by Anne Timmermans.

- Trace upsampling to decrease sampling to 1 ns
- Identification of the differentiated traces' peaks
- Selection of the two nearest neighbours of the maximum time sample, and fit of a parabola through these three points
- Apply a phase correction to account for systematics arising because the three points do not form a perfect parabola

- The changes in the shape of the traces as they reach saturation are corrected for with a slewing correction. This is a charge-dependent correction.

The time resolution as a function of pixel charge in PE is shown in Fig. 4.32, along with the CTAO requirements and the FlashCam specification. The time resolution is defined here as the RMS difference in the reconstructed time between any two simultaneously illuminated pixels. The curve must not exceed 2 ns at amplitudes of 5 PEs at an NSB rate of 125 MHz. Furthermore, Fig. 4.33 shows the RMS uncertainty on the mean relative reconstructed arrival time in every pixel of a FlashCam camera being illuminated in a dark room by a uniform simultaneous pulsed illumination. The plots in this figure show how the RMS uncertainty changes with:

- Changing illumination level (top left)
- Long-term behaviour for continuous operation over several days (top right)
- Changing background illumination up to 1500 MHz (bottom left)
- Changing the camera internal temperature (bottom right)

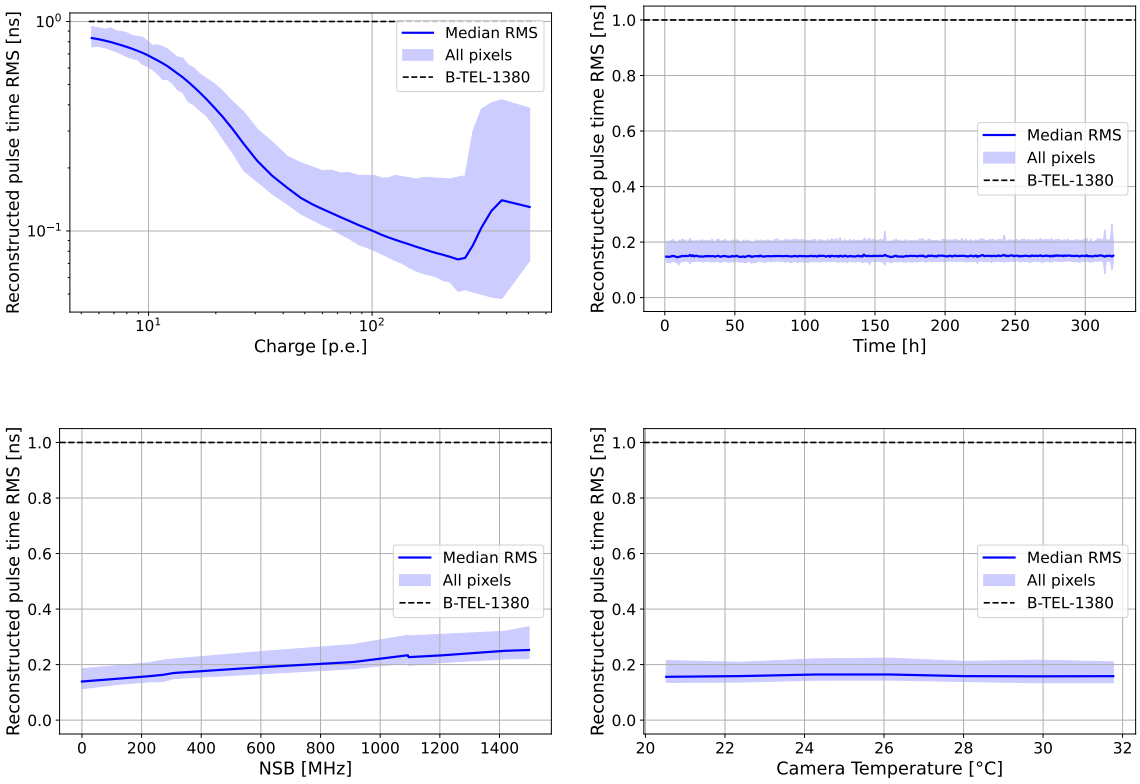

Figure 4.33: Uncertainty in pixel timing as a function of reconstructed charge (upper left), time (upper right), NSB level (lower left), and camera temperature (lower right). Provided by Anne Timmermans.

No systematic effects play an important role. Furthermore, in each case, the CTAO requirement is satisfied. The requirements are shown as dashed black lines in each plot.

4.6 Summary and outlook

Two main topics were discussed. The first part of this chapter focused on the fast-online identification of muon rings on FlashCam. The method is camera-dependent, but a similar principle can be used in other Cherenkov cameras. The output of the FlashCam trigger system was used to distinguish muons that produce a ring on the camera from other events. As muon rings extend over larger regions of the cameras and emit all Cherenkov light within a short time window, the number of triggered patches and cards within 2 time samples of the first trigger is a reliable tag for these events. Protons do not have the same characteristics and tend to trigger on fewer patches and cards. Events are therefore discriminated by applying two simple cuts. The efficiency of detecting muon rings with this method exceeds 90%, still rejecting the vast majority of background events. All the CTAO requirements are satisfied.
In the field, the number of triggered patches will be obtained from firmware. The number of cards is provided by the master card distribution. The cuts will be applied in the software running on the camera server so that it can communicate with SWAT to indicate that a muon ring candidate was detected. The SWAT can then reply, sending this event to the ADH, even if it does not coincide with triggers from other telescopes.

In the second part of this chapter, the charge extractor algorithm in the linear and saturation regimes was validated on flat-field events and compared to simulations. The linear method, described and optimised in an earlier section, was further tested on laboratory data, demonstrating good charge resolution and good agreement with simulations. Saturation was studied in detail. A simple description of saturation was incorporated in simulations and compared to data. A new reconstruction method at saturation was introduced. The final performance of the charge reconstruction in the linear and saturation regimes meets the CTAO requirements for resolution.

5

VALIDATION AND IMPROVEMENTS OF THE H.E.S.S. CHAIN

The first part of this chapter presents a detailed study of the consistency between simulated and observed data from the CT1–4 telescopes of the H.E.S.S. array. The validation of the CT1-4 telescopes during the H.E.S.S. I and H.E.S.S. II phases is presented (phases discussed in Section 2.2). All validation steps described here were carried out by the author of this thesis, except for the optical PSF analysis, which Gerrit Roellinghoff provided. The study follows an approach similar to that of [206], [109], and [207].
The second part of this chapter presents improvements to the IRF of FlashCam in CT5 achieved by incorporating weights into the DBSCAN component of the image cleaning algorithm. This weighted DBSCAN approach was motivated by the author's previous studies on DVR optimisation (see Section 3.2.5). The implementation of the weights was completed by the author of this thesis and Simon Steinmassl. Nevertheless, the core code of this image-cleaning algorithm was implemented several years ago by Simon Steinmassl [109]. The performance tests on IRFs were conducted by Jelena Celic and Helena Ren, who captured images of example showers after cleaning.

5.1 Monte Carlo-data consistency of H.E.S.S. I/II CT1-4

The reconstruction of air showers relies on accurate simulations of the shower development, Cherenkov light emission, and the telescopes' response to that light. Achieving good agreement between data and simulations is essential for reliable energy and direction reconstruction and for effective particle-type classification. A

more detailed discussion on the importance of simulations in shower reconstruction can be found in Section 2.4.4.
Since the installation of H.E.S.S. and the start of data taking, H.E.S.S. has undergone multiple phases. The first phase (H.E.S.S. I) consisted only of the four small telescopes; the cameras of these telescopes were upgraded around 2016 to transition to phase H.E.S.S. IU. In 2012, a fifth telescope, larger than the other four, was introduced in the middle of the array, initiating phase H.E.S.S. II. During H.E.S.S. II, the original cameras of CT1-4 were still functioning. A subsequent upgrade for the larger central telescope involved replacing the camera with a FlashCam. More details in Section 2.2.
The consistency between data and simulations has already been validated in H.E.S.S. for the H.E.S.S. IU array and CT5 in the H.E.S.S. II era, as well as for the FlashCam era. However, the simulations of the H.E.S.S. I and H.E.S.S. II cameras, telescopes, atmosphere, and related components were tested against observational data several years ago. A renewed validation is therefore needed to verify that those early consistency checks remain accurate.
Consistency checks for the first telescopes used in the H.E.S.S. I and H.E.S.S. II phases are carried out, employing tests analogous to those used for the FlashCam era in [206], [109], and [207]. The validation covers the consistency of the muon efficiencies, the trigger performance, the Hillas and image-cleaning reconstruction, and the optical PSF.

5.1.1 *Data run selection*

Validation is performed on data runs recorded between the beginning of November 2014 and roughly the end of September 2016. During this time, CT5 was already taking data. The time window is restricted to avoid significant changes in, for example, hardware settings and optical throughput over time. During this period, the data are split into two phases, with the cut occurring on the August, 1st 2015. The difference between the phases is a degradation in the optical throughput around that time. Additionally, CT1 is also upgraded around this time. The change in the average per-run muon efficiency of CT2 is shown in Fig. 5.1a for each run number. Prod2b4 and Prod2b5 are two distinct production runs in sim_telarray that correspond to each phase. Tests of trigger rates are performed separately for Prod2b4 and Prod2b5, because even small changes in muon efficiencies can

significantly affect trigger rates. CT1 was upgraded during that Prod2b5. Therefore, this telescope is only checked in Prod2b4.

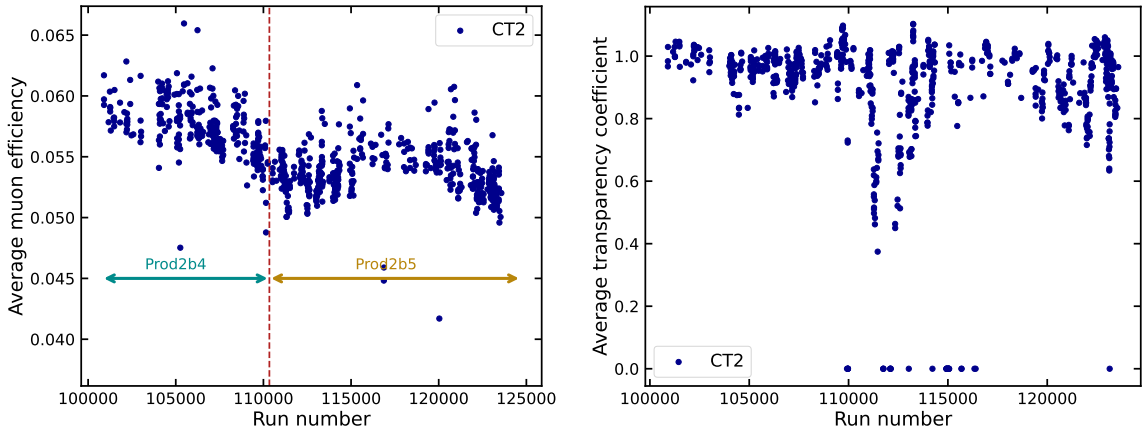

(a) Muon efficiency

(b) Atmospheric transparency coefficient

Figure 5.1: Evolution of the muon efficiency and average transparency coefficient, averaged for each run, as a function of the run number from the beginning of Prod2b4 until the end of Prod2b5. The zenith angle is chosen as $20° \pm 5°$.

A valid comparison between simulations and data requires careful selection of runs, excluding those affected by technical issues or poor observational conditions. Atmospheric conditions are particularly important for this validation, as the simulated atmosphere must closely match the observed conditions to enable accurate comparison [208]. However, atmospheric properties can change abruptly over short timescales due to clouds or varying aerosol levels. To account for this variability, atmospheric conditions are quantified using the Atmospheric Transparency Coefficient (ATC) [209], which is recorded and stored in the datasets for each observation run. The average ATC of each run is shown in Fig. 5.1b for CT2 as a function of the run number.

The runs shown in both plots of Fig. 5.1 are those that pass the following quality cuts:

- Minimum duration of 600 s; shorter runs may indicate problems during data taking. Observation runs are scheduled by default for 28 min
- The RMS error in the averaged trigger rate over each event should be $\leq$30 Hz, to avoid the effect of e.g., clouds
- Pixels are automatically deactivated when a bright star or satellite enters the camera's field of view to prevent damage to the PMTs. Therefore, additional

cuts are applied: < 120 broken pixels due to hardware issues and < 50 pixels with deactivated high voltage.

Additionally, and based on Fig. 5.1b, a minimum cut in the ATC is set at 0.6 and up to 1.3 to reject outliers. Tighter cuts in ATC are avoided to make sure that the consistency checks do not depend on historical values of the trigger rates from which the ATC is calculated. For certain consistency checks, the observation runs are also selected based on zenith angle. The tolerance around the zenith angle of interest is ±5°. The data runs are compared to simulations at the same zenith angle.

5.1.2 *Monte Carlo simulations*

Simulations were performed for the full 5-telescope H.E.S.S. II array and for some of the checks only for the CT1-4 subarray. The used CORSIKA version is 78000, and the sim_telarray release was on March 4th, 2025, with a few recent modifications following internal discussions with Konrad Bernlöhr to enable simulations of muon showers with the fifth telescope. Proton shower and muon-only event simulations are performed for validation. Some examples of images of proton- and muon-initiated showers can be seen in Fig. 5.2. The quantity shown in every pixel is equivalent to the recorded 16-sample (1 sample being equivalent to 1 ns) pulse sums for each pixel.

Proton simulations are run with the following initial parameters. The energy range is between 10 GeV and 120 TeV. The maximum impact distance, RSCAT, in sim_telarray is set to 1200 m, which encompasses the vast majority of showers that can trigger the array. The viewcone around the simulated telescope direction is chosen to have a solid angle of 9°. Choosing a small viewcone or impact distance in sim_telarray results in missing phase-space coverage, leading to biased trigger rates and invalid comparisons between simulations and real data. Almost no events are missed with the selected viewcone and impact distance, thereby minimising the effect of systematics.

On the other hand, muon showers are simulated with a starting altitude depth of 680 g/cm^2 when only CT1-4 can trigger, but 550 g/cm^2 when CT5 is also included. The energy range is 10 GeV to 100 GeV, and the maximum impact distance is 20 m when only CT1-4 form the array and 32 m with CT5. These represent the default sim_telarray impact distances from which muons originate in the simulation. The

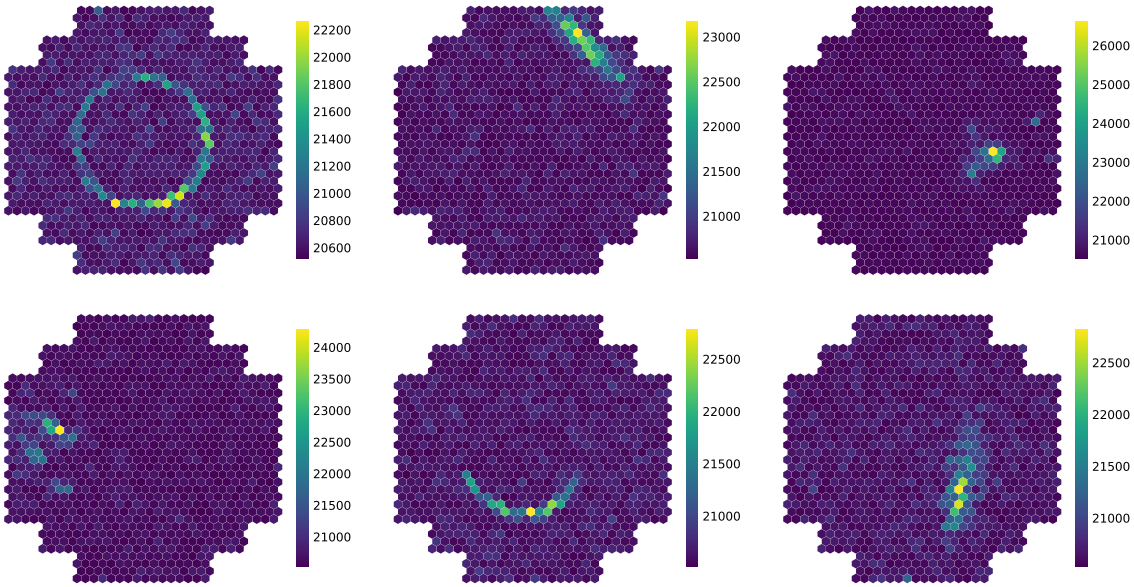

Figure 5.2: Images from simulated showers being detected by the cameras of CT1-4. Each pixel shows the sum over a fixed window of 16 samples (1 sample is 1 ns). Simulations of the old H.E.S.S. phases do not produce the waveforms for each pixel.

distances are chosen to ensure that a substantial fraction of the lowest-energy muons with significant scattering are captured, thereby avoiding bias against them. In every simulation, atmospheric light attenuation is accounted for in sim_telarray using the atmospheric transmission tables generated by the Moderate Resolution Atmospheric Transmission software (MODTRAN). The tables present the optical thickness as a function of height above the ground and wavelength. Simulations take into account the reduction by 50% of the aerosol level discovered during the consistency checks of the FlashCam era ([206], [109], [207]) based on measurements of the atmospheric optical depth by the Aerosol Robotic Network (AERONET) [210]. Consistency checks in the FlashCam era also revealed that the NSB in simulations needs to be enhanced to better match observations. This is also taken into account.

5.1.3 *Muon efficiency*

The consistency of the optical throughput is cross-checked by examining the muon efficiency distribution. Further details on muon calibration are provided in Section 4.2.1. The ratio of the average muon efficiencies of data runs over simulations can be written as,

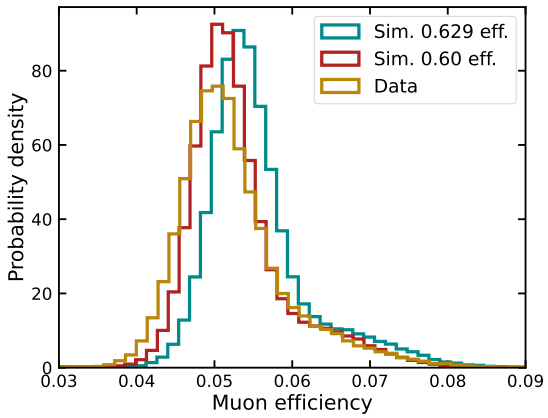

(a) CT2

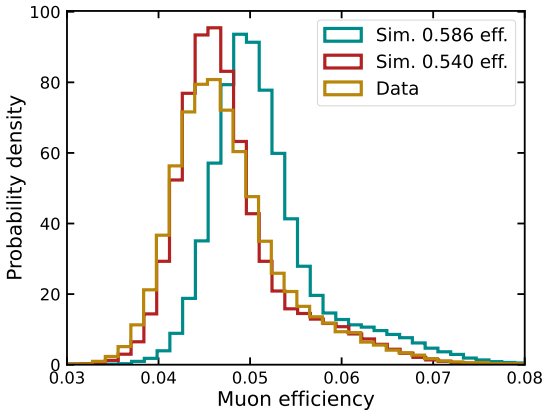

(b) CT3

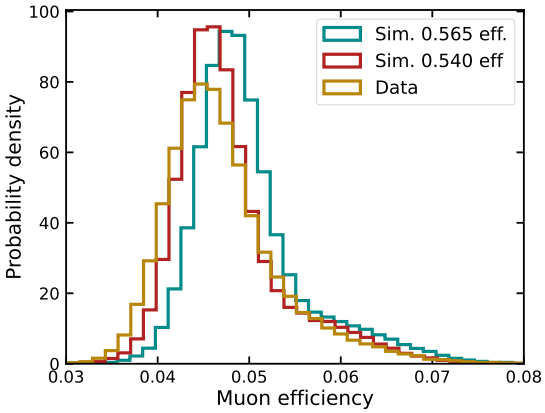

(c) CT4

Figure 5.3: Phase Prod2b5. Muon efficiencies for CT2, CT3, and CT4 telescopes using default and updated simulated mirror reflectivities, compared with the muon efficiency distribution from observations.

$$C_{\mu} = \frac{\langle \varepsilon_{\mu,\mathrm{sim}} \rangle}{\langle \varepsilon_{\mu,\mathrm{dat}} \rangle}, \tag{5.1.1}$$

where $\varepsilon_{\mu,\mathrm{dat}}$ and $\varepsilon_{\mu,\mathrm{sim}}$ are the muon efficiencies for the data and simulations, respectively. The same factor also yields the mirror degradation ratio, assuming that the change in optical throughput is entirely attributable to it. Therefore, the new simulated mirror reflectivity is provided by,

$$\varepsilon_{\mathrm{mirror,new}} = \varepsilon_{\mathrm{mirror,old}} \times C_{\mu}. \tag{5.1.2}$$

The corrected mirror degraded efficiency of the simulations ($\varepsilon_{\text{mirror,new}}$) is equivalent to the original simulated mirror degradation ($\varepsilon_{\text{mirror,old}}$) multiplied by the muon efficiency ratio. If the simulations were initially correct, the muon efficiency ratio would equal 1.0, and no changes to mirror degradation would be required.

	prod2b4		**prod2b5**	
	Default	**Updated**	**Default**	**Updated**
CT1	0.680	0.668	–	–
CT2	0.658	0.623	0.629	0.60
CT3	0.617	0.593	0.586	0.540
CT4	0.637	0.602	0.565	0.540

Table 5.1: Mirror degraded efficiencies for the configurations Prod2b5 and Prod2b5 before (default) and after (updated) the muon efficiency validation.

The distribution of muon efficiencies of data runs in the Prod2b5 phase is shown in Fig. 5.3 and is compared to the simulated muon efficiency distribution for the default simulation configuration in dark cyan and the new configuration in dark red. The previous mirror degradation and the updated values are shown in Table 5.1. The same evaluation is done for Prod2b4 in Fig. 5.4. As for the other phase, the muon efficiencies in the default simulations were higher than those in the data runs. The mirror degradation value was lowered to match the muon efficiency distributions. Table 5.1 also shows the new mirror reflectivities for Prod2b4.

5.1.4 *Trigger threshold*

The per-camera trigger mechanism is based on a multiplicity trigger (trigger described in detail in [211]). The trigger is calculated from multiple overlapping sectors, each containing 64 pixels. These sectors overlap to achieve a more homogeneous trigger response. The CT1-4 cameras trigger if the signals of at least M pixels (where M is the so-called sector threshold) within one sector simultaneously exceed a pixel threshold, referred to as N.
The third-brightest pixel intensity distributions of simulated and observation runs could pinpoint possible differences in the trigger threshold. Proton simulations are used for threshold validation because they account for the majority of triggers. The showers are simulated with a zenith of 20°. The simulations are scaled to a

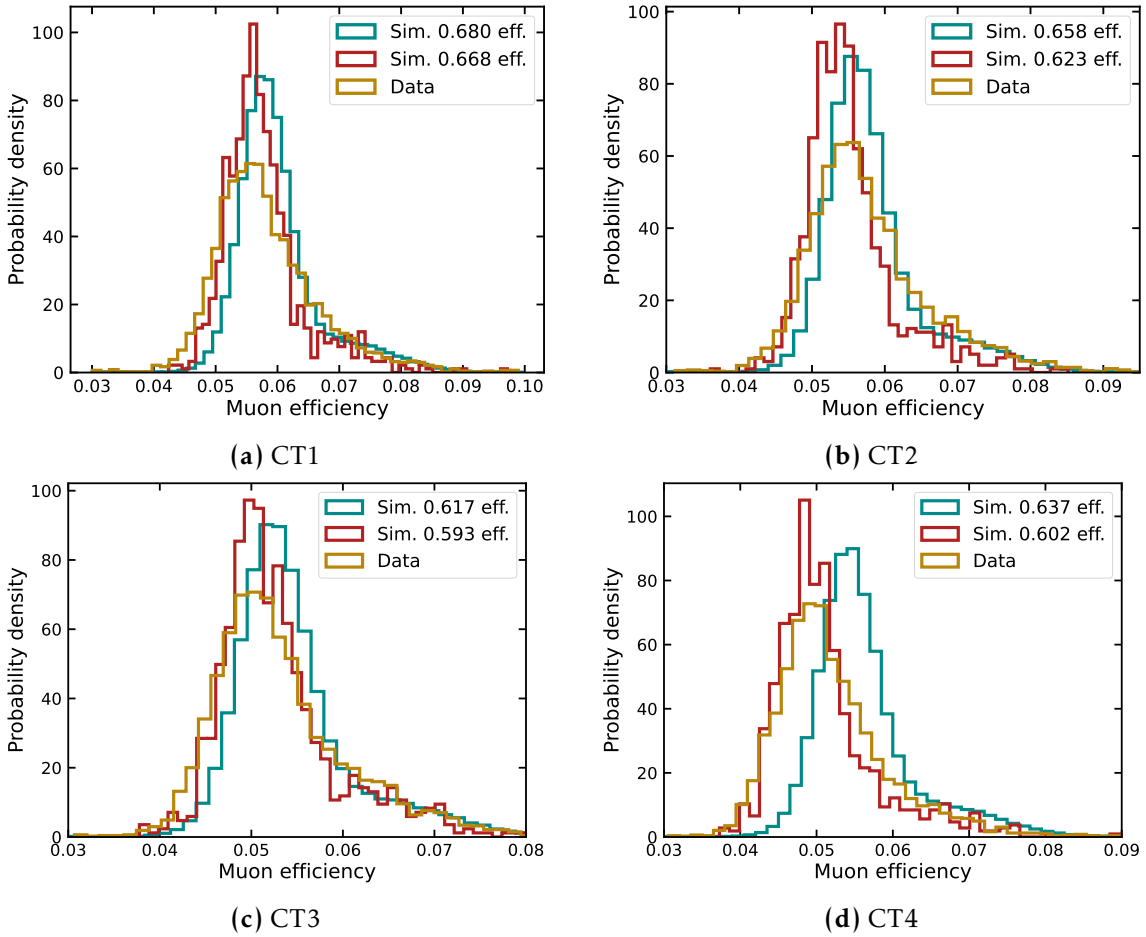

(a) CT1 **(b)** CT2 **(c)** CT3 **(d)** CT4

Figure 5.4: Phase Prod2b4. Muon efficiencies for CT1-4 using default and updated simulated, averaged, mirror-degraded efficiencies, compared with the muon efficiency distribution from observations.

power-law spectrum with a spectral index of −2.6 to match observations. −2.6 is chosen instead of −2.7 to account for the presence of heavier nuclei in the data. This is compared to the third-brightest pixel distribution from data observation runs that pass the quality cuts described earlier and have a zenith angle within the limits: $> 15°$ and $< 25°$. The third-brightest distributions of the CT1-4 cameras are shown in Fig. 5.5. Prod2b5 is shown for CT2, CT3, and CT4, while Prod2b4 for CT1. The observations are selected to include CT5 in the trigger (telescope pattern 62). The telescope pattern refers to which telescopes can participate in the trigger. A summary of telescope patterns is found in Table 5.2.

Fig. 5.5 shows that the position of the rising edge using simulations and observation runs coincides after adjusting the mirror degradation in the simulations. The distributions' peaks are at similar locations, and overall, they are comparable in

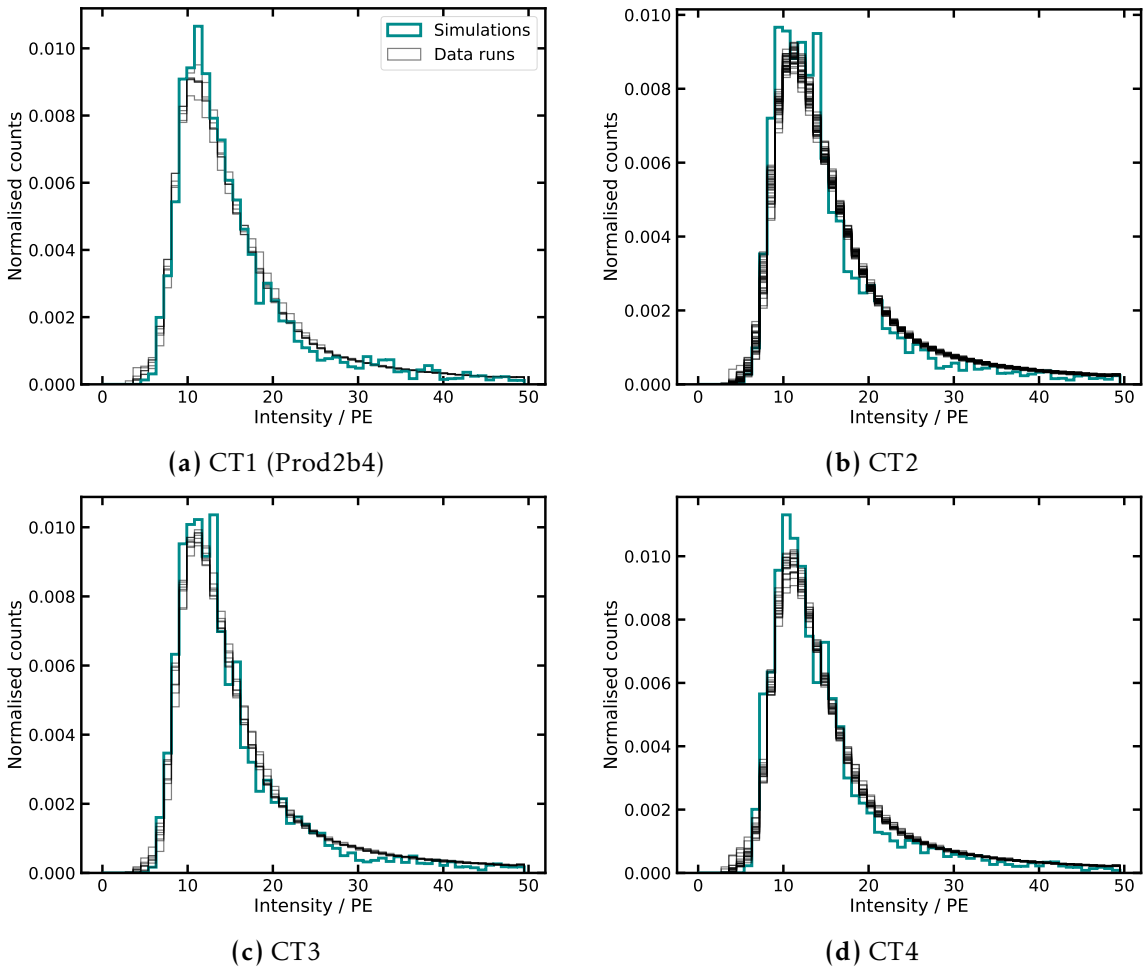

(a) CT1 (Prod2b4)

(b) CT2

(c) CT3

(d) CT4

Figure 5.5: Third-brightest pixel intensity distribution for CT1-4. CT2-4 are shown in Prod2b5 and only CT1 in Prod2b4. Telescope pattern 62. The black lines show the distributions of the data runs that pass the quality cuts. The distribution from simulations is also displayed.

shape. The distribution of CT1 for the Prod2b4 configuration is shown. Notice that these two phases only differ in the mirror degradation and, therefore, muon efficiency. The remaining telescope and atmospheric description parameters are equal.

5.1.5 *Trigger rate consistency*

The trigger rate of each telescope before any cuts are applied is a key quantity that enables checking whether the atmosphere, optical throughput, night-sky background, and trigger threshold are chosen appropriately in the simulations.

Telescope pattern	Description
30	Neither CT1 nor CT5, CT2-4
32	Every small telescope, CT1-4
60	CT1 is not available, CT2-5
62	All telescopes, CT1-5

Table 5.2: Description of telescope patterns for H.E.S.S. Four telescope patterns are highlighted: 30, 32, 60, and 62, which differ in the telescopes involved in the trigger.

As hadronic showers dominate the trigger rates, simulations of proton-induced showers provide a reasonable estimate of this rate after a correction factor is applied to account for heavier nuclei. The simulations do not offer time information of the arrival of each simulated shower; therefore, the trigger rates cannot be extracted directly (see [207]). However, simulated trigger rates can be calculated from folding the effective area (Aeff(E)), as a function of energy, with the cosmic ray flux (Φ(E)). The trigger rate of simulations is given by,

$$\mathrm{R}(E) = \mathrm{Aeff}(E) \times \Phi(E) \times a_{\mathrm{corr}}, \tag{5.1.3}$$

where $\mathrm{a_{corr}}$ is the correction factor that accounts for additional triggers from air showers induced by heavier nuclei. A predetermined value of $a_{\mathrm{corr}} = 1.34$ is used because simulating heavy nuclei is computationally expensive due to their higher kinetic energy and larger shower production. This factor has been verified in previous studies (see [207]).

Furthermore, the Global Spline Fit (GSF) model [212] is chosen to model the proton spectrum, as it accounts for the spectral features that do not follow a power law as compared to the simple power law approximation from the BESS experiment in 1998 [213]. GSF uses data from several instruments. The effective area of the simulations is computed as the ratio of events that triggered the array to the total number of simulated showers, multiplied by the simulated area. The effective area and, therefore, trigger rates are computed at multiple zenith angles. Simulations of Prod2b4 and Prod2b5 are compared separately with the observation runs for those two phases.

The trigger rate of data runs before any cuts is obtained from data runs from 100800 to 110340 for Prod2b4 and from 110340 to 124680 for Prod2b5. The evolution of the average trigger rate of CT2 before any ATC cut is shown in Fig. 5.6 for a mean zenith angle of $20° \pm 5°$. Four telescope patterns are represented. These

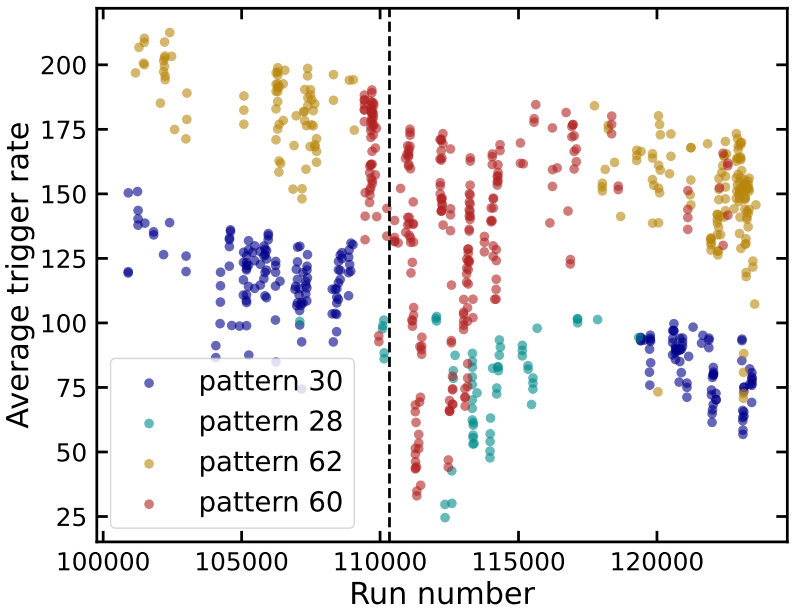

Figure 5.6: Average CT2 trigger rate before a cut on the ATC as a function of the run number in Prod2b4 and Prod2b5. Each run is coloured according to the telescope pattern.

are patterns 28, 30, 60, and 62. The trigger rate when CT5 is included (i.e., patterns 60 and 62) is higher than without CT5. The very low ATC values could influence some of these trigger rates. Therefore, for the following verification plots, a cut on ATC is done for ≥ 0.6 and ≤ 1.3). This way, outliers are rejected.

The total trigger rate is computed at multiple zenith angles from 0° to 60° in steps of 10° for simulations and from 10° to 50° for observations. The lack of sufficient observations at 60° and, often, at 0° makes it impossible to compare it with simulations. For each zenith angle, trigger rates of runs with a zenith angle within ±5° are included. As discussed in Section 2.2, the H.E.S.S. array multiplicity trigger works in a hybrid way. On one side, the array triggers on stereo events on all the small telescopes and CT5; on the other, it also triggers on mono events with CT5 only. For CT1-4, the participation trigger rate for each telescope is obtained from the H.E.S.S. database.

The resulting participation trigger rates before any cuts, as a function of zenith angle, are shown in Fig.5.7 for all small telescopes. The trigger rates from the CT1 data runs are compared with those from Prod2b4 simulations. However, the CT2-4 simulations are shown alongside Prod2b5 rates. This analysis shows that the trigger rates remain consistent across both observational phases after applying the muon efficiency corrections. Splitting the data into these two phases is essential, as

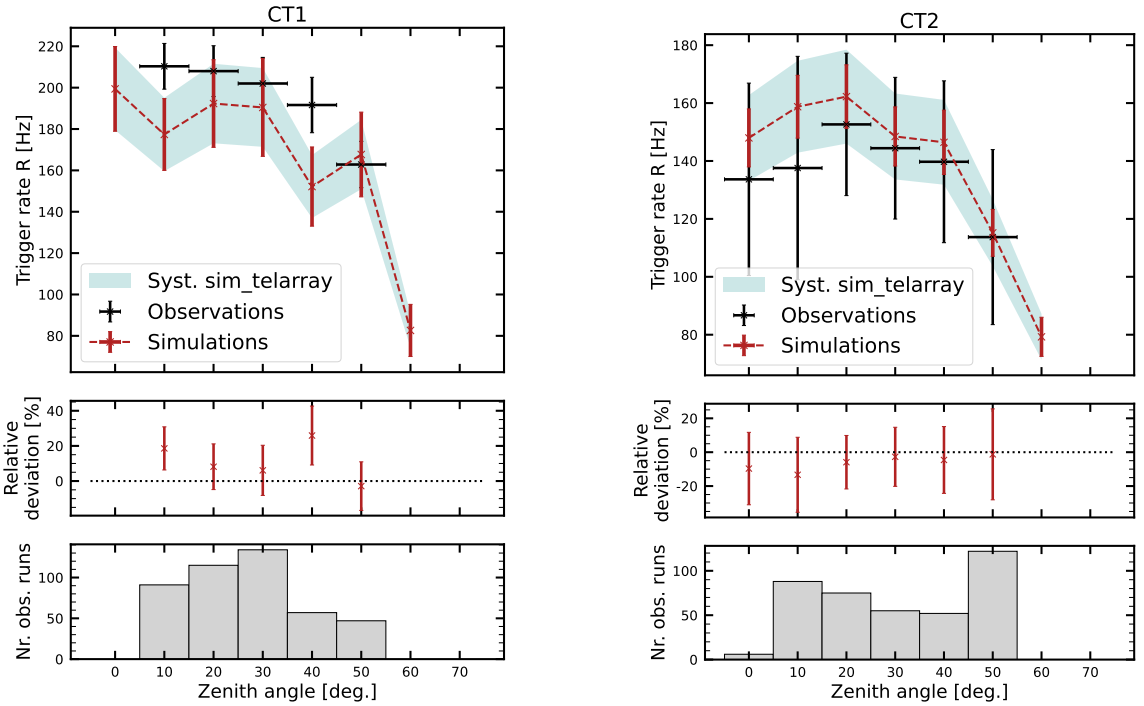

(a) CT1 (Prod2b4)

(b) CT2

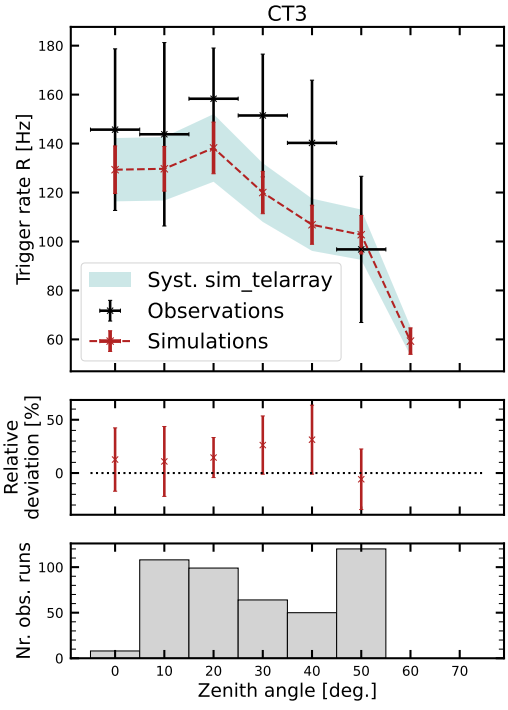

(c) CT3

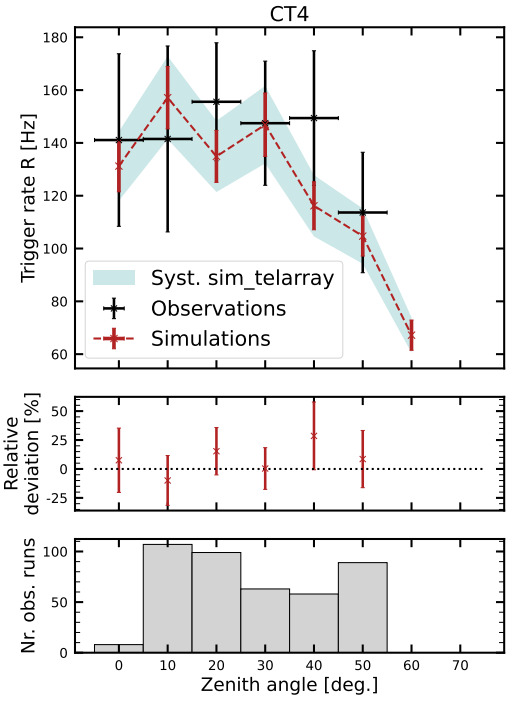

(d) CT4

Figure 5.7: Participation trigger rates of simulations and observations of CT1, CT2, CT3, and CT4 telescopes. Simulations are performed with the updated mirror-degraded efficiencies. A systematic uncertainty of 10% is assumed due to sim_telarray. The relative deviation in % between simulations and data is also shown, as well as the number of observations for each zenith angle.

differences in muon efficiency significantly affect the trigger rate. As shown here, the trigger rate of CT1 in Prod2b4, with a higher mirror-degraded efficiency, is considerably higher than that of the other telescopes in Prod2b5.
The systematic error is shown in Fig. 5.7 as an error band around the simulated points. Systematic errors are assumed to be 10% for the use of sim_telarray simulations, as reported by Konrad Bernlöhr. Overall, there is good consistency between simulations and data for the trigger rates after the changes in muon efficiency are introduced. The performance of CT2-4 in Prod2b4 is similar.

5.1.6 *Optical misalignments*

In this section, the validation of the telescope's optical PSF is described. The telescope mirrors focus the incoming light onto the focal plane, where the camera is installed. Because this focus is imperfect, techniques were developed to measure and quantify these imperfections. One approach is the use of starlight. For these measurements, the lid in front of the camera is closed. The light from a star is reflected by the mirror dish onto the camera lid, producing an image captured by a CCD camera pointing at the camera lid. Because the positions of the stars are known, they can be used to measure the camera's alignment relative to the mirror-pointing axis.
The optical PSF is validated using the ray-tracing package in sim_telarray. Light is simulated as coming from a point-like source, a star at almost infinite distance. The telescope is pointed at the reference star or close to it. The optical PSF is described by a 2D Gaussian fit centred on the star image. The resulting optical PSF for data (blue and orange dots) and simulations (black solid line) are shown in Fig.5.8 for CT1-4. Two sets of data points are shown. They comprise two periods: the pre-refurbishment and post-refurbishment periods. In between, the mirrors were coated and realigned, resulting in a different optical PSF. Therefore, simulations are compared separately to the two observation periods.
From Fig.5.8, it can be concluded that simulations and data generally match well. The observation runs do not deviate significantly from the simulated curve in any case or telescope.

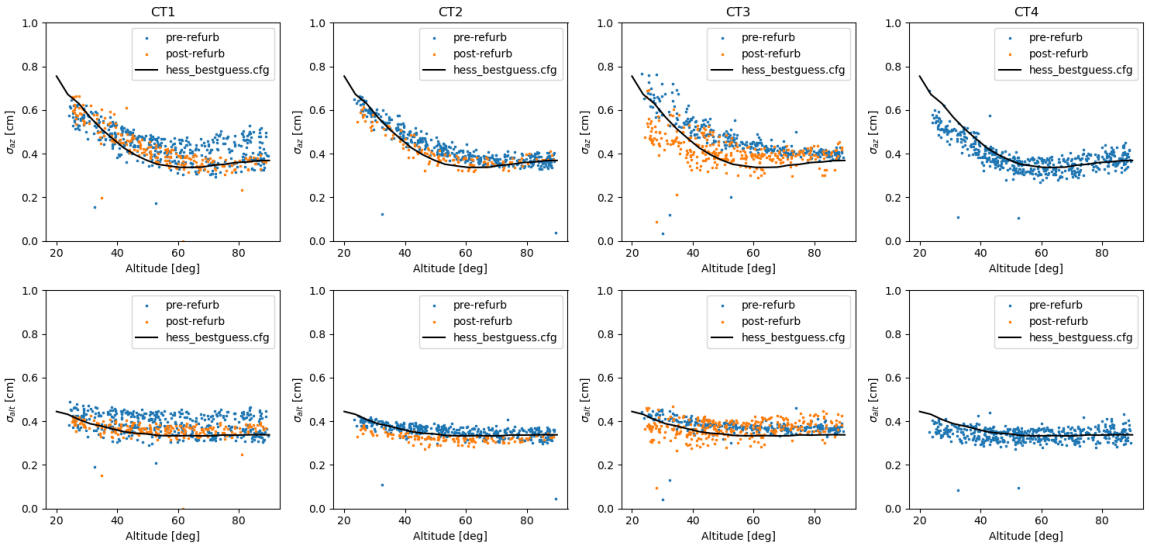

Figure 5.8: The optical PSF described as the x/y Gaussian fit for CT1-4 as a function of the altitude. The orange dots indicate observations after the mirror refurbishment, and the blue dots indicate observations before the refurbishment. The solid black lines show the optical PSF of the simulations. Provided by Gerrit Roellinghoff.

5.1.7 *Hillas parameters*

The consistency between observations and simulations must also be confirmed after image cleaning. The reconstructed images of each camera are cleaned with Tailcuts. The parameters for Tailcuts cleaning on CT1-4 cameras are 10 PEs and 5 PEs for the picture and boundary thresholds, respectively, and 0 neighbouring picture pixels (see Section 2.4.2).
The Hillas parameters (see Section 2.4.3) are computed in the same way for simulations of proton-induced showers and for data runs. The distribution is reweighted to a power-law spectrum with spectral index -2.6 to match the cosmic-ray spectrum, accounting for the effect of heavier nuclei. The simulations are run at a zenith angle of 20° and are compared to observation runs with similar zenith angles between 15° and 25°. Quality cuts are also applied in the number of broken pixels, run duration, and ATC, as described earlier.
The distribution of the Hillas length-to-amplitude ratio traces muons originating from high in the atmosphere. It is a valuable method for assessing the consistency of the atmospheric description between simulations and observations. Fig. 5.9 shows the distribution of the Hillas length over the Hillas amplitude. Fig. 5.9a shows the CT3 distribution when CT5 is not included in the trigger, which can be

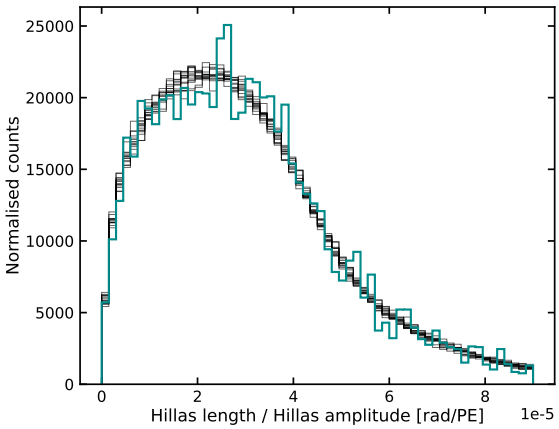

(a) CT3. Telescope pattern 30

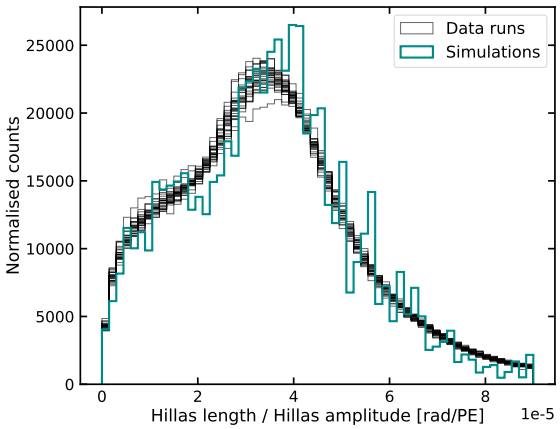

(b) CT4. Telescope pattern 62

Figure 5.9: Distribution of the Hillas length over the Hillas amplitude of data runs (black lines) using two of the small telescopes (CT3, CT4) and two telescopes patterns (30, 62). Simulations of proton showers at 20° are also included.

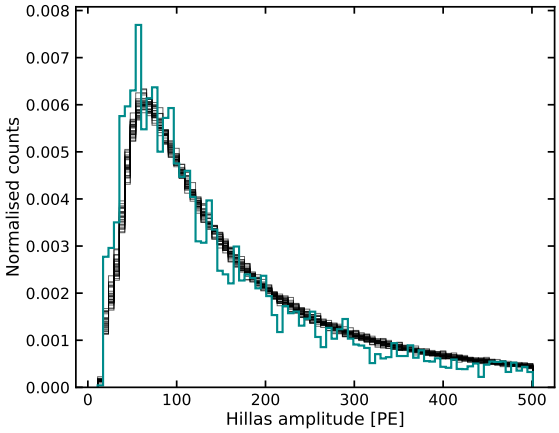

(a) CT4. Telescope pattern 30

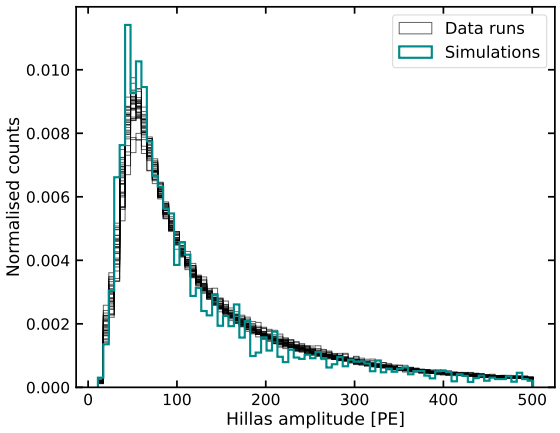

(b) CT2. Telescope pattern 62

Figure 5.10: Distribution of the Hillas amplitude of good quality observation runs (black lines) of two of the small telescopes (CT4, CT2) and two telescope patterns (30, 62). The corresponding distributions from simulations are also shown.

compared to Fig. 5.9b, which shows CT4 when CT5 is also triggering on events. Different telescope distributions are shown to demonstrate that, for all telescopes, observations and simulations match. All small telescopes have a similar Hillas distribution when the same telescope patterns are used.
It is evident that removing the large central telescope (CT5) results in the suppression of the prominent excess around 3 PEs to 4 PEs in Fig. 5.9a. As discussed in [211], this is because muons have a considerable Hillas length compared to the total light content [125], as reflected in Fig. 5.9b. The trigger on monoscopic events detected by one of the small telescopes is only possible when CT5 also triggers. As many muons trigger only on one telescope, including CT5 in the trigger significantly enhances muon detection in the small telescopes. In the absence of CT5, a significant suppression of muons is observed.
Fig. 5.10 shows the distribution of the Hillas amplitude. The Hillas amplitude can indicate potential discrepancies in the optical response between data and simulation. As before, the Hillas amplitude distributions with and without CT5 are compared. The distribution without CT5 (Fig.5.10a) is wider than the distribution with CT5 (Fig.5.10b). In both cases, simulations and data align closely.

5.2 Image cleaning for H.E.S.S. FlashCam

H.E.S.S. employs two main cleaning algorithms for noise removal: Tailcuts cleaning is typically applied to images from the small CT1-4 telescopes, whereas a DBSCAN clustering algorithm is used for events recorded by FlashCam [176]. The DBSCAN algorithm is similar to the one described in Section 3.2.7, but the second step of detecting pixels with high intensity even if they were not clustered is not included. Time-clustering methods improve the detection of low-amplitude pixels that Tailcuts would otherwise remove. Detecting these small clusters that would otherwise be cleaned away is especially crucial for the Algorithm for Background Rejection using Image Residuals (ABRIR) [214]. These secondary clusters are used by ABRIR to improve gamma-hadron separation.

	n_{hard} **[PE]**	$n_{\mathbf{noise}}$ $[\sigma_{\mathbf{noise}}]$	**minPts**	**d_scale [m]**	**t_scale [ns]**	**A [PE]**	**B [PE]**
Clustering	3	1	9	0.3	0.75	-	-
weighted Clustering	-	2.5	2	0.17	3.5	0	7

Table 5.3: Parameters for each H.E.S.S. image cleaning algorithm used and validated in this section.

Studies on image cleaning in H.E.S.S. [109] revealed that the clustering method on FlashCam CT5 images results in an enhancement of total intensity recorded with fewer lost signal pixels, resulting in a higher effective area and an improved angular resolution with respect to the default Tailcuts used in H.E.S.S. at the moment. Building upon this, the addition of weights, as in Section 3.2.5, improves the detection of small clusters with only a few pixels, which are typically rejected by this cleaning but are essential for gamma-hadron separation.
The optimised parameters of the unweighted clustering algorithm used in the following plots for comparison are obtained from [176], which optimises the cleaning methods based on the performance of the instrument response functions. The parameters of the default clustering method are those of TIME3D_1 as described in [176]. However, the parameters for the weighted clustering are not optimised; they are based on the parameter set defined in [109]. With respect to the original set of parameters, n_{noise} and minPts were reduced to enable the algorithm to identify smaller clusters.

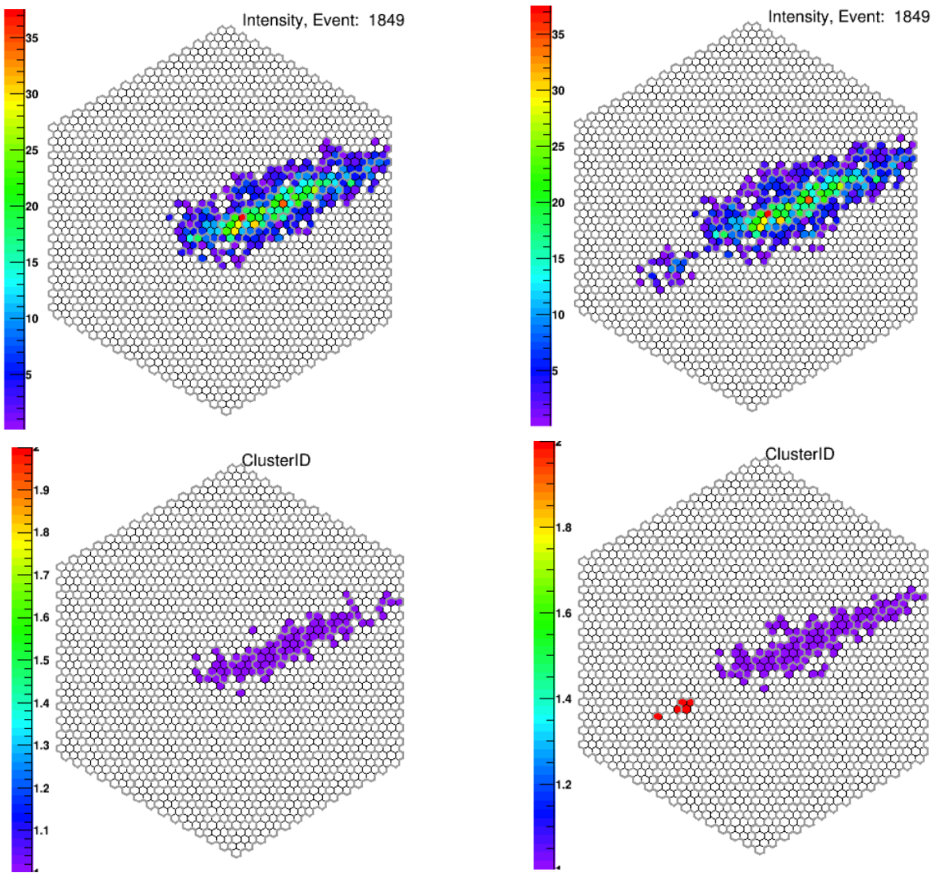

Figure 5.11: Example event selected from Crab Nebula observations with CT5. The left panel shows the intensity image (upper) and corresponding cluster IDs (lower) after cleaning with the default clustering method. The right panel shows the same event processed with weighted clustering. Figure provided by Helena Ren.

The parameters of the two cleaning methods that are being compared are shown in Table 5.3. The parameters A and B are described in Section 3.2.5, and the rest of the parameters are defined as in Section 3.2.1. n_{hard} is a hard cut in PEs on the minimum charge that a pixel should exceed to be input into DBSCAN. n_{noise} is also an intensity threshold, but with respect to the noise level (σ_{noise}).
Fig. 5.11 shows an example event generated by Helena Ren from FlashCam observations of the Crab Nebula. The weighted clustering algorithm detects small clusters with only a few pixels that unweighted methods miss, and generally identifies more pixels per cluster. These small clusters are important for ABRIR. Jelena Celic conducted high-level comparisons of the two cleaning methods. The results on effective area, angular resolution, and energy bias and resolution are shown in Fig. 5.12. For both cleanings, the instrument response functions are computed

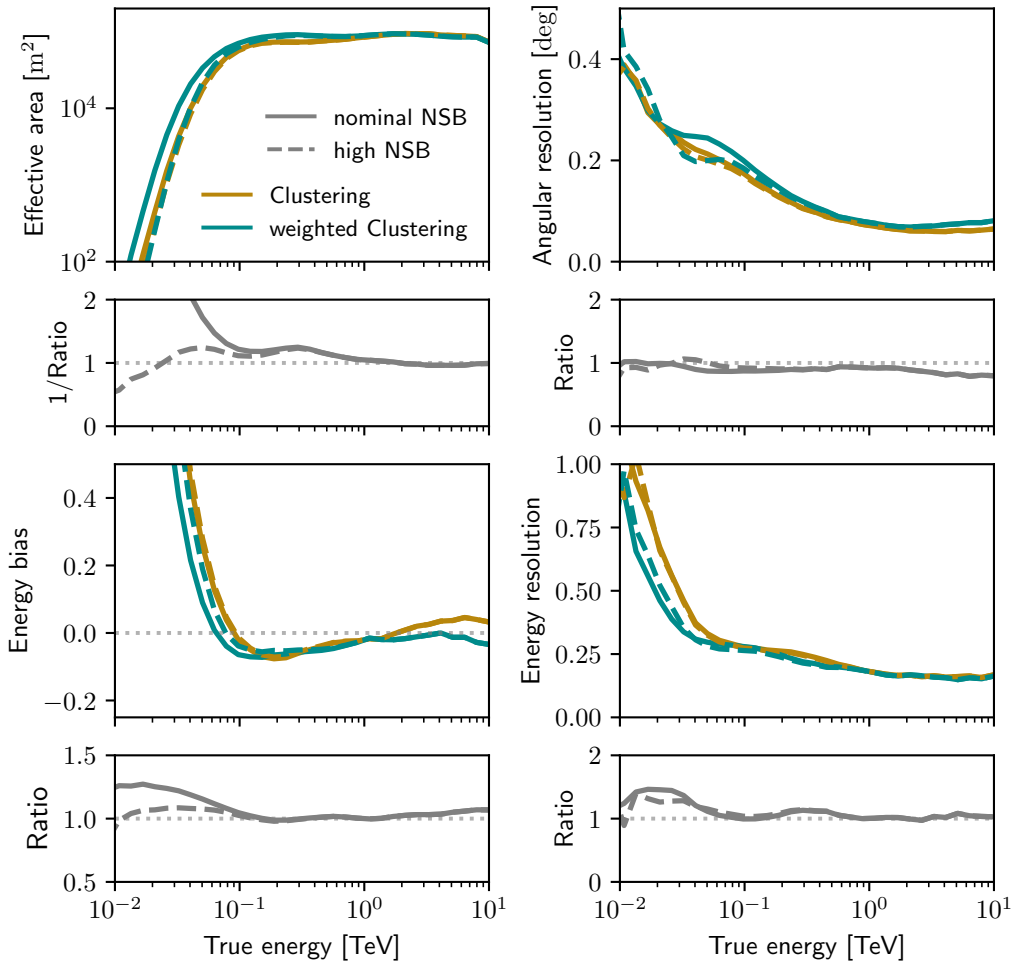

Figure 5.12: Instrument response functions of CT5 simulations using the weighted and unweighted image cleaning methods during reconstruction. Two NSB levels are compared: nominal (pedestal width of 1.65 PEs) and high (1.5 times the nominal). Curves provided by Jelena Celic.

using simulations. Two sets of simulations are conducted for the two NSB levels: nominal (with pedestal width 1.65 PEs [215]) and high (1.5 times the nominal NSB). IRFs are calculated only on events that trigger on CT5, ignoring CT1-4.
The IRFs (see Fig. 5.12) at nominal NSB show a better performance when weights are included. This is clearly evident in the ratios between the unweighted and weighted cases. The effective area at low energies is significantly better when weights are added, as well as the energy reconstruction (both resolution and

bias). However, the angular resolution is very similar. At high NSB, the weighted clustering method loses significant effective area with respect to nominal NSB to a point where it coincides with the curve of the unweighted method at nominal NSB. On the other hand, the unweighted clustering method is much more robust to NSB, and the effective areas at the two NSB levels overlap. Overall, energy reconstruction is improved by weighted clustering, even at high NSB, but angular resolution is slightly worse between 0.03 and 0.1 TeV.

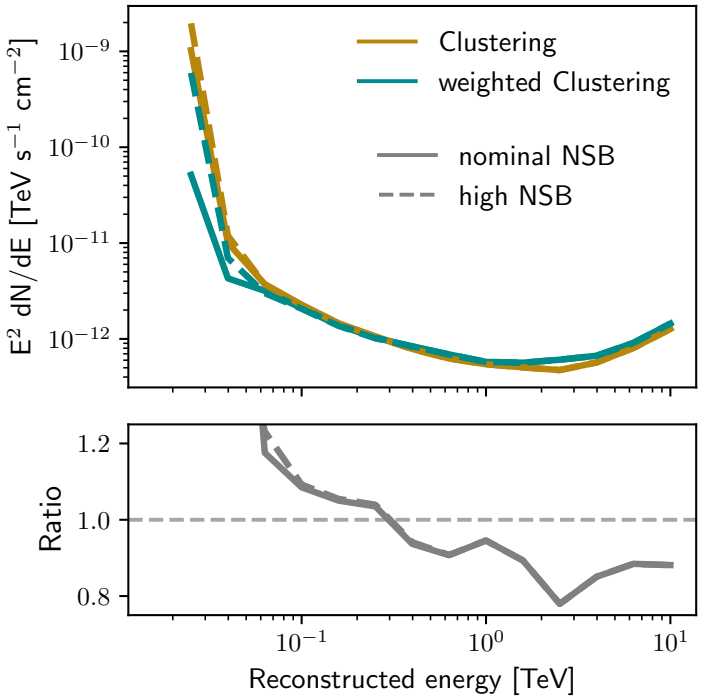

Figure 5.13: Sensitivity curves of H.E.S.S. CT5 FlashCam after applying two image cleaning methods: the weighted and unweighted time clustering algorithms. The nominal and high NSB levels are evaluated. Curves provided by Jelena Celic.

The sensitivity curve (see Fig. 5.13) shows that weighted clustering achieves significantly higher sensitivity at low energies (< 0.3 TeV), but at higher energies the weights slightly degrade sensitivity. The same tendency is seen for both nominal and high NSB. The sensitivity curves at high NSB are worse than at nominal NSB. This is especially noticeable at low energy levels when using weighted DBSCAN.

5.3 Summary and outlook

The H.E.S.S. I telescope simulations were validated through end-to-end verification using observation runs that span two phases, each with a different muon efficiency. First, the muon efficiencies during Phase2b4 and Phase2b5 were evaluated; as a consequence of this analysis, the mirror-degraded efficiencies of all telescopes were reduced. The following tests, using the updated mirror reflectivities, showed that the simulations are consistent with observations.

The evaluation of trigger rates showed a reduction when transitioning from Prod2b4 to Prod2b5, attributed to a decrease in mirror reflectivity. Trigger rates are overall consistent. The trigger threshold was validated with the intensity distribution of the third-brightest pixel. Finally, the effect on the Hillas parameters was assessed, demonstrating that simulations accurately reproduce the hadronic background, the atmospheric model, and the optical throughput. This study can be extended to the full H.E.S.S. I era, maintaining the validity of the trigger-response. Careful adjustment of the mirror reflectivity in simulations could enable expansion to the full 12-year time span.

The second part of this section focused on improving CT5 image cleaning by introducing charge-dependent weights into the DBSCAN clustering. This development was motivated by the weighting studies presented in Section 3.2.5. The IRFs obtained with weighted cleaning showed a clear improvement in performance. The use of weights in DBSCAN is beneficial for ABRIR and could be applied to datasets with NSB values very close to the simulated NSB to improve overall sensitivity. However, it cannot be used for robust reconstruction across a broader range of NSB conditions.

6

H.E.S.S. ANALYSIS OF RX J1713.7-3946

The supernova remnant RX J1713.7-3946 ranks among the brightest gamma-ray sources in the Galaxy. Despite multiple attempts to explain the particle composition and acceleration mechanisms, no consensus exists on the nature of the high-energy particles within the remnant. While electron acceleration appears well established, the contribution of protons to the gamma-ray emission remains unconfirmed, as discussed in Section 1.5.1. Given the scientific importance of this source, the H.E.S.S. array began observing RX J1713.7-3946 early in its operational phase. A previous H.E.S.S. paper from 2018 [67] reported gamma-ray emission outside the X-ray contours, interpreted as particles escaping the shock front. However, the results neither confirmed nor excluded a hadronic origin for the observed gamma-ray emission.
This chapter and the following present a new preliminary analysis of RX J1713.7-3946, aimed at addressing two key questions: the nature of particle acceleration within the remnant and the origin of the gamma-ray emission escaping the shock front. The H.E.S.S. analysis was performed entirely by the author of this thesis, with some components independently verified by Quentin Remy. All plots in this chapter were produced by the author. The analysis is performed with *gammapy* following the methods described in Section 2.5.

6.1 H.E.S.S. observations

The supernova remnant RX J1713.7-3946 is analysed in this thesis using previously published datasets recorded between 2004 and 2016 with the original cameras of the CT1-4 telescopes (see Section 5). No further observations were conducted following the cameras upgrade in 2016. CT5 itself was not included in these

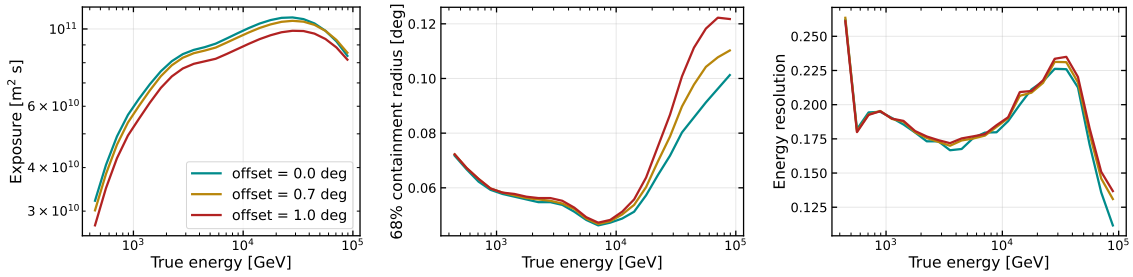

Figure 6.1: Instrument response functions of the H.E.S.S. observations used in the analysis of RX J1713.7-3946. The exposure (m^2s), 68% containment radius, and the energy resolution are shown at three different offsets: 0°, 0.7°, and 1.0° as a function of the true energy.

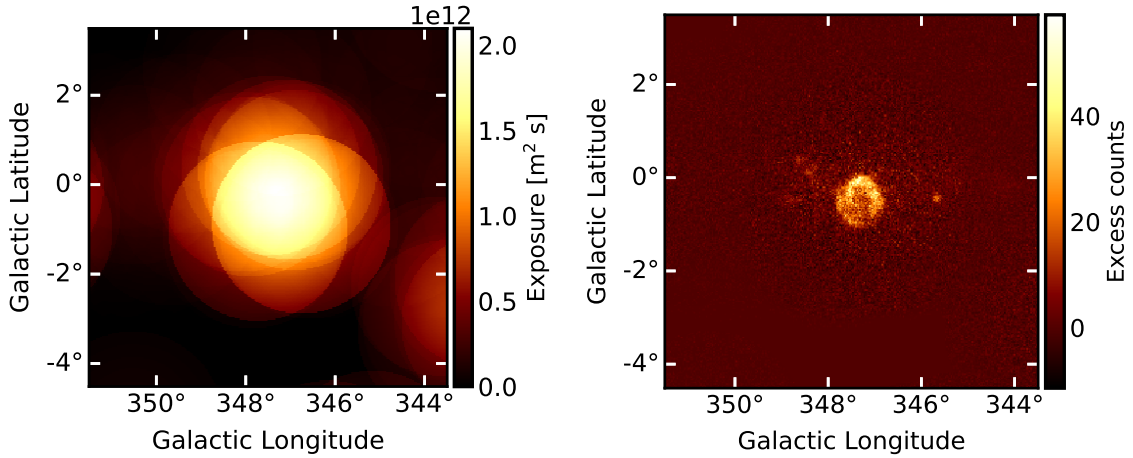

Figure 6.2: The exposure map (on the left) and the excess counts map (on the right) in the RX J1713.7-3946 region using H.E.S.S. data with energy > 500 GeV.

observations. The trigger condition requires at least three telescopes to register an event, ensuring that stereoscopic observations are obtained. Event reconstruction is performed using ImPACT (see Section 2.4.4). Quality selection criteria include: zenith angle below 65°, quality flag "zero", and offset below 2°. The offset denotes the angular distance between the telescope pointing and the source. The quality flag "zero" indicates that observation runs pass selection cuts based on weather conditions, hardware status, observation stability, etc.

The resulting event lists and IRFs are binned into spatial maps with a pixel size of 0.03° and a binned energy axis, for reconstructed energies > 500 GeV. The datasets considered in this analysis have been used previously for the second H.E.S.S. Galactic Plane Survey (2HGPS) [216]. The exposure, angular resolution at 68% containment, and the energy resolution of the H.E.S.S. observations are shown in Fig. 6.1 as a function of the true energy for three different offset angles: 0.0, 0.7,

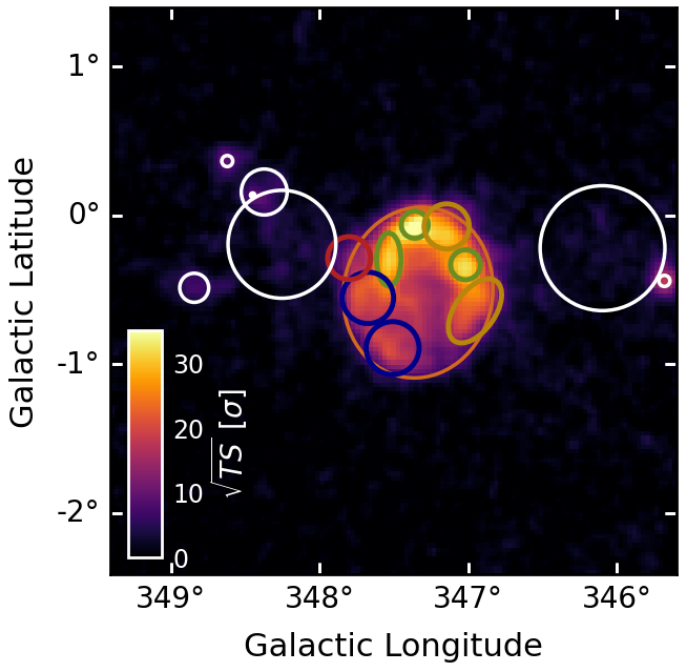

Figure 6.3: Source candidates in the vicinity of RX J1713.7-3946 and inside the remnant obtained by the 2HGPS catalogue. Sources in white are outside the remnant, and sources within are highlighted in different colours and grouped by spectral similarity.

and 1.0 deg. The IRFs are obtained with *gammapy*. The exposure is the effective area of the array multiplied by the observation time. As the offset increases, the exposure also increases slightly. However, smaller offsets result in better angular resolution at high energies.
The excess count map and exposure map around the location of RX J1713.7-3946 are shown in Fig. 6.2. The excess counts map shows the number of gamma-ray events after subtracting the estimated background. The background is modelled with a field-of-view (FoV) background model [135]. On this map, the supernova remnant is clearly visible at the centre as an extended source. The exposure as seen in Fig. 6.2 (left) is concentrated on the middle of the map where the remnant is located.

6.1.1 *Source candidates from the H.E.S.S. catalogue*

2HGPS provides a model to describe all the Galactic emission detected by H.E.S.S. up to 2019. The source models from the catalogue are used as a starting point for the analysis.

Within the RX J1713.7-3946 region, several significant objects are considered in order to model the complex morphology of the SNR as shown in Fig. 6.3. Background sources located outside the remnant are highlighted in white, while substructures inside the remnant are colour-coded according to their spectral similarity, as shown later. The spatial distribution of these objects is modelled using the *gammapy* Generalised Gaussian spatial model[1], defined as:

$$\phi(r) = N \times \exp\left[-\left(\frac{r}{r_0}\right)^{1/\eta}\right], \tag{6.1.1}$$

where r is the angular distance from the source centre and r_0 is the characteristic radius of the source. N is the normalisation constant. The parameter η controls the shape of the distribution: $\eta = 1/2$ produces a Gaussian distribution, $\eta = 1$ yields a Laplace distribution, and $\eta \to 0$ results in a disk-like structure.

6.2 The morphology of RX J1713.7-3946

RX J1713.7-3946 is a bright, extended source observed by H.E.S.S. with very high significance, exhibiting complex internal morphology. Remarkably, the morphology remains largely consistent across the energy range to which H.E.S.S. is sensitive, as shown in Fig. 6.4 for three energy bands: 0.5 – 2.5 TeV, 2.5 – 10 TeV, and > 10 TeV. Although the significance decreases considerably above 10 TeV, the source remains detectable and above 5σ. Similar features are observed across all energy ranges: the shell structure is visible throughout the spectrum, and the internal morphology shows consistent intensity peak positions.

The remnant's morphology broadly correlates with X-ray observations. However, notable differences emerge in Fig. 6.5 (left), which shows the significance map of gamma-ray excess using H.E.S.S. data with superimposed X-ray XMM-Newton (1-6 keV) contours. The most prominent difference is excess emission beyond the X-ray contour boundaries, previously identified in the 2018 H.E.S.S. paper [67]. While the square root of the X-ray template matches the H.E.S.S. morphology (Fig. 6.5, right) better, it still fails to fully capture the spatial features. Fitting H.E.S.S. observations with the X-ray spatial template yields unreliable results with highly significant residuals. These discrepancies may indicate that the acceleration mech-

[1] https://docs.gammapy.org/2.0/user-guide/model-gallery/spatial/plot_gen_gauss.html

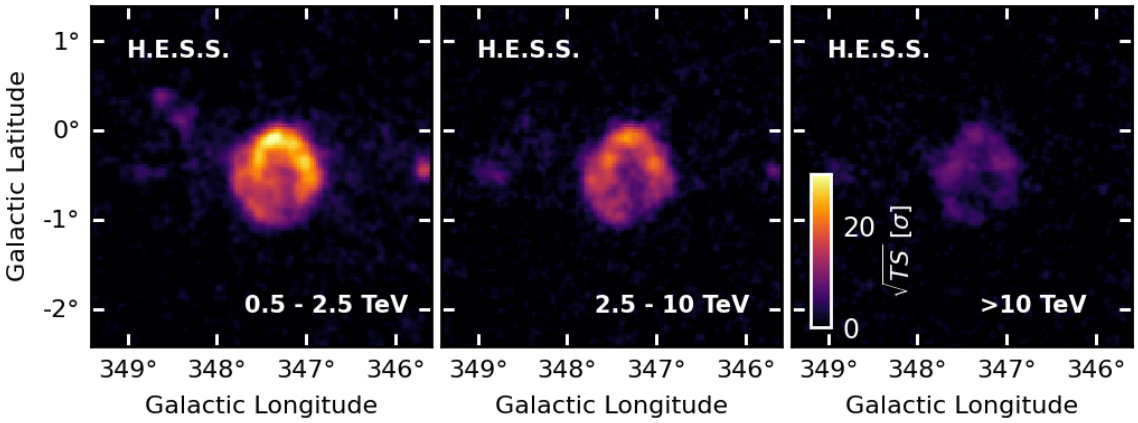

Figure 6.4: Significance maps of the RX J1713.7-3946 region using H.E.S.S. data divided into three energy bands: 0.5 – 2.5 TeV, 2.5 – 10 TeV, and > 10 TeV from left to right.

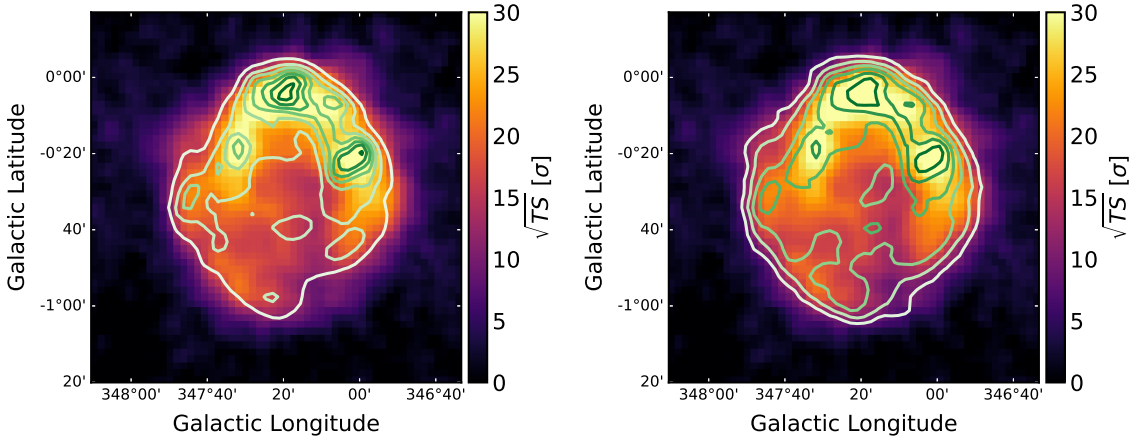

Figure 6.5: RX J1713.7-3946 significance map for the full energy range (> 500 GeV) of H.E.S.S. observations with the X-ray XMM-Newton (1-6 keV) contour lines superimposed using the unmodified template (left) and the square root of the template (right). The template was provided by Fabio Acero. The X-ray contours are convolved with the H.E.S.S. PSF.

anism is not solely leptonic but also involves proton interactions leading to π^0 decays.

6.3 Spectral energy distribution inside the SNR

The energy spectrum across the remnant is studied using different spatial models. First, the spectrum is evaluated separately for the western and eastern halves of the remnant, revisiting previous work by the collaboration [67]. Second, the spectrum is analysed for each substructure identified within the remnant by the 2HGPS.
In both cases, all background components are accounted for. The energy spectrum of every resolved background source outside the remnant (white regions in Fig. 6.3) is modelled with a log-parabola, as in Equation 2.5.6. The parameters of the spatial models are frozen to the values given by the 2HGPS, and the spectrum is left free. An important background contribution to the H.E.S.S. dataset is diffuse Galactic gamma-ray emission, which arises from interactions between cosmic rays and the interstellar gas and radiation fields. This background is particularly significant for sources located in the Galactic plane, where the interstellar gas density is higher, as is the case for RX J1713.7-3946. An interstellar emission model (IEM) from the H.E.S.S. catalogue is fitted to the data. The IEM is computed using the HERMES code [217]. As described in [99], the IEM-varmin rescaled diffuse model is used. The normalisation parameter is left free to account for potential variations of the model at smaller spatial scales, as it was originally fitted over a larger region of the catalogue.

6.3.1 *Western and Eastern halves*

The morphology of the remnant indicates two distinct regions: the western and eastern halves. The western half is denser and brighter and, as discussed in Section 1.5.1, correlates with the presence of molecular clouds, which could indicate proton-proton interactions [70]. There is a paucity of molecular clouds in the eastern region, along with lower magnetic fields [67] and densities. Therefore, a logical way to split the remnant is by fitting the spectrum of the two halves of the remnant separately. The exact split is shown in Fig. 6.6.
The spectral shapes of those two sides of the remnant are extracted and compared in Fig. 6.7 using the previously described H.E.S.S. observations. The spectral

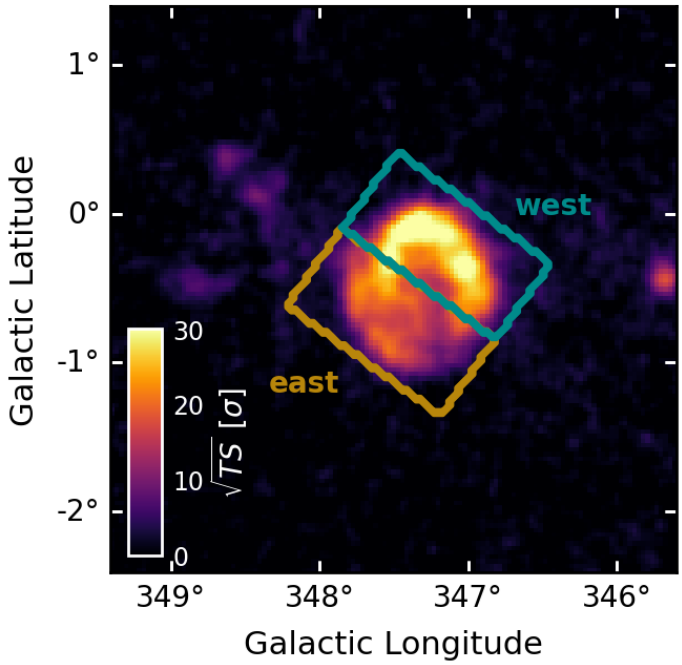

Figure 6.6: Significance map of the RX J1713.7-3946 region using H.E.S.S. data with energy > 500 GeV with the two sides (east and west) of the remnant marked.

model is assumed to be an exponential-cutoff power law, as given in Equation 2.5.5. The spatial models of the two sides are computed by taking the spatial contours of the extended source map describing RX J1713.7-3946 from the Fermi-LAT fourth Galactic catalogue (4FGL) [218] and convolving those with the east and west regions highlighted in Fig. 6.6. The 4FGL catalogue is public and available in *gammapy*[2].

The spectral shape of the two sides is described by the best-fit parameters shown in Table 6.1. The table presents two fitting scenarios: one in which the spectral index, lambda, and alpha vary independently across the east and west halves, and another in which these parameters are constrained to be identical on both sides (with only the amplitude allowed to differ). To assess whether the east and west sides differ significantly, two hypotheses are compared: Hypothesis 0 ($\mathcal{H}_0$), assuming that the spectral index, lambda, and alpha are identical for both halves, and Hypothesis 1 ($\mathcal{H}_1$), allowing these parameters to vary independently. $\mathcal{H}_1$ is only preferred over $\mathcal{H}_0$ by 1.4σ, indicating no significant spectral difference between the two halves. This is consistent with previous studies. The two regions may be too large, and

[2] https://docs.gammapy.org/2.0.1/user-guide/model-gallery/spatial/plot_template.html

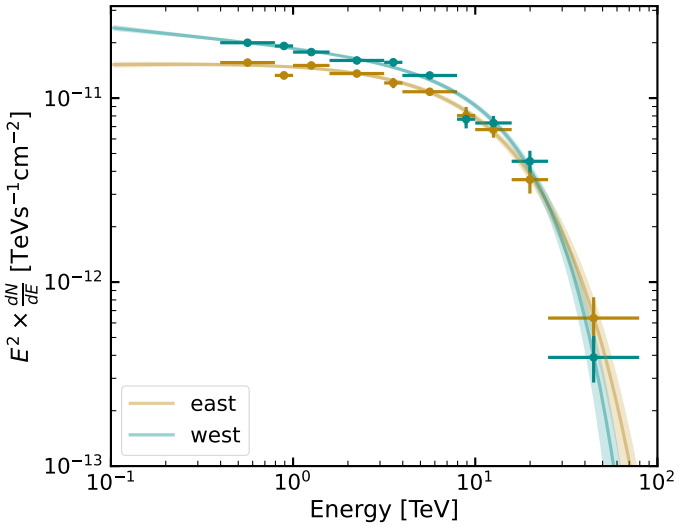

Figure 6.7: Resulting spectral models from fitting an exponential cutoff power law to both the east and the west sides of the remnant. The flux points are shown together with the solid lines, which represent the best-fit models. The shaded area shows the models' errors.

spectral differences within each region may be averaged out, thereby obscuring those differences. Therefore, spectral differences can be further investigated by subdividing the remnant into smaller components.

	index	**lambda (TeV^{-1})**	**alpha**
east	1.983 ± 0.015	0.074 ± 0.004	0.986 ± 0.053
west	2.103 ± 0.017	0.059 ± 0.004	1.295 ± 0.120
together	2.051 ± 0.044	0.064 ± 0.010	1.147 ± 0.188

Table 6.1: Fit results of the power law spectral model with an exponential cutoff to the eastern and western halves of the remnant. Two scenarios are shown: parameters varying independently on the east and west sides, and parameters constrained on both sides (together). In the latter, the amplitude of each half is allowed to differ.

6.3.2 *Components of the catalogue*

A novel analysis approach is employed to identify spectral variations within the remnant by examining overlapping components from the H.E.S.S. catalogue. The high detection significance achieved by H.E.S.S. enables detailed investigation of small-scale sub-structures within the remnant. The spectrum of regions outside the remnant remains free, as before. The spectrum of each object from the catalogue is

modelled with a log-parabola from Equation 2.5.6. The α and β parameters are free in the fit with limits of $[0,5]$ and $[0,1]$, respectively, along with the amplitude. The diffuse model is included in the fit.

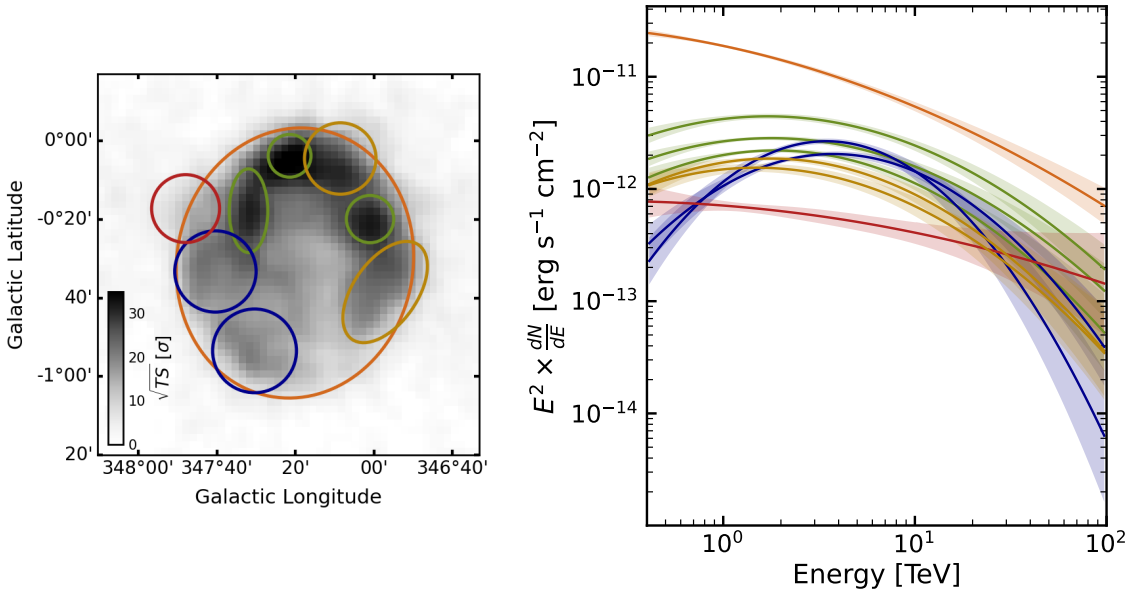

Figure 6.8: Spectrum of each object from the second H.E.S.S. catalogue inside RX J1713.7-3946. The spectral model within each component highlighted in the left plot (the significance map) is fitted, yielding the right plot. This figure shows the spectral shapes of all regions, coloured by similarity. The fit is performed using a log parabola spectral model.

Fig. 6.8 shows the resulting spectral shape of each component inside the SNR. The left plot displays the significance map, with contours indicating the radius of each object, while the right plot shows their spectra, coloured by spectral similarity. A large component covering the entire remnant overlaps with all other components within it. Its spectrum, which exhibits the highest flux, is also shown in Fig. 6.8. Spectral differences are observed across the remnant. The small red component in the outer part of the remnant exhibits a distinct spectrum modelled by a simple power-law with index 2.3 ($\beta = 0$). The dark blue components, in contrast, exhibit a hard low-energy spectrum ($\alpha \simeq 1.4$) and strong curvature (β) between $0.4 - 0.5$. All objects in the western region have similar spectral properties: less pronounced curvature than the blue regions and larger α values of around 1.9. In all cases, lower-energy data points are required to further constrain the fit parameters.

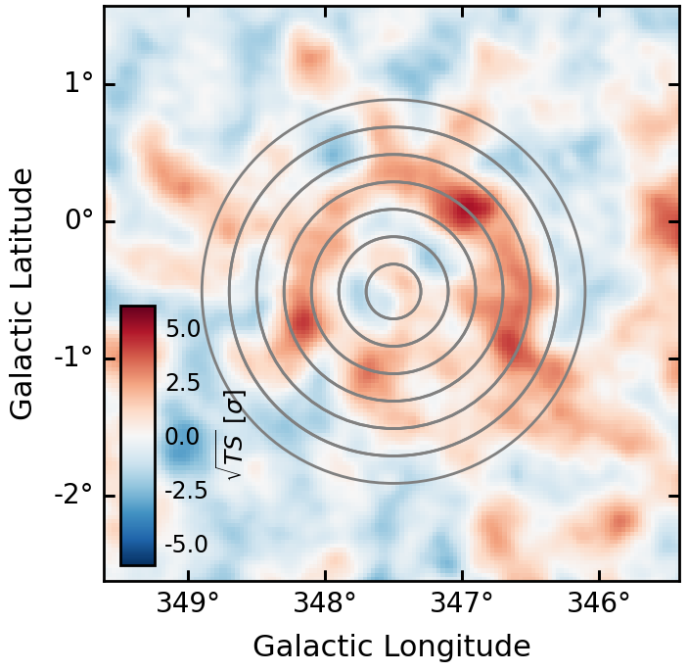

Figure 6.9: Significance map in the region of RX J1713.7-3946 using H.E.S.S. data. The significance map is computed by subtracting all best-fit background models and models inside the remnant. Therefore, this figure shows the residual of the fit in Section 6.3.2. Concentric annuli of width 0.2° are superimposed on the significance where the excess flux is computed.

6.4 Emission outside the remnant

All previous analyses yield residuals after fitting that show a distinct and significant excess ($> 5\sigma$) surrounding the remnant's position. The significance of this excess after fitting all other components of the map is studied in this section. The excess flux around the remnant is quantified as a function of radius from the centre, using seven consecutive full rings of width 0.2°, as shown in Figure 6.9, which also shows the highly significant residuals observed outside the remnant.
Fig. 6.10 shows the corresponding radial flux profile computed with the *gammapy* function `FluxProfileEstimator`[3] for three energy bands. In the 0.5–1.0 TeV band, the excess flux is prominent for the two rings centred at radii 0.6° and 1.0°. The surrounding rings show no significant negative or positive residual flux. At higher energies, 1.0 – 10 TeV, an excess flux is observed in the same concentric rings as for the previous energy band, but with a lower excess flux. At energies > 10 TeV, no

[3] https://docs.gammapy.org/2.0.1/api/gammapy.estimators.FluxProfileEstimator.html

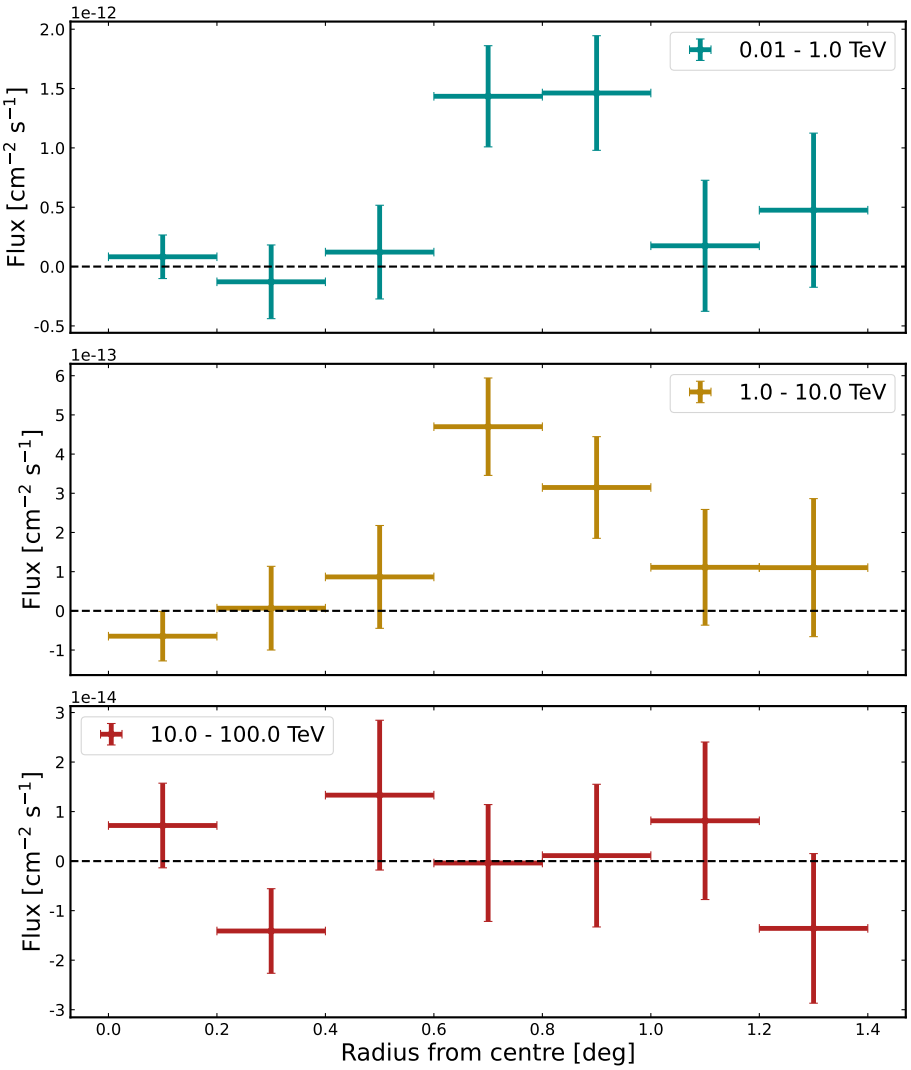

Figure 6.10: The radial flux profile of the residuals is computed after fitting the remnant with the 2HGPS components and all background models. The flux is calculated inside consecutive concentric annuli centred on the remnant, each with a radial width of 0.2°.

significant excess flux is observed outside the remnant. The negative flux centred at 0.3° could be the result of overfitting that attempts to compensate for the leak excess not accounted for in the fit.

The residual map after fitting the remnant without accounting for the leak emission is shown in Fig. 6.11. Based on preliminary studies of this region by Marianne Lemoine-Goumard with Fermi-LAT, the spatial template for the leak is highlighted in Fig. 6.11 (left). It is a half-ring that covers the most significant part of the leak around the western half of the remnant, extending radially from 0.55° to 1.2°. The gamma-ray emission is studied across the full spatial template of Fig. 6.11 (left)

and in two separate subregions to account for spatial variations in significance and spectral properties with increasing distance from the remnant. Hence, the original spatial template is divided into two smaller regions, each with half the original's width. The inner and outer parts are shown in the centre and right plots of Fig. 6.11, respectively.

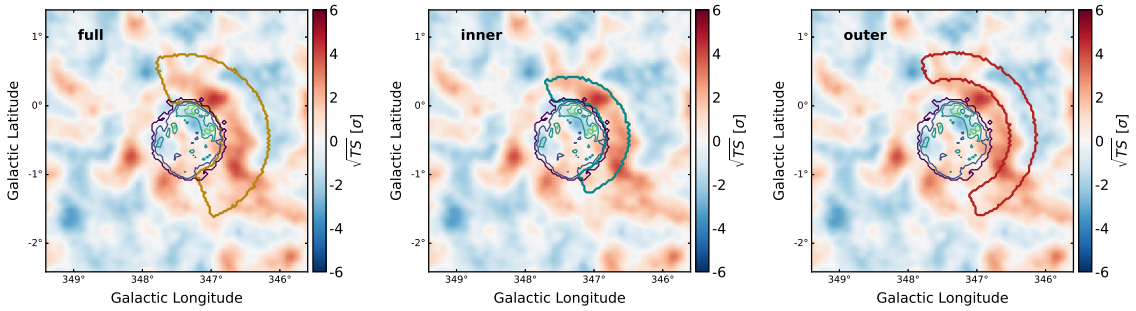

Figure 6.11: Three spatial templates used in the modelling of the leaking emission outside the remnant. The first figure shows the Fermi-LAT template used to account for the excess observed by this instrument. The other two templates are the inner and outer halves of the Fermi-LAT spatial template. The X-ray contours are marked in all three maps.

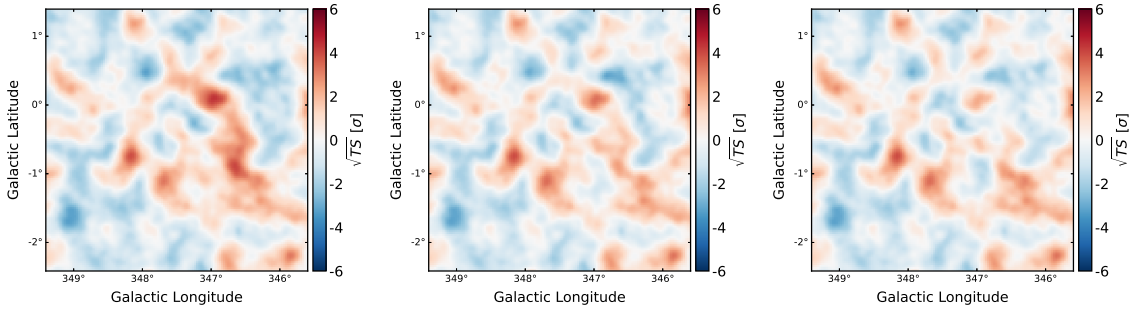

(a) Baseline **(b)** Full layer **(c)** Inner and outer layers

Figure 6.12: Residual maps using H.E.S.S. dataset fits after fitting different spatial models for the leak. The left plot shows no fit to the excess; the middle plot shows a fit using the full spatial template of the leak, as described in the text. The right plot shows the residual significance map after fitting the excess separately in the inner and outer regions to account for spectral changes in the emission.

The gamma-ray emission spectrum outside the remnant is investigated by including a model for the leak, assuming a simple power-law spectrum. The spatial region of the leak is fitted using either the full template or the inner and outer regions separately in the same fit. Fig. 6.12 shows the resulting residuals comparing different spatial region configurations to the baseline case (a). The middle panel

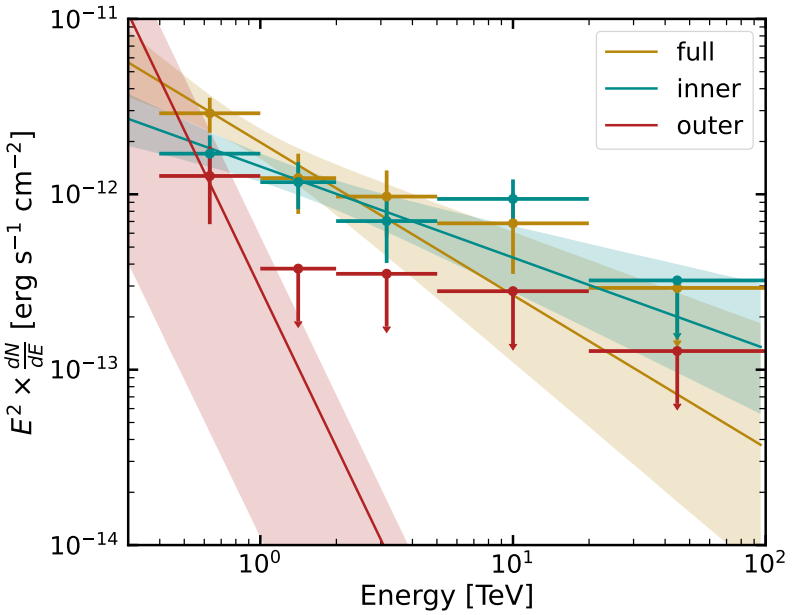

Figure 6.13: Best-fit spectral model of the leak assuming three different spatial templates: full, inner, and outer regions. Both the inner and outer spatial templates are included in the same fit but are fitted separately. All layers are modelled with a power-law spectral model. The flux points of each region are also shown. The solid line shows the best-fit model, and the shaded area shows the model's error.

shows the residuals when modelling the leak with the full spatial template (see Fig. 6.11, left), which improves upon the left panel but exhibits slight overfitting: marginally positive residuals in the inner region and marginally negative residuals in the outer region. The right panel shows the best-fit residuals when the inner and outer regions of the leak are modelled separately. Positive residuals remain outside the eastern half of the remnant, suggesting that the leakage forms a complete ring around the SNR. Future work will investigate a full-ring model.

Fig. 6.13 shows the resulting spectrum of the full spatial template alongside the spectra of the inner and outer regions when fitted together as an alternative to the full template. Flux points are also shown and are extracted as discussed in Section 2.5.4. The flux points of the full and inner regions of the leak are similar and overall compatible, yielding spectral indices of 2.871 ± 0.35 and 2.519 ± 0.20, respectively. The fit error in the inner region is significantly lower than in the full region. The outer ring of the leak shows a single flux point that coincides with the inner region, suggesting that the best spatial model to account for the significant emission from the leak extends slightly beyond the inner region, but not to the full region's maximum extent. At high energies > 1 TeV, the outer layer

becomes less significant. The detection significance of the inner and outer layers is computed by comparing two hypotheses. $\mathcal{H}_0$: Either only the inner or the outer model is included in the fit. $\mathcal{H}_1$: Both the inner and outer models are included. The significance of the emission in the inner layer is 5.74σ, while it reaches only 1.76σ in the outer layer. The significance of the full model is computed in a similar way and gives 5.20σ.

6.5 Summary and outlook

RX J1713.7-3946 exhibits complex internal morphology, with western and eastern regions that, despite apparent morphological differences, show no significant spectral variation. To avoid averaging out potential spectral differences over large areas, the remnant is further subdivided into multiple smaller regions. This subdivision follows a systematic approach based on substructures identified in the 2HGPS catalogue. Analysis of these substructures reveals interesting spectral differences that require additional low-energy constraints to better understand the particle acceleration processes responsible for the gamma-ray emission in each substructure.

Previous H.E.S.S. publications [67] hinted at gamma-ray emission outside the remnant, interpreted as particles escaping the shock. In this section, this external emission has been demonstrated to be significant and to decrease with increasing distance from the centre of the remnant. The leak has been modelled with a power-law spectrum. Therefore, the leak emission shows a significantly different spectrum from the spectra of the components inside the remnant. However, lower-energy data are essential for determining whether an energy break is present, thereby distinguishing between leptonic and hadronic emission scenarios. In the next chapter, a joint analysis combining the H.E.S.S. datasets described here with Fermi-LAT observations will be performed to investigate the nature of this emission.

Future H.E.S.S. analysis can be improved by incorporating algorithms described in this thesis that were tested on the CTAO but remain applicable to H.E.S.S.. The high-energy region could benefit significantly from the method described in Section 3.3. The author is currently implementing and testing this algorithm on the H.E.S.S. data analysis chain. Furthermore, the improvements in simulation-data

consistency and image cleaning for H.E.S.S. presented in Chapter 5 will enhance the event reconstruction and sensitivity of the array.

7

JOINT ANALYSIS OF RX J1713.7-3946

This chapter presents a joint analysis of the supernova remnant RX J1713.7-3946 using the previously analysed H.E.S.S. data (Chapter 6) together with Fermi-LAT observations. The study was motivated by a reanalysis of Fermi-LAT data by Marianne Lemoine-Goumard, which revealed highly significant gamma-ray emission outside the remnant. At this location, H.E.S.S. also detects a significance larger than 5σ, with an energy spectrum consistent with a simple power law. This new joint analysis examines the nature of particle emission from the remnant. It also presents the spectral differences within the remnant from east to west.
Building on complementary findings from the individual analysis of Fermi-LAT and H.E.S.S., the author performs a joint analysis combining data from both instruments. All results presented in this chapter are preliminary and were obtained by the author. Additionally, Marianne Lemoine-Goumard conducted an alternative analysis that yielded consistent results with those presented in this chapter. The Fermi-LAT datasets were provided.

7.1 Fermi-LAT observations

The joint analysis of H.E.S.S. and Fermi-LAT uses data from the LAT detector on board the Fermi satellite (see Section 2.7.1). The data were recorded between the years of 2008 and 2024. The events for each observation were reconstructed using the updated Pass 8 analysis, which incorporates improved reconstruction techniques (see Section 2.7.2). The selected event class is SOURCE, as it is the preferred choice for extended sources (see Section 2.7.2).
The Fermi-LAT analysis uses two datasets that span different energy ranges. The first dataset covers reconstructed energies from $> 200\,\mathrm{MeV}$ to $< 5\,\mathrm{GeV}$. The second

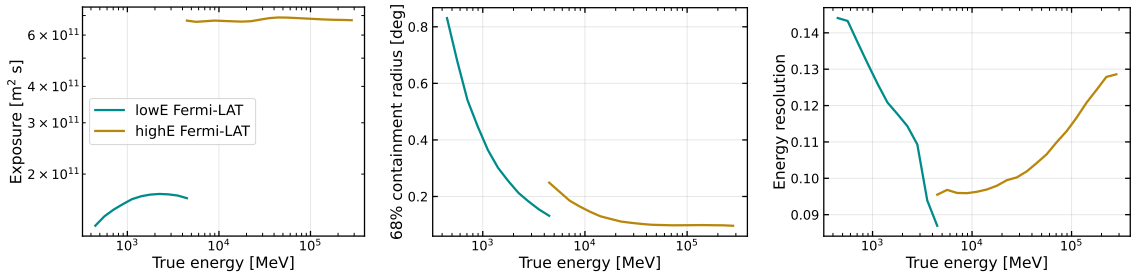

Figure 7.1: Instrument response functions of the Fermi-LAT observations used in the analysis of RX J1713.7-3946. Two datasets with complementary energy ranges and different event types are used, as described in the text. The exposure (m^2s), 68% containment radius, and the energy resolution are shown.

dataset spans from approximately 2 GeV to 400 GeV. An energy mask is applied to limit the minimum reconstructed energy to 500 MeV because lower energies have poor PSF resolution, preventing the disentanglement of sub-components within the remnant. The mask also ensures that no events are double-counted in the overlapping reconstructed energy range between the two datasets by setting the transition at 5 GeV.

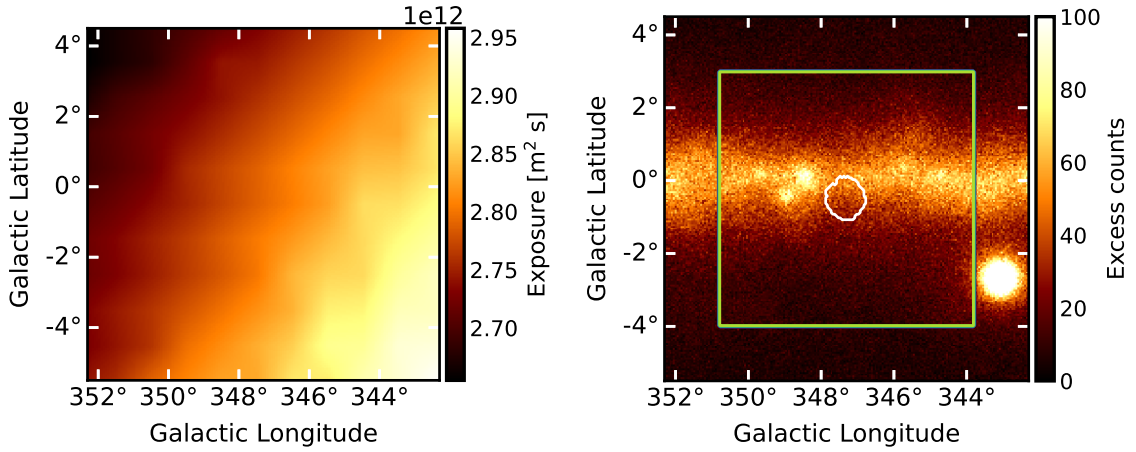

Figure 7.2: The exposure map (on the left) and the excess counts map (on the right) centred at the location of RX J1713.7-3946 using Fermi-LAT data with reconstructed energies > 200 MeV and < 5 GeV (before energy mask). The excess counts map also shows the outer contour line of the X-ray map and a green square representing the boundary mask.

Both datasets use the same SOURCE event class but differ in the event types they include. The first dataset uses only PSF3 event types, selecting events from the best angular-resolution quartile. This selection significantly reduces exposure, as shown in Fig. 7.1, but helps in resolving the remnant at low energies. The

second dataset includes all event types—FRONT and BACK—which is equivalent to selecting all four PSF quartiles (PSF0, 1, 2, 3), increasing exposure at the cost of reduced resolution. The instrument response functions for each dataset are shown in Fig. 7.1, including exposure, angular resolution, and energy resolution.

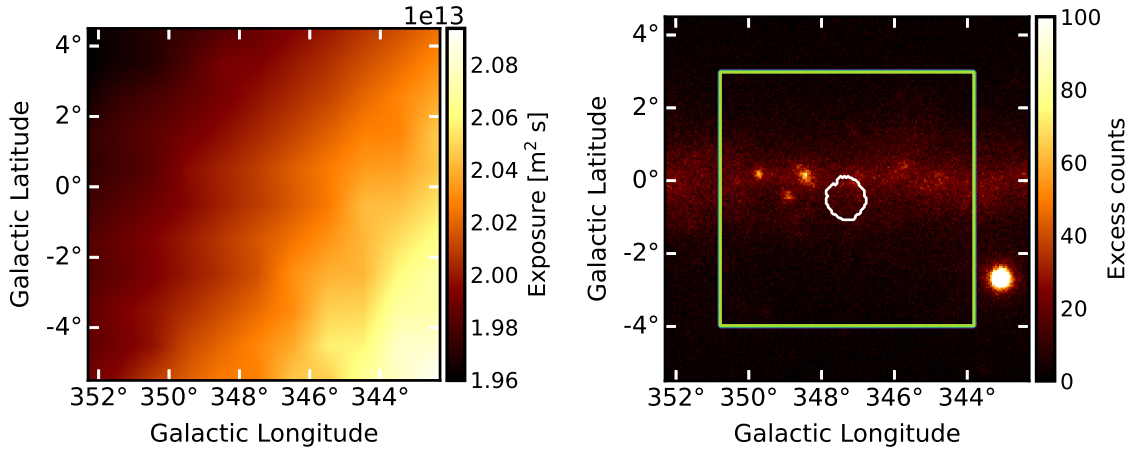

Figure 7.3: The exposure map (on the left) and the excess counts map (on the right) centred at the location of RX J1713.7-3946 using Fermi-LAT data for reconstructed energies > 2 GeV and < 500 GeV (before energy mask). The excess counts map also shows the outer contour line of the X-ray map, and the green square is the boundary mask.

The excess count map and exposure map around the location of RX J1713.7-3946 are shown in Fig. 7.2 for the low energy observation runs before the energy mask is applied. The excess count map (right) displays the outer X-ray contour of the remnant, indicating its position and extension. The boundary mask appears as a green square centred on the map. This mask excludes all pixels within 1.5° of the map edge from the fit. This is done to ensure *gammapy* performs a safe calculation of the expected counts from sources outside the analysis region that contribute inside due to PSF. The value of 1.5° is chosen to be greater than the 68% containment radius at the minimum reconstructed energy.
In Fig. 7.2, the supernova remnant is not visible due to the significant diffuse emission around the Galactic disk. The exposure map is almost perfectly uniform, with variation lower than 5%. Fig. 7.3 shows the exposure and excess count maps of the observations at higher energies. The exposure is still very homogeneous, and the excess-counts map shows results similar to the previous dataset, but slightly less bright; the same safe mask is applied to this dataset.

7.1.1 *Background components*

Figure 7.4 shows the significance of the RX J1713.7-3946 region using combined Fermi-LAT data from the two datasets previously described.

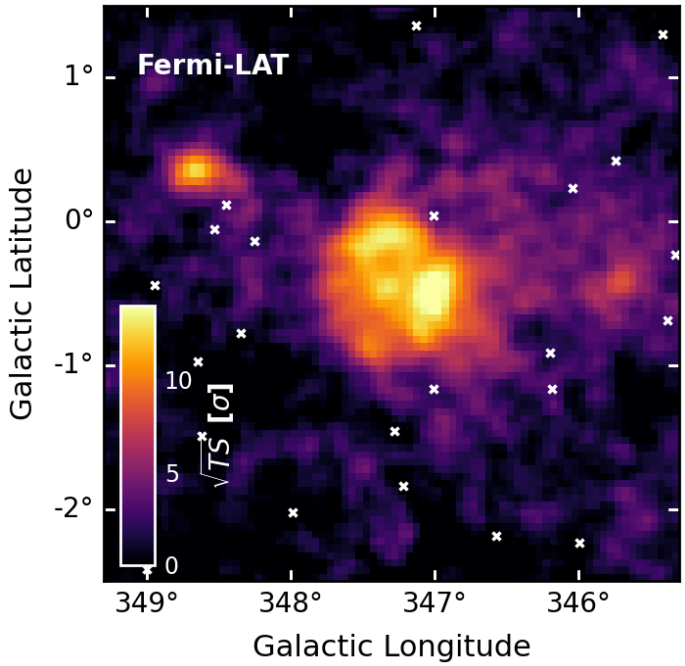

Figure 7.4: Significance map of Fermi-LAT observations with reconstructed energy greater than 500 MeV. The removed source candidates from the 4FGL around the remnant are highlighted in white.

Figure 7.4 displays the significance map of the remnant after subtracting the best-fit models for all background source candidates from the Fermi catalogue (highlighted in white) and Galactic and extragalactic gamma-ray emission. These source candidates, taken from the fourth source catalogue 4FGL [218] (data available in [219]), are modelled as point sources. However, significant gamma-ray emission outside the remnant persists even after removing these background sources. This occurs because some sources catalogued as point sources appear extended in the map. This discrepancy can be addressed by incorporating background sources from the H.E.S.S. catalogue (Fig. 6.3). In the following joint analysis, all components outside the remnant from both catalogues (see Fig. 7.4 and 6.3) are combined and fitted together to account for all the known background sources in the region.
There is an extra background component relevant in the analysis of the Fermi-LAT datasets. This is the background from extragalactic diffuse gamma-rays and

residual CR contamination. This background is isotropic and is introduced in the analysis using the spectral template file iso_P8R3_SOURCE_V3_v1.txt, available in [220]. The template is computed on the all-sky emission, excluding the Galactic plane and the celestial poles.
Furthermore, an accurate model of the diffuse Galactic emission is crucial, as most of the gamma rays seen by Fermi-LAT originate from particle interactions with the interstellar medium (Fig. 7.2 and 7.3). This diffuse emission results from proton interactions producing gamma rays via π^0 decay, and from electron interactions via Bremsstrahlung or IC scattering with the radiation field. Additionally, large-scale structures extending above and below the Galactic plane are also modelled, such as the Fermi bubbles. The Fermi-LAT IEM template model used in the joint fit follows the development described in [221], with further and more specific details for this particular model provided in [222]. In the following analysis, each Galactic diffuse component is fitted with two free parameters: a normalisation and a spectral index correction. Unlike the H.E.S.S.-only analysis, where only the normalisation was fitted, the stronger diffuse emission in the Fermi-LAT data requires additional free parameters.

7.2 Morphology

The previous chapter showed that the remnant's morphology remains stable within the H.E.S.S. energy range. At lower energies, however, the morphology reveals distinct features. Figure 7.5 presents the H.E.S.S. and Fermi-LAT significance maps side by side. The H.E.S.S. map shows substantially higher significance than Fermi-LAT, reflecting the stronger detection at higher energies. While Fermi-LAT detects the basic remnant shell structure with a similar extension as H.E.S.S., the two maps differ notably: the intensity peaks are distributed across different regions, and the internal structure shows distinct contour patterns. Fig. 7.6 shows the joint significance map using combined Fermi-LAT and H.E.S.S. data after subtracting all background gamma-ray emission from catalogued sub-components and the isotropic and Galactic diffuse components.

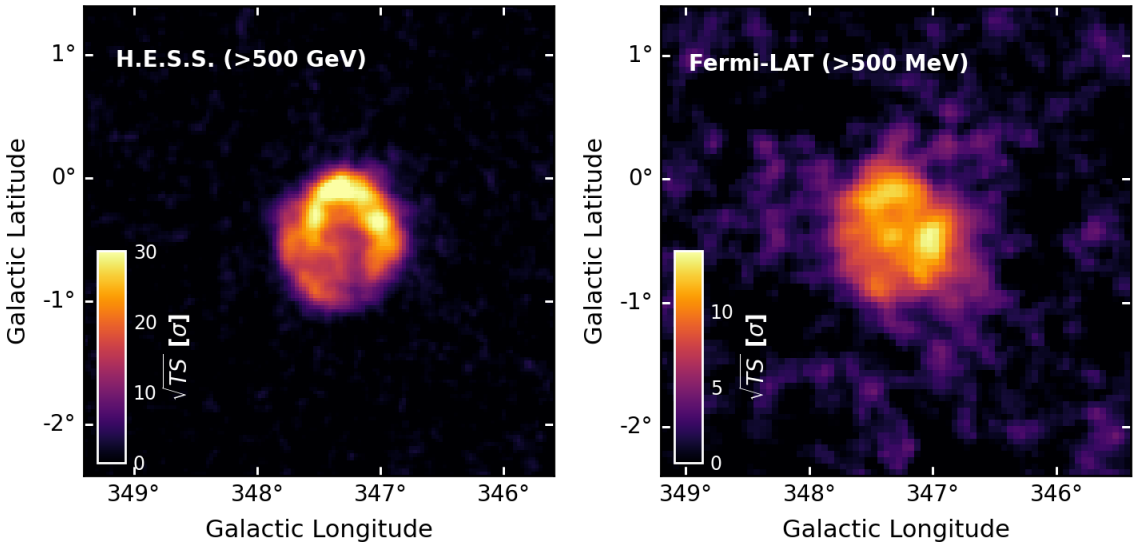

Figure 7.5: Significance map of the region of RX J1713.7-3946 using H.E.S.S. (left panel) and Fermi-LAT (right panel) data with energies > 500 GeV and 500 MeV to 400 GeV, respectively. Computed after subtracting the Galactic diffuse, extragalactic isotropic emissions, and background components from both catalogues.

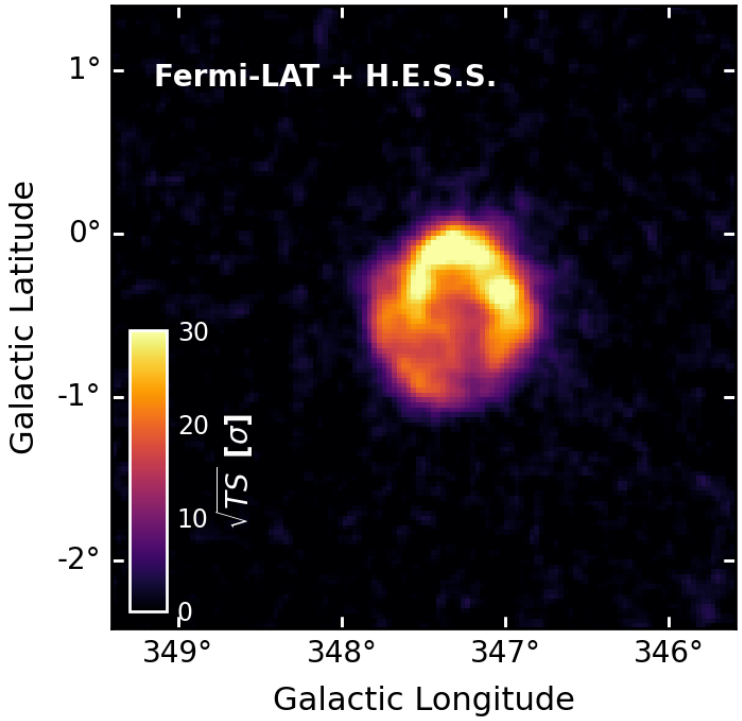

Figure 7.6: Significance map of the region of RX J1713.7-3946 using joint Fermi-LAT and H.E.S.S. data after subtracting the Galactic diffuse and extragalactic isotropic emissions and background sources from the Fermi-LAT and H.E.S.S. catalogues.

7.3 Joint spectral analysis of the remnant interior

Following the approach in the previous chapter, objects within the remnant extracted from 2HGPS are re-evaluated through a joint Fermi-LAT and H.E.S.S. fit. The sub-components inside the remnant from 2HGPS are modelled with an exponential cutoff power law (Equation 2.5.5), except for the red region located slightly outside the remnant, which uses a simple power law. The α parameter of each component is set to 0.5 in the fit and is frozen.

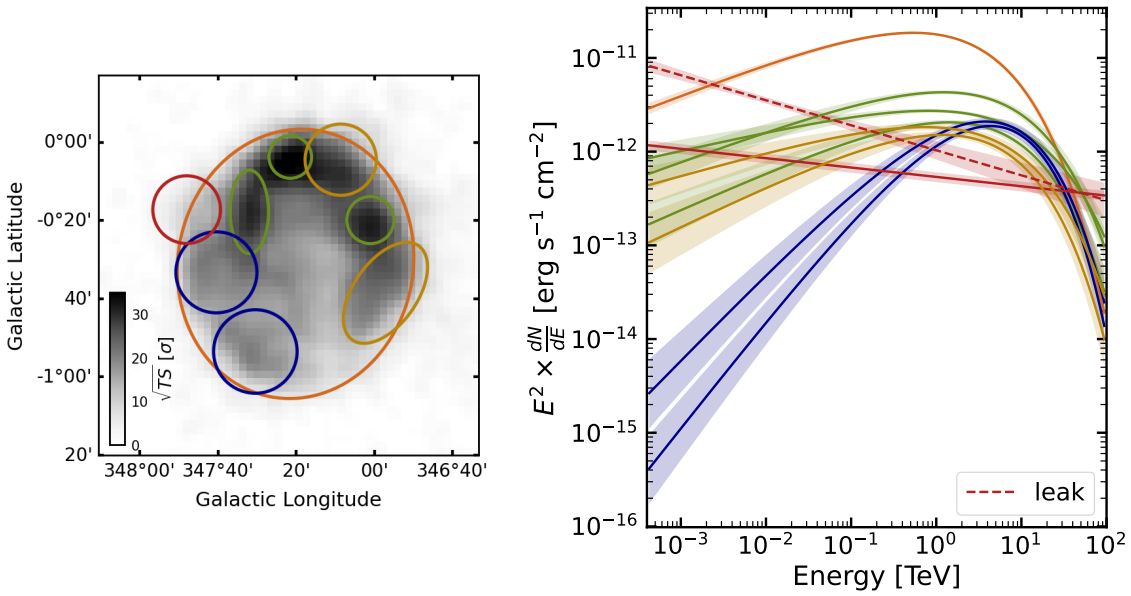

Figure 7.7: Spectral shapes of source candidates from the second H.E.S.S. catalogue after joint fitting using combined H.E.S.S. and Fermi-LAT data. The left panel shows the significance map of RX J1713.7-3946 with highlighted 2HGPS sources. The right panel displays the fitted spectral shapes for all regions, coloured by similarity, using an exponential-cutoff power-law model. The red region and the leak, on the other hand, are modelled with a simple power law.

The spectral models for all background components outside the remnant from the 2HGPS catalogue are described by a log-parabola, as in the previous analysis. Unlike for the H.E.S.S.-only analysis, the spatial and spectral parameters are frozen to the values provided by the 2HGPS, except for three sources: one large source to the right of the remnant in Fig. 6.3 at Galactic coordinates (-13.905, -0.220)°, and two bright sources to the left at coordinates (-11.380, 0.365)° and (-11.157, -0.486)°.

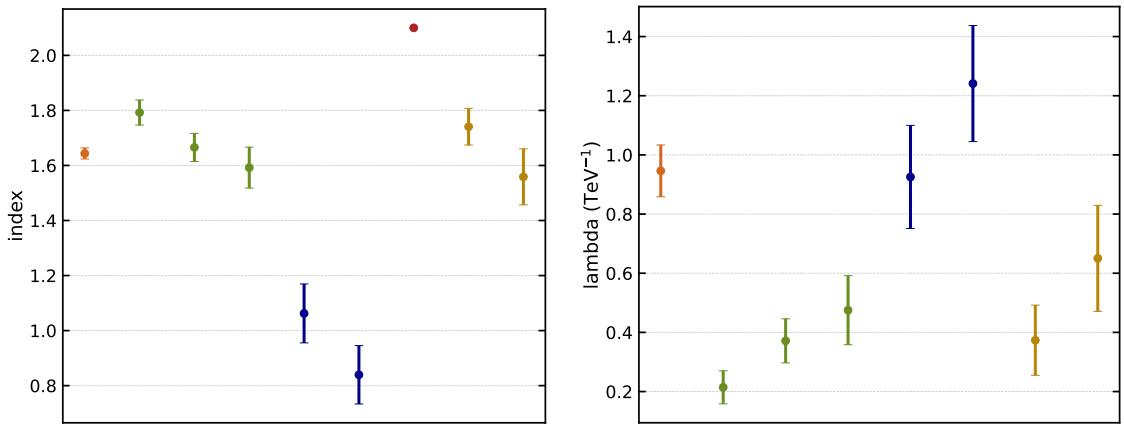

Figure 7.8: Best-fit parameters of each region inside the remnant. Each region is fitted with an exponential cutoff power law with two free parameters, the index and lambda, with α frozen at 0.5. The region in red, however, is fitted with a simple power law with two free parameters, the index and amplitude.

Therefore, the joint fit includes models for the background sources from the 2HGPS and 4FGL, the sources in the remnant's interior from the 2HGPS, the isotropic Fermi-LAT model, the Fermi-LAT Galactic IEM, and the gamma-ray emission from the leak. The leak is modelled as for H.E.S.S.-only, using a simple power-law spectral model and the full spatial region (Fig. 6.11 left). The resulting models of the remnant's interior after the fit are shown in Fig. 7.7. The left panel displays the significance map of the combined datasets with H.E.S.S. catalogue sources highlighted using the same colour scheme as for the H.E.S.S.-only analysis. The right panel shows the best-fit spectral models. The leak model is also included (dashed red line) for reference.

Fig. 7.7 reveals clear spectral differences between the eastern and western components of the remnant. The eastern regions exhibit a harder spectrum with an earlier cutoff compared to the western regions. The region extending partially outside the remnant is well described by a simple power law, similar to the leakage component but with a harder spectral index. All western regions show similar spectra.

The differences between regions can be further investigated by examining the fit parameters. Fig. 7.8 shows the best-fit parameters of the index and lambda as well as the corresponding parameter error. Each point is coloured according to its location inside the remnant (Fig. 7.7). This reinforces what was previously described. Softer spectra on the western side and a significantly larger index for the red component halfway outside the remnant shell, as well as slightly distinct

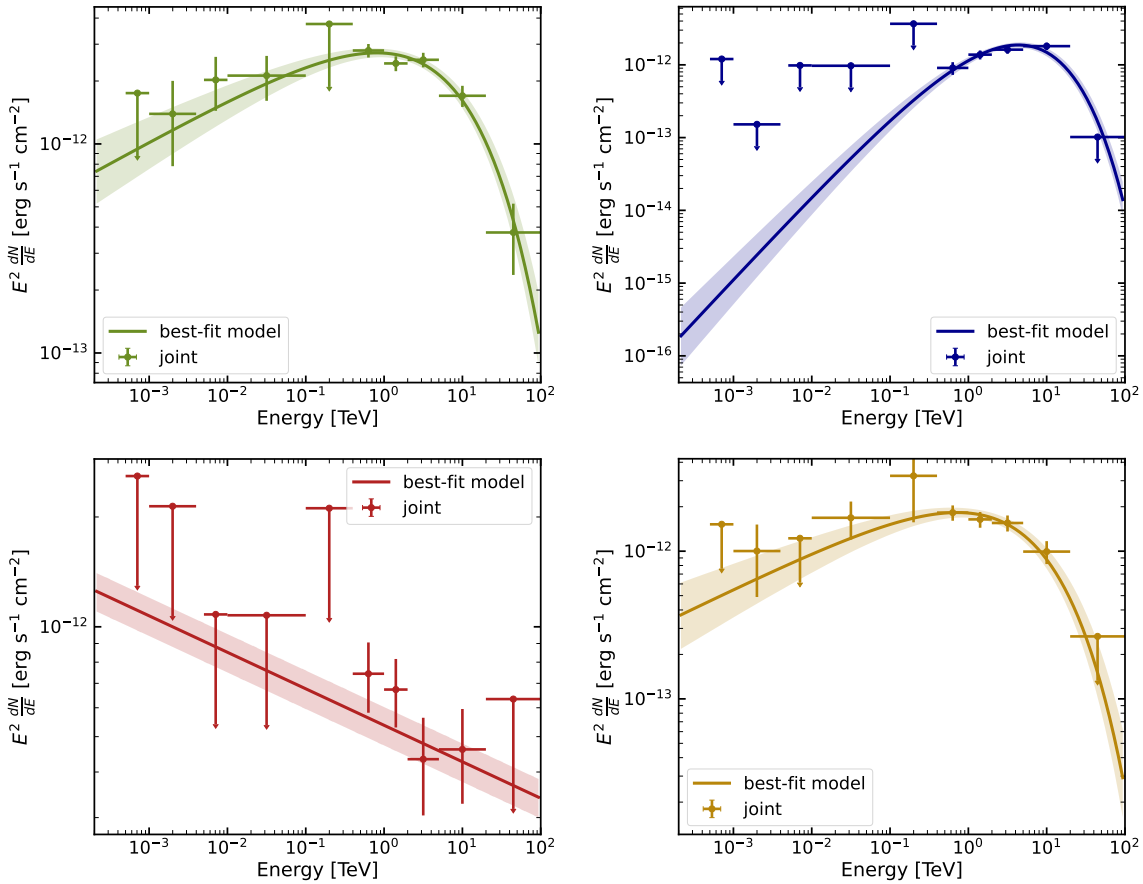

Figure 7.9: Best-fit model and flux points of each region inside RX J1713.7-3946. Four regions from the H.E.S.S. catalogue are shown and coloured according to Fig. 7.7. The best-fit model is shown in the solid line, and the model error is shown with the shaded area. The flux points for each region are superimposed.

values for lambda. As the red region is modelled with a power law, no value for λ is provided.

To assess how well these parameters are constrained at low-energy, flux points are computed for each region as discussed in Section 2.5.4. All regions are shown in Appendix C Fig. C.1, while Fig. 7.9 displays four representative components of the remnant, one from each group. The western half (green and golden components) is more significant and brighter, and therefore, the low-energy data can further constrain the model at these energies. The lower brightness of the eastern half (blue), combined with its division into small components, results in only upper error bars at Fermi-LAT energies. However, the blue eastern regions already show different curvature from the western regions from energies above $\sim 400\,\mathrm{GeV}$, indicating stronger curvature despite low significance at low energies. In contrast, the red

region shows no evidence of spectral curvature, even in the well-constrained energy range, suggesting that any energy break occurs at an energy significantly different from that of the other components.

7.4 Beyond the remnant shell

Fig. 7.10 shows the gamma-ray emission outside the remnant. The significance map displays the gamma-ray excess from combined Fermi-LAT and H.E.S.S. data after subtracting best-fit models for all sources, both inside and outside the remnant, and for the diffuse and isotropic background emission. Only the leak is displayed. A significant excess is observed around the full spatial template of the leak.

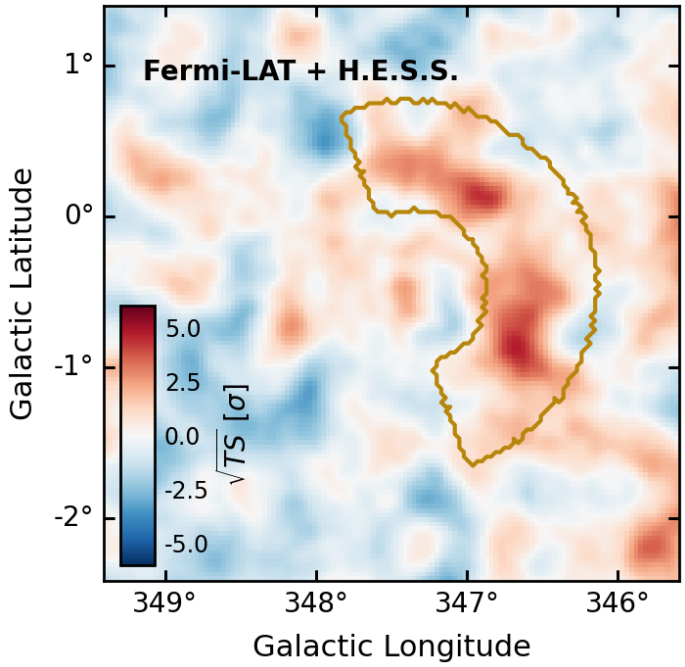

Figure 7.10: Joint significance map of the gamma-ray excess of the region of RX J1713.7-3946 using Fermi-LAT and H.E.S.S. data after subtracting the Galactic diffuse and extragalactic isotropic emissions, background sources from the Fermi-LAT and H.E.S.S. catalogues, and the sources inside the remnant. The figure shows the emission from the particle leakage from the western side of the remnant. The full half-ring spatial template is highlighted.

The gamma-ray emission outside the remnant is modelled using a joint fit. The leak is fitted as before with a simple power law with two free parameters: the amplitude and index over the spatial region highlighted in Fig. 7.10. Fig. 7.11

shows the flux points together with the model and its error. The best-fit model gives an index of 2.27 ± 0.05. The corresponding flux points and models computed on H.E.S.S. and Fermi-LAT data individually are superimposed. The joint-fit flux points are overall consistent with the flux points from the individual analyses for each instrument. It is worth noticing that the H.E.S.S. flux points in the joint fit are less significant (i.e. show more upper limits) than when doing the H.E.S.S.-only analysis. This can be due to the choice of a different diffuse model between the two analyses. The diffuse model used for both instruments in the joint analysis has more free parameters than the diffuse model fitted in the previous H.E.S.S.-only analysis, so it has more freedom to absorb part of the excess. Moreover, the diffuse model was computed for Fermi-LAT and is therefore less accurate at high energies than the previous diffuse model used in the H.E.S.S.-only analysis.

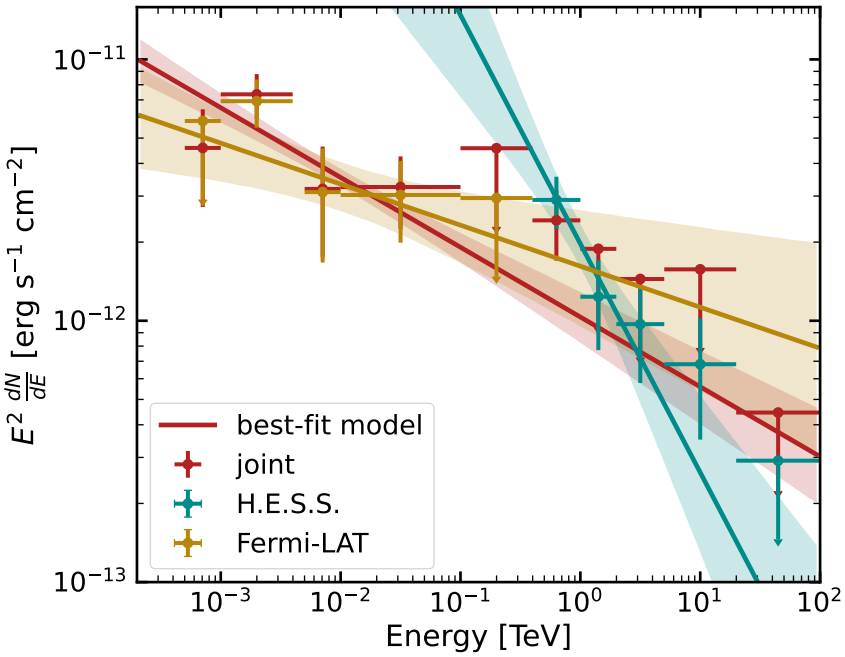

Figure 7.11: H.E.S.S., Fermi-LAT, and joint energy spectrum of the leak. Resulting best-fit spectral models from the full spatial template of the emission outside the remnant after fitting only H.E.S.S., only Fermi-LAT, and a joint fit of both. The flux points are superimposed.

7.4.1 *Nature of the emission*

The gamma-ray emission within the full spatial template of the leak (Fig. 7.10) is refitted using IC and π^0 decay models, both assuming a power-law particle distribution. The fitting is performed with naima [223], assuming the remnant lies at a distance of 1 kpc [63]. Fig. 7.12 shows the gamma-ray flux points overlaid on the hadronic and leptonic models. The left panel displays the π^0 spectrum, which can be explained with a proton power-law index of 2.37 ± 0.05. For a target hydrogen column density of $n_H\,\mathrm{cm}^{-3}$, the total energy in protons W_p required to explain the gamma-ray emission is:

$$W_\mathrm{p} = 2.9 \times 10^{49} \left(\frac{n_H}{\mathrm{cm}^{-3}} \right)^{-1} \mathrm{erg}. \tag{7.4.1}$$

The total energy in protons is related to the efficiency ϵ of the remnant at accelerating protons as:

$$W_\mathrm{p} \approx 10^{51} \times \frac{\Omega}{4\pi} \times \epsilon, \tag{7.4.2}$$

where Ω is the solid angle of the remnant that participates in providing energy to the protons; in this case, it is half of the remnant, as the gamma-ray emission is evaluated with a half-ring. Therefore, $\epsilon = 5.8\% \times \left(\frac{n_H}{\mathrm{cm}^{-3}} \right)^{-1}$. A proton distribution with an exponential cutoff was also modelled and fitted to the leak. The result of such a fit is shown in Fig. C.3. The error in the energy cutoff is very large (Table C.1), indicating that the energy cutoff cannot be constrained with the current data. The index gives a value of 2.28 ± 0.10.

In the right panel of Fig. 7.12, the IC model is fitted using the same seed photon fields as in the H.E.S.S. paper [67]: the CMB and a far-infrared component with temperature 26.5 K and density $0.417\,\mathrm{eV/cm}^3$. This fit yields an electron spectral index of 3.33 ± 0.08. Such a steep index cannot be explained by particle acceleration via DSA. As described in Section 1.4, standard DSA predicts an injection index of ~ 2.0, which is too flat to explain the observed CR flux. While theories remain debated, nonlinear DSA [40] provides a satisfactory explanation for CR observations, predicting an index of ~ 2.3. However, there is consensus that indices as steep as 3.3 cannot be achieved solely through acceleration. Therefore, the electrons must have already undergone cooling.

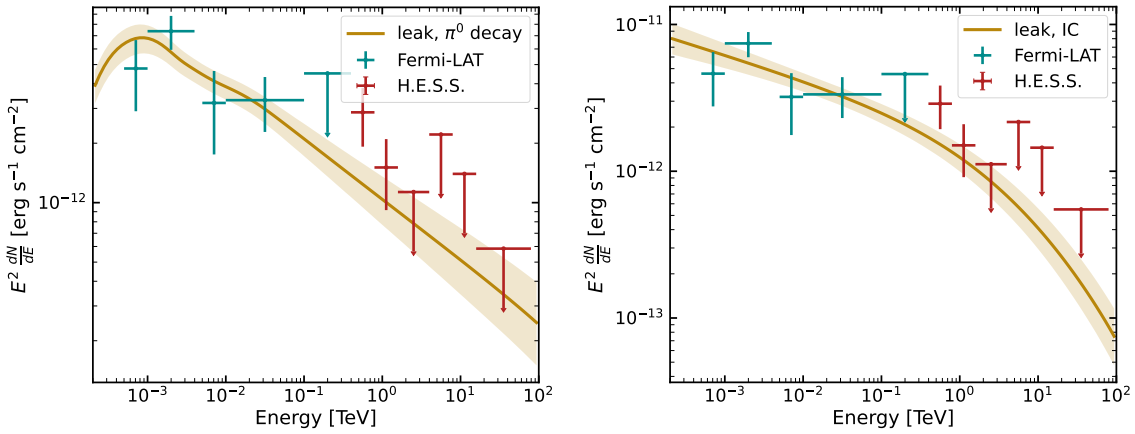

Figure 7.12: Gamma-ray spectrum outside the remnant with fits of hadronic (left) and leptonic (right) power-law models. The left panel shows the fitted π^0 power-law injection spectrum, with corresponding flux points superimposed. The right panel shows a fitted inverse-Compton power-law injection model. The best-fit spectral indices are 2.37 ± 0.05 (hadronic) and 3.33 ± 0.08 (leptonic).

Electrons cool predominantly via synchrotron losses. Electron cooling is energy-dependent; higher-energy electrons cool faster, producing an energy break where a change in the spectral index is observed. The energy of the cooling break depends on the magnetic field $B_{\mu G}$ and the cooling time t_{yr}. The cooling time is set to the remnant's age, representing the maximum possible cooling time for a particle. This relationship can be approximated as [67]:

$$E_{e,\mathrm{TeV}} \approx (1.25\ \mathrm{TeV}) \times \left(\frac{t_{\mathrm{yr}}}{10^3 \mathrm{yr}}\right)^{-1} \times \left(\frac{B_{\mu G}}{100\,\mu G}\right)^{-2}. \tag{7.4.3}$$

The age of RX J1713.7-3946 is estimated to be approximately 1500 yrs [64] [65]. However, the magnetic field remains poorly constrained. To account for this uncertainty, the energy break is computed over a wide range of magnetic field values: from 5 µG (approximating the field outside the remnant) to 20 µG (the average field inside). This yields $E_{e,\mathrm{TeV}}$ values ranging from ~ 330 TeV to ~ 20 TeV. As described in Section 1.3.2, the electron index is expected to approximately change from α_e to $\alpha_e + 1$, which in this case would mean $\alpha_e \approx 2.3$ to a good approximation. These predictions are incompatible with the observations.
Fig. 7.13 shows the flux points superimposed to the IC models fitted with a broken power-law electron distribution. A fit of the indices and break energies yields unreliable results. Therefore, the models use fixed spectral indices of 2.3 before the break and 3.3 after the break, with the break energy determined from Equa-

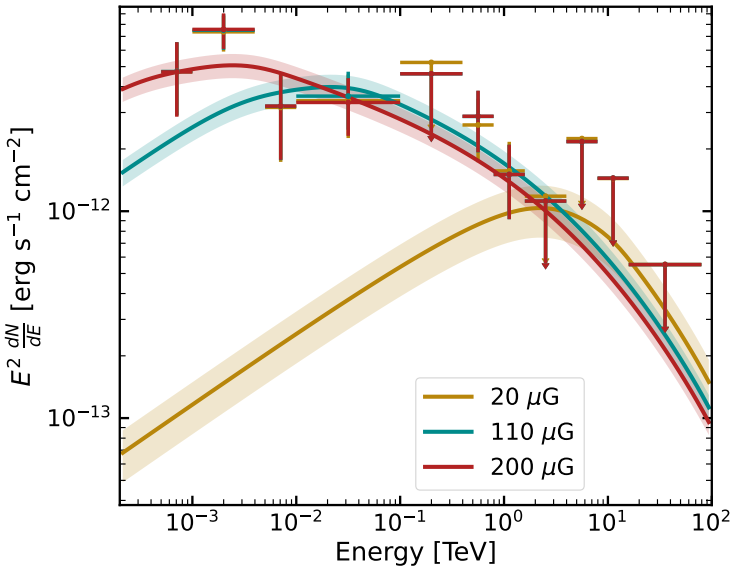

Figure 7.13: IC spectrum of the leaking emission. The flux points are overlaid with IC models assuming an electron distribution of a broken power law. All parameters are fixed except for the normalisation. The energy break is predicted from the magnetic field values. Magnetic fields below ~200 µG yield incompatible results with the flux points.

tion 7.4.3. The amplitude is left free and is fitted to the data. However, the data reveal that the energy break is incompatible with magnetic field values below ~200 µG. A compatible spectral break would only occur for magnetic fields as high as 200 µG, which is unlikely as discussed below.

7.5 Discussion

The supernova remnant RX J1713.7-3946 was studied using a joint analysis of Fermi-LAT and H.E.S.S. data. The analysis consisted of two main parts: the remnant interior and the emission outside the shock. Low-energy Fermi-LAT data further constrained both the spectra within the remnant and the gamma-ray emission beyond it as compared to Chapter 6.
Inside the remnant, the eastern and western regions exhibit clear spectral differences. Substructures on each side are very similar to one another. The eastern regions appear highly leptonic-dominated, as evidenced by their harder spectra and more pronounced curvature. In contrast, the western regions exhibit softer spectra, potentially due to gamma-ray emission from both protons and electrons.

There is a significant emission outside the western side of the remnant. The gamma-ray emission is consistent between Fermi-LAT and H.E.S.S. and can be explained with a π^0 decay model, where the proton distribution follows a simple power law with an index close to 2.3, as predicted by nonlinear DSA. The leak was also modelled with an exponential cutoff power law and shown in Fig. C.3. The energy cutoff cannot be constrained with the current H.E.S.S. dataset. The CTA Observatory will be capable of constraining this energy cutoff [224].
A purely leptonic origin is highly unlikely and would require a magnetic field of more than 100 µG. Previous papers [225] [226] have reported on strong amplification of the magnetic field within RX J1713.7-3946 in some filaments. These amplifications could range from 100 µG to magnetic field strengths of *m*G scales. However, these are localised small areas within the remnant. On average, the magnetic field of the remnant is not likely to be larger than ∼20 µG as obtained by [67] and predicted in other shell-type SNRs [227] [228]. Moreover, electrons are very unlikely to have cooled inside the remnant because the spectrum of the leak (see Fig. 7.9) is different from the spectrum inside the remnant (see Fig. 7.11). There is no reason to expect that cooled electrons escaping the remnant would exhibit a significantly different spectrum and energy break outside the remnant compared to the spectrum within it.
Outside the remnant, the magnetic field is much lower and around 5 µG [42]. Such low magnetic fields would need a much longer cooling time than the age of the SNR to be able to explain the observed spectrum. Therefore, it is highly unlikely that electrons dominate the gamma-ray emission from the leakage region, and the emission is primarily hadronic in origin.
Two main scenarios can be studied to explain the particle leakage. These are a CR precursor ahead of the shock, as described in [229], or particles escaping the shock front. An upper limit on the diffusion length scale for the case of a CR precursor can be calculated from:

$$r_{\mathrm{p}} \approx \frac{D(E)}{u_{\mathrm{shock}}}, \tag{7.5.1}$$

with u_{shock} and $D(E)$ being the velocity of the shock and the diffusion coefficient, respectively. The H.E.S.S. paper [67] gives an estimate for r_{p}, assuming Bohm diffusion, of $\sim 9\%$ of the radius of the remnant. Given the remnant radius of $\sim 10\,\mathrm{pc}$ [230], a precursor scenario would require CRs to extend a maximum

distance of no more than $r_p = 0.9\,\mathrm{pc}$ (or 0.05°) from the remnant shell. This is much smaller than the observed extension of the leakage region, where significant emission is detected over the full (0.65°) or half (0.325°) spatial template. Therefore, CR precursor can be discarded, and particles must have escaped the acceleration region.

The gamma-ray emission could result from escaped protons interacting with gas, producing faint gamma rays detectable at lower significance than the remnant emission. However, the emission from CO molecules integrated over a velocity range compatible with the distance of the SNR does not show bright structures within the leak contour (Fig. 7.14). There is no clear correlation between the leak emission and the presence of molecular gas clumps.

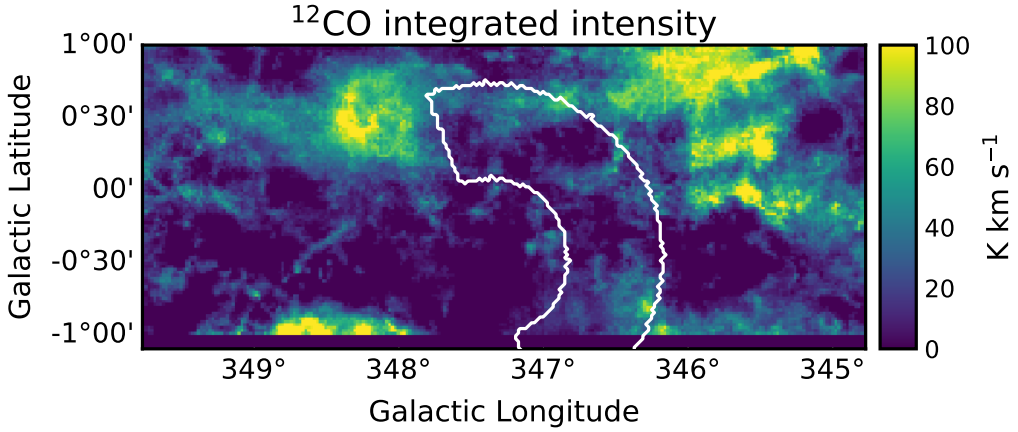

Figure 7.14: ^{12}CO(J = 1-0) intensity distribution in the vicinity of the remnant for Galactic latitudes between −1° and 1°, integrated over velocities from $-20\,\mathrm{km\,s^{-1}}$ to $0\,\mathrm{km\,s^{-1}}$. Data published in [231] and available in [232].

The study provides a unique view of proton escape from an SNR. Evidence supports energy-independent particle escape, though an energy-dependent scenario cannot be ruled out and requires further investigation. This energy-independent scenario aligns with earlier findings from H.E.S.S. studies [67]. The spectrum observed in the broad half-ring outside the remnant maintains a consistent index of 2.3 across all energies, indicating that escape probability remains constant regardless of particle energy. The H.E.S.S.-only emission in the inner half-ring shows a similar energy spectrum to the full half-ring, though with subtle differences. The outer layer of the half-ring shows significantly weaker gamma-ray emission, suggesting that protons reaching this distance from the remnant have diffused over larger regions. Further investigation is needed to determine whether the emission in

the outer layers also decreases for low-energy particles. The Fermi-LAT emission appears to extend slightly farther from the remnant, but this may be due to the poorer PSF.
This discovery is noteworthy because, in theory, particle escape should depend on energy: higher-energy particles typically have longer mean free paths and are expected to exit the shock region sooner. The energy-independent escape could indicate other escape mechanisms, such as ion-neutral damping [233] or field-line diffusion [234].
Furthermore, the emission has been evaluated only around half of the remnant. The H.E.S.S. significance map of the excess emission around the remnant (Fig. 6.12, left panel) shows a clear emission around the opposite side. Furthermore, a component located halfway outside the remnant shows an interesting spectrum with a power-law index of ~ 2.1, similar to that of the leak west of the SNR. This could indicate that gamma-ray emission outside the remnant extends not only along the investigated half-ring but also around the entire remnant, suggesting that protons are leaking from the shock front in all directions. Despite these similarities, the small region's spectrum requires further constraints at lower energies.

7.6 Outlook

This chapter and the previous one presented a preliminary analysis of the supernova remnant RX J1713.7-3946. Several avenues exist for extending and refining this analysis:

- **Emission outside the remnant.** The spatial template of the leak needs to be extended beyond the western half to investigate emission around the entire structure. This extension is motivated by significant emission detected in the H.E.S.S. maps on the eastern side (though less significant than in the west), and by the presence of a catalogued object located just outside the remnant with a spectrum consistent with that of the leak.
- **Inside the remnant.** The hadronic and leptonic contributions to the subcomponents within the remnant need to be investigated by deriving magnetic-field and hydrogen-column-density maps. The ultimate objective is to determine the ratio of hadronic to leptonic gamma-ray emission within the remnant.

- **Further investigations of particle escape.** RX J1713.7-3946 provides a unique scenario for the study of particle escape from SNRs. Despite the significant results, further investigations are needed to constrain the particle escape mechanism. The gamma-ray flux and spectral variations need to be further studied as a function of the distance from the remnant.

8

CONCLUSIONS

This thesis provides a comprehensive overview, from the inner workings of a Cherenkov camera through substantial improvements to the analysis chain, to high-level scientific analysis.

In the first part, the CTAO was covered. It is designed to achieve unprecedented sensitivity for detecting high-energy gamma-ray sources in the universe. To achieve the highest accuracy in reconstructing direction, energy, and gamma-hadron separation, highly sensitive detector components alone are insufficient—innovative data analysis techniques and detector calibration that push the limits of gamma-ray astronomy are imperative.
Throughout this thesis, multiple methods have been explored to improve the CTAO's overall detection capabilities, with particular emphasis on FlashCam. Special focus has been placed on algorithm robustness to ensure the reliability of the analysis. Data analysis techniques were developed for both online and offline analysis and span from signal extraction to image parameterisation. The contributions of this thesis to several data processing steps of the CTAO are highlighted in Fig. 8.1.

- A fast-online muon tagging algorithm based on the FlashCam trigger system was developed. The method employs a fast comparison of the number of triggered patches and cards with two thresholds. This is a very efficient and effective algorithm that detects more than 90% of muon rings triggered by the camera while introducing only a small additional background rate. The method was shown to remain highly robust to an increasing number of broken pixels and to perform similarly under nominal and high NSB.
- The next chapter developed and validated a real-time Data Volume Reduction method through detailed verification tests. The technique extends prior methods by using all information from an image: the charge and time per pixel.

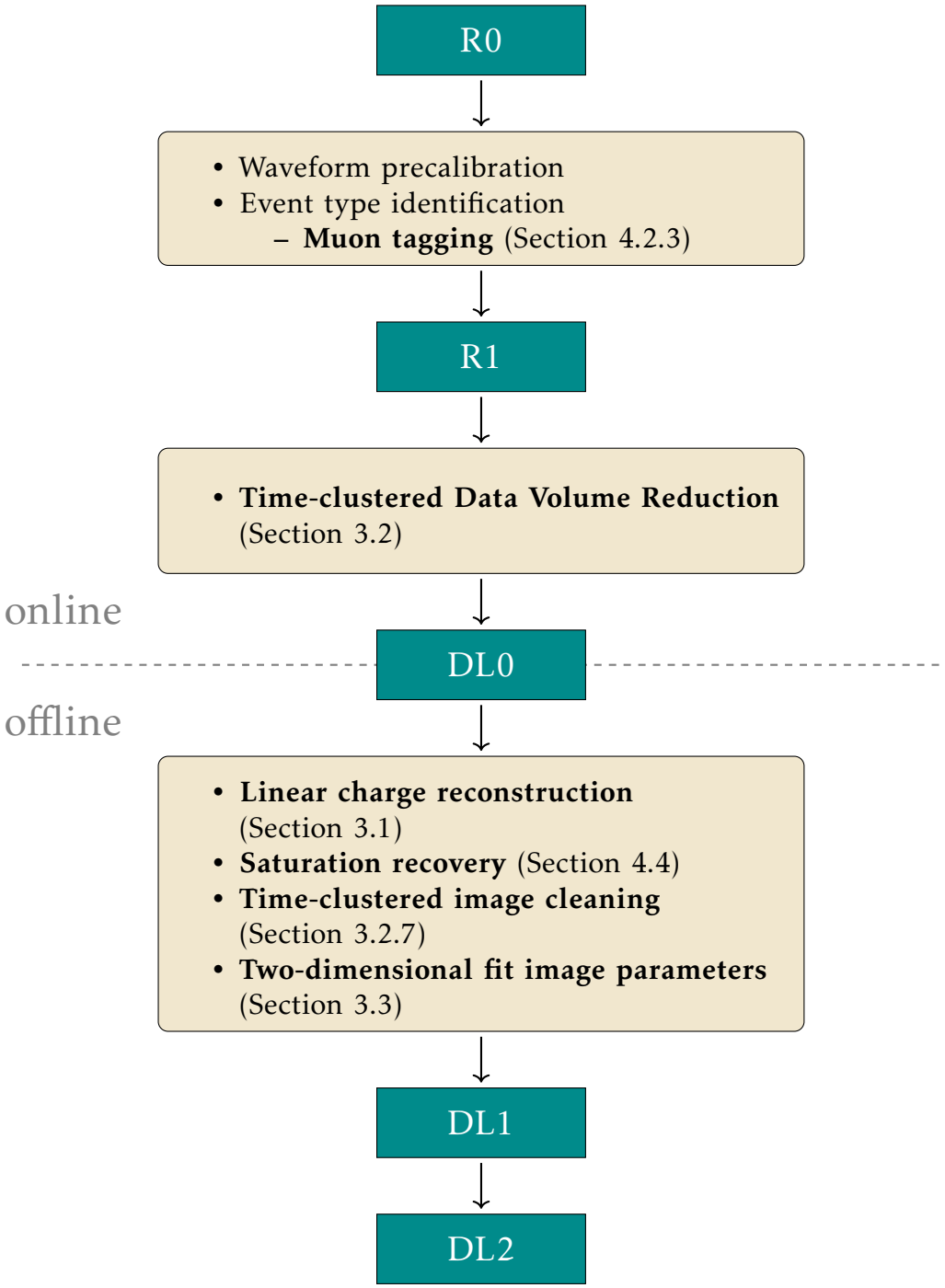

Figure 8.1: Workflow of the CTAO data processing steps. The contribution of this thesis to the conversion from each data level to the next is highlighted, and the relevant sections are indicated.

The method was tested across all camera types of the observatory and, in every case, outperforms standard Tailcuts. The time-based clustering method

is highly robust to broken pixels, NSB, and gain calibration uncertainty. This method was furthermore applied to image cleaning and maintains IRF performance at least as good as that of Tailcuts.

- Signal extraction for the FlashCam is thoroughly studied in the linear and saturation regimes. The resulting charge resolution presents an increase in performance over traditional methods. The performance is homogeneous across different pixels. The resolution at high NSB also outperforms the observatory's requirements.
- Image parameters were extracted with a two-dimensional fitting procedure by assuming a model that resembles the imaged shower. This method was compared to the standard Hillas parameters. The preliminary performance on direction reconstruction exceeds that of the standard approach. The method enables looser truncation cuts, allowing more events to pass the quality selection and yielding larger effective areas while maintaining angular resolution comparable to that obtained for the standard Hillas approach.

This thesis also contributed to the H.E.S.S. data chain and to the validation of simulations. A validation of the simulations of the original cameras installed in the four small telescopes was conducted. This validation was intended to improve the reconstruction of observation runs. In particular, data runs for RX J1713.7-3946 were recorded with CT1-4 using those cameras. The trigger rates, Hillas distributions, third-brightest-pixel distributions, and muon efficiencies were generated in simulations and compared with observations using the same approach. After updating the mirror degradation efficiency in the simulations, all tests showed good agreement. The trigger rate values obtained from simulations and observational runs are in close agreement.

Finally, the supernova remnant RX J1713.7-3946 was analysed using joint H.E.S.S. and Fermi-LAT observations. The analysis of the remnant interior revealed distinct spectral features across different regions. The eastern half exhibits characteristics consistent with leptonic-dominated emission, while the western half shows evidence of proton contribution. Both H.E.S.S. and Fermi-LAT detect significant gamma-ray emission outside the remnant boundaries. The gamma-ray spectra from both instruments agree well, and a joint fit provides strong evidence for protons escaping the shock front. RX J1713.7-3946 provides a unique opportunity to study particle escape mechanisms and particle transport from supernova remnants.

However, further studies are needed to challenge the popular theoretical models that predict an earlier decoupling of high-energy particles from the remnant.

This thesis could, of course, only give a small insight into the vast field of gamma-ray astronomy. With the CTAO close to first data, gamma-ray astronomy is set for great discoveries in the next few years. While this undertaking is a joint effort of hundreds of scientists, this thesis made a humble contribution to it.

PERSONAL BIBLIOGRAPHY

Publications

The list includes all publications in which I am the main author. As part of the H.E.S.S. and CTAO collaboration, I have been an author of collaboration papers. I am also a member of the FlashCam collaboration. A full and up-to-date list of publications can be found at https://orcid.org/0000-0002-7297-8126

A1. **Escañuela Nieves, Clara**, Werner, Felix and Hinton, Jim, A systematic assessment of Data Volume Reduction for IACTs, Astroparticle Physics. Volume 167 (2025) 103078, ISSN 0927-6505. https://doi.org/10.1016/j.astropartphys.2025.103078.

Conference proceedings

List of proceedings of which I am the first author:

B1. **Escañuela Nieves, Clara**, et al., Flashcam: A high-performance camera for IACTS, EPJ Web Conf. 319 (2025) 12006. doi: 10.1051/epjconf/202531912006.

Presentations

C1. **Escañuela Nieves, C.** Signal extraction of raw simulated and laboratory data with the FlashCam camera for Medium Sized Telescopes in CTA, *contributed talk* at "DPG Meeting", Dresden, Germany, 2023

C2. **Escañuela Nieves, C.** Image parametrisation: 2D Image Fitting, *contributed talk* at "DataPipe F2F Meeting and Hackathon", Paris-Saclay, France, 2023

C3. **Escañuela Nieves, C.** Data Volume Reduction for the Cherenkov Telescope Array, *invited talk* at "Astroparticle School", Obertrubach, Germany, 2023

C4. **Escañuela Nieves, C.** First test results of a candidate algorithm for the online Data Volume Reduction, *plenary talk* at "CTAO Collaboration meeting", Berlin, Germany, 2023

C5. **Escañuela Nieves, C.** The current state of FlashCam in ctapipe, *contributed talk* at "FlashCam Collaboration meeting", Heidelberg, Germany, 2023

C6. **Escañuela Nieves, C.** Online muon tagging for the FlashCam using trigger information, *contributed talk* at "CTAO Collaboration meeting", Berlin, Germany, 2023

C7. **Escañuela Nieves, C.** Flashcam: A high-performance camera for IACTS, *contributed talk* at "RICAP24", Frascati, Italy, 2024

REFERENCES

[1] IV Dorman and LI Dorman. How cosmic rays were discovered and why they received this misnomer. *Advances in Space Research*, 53(10):1388–1404, 2014. doi:10.1016/j.asr.2013.04.022.

[2] Theodor Wulf. Beobachtungen über die Strahlung hoher Durchdringungsfähigkeit auf dem Eiffelturm. *Physikalische Zeitschrift*, 11:811–813, 1910.

[3] Victor Francis Hess. Über beobachtungen der durchdringenden strahlung bei sieben freiballonfahrten. *Z. Phys.*, 13:1084, 1912.

[4] EDUARD Steinke. Neue Untersuchungen über die durchdringende Hesssehe Strahlung. *Zeitschrift für Physik*, 48(9):647–689, 1928.

[5] Erich Regener. Die absorptionskurve der ultrastrahlung und ihre deutung. *Phys. Z*, 34: 306–323, 1933.

[6] Jacob Clay. Penetrating radiation. In *Proceedings of the royal academy of sciences amsterdam*, volume 30, pages 1115–1127, 1927.

[7] W Kolhörster, I Matthes, and E Weber. Gekoppelte höhenstrahlen. *Naturwissenschaften*, 26 (35):576–576, 1938.

[8] Jörg R. Hörandel. Early cosmic-ray work published in german. In *Centenary Symposium 2012: Discovery of Cosmic Rays*, volume 1516 of *AIP Conference Proceedings*, pages 52–60, 2012. doi:10.1063/1.4792540.

[9] Mathieu de Naurois and Daniel Mazin. Ground-based detectors in very-high-energy gamma-ray astronomy. *Comptes Rendus. Physique*, 16(6-7):610–627, 2015. doi:10.1016/j.crhy.2015.08.011.

[10] C. M. Hoffman, C. Sinnis, P. Fleury, and M. Punch. Gamma-ray astronomy at high energies. *Reviews of Modern Physics*, 71(4):897–936, 1999. doi:10.1103/RevModPhys.71.897.

[11] David Berge. *A detailed study of the gamma-ray supernova remnant RX J1713.7-3946 with H.E.S.S.* PhD thesis, Ruprecht-Karls-Universität Heidelberg, 2006. URL https://archiv.ub.uni-heidelberg.de/volltextserver/6156/. PhD thesis; Max-Planck-Institut für Kernphysik.

[12] Mateusz Ruszkowski and Christoph Pfrommer. Cosmic ray feedback in galaxies and galaxy clusters: A pedagogical introduction and a topical review of the acceleration, transport, observables, and dynamical impact of cosmic rays. *The Astronomy and Astrophysics Review*, 31(1):4, 2023. doi:10.1007/s00159-023-00149-2.

[13] Pasquale Blasi and Elena Amato. Diffusive propagation of cosmic rays from supernova remnants in the galaxy. I: spectrum and chemical composition. *Journal of Cosmology and Astroparticle Physics*, 2012(01):010, 2012. doi:10.1088/1475-7516/2012/01/010.

[14] A. R. Bell, K. M. Schure, B. Reville, and G. Giacinti. Cosmic-ray acceleration and escape from supernova remnants. *Monthly Notices of the Royal Astronomical Society*, 431(1):415–429, 02 2013. ISSN 0035-8711. doi:10.1093/mnras/stt179. URL https://doi.org/10.1093/mnras/stt179.

[15] Kenneth Greisen. End to the Cosmic-Ray Spectrum? *Phys. Rev. Lett.*, 16:748–750, Apr 1966. doi:10.1103/PhysRevLett.16.748. URL https://link.aps.org/doi/10.1103/PhysRevLett.16.748.

[16] Georgi T Zatsepin and Vadem A Kuz'min. Upper limit of the spectrum of cosmic rays. *Soviet Journal of Experimental and Theoretical Physics Letters*, 4:78, 1966.

[17] Malcolm S. Longair. *High Energy Astrophysics*. Cambridge University Press, Cambridge, 3rd edition, 2011. ISBN 978-0-521-75618-1.

[18] Joseph Larmor. LXIII. On the theory of the magnetic influence on spectra; and on the radiation from moving ions. *The London, Edinburgh, and Dublin Philosophical Magazine and Journal of Science*, 44(271):503–512, 1897. doi:10.1080/14786449708621095.

[19] Roger Blandford and David Eichler. Particle acceleration at astrophysical shocks: A theory of cosmic ray origin. *Physics Reports*, 154(1):1–75, 1987. doi:10.1016/0370-1573(87)90134-7.

[20] Enrico Fermi. On the origin of the cosmic radiation. *Physical Review*, 75(8):1169–1174, 1949. doi:10.1103/PhysRev.75.1169.

[21] James H. Matthews, Anthony R. Bell, and Katherine M. Blundell. Particle acceleration in astrophysical jets. *New Astronomy Reviews*, 89:101543, September 2020. ISSN 1387-6473. doi:10.1016/j.newar.2020.101543. URL http://dx.doi.org/10.1016/j.newar.2020.101543.

[22] L O'C Drury. An introduction to the theory of diffusive shock acceleration of energetic particles in tenuous plasmas. *Reports on Progress in Physics*, 46(8):973–1027, 1983. doi:10.1088/0034-4885/46/8/002.

[23] H. Alfvén. Existence of Electromagnetic-Hydrodynamic Waves. *Nature*, 150:405–406, 1942. doi:10.1038/150405d0.

[24] Roger D Blandford and James P Ostriker. Particle acceleration by astrophysical shocks. *Astrophysical Journal, Part 2-Letters to the Editor, vol. 221, Apr. 1, 1978, p. L29-L32.*, 221: L29–L32, 1978. doi:10.1086/182658.

[25] Luke O'C. Drury. Origin of cosmic rays. *Astroparticle Physics*, 39-40:52–60, 2012. ISSN 0927-6505. doi:https://doi.org/10.1016/j.astropartphys.2012.02.006. URL https://www.sciencedirect.com/science/article/pii/S092765051200045X. Cosmic Rays Topical Issue.

[26] Frank M Rieger and Peter Duffy. Shear acceleration in relativistic astrophysical jets. *The Astrophysical Journal*, 617(1):155–161, 2004. doi:10.1086/425167.

[27] Felix A Aharonian. *Very high energy cosmic gamma radiation: a crucial window on the extreme Universe*. World Scientific, Singapore, 2004. ISBN 978-981-02-4573-3. doi:10.1142/4657.

[28] Stefan Funk. Ground- and space-based gamma-ray astronomy. *Annual Review of Nuclear and Particle Science*, 65(1):245–277, 2015. doi:10.1146/annurev-nucl-102014-022036.

[29] Gabriele Ghisellini. *Radiative Processes in High Energy Astrophysics*. Springer International Publishing, Cham, 2013. ISBN 978-3-319-00612-3. doi:10.1007/978-3-319-00612-3.

[30] Frank C Jones. Inverse compton scattering of cosmic-ray electrons. *Physical Review*, 137(5B): B1306, 1965. doi:https://doi.org/10.1103/PhysRev.137.B1306.

[31] Oskar Klein and Yoshio Nishina. Über die streuung von strahlung durch freie elektronen nach der neuen relativistischen quantendynamik von dirac. *Zeitschrift für Physik*, 52(11): 853–868, 1929.

[32] JA Hinton and W Hofmann. Teraelectronvolt astronomy. *Annual Review of Astronomy and Astrophysics*, 47(1):523–565, 2009. doi:10.1146/annurev-astro-082708-101816.

[33] Ervin Kafexhiu, Felix Aharonian, Andrew M Taylor, and Gabriela S Vila. Parametrization of gamma-ray production cross sections for *pp* interactions in a broad proton energy range from the kinematic threshold to PeV energies. *Physical Review D*, 90(12):123014, 2014. doi:10.1103/PhysRevD.90.123014.

[34] Rui-zhi Yang, Ervin Kafexhiu, and Felix Aharonian. Exploring the shape of the γ-ray spectrum around the "π^0-bump". *Astronomy & Astrophysics*, 615:A108, July 2018. ISSN 1432-0746. doi:10.1051/0004-6361/201730908. URL http://dx.doi.org/10.1051/0004-6361/201730908.

[35] M Aguilar, L Ali Cavasonza, G Ambrosi, L Arruda, N Attig, S Aupetit, P Azzarello, A Bachlechner, F Barao, A Barrau, et al. Precision measurement of the boron to carbon flux ratio in cosmic rays from 1.9 GV to 2.6 TV with the alpha magnetic spectrometer on the international space station. *Physical Review Letters*, 117(23):231102, 2016. doi:10.1103/PhysRevLett.117.231102.

[36] Oscar Adriani, GC Barbarino, GA Bazilevskaya, Roberto Bellotti, M Boezio, EA Bogomolov, Massimo Bongi, V Bonvicini, S Bottai, Alessandro Bruno, et al. Measurement of boron and carbon fluxes in cosmic rays with the PAMELA experiment. *The Astrophysical Journal*, 791(2): 93, 2014. doi:10.1088/0004-637X/791/2/93.

[37] F Alemanno, Q An, P Azzarello, F C T Barbato, P Bernardini, X J Bi, M S Cai, E Catanzani, J Chang, D Y Chen, et al. Detection of spectral hardenings in cosmic-ray boron-to-carbon and boron-to-oxygen flux ratios with DAMPE. *Science Bulletin*, 67(21):2162–2166, 2022. doi:10.1016/j.scib.2022.10.002.

[38] SP Swordy. The energy spectra and anisotropies of cosmic rays. *Space Science Reviews*, 99(1): 85–94, 2001. doi:10.1023/A:1013828611730.

[39] Thibault Vieu and Brian Reville. Massive star cluster origin for the galactic cosmic ray population at very-high energies. *Monthly Notices of the Royal Astronomical Society*, 519(1): 136–147, 2023. doi:10.1093/mnras/stac3469.

[40] Damiano Caprioli. Cosmic-ray acceleration in supernova remnants: non-linear theory revised. *Journal of cosmology and astroparticle physics*, 2012(07):038, 2012. doi:10.1088/1475-7516/2012/07/038.

[41] JG Kirk and RO Dendy. Shock acceleration of cosmic rays-a critical review. *Journal of Physics G: Nuclear and Particle Physics*, 27(7):1589, 2001. doi:10.1088/0954-3899/27/7/316.

[42] Jacco Vink. Supernova remnants: the X-ray perspective. *The Astronomy and Astrophysics Review*, 20(1):49, 2012. doi:10.1007/s00159-011-0049-1.

[43] EG Berezhko, LT Ksenofontov, and HJ V"olk. Confirmation of strong magnetic field amplification and nuclear cosmic ray acceleration in SN 1006. *Astronomy 'I&' Astrophysics*, 412(1): L11–L14, 2003. doi:10.1051/0004-6361:20031667.

[44] Donald C Ellison and Andrey Vladimirov. Magnetic field amplification and rapid time variations in SNR RX J1713. 7–3946. *The Astrophysical Journal*, 673(1):L47, 2007. doi:10.1086/527296.

[45] AR Bell. Turbulent amplification of magnetic field and diffusive shock acceleration of cosmic rays. *Monthly Notices of the Royal Astronomical Society*, 353(2):550–558, 2004. doi:https://doi.org/10.1111/j.1365-2966.2004.08097.x.

[46] E. G. Berezhko, L. T. Ksenofontov, and H. J. V"olk. Emission of SN 1006 produced by accelerated cosmic rays. *Astronomy 'I&' Astrophysics*, 395(3):943–953, 2002. doi:10.1051/0004-6361:20021219.

[47] Stefano Gabici and Felix A. Aharonian. Hadronic gamma-rays from rx j1713.7-3946? *Monthly Notices of the Royal Astronomical Society: Letters*, 445(1):L70–L73, 2014. doi:10.1093/mnrasl/slu132.

[48] H. Sano, Gavin Rowell, Estela M. Reynoso, I. Jung-Richardt, Yumiko Yamane, et al. Possible Evidence for Cosmic-Ray Acceleration in the Type Ia SNR RCW 86: Spatial Correlation between TeV Gamma-Rays and Interstellar Atomic Protons. *The Astrophysical Journal*, 876 (1):37, 2019. doi:10.3847/1538-4357/ab108f.

[49] M. Ackermann, M. Ajello, A. Allafort, L. Baldini, J. Ballet, G. Barbiellini, M. G. Baring, D. Bastieri, K. Bechtol, R. Bellazzini, et al. Detection of the characteristic pion-decay signature in supernova remnants. *Science*, 339(6121):807–811, 2013. doi:10.1126/science.1231160.

[50] Adam Burrows. Colloquium: Perspectives on core-collapse supernova theory. *Rev. Mod. Phys.*, 85:245–261, Feb 2013. doi:10.1103/RevModPhys.85.245. URL https://link.aps.org/doi/10.1103/RevModPhys.85.245.

[51] Wolfgang Hillebrandt, Jens C. Niemeyer, and Martin Reinecke. Type Ia supernova explosion models: Homogeneity versus diversity. *AIP Conference Proceedings*, 522(1):53–64, 06 2000. ISSN 0094-243X. doi:10.1063/1.1291695. URL https://doi.org/10.1063/1.1291695.

[52] Hans A Bethe and James R Wilson. Revival of a stalled supernova shock by neutrino heating. *Astrophysical Journal, Part 1 (ISSN 0004-637X), vol. 295, Aug. 1, 1985, p. 14-23.*, 295:14–23, 1985. doi:10.1086/163343.

[53] Stephen P Reynolds. Dynamical Evolution and Radiative Processes of Supernova Remnants. In *Handbook of Supernovae*, pages 1981–2004. Springer, 2017.

[54] H. Th. Janka, R. Buras, K. Kifonidis, M. Rampp, and T. Plewa. Explosion Mechanisms of Massive Stars, 2002. URL https://arxiv.org/abs/astro-ph/0212314.

[55] John M Blondin, Eric B Wright, Kazimierz J Borkowski, and Stephen P Reynolds. Transition to the radiative phase in supernova remnants. *The Astrophysical Journal*, 500(1):342, 1998. doi:10.1086/305708.

[56] Andrea Giuliani and Martina Cardillo. Supernova Remnants in Gamma Rays. *Universe*, 10 (5):203, 2024. doi:https://doi.org/10.3390/universe10050203.

[57] Leonid Ivanovich Sedov. *Similarity and dimensional methods in mechanics*. CRC press, 2018.

[58] E Pfeffermann and B Aschenbach. ROSAT observation of a new supernova remnant in the constellation Scorpius. In *Roentgenstrahlung from the Universe*, pages 267–268, 1996.

[59] Katsuji Koyama, Kenzo Kinugasa, Keiichi Matsuzaki, Mamiko Nishiuchi, Mutsumi Sugizaki, Ken'ichi Torii, Shigeo Yamauchi, and Bernd Aschenbach. Discovery of non-thermal X-rays from the northwest shell of the new SNR RX J1713. 7–3946: The second SN 1006? *Publications of the Astronomical Society of Japan*, 49(3):L7–L11, 1997.

[60] Satoru Katsuda, Fabio Acero, Nozomu Tominaga, Yasuo Fukui, Junko S Hiraga, Katsuji Koyama, Shiu-Hang Lee, Koji Mori, Shigehiro Nagataki, Yutaka Ohira, et al. Evidence for thermal X-ray line emission from the synchrotron-dominated supernova remnant RX J1713. 7-3946. *The Astrophysical Journal*, 814(1):29, 2015. doi:10.1088/0004-637X/814/1/29.

[61] JS Lazendic, PO Slane, Bryan M Gaensler, PP Plucinsky, JP Hughes, Duncan Kenneth Galloway, and F Crawford. X-Ray Observations of the Compact Central Object in Supernova Remnant G347. 3–0.5. *The Astrophysical Journal*, 593(1):L27, 2003. doi:10.1086/378183.

[62] George G Pavlov, Divas Sanwal, and Marcus A Teter. Central compact objects in supernova remnants. In *Symposium-International Astronomical Union*, volume 218, pages 239–246. Cambridge University Press, 2004. doi:10.1063/1.2900173.

[63] Y Fukui, H Sano, J Sato, K Torii, H Horachi, T Hayakawa, NM McClure-Griffiths, Gavin Rowell, T Inoue, S Inutsuka, et al. A detailed study of the molecular and atomic gas toward the γ-ray supernova remnant RX J1713. 7- 3946: spatial TeV γ-ray and interstellar medium gas correspondence. *The Astrophysical Journal*, 746(1):82, 2012. doi:10.1088/0004-637X/746/1/82.

[64] Naomi Tsuji and Yasunobu Uchiyama. Expansion measurements of supernova remnant RX J1713. 7- 3946. *Publications of the Astronomical Society of Japan*, page psw102, 2016.

[65] Fabio Acero, Satoru Katsuda, Jean Ballet, and Robert Petre. Measurement of the X-ray proper motion in the south-east rim of RX J1713. 7- 3946. *Astronomy & Astrophysics*, 597:A106, 2017. doi:10.1051/0004-6361/201629618.

[66] Junko S Hiraga, Yasunobu Uchiyama, Tadayuki Takahashi, and Felix A Aharonian. Spectral properties of nonthermal X-ray emission from the shell-type SNR RX J1713. 7–3946 as revealed by XMM-Newton. *Astronomy & Astrophysics*, 431(3):953–961, 2005. doi:10.1051/0004-6361:20047015.

[67] H Abdalla, A Abramowski, F Aharonian, Faical Ait Benkhali, AG Akhperjanian, Tom Andersson, EO Angüner, M Arrieta, P Aubert, M Backes, et al. HESS observations of RX J1713. 7- 3946 with improved angular and spectral resolution: Evidence for gamma-ray emission extending beyond the X-ray emitting shell. *Astronomy & Astrophysics*, 612:A6, 2018. doi:10.1051/0004-6361/201629790.

[68] Nigel I Maxted, Gavin P Rowell, Bruce R Dawson, Michael G Burton, Yasuo Fukui, Jasmina Lazendic, Akiko Kawamura, Hirotaka Horachi, Hidetoshi Sano, Andrew J Walsh, et al. Dense Gas Towards the RX J1713. 7–3946 Supernova Remnant. *Publications of the Astronomical Society of Australia*, 30:e055, 2013. doi:10.1017/pasa.2013.35.

[69] Takaaki Tanaka, Yasunobu Uchiyama, Felix A Aharonian, Tadayuki Takahashi, Aya Bamba, Junko S Hiraga, Jun Kataoka, Tetsuichi Kishishita, Motohide Kokubun, Koji Mori, et al. Study of nonthermal emission from snr rx j1713. 7–3946 with suzaku. *The Astrophysical Journal*, 685(2):988, 2008. doi:10.1086/591020.

[70] Yasuo Fukui and NANTEN team. Sub-mm/mm studies of the molecular gas in the Galactic disk; the TeV gamma ray SNR RXJ1713.7-3946 and the W28 high mass star forming region. *AIP Conference Proceedings*, 1085(1):104–111, 12 2008. ISSN 0094-243X. doi:10.1063/1.3076625. URL https://doi.org/10.1063/1.3076625.

[71] Nigel I Maxted, Gavin P Rowell, Bruce R Dawson, Michael G Burton, Brent P Nicholas, Yasuo Fukui, Andrew J Walsh, Akiko Kawamura, Hirotaka Horachi, and Hidetoshi Sano. 3 to 12 millimetre studies of dense gas towards the western rim of supernova remnant RX J1713. 7- 3946. *Monthly Notices of the Royal Astronomical Society*, 422(3):2230–2245, 2012. doi:10.1111/j.1365-2966.2012.20766.x.

[72] Pierre Auger, Paul Ehrenfest, Roland Maze, Jean Daudin, and Robley A Fréon. Extensive cosmic-ray showers. *Reviews of modern physics*, 11(3-4):288, 1939. doi:https://doi.org/10.1103/RevModPhys.11.288.

[73] Peter K. F. Grieder. *Extensive Air Showers: High Energy Phenomena and Astrophysical Aspects – A Tutorial, Reference Manual and Data Book*. Springer Science & Business Media, 2010. ISBN 978-3-540-76941-5. doi:10.1007/978-3-540-76941-5.

[74] Walter Heitler. *The quantum theory of radiation*. Courier Corporation, 1984.

[75] Hans Bethe and Walter Heitler. On the stopping of fast particles and on the creation of positive electrons. *Proceedings of the Royal Society of London. Series A, Containing Papers of a Mathematical and Physical Character*, 146(856):83–112, 1934. doi:https://doi.org/10.1098/rspa.1934.0140.

[76] Ralph Engel, Dieter Heck, and Tanguy Pierog. Extensive air showers and hadronic interactions at high energy. *Annual review of nuclear and particle science*, 61(1):467–489, 2011. doi:10.1146/annurev.nucl.012809.104544.

[77] James Matthews. A Heitler model of extensive air showers. *Astroparticle Physics*, 22(5-6): 387–397, 2005. doi:10.1016/j.astropartphys.2004.09.003.

[78] Edna Loredana Ruiz Velasco. *Search and first detection of very-high-energy photons in gamma-ray bursts: an analysis with HAWC and HESS*. PhD thesis, Ruprecht-Karls-Universit"at Heidelberg, 2021.

[79] Stefan Ohm. *Development of an advanced gamma/hadron separation technique and application to particular gamma-ray sources with HESS*. PhD thesis, Ruprecht-Karls-Universität Heidelberg, 2010.

[80] Pavel A Cherenkov. Visible light from clear liquids under the action of gamma radiation. *Comptes Rendus (Doklady) de l'Aeademie des Sciences de l'URSS*, 2(8):451–454, 1934.

[81] Stephanie Sabina Pürckhauer. *Characterising Light Concentrators for CTA and Optimising the Data Selection to Improve Angular Resolution and Sensitivity*. Phd thesis, Ruprecht-Karls-Universität Heidelberg, Heidelberg, Germany, 2018.

[82] IE Tamm and IM Frank. Coherent radiation of fast electrons in a medium. In *Dokl. Akad. Nauk SSSR*, volume 14, pages 107–112, 1937.

[83] Simon Sailer. *The FlashCam camera for CTA: trigger verification and fluorescence light detection capabilities*. PhD thesis, Ruprecht-Karls-Universität Heidelberg, 2020. URL https://nbn-resolving.de/urn:nbn:de:bsz:16-heidok-291056. PhD thesis; supervisor: Prof. Dr. Jim Hinton.

[84] F. Bradascio, H. Rueda, J.A. Barrio, J. Biteau, F. Brun, C. Champion, J.-F. Glicenstein, D. Hoffmann, P. Jean, J.P. Lenain, F. Louis, A. Pérez, M. Punch, P. Sizun, K.-H. Sulanke, L.A. Tejedor, and B. Vallage. The NectarCAM timing system. *Nuclear Instruments and Methods in Physics Research Section A: Accelerators, Spectrometers, Detectors and Associated Equipment*, 1054: 168398, 2023. ISSN 0168-9002. doi:https://doi.org/10.1016/j.nima.2023.168398. URL https://www.sciencedirect.com/science/article/pii/S0168900223003881.

[85] Cherenkov Telescope Array-CTA, D Depaoli, Antonelli Angelo, Tora Arnesen, Jann Aschersleben, Attin'a Primo, Balbo Matteo, Bang Sunghyun, Andrei Barychev, and Manuela Vecchi. Status of the sst camera for the cherenkov telescope array. In *38th International Cosmic Ray Conference (ICRC2023)-Gamma-ray Astronomy (GA)*, page 771. Sissa Medialab, 2024. doi:10.22323/1.444.0771.

[86] Heinrich J V"olk and Konrad Bernl"ohr. Imaging very high energy gamma-ray telescopes. *Experimental Astronomy*, 25(1):173–191, 2009. doi:10.1007/s10686-009-9151-z.

[87] Baiyang Bi, Miquel Barcelo, Christian Bauer, Faical Ait Benkhali, Jacqueline Catalano, Sebastian Diebold, Christian Föhr, Stefan Funk, Gianluca Giavitto, German Hermann, et al. Performance of the New FlashCam-based Camera in the 28\, m Telescope of HESS. *arXiv preprint arXiv:2108.03046*, 2021. doi:https://doi.org/10.48550/arXiv.2108.03046.

[88] Albert Einstein. "Uber einen die erzeugung und verwandlung des lichtes betreffenden heuristischen gesichtspunkt. *Annalen der Physik*, 322(6):132–148, 1905. doi:10.1002/andp.19053220607.

[89] VA Morozov, NV Morozova, and P Budzyński. Delayed electron emission in photomultiplier tubes. *Nuclear Instruments and Methods in Physics Research Section A: Accelerators, Spectrometers, Detectors and Associated Equipment*, 1053:168323, 2023. doi:https://doi.org/10.1016/j.nima.2023.168323.

[90] Hamamatsu Photonics K.K. *Photomultiplier Tubes: Basics and Applications*. Hamamatsu Photonics K.K., Hamamatsu City, Japan, 4th edition, 2017.

[91] Anthony G Wright. *The photomultiplier handbook*. Oxford University Press, 2017.

[92] Stefan Ohm, Stefan Wagner, HESS Collaboration, et al. Current status and operation of the hess array of imaging atmospheric cherenkov telescopes. *Nuclear Instruments and Methods in Physics Research Section A: Accelerators, Spectrometers, Detectors and Associated Equipment*, 1055:168442, 2023. doi:https://doi.org/10.1016/j.nima.2023.168442.

[93] Gianluca Giavitto, Simon Bonnefoy, Terry Ashton, Michael Backes, Arnim Balzer, David Berge, Francois Brun, Thomas Chaminade, Eric Delagnes, Gerard Fontaine, et al. Performance of the upgraded HESS cameras. In *Proceedings of 35th International Cosmic Ray Conference—PoS (ICRC2017)*, 2018. doi:10.22323/1.301.0805.

[94] Markus Holler, D Berge, C Van Eldik, J-P Lenain, Vincent Marandon, Thomas Murach, Mathieu de Naurois, RD Parsons, Heike Prokoph, and Dmitry Zaborov. Observations of the Crab Nebula with HESS phase II. *arXiv preprint arXiv:1509.02902*, 2015. doi:https://doi.org/10.48550/arXiv.1509.02902.

[95] Felix Aharonian, AG Akhperjanian, AR Bazer-Bachi, M Beilicke, Wystan Benbow, David Berge, K Bernlöhr, C Boisson, Oliver Bolz, V Borrel, et al. Observations of the Crab nebula with HESS. *Astronomy & Astrophysics*, 457(3):899–915, 2006. doi:10.1051/0004-6361:20065351.

[96] Cta Consortium et al. *Science with the Cherenkov Telescope Array*. World Scientific, 2018. doi:https://doi.org/10.1142/10986.

[97] Werner Hofmann and Roberta Zanin. The Cherenkov telescope array. In *Handbook of X-ray and Gamma-ray Astrophysics*, pages 1–47. Springer, 2023.

[98] Gernot Maier, L Arrabito, K Bernlöhr, J Bregeon, P Cumani, T Hassan, J Hinton, and A Moralejo. Performance of the cherenkov telescope array. *arXiv preprint arXiv:1907.08171*, 2019. doi:https://doi.org/10.22323/1.301.0846.

[99] Shinsuke Abe, Jayant Abhir, Abhishek Abhishek, F Acero, A Acharyya, R Adam, A Aguasca-Cabot, I Agudo, A Aguirre-Santaella, J Alfaro, et al. Prospects for a survey of the galactic plane with the Cherenkov Telescope Array. *Journal of cosmology and astroparticle physics*, 2024(10):081, 2024. doi:10.1088/1475-7516/2024/10/081.

[100] The CTAO collaboration. CTAO Website, layouts for alpha configuration, 2025. URL https://www.ctao.org/news/ctao-releases-layouts-for-alpha-configuration/. Accessed: 18 November 2025.

[101] Abelardo Moralejo. LST-1, the Large-Sized Telescope prototype of CTA. Status and first observations. In *Journal of Physics: Conference Series*, volume 2156, page 012089. IOP Publishing, 2021. doi:10.1088/1742-6596/2156/1/012089.

[102] Federico Di Pierro and on behalf of the CTA-LST Project. Status of the Large-Sized Telescope of the Cherenkov Telescope Array. *Journal of Physics: Conference Series*, 2429(1):012020, feb 2023. doi:10.1088/1742-6596/2429/1/012020. URL https://doi.org/10.1088/1742-6596/2429/1/012020.

[103] Cherenkov Telescope Array Observatory (CTAO). Technical specifications — for scientists, 2025. URL https://www.ctao.org/for-scientists/technical-specifications/. Accessed: 2025-12-28.

[104] G Pühlhofer, Christian Bauer, A Biland, D Florin, C Föhr, A Gadola, German Hermann, C Kalkuhl, J Kasperek, T Kihm, et al. FlashCam: A fully digital camera for CTA telescopes. In *AIP Conference Proceedings*, volume 1505, pages 777–780. American Institute of Physics, 2012. doi:10.1063/1.4772375.

[105] J-F Glicenstein, M Shayduk, NectarCAM Collaboration, and CTA Consortium. NectarCAM, a camera for the medium sized telescopes of the Cherenkov telescope array. In *AIP Conference Proceedings*, volume 1792, page 080009. AIP Publishing LLC, 2017. doi:10.22323/1.236.0937.

[106] Cherenkov Telescope Array Observatory (CTAO). Cherenkov Telescope Array Observatory (CTAO) — A Growing International Observatory, 2025. URL https://www.ctao.org/. Accessed: 2025-12-28.

[107] Guillaume Grolleron, Halim Ashkar, François Brun, Heide Costantini, Denis Dumora, Pierre Jean, Daniel Kerszberg, Jean-Philippe Lenain, Vincent Marandon, Sonal R. Patel, and Luigi Tibaldo. NectarChain, the scientific software for the CTA-NectarCAM. In *Proceedings of Science (38th International Cosmic Ray Conference, ICRC2023)*, volume 444 of *PoS*, page 862, 2023. doi:10.22323/1.444.0862. URL https://pos.sissa.it/444/862/. Presented on behalf of the CTA NectarCAM Collaboration.

[108] F Aharonian, AG Akhperjanian, K-M Aye, AR Bazer-Bachi, M Beilicke, W Benbow, D Berge, P Berghaus, K Bernl"ohr, O Bolz, et al. Calibration of cameras of the HESS detector. *Astroparticle Physics*, 22(2):109–125, 2004. doi:10.1016/j.astropartphys.2004.06.006.

[109] Simon Steinmaßl. *Probing particle acceleration in stellar binary systems using gamma-ray observations*. PhD thesis, Ruprecht-Karls-Universität Heidelberg, 2023.

[110] Maximilian Linhoff, Lukas Beiske, Noah Biederbeck, Stefan Fröse, Karl Kosack, and Lukas Nickel. ctapipe – Prototype Open Event Reconstruction Pipeline for the Cherenkov Telescope Array. In *Proceedings, 38th International Cosmic Ray Conference*, volume 444, 2023. doi:10.22323/1.444.0703.

[111] Cherenkov Telescope Array Observatory (CTAO). Data and computing — emission to discovery, 2025. URL https://www.ctao.org/emission-to-discovery/data-and-computing/. Accessed: 2025-12-28.

[112] I Oya, P Aubert, L Baroncelli, P Bolle, P Bruno, A Bulgarelli, S Caroff, L Castaldini, V Conforti, A Costa, et al. The first release of the Cherenkov Telescope Array Observatory array control and data acquisition software. In *Software and Cyberinfrastructure for Astronomy VIII*, volume 13101, pages 537–548. SPIE, 2024. doi:10.1117/12.3017568.

[113] É. Lyard, A. Muraczewski, M. Schefer, B. Schleicher, A. Tramacere, R. Walter, and F. Werner. Design and Implementation of the Array Data Handler of the Cherenkov Telescope Array Observatory. In *Proceedings of the 39th International Cosmic Ray Conference (ICRC2025)*, 2025. doi:10.22323/1.501.0741.

[114] Andrea Bulgarelli, Sami Caroff, Antonio Addis, Pierre Aubert, Leonardo Baroncelli, Giovanni De Cesare, Ambra DiPiano, Valentina Fioretti, Enrique Garcia, Gilles Maurin, et al. The Science Alert Generation system of the Cherenkov Telescope Array Observatory. *arXiv preprint arXiv:2108.04470*, 2021. doi:https://doi.org/10.48550/arXiv.2108.04470.

[115] Andrea Zoli, Andrea Bulgarelli, Adriano De Rosa, Alessio Aboudan, Valentina Fioretti, Giovanni De Cesare, and Ramin Marx. Parallel waveform extraction algorithms for the Cherenkov Telescope Array Real-Time Analysis. *arXiv preprint arXiv:1509.01953*, 2015. doi:https://doi.org/10.48550/arXiv.1509.01953.

[116] G Lamanna, LA Antonelli, JL Contreras, Jürgen Knödlseder, K Kosack, N Neyroud, A Aboudan, L Arrabito, C Barbier, D Bastieri, et al. Cherenkov telescope array data management. *arXiv preprint arXiv:1509.01012*, 2015. doi:https://doi.org/10.48550/arXiv.1509.01012.

[117] Jose Luis Contreras, Konstancja Satalecka, K Bernlöhr, Catherine Boisson, Johan Bregeon, Andrea Bulgarelli, Giovanni de Cesare, R Reyes, Valentina Fioretti, Karl Kosack, et al. Data model issues in the Cherenkov Telescope Array project. *arXiv preprint arXiv:1508.07584*, 2015. doi:10.48550/arXiv.1508.07584.

[118] Cosimo Nigro, Tarek Hassan, and Laura Olivera-Nieto. Evolution of data formats in very-high-energy gamma-ray astronomy. *Universe*, 7(10):374, 2021. doi:10.3390/universe7100374.

[119] Dieter Heck, Johannes Knapp, JN Capdevielle, G Schatz, T Thouw, et al. CORSIKA: A Monte Carlo code to simulate extensive air showers. *Report fzka*, 6019(11), 1998. doi:10.5445/IR/270043064.

[120] Konrad Bernlöhr. Simulation of imaging atmospheric Cherenkov telescopes with CORSIKA and sim_telarray. *Astroparticle Physics*, 30(3):149–158, 2008. doi:https://doi.org/10.1016/j.astropartphys.2008.07.009.

[121] S Ostapchenko. QGSJET-II: towards reliable description of very high energy hadronic interactions. *Nuclear Physics B-Proceedings Supplements*, 151(1):143–146, 2006. doi:https://doi.org/10.1016/j.nuclphysbps.2005.07.026.

[122] K. Bernlöhr. CTA simulations with CORSIKA/sim_telarray. *AIP Conference Proceedings*, 1085 (1):874–877, 12 2008. ISSN 0094-243X. doi:10.1063/1.3076816. URL https://doi.org/10.1063/1.3076816.

[123] M Punch, CW Akerlof, MF Cawley, DJ Fegan, RC Lamb, MA Lawrence, MJ Lang, DA Lewis, DI Meyer, KS O'Flaherty, et al. Supercuts: an improved method of selecting gamma-rays. In *Proceedings of the 22nd International Cosmic Ray Conference. 11-23 August, 1991. Dublin, Ireland. Under the auspices of the International Union of Pure and Applied Physics (IUPAP), Volume 1, Contributed Papers, OG Sessions 1-5. Dublin: The Institute for Advanced Studies, 1991., p. 464*, volume 1, page 464, 1991.

[124] A Michael Hillas. Cerenkov light images of EAS produced by primary gamma. In *19th Intern. Cosmic Ray Conf-Vol. 3*, number OG-9.5-3, 1985.

[125] David J Fegan. gamma/hadron separation at TeV energies. *Journal of Physics G: Nuclear and Particle Physics*, 23(9):1013, sep 1997. doi:10.1088/0954-3899/23/9/004. URL https://doi.org/10.1088/0954-3899/23/9/004.

[126] A. Demichev and A. Kryukov. Using deep learning methods for IACT data analysis in gamma-ray astronomy: A review. *Astronomy and Computing*, 46:100793, 2024. ISSN 2213-1337. doi:https://doi.org/10.1016/j.ascom.2024.100793. URL https://www.sciencedirect.com/science/article/pii/S2213133724000088.

[127] W. Hofmann, I. Jung, A. Konopelko, H. Krawczynski, H. Lampeitl, and G. Pühlhofer. Comparison of techniques to reconstruct VHE gamma-ray showers from multiple stereoscopic Cherenkov images. *Astroparticle Physics*, 12(3):135–143, 1999. ISSN 0927-6505. doi:https://doi.org/10.1016/S0927-6505(99)00084-5. URL https://www.sciencedirect.com/science/article/pii/S0927650599000845.

[128] R.D. Parsons and J.A. Hinton. A Monte Carlo template based analysis for air-Cherenkov arrays. *Astroparticle Physics*, 56:26–34, 2014. ISSN 0927-6505. doi:https://doi.org/10.1016/j.astropartphys.2014.03.002. URL https://www.sciencedirect.com/science/article/pii/S0927650514000231.

[129] FA Aharonian, AG Akhperjanian, JA Barrio, K Bernlöhr, H Bojahr, I Calle, JL Contreras, J Cortina, S Denninghoff, V Fonseca, et al. The Energy Spectrum of TeV Gamma Rays from the Crab Nebula as Measured by the HEGRA System of Imaging Air Cerenkov Telescopes. *The Astrophysical Journal*, 539(1):317, 2000. doi:10.1086/309225.

[130] Thomas Murach, Michael Gajdus, and Robert Daniel Parsons. A neural network-based monoscopic reconstruction algorithm for HESS II. *arXiv preprint arXiv:1509.00794*, 2015. doi:https://doi.org/10.48550/arXiv.1509.00794.

[131] S. Ohm, C. van Eldik, and K. Egberts. γ/hadron separation in very-high-energy γ-ray astronomy using a multivariate analysis method. *Astroparticle Physics*, 31(5):383–391, 2009. ISSN 0927-6505. doi:https://doi.org/10.1016/j.astropartphys.2009.04.001. URL https://www.sciencedirect.com/science/article/pii/S0927650509000589.

[132] Rune Michael Dominik, Maximilian Linhoff, and Julian Sitarek. Interpolation of Instrument Response Functions for the Cherenkov Telescope Array in the context of pyirf. *arXiv preprint arXiv:2309.16488*, 2023. doi:https://doi.org/10.48550/arXiv.2309.16488.

[133] Axel Donath, Régis Terrier, Quentin Remy, Atreyee Sinha, Cosimo Nigro, Fabio Pintore, Bruno Khélifi, Laura Olivera-Nieto, Jose Enrique Ruiz, Kai Brügge, et al. Gammapy: A Python package for gamma-ray astronomy. *Astronomy & Astrophysics*, 678:A157, 2023. doi:10.1051/0004-6361/202346488.

[134] H.E.S.S. Collaboration. Gammapy selected as open-source software of choice for analysis of H.E.S.S. data, 2021. URL https://hess.in2p3.fr/hess_news/gammapy-selected-as-open-source-software-of-choice-for-analysis-of-h-e-s-s-data/. Accessed: 2025-12-28.

[135] Lars Mohrmann, Andreas Specovius, Domenico Tiziani, Stefan Funk, Dmitry Malyshev, Kaori Nakashima, and Christopher van Eldik. Validation of open-source science tools and background model construction in γ-ray astronomy. *Astronomy & Astrophysics*, 632:A72, 2019. doi:10.1051/0004-6361/201936452.

[136] Christoph Deil, Roberta Zanin, Julien Lefaucheur, Catherine Boisson, Bruno Khélifi, Régis Terrier, Matthew Wood, Lars Mohrmann, Nachiketa Chakraborty, Jason Watson, et al. Gammapy-A prototype for the CTA science tools. *arXiv preprint arXiv:1709.01751*, 2017. doi:https://doi.org/10.48550/arXiv.1709.01751.

[137] Cherenkov Telescope Array Observatory (CTAO). Ctao adopts the gammapy software package for science analysis, 2021. URL https://www.ctao.org/news/ctao-adopts-the-gammapy-software-package-for-science-analysis/. Accessed: 2025-12-28.

[138] David Berge, S Funk, and J Hinton. Background modelling in very-high-energy γ-ray astronomy. *Astronomy & Astrophysics*, 466(3):1219–1229, 2007. doi:10.1051/0004-6361:20066674.

[139] Webster Cash. Parameter estimation in astronomy through application of the likelihood ratio. *Astrophysical Journal, Part 1*, 228:939–947, 1979. doi:10.1086/156922.

[140] James R Mattox, DL Bertsch, J Chiang, BL Dingus, SW Digel, JA Esposito, JM Fierro, RC Hartman, SD Hunter, G Kanbach, et al. The likelihood analysis of EGRET data. *Astrophysical Journal v. 461, p. 396*, 461:396, 1996. doi:10.1086/177068.

[141] T-P Li and Y-Q Ma. Analysis methods for results in gamma-ray astronomy. *Astrophysical Journal, Part 1 (ISSN 0004-637X), vol. 272, Sept. 1, 1983, p. 317-324.*, 272:317–324, 1983. doi:10.1086/161295.

[142] F Aharonian, F Ait Benkhali, J Aschersleben, H Ashkar, M Backes, A Baktash, V Barbosa Martins, R Batzofin, Yvonne Becherini, D Berge, et al. Spectrum and extension of the inverse-compton emission of the crab nebula from a combined fermi-lat and hess analysis. *Astronomy & Astrophysics*, 686:A308, 2024. doi:10.1051/0004-6361/202348651.

[143] GLAST Facility Science Team, Neil Gehrels, and Peter Michelson. GLAST: the next-generation high energy gamma-ray astronomy mission. *Astroparticle Physics*, 11(1):277–282, 1999. ISSN 0927-6505. doi:https://doi.org/10.1016/S0927-6505(99)00066-3. URL https://www.sciencedirect.com/science/article/pii/S0927650599000663. TeV Astrophysics of Extragalactic Sources.

[144] David J Thompson and Colleen A Wilson-Hodge. Fermi gamma-ray space telescope. In *Handbook of X-ray and Gamma-ray Astrophysics*, pages 2383–2413. Springer, 2024.

[145] William B Atwood, Aous A Abdo, Markus Ackermann, W Althouse, B Anderson, M Axelsson, Luca Baldini, J Ballet, DL Band, Guido Barbiellini, et al. The large area telescope on the Fermi gamma-ray space telescope mission. *The Astrophysical Journal*, 697(2):1071, 2009. doi:10.1088/0004-637X/697/2/1071.

[146] C. Cecchi and (for the GLAST LAT Collaboration). Glast: the gamma ray large area space telescope. *Journal of Physics: Conference Series*, 120(6):062017, jul 2008. doi:10.1088/1742-6596/120/6/062017. URL https://doi.org/10.1088/1742-6596/120/6/062017.

[147] A.A. Moiseev, R.C. Hartman, J.F. Ormes, D.J. Thompson, M.J. Amato, T.E. Johnson, K.N. Segal, and D.A. Sheppard. The anti-coincidence detector for the GLAST large area telescope. *Astroparticle Physics*, 27(5):339–358, 2007. ISSN 0927-6505. doi:https://doi.org/10.1016/j.astropartphys.2006.12.003. URL https://www.sciencedirect.com/science/article/pii/S0927650506001885.

[148] NASA Goddard Space Flight Center. Fermi gamma-ray space telescope: Large area telescope (lat) instrument, 2025. URL https://fermi.gsfc.nasa.gov/science/instruments/lat.html. Accessed: 2025-12-28.

[149] P Bruel, TH Burnett, SW Digel, G Johannesson, N Omodei, and M Wood. Fermi-LAT improved Pass 8 event selection. *arXiv preprint arXiv:1810.11394*, 2018. doi:https://doi.org/10.48550/arXiv.1810.11394.

[150] WB Atwood, Luca Baldini, J Bregeon, P Bruel, A Chekhtman, J Cohen-Tanugi, A Drlica-Wagner, J Granot, Francesco Longo, Nicola Omodei, et al. New Fermi-LAT event reconstruction reveals more high-energy gamma rays from gamma-ray bursts. *The Astrophysical Journal*, 774(1):76, 2013. doi:10.1088/0004-637X/774/1/76.

[151] Markus Ackermann, Marco Ajello, Andrea Albert, A Allafort, WB Atwood, Magnus Axelsson, Luca Baldini, Jean Ballet, Guido Barbiellini, Denis Bastieri, et al. The Fermi large area telescope on orbit: event classification, instrument response functions, and calibration. *The Astrophysical Journal Supplement Series*, 203(1):4, 2012. doi:10.1088/0067-0049/203/1/4.

[152] Leon Rochester, Tracy Usher, Robert P Johnson, and Bill Atwood. Upgrades to the Event Simulation and Reconstruction for the Fermi Large Area Telescope. *arXiv preprint arXiv:1001.5005*, 2010. doi:https://doi.org/10.48550/arXiv.1001.5005.

[153] Fermi Science Support Center (FSSC) / NASA. LAT Data Products — Cicerone: Data, 2025. URL https://fermi.gsfc.nasa.gov/ssc/data/analysis/documentation/Cicerone/Cicerone_Data/LAT_DP.html. Online documentation; archival Cicerone page accessed 2025-12-28.

[154] Donald Carson Wells and Eric W Greisen. FITS-a flexible image transport system. In *Image processing in astronomy*, page 445, 1979.

[155] Clara Escañuela Nieves, Felix Werner, and Jim Hinton. A systematic assessment of Data Volume Reduction for IACTs. *Astroparticle Physics*, 167:103078, 2025. ISSN 0927-6505. doi:https://doi.org/10.1016/j.astropartphys.2025.103078. URL https://www.sciencedirect.com/science/article/pii/S0927650525000015.

[156] Karl Kosack. cta-observatory/ctapipe: v0. 19.0–2023-03-31. *Zenodo*, 2023. doi:10.5281/zenodo.7788918. URL https://zenodo.org/records/7788918.

[157] clara-escanuela and contributors. Pull request #2188: Flashcam extractor, 2023. URL https://github.com/cta-observatory/ctapipe/pull/2188. GitHub repository for ctapipe; merged into ‘main‘ (Mar 30, 2023).

[158] J. Albert, E. Aliu, H. Anderhub, P. Antoranz, A. Armada, M. Asensio, C. Baixeras, J.A. Barrio, et al. FADC signal reconstruction for the MAGIC telescope. *Nuclear Instruments and Methods in Physics Research Section A: Accelerators, Spectrometers, Detectors and Associated Equipment*, 594(3):407–419, 2008. ISSN 0168-9002. doi:https://doi.org/10.1016/j.nima.2008.06.043. URL https://www.sciencedirect.com/science/article/pii/S0168900208009091.

[159] Hendrik Bartko, M Gaug, A Moralejo, and N Sidro. FADC pulse reconstruction using a digital filter for the MAGIC telescope. *arXiv preprint astro-ph/0506459*, 2005. doi:https://doi.org/10.48550/arXiv.astro-ph/0506459.

[160] Gerd Puehlhofer, Christian Bauer, Sabrina Bernhard, Massimo Capasso, Sebastian Diebold, Felix Eisenkolb, et al. FlashCam: a fully-digital camera for the medium-sized telescopes of the Cherenkov Telescope Array. *arXiv preprint arXiv:1509.02434*, 2015. doi:https://doi.org/10.48550/arXiv.1509.02434.

[161] SciPy Community. SciPy documentation: `scipy.signal.filtfilt`, 2025. URL https://docs.scipy.org/doc/scipy/reference/generated/scipy.signal.filtfilt.html. Accessed: 2025-12-28.

[162] Pauli Virtanen, Ralf Gommers, Travis E Oliphant, Matt Haberland, Tyler Reddy, et al. SciPy 1.0: fundamental algorithms for scientific computing in Python. *Nature methods*, 17(3): 261–272, 2020. doi:https://doi.org/10.1038/s41592-019-0686-2.

[163] CH Nowlin and JL Blankenship. Elimination of undesirable undershoot in the operation and testing of nuclear pulse amplifiers. *Review of Scientific Instruments*, 36(12):1830–1839, 1965. doi:10.1063/1.1719475.

[164] Steven W. Smith. *The Scientist and Engineer's Guide to Digital Signal Processing*. California Technical Publishing, San Diego, CA, 1997.

[165] cta-observatory / ctapipe contributors. ctapipe: `invalid_pixels.py` — invalid pixel handling in image cleaning, 2025. URL https://github.com/cta-observatory/ctapipe/blob/main/src/ctapipe/image/invalid_pixels.py. GitHub source file — accessed 2025-12-28.

[166] Colin B Adams, William Benbow, A Brill, James H Buckley, Jodi L Christiansen, Abraham Falcone, Qi Feng, Jason P Finley, GM Foote, Lucy Fortson, et al. The throughput calibration of the VERITAS telescopes. *Astronomy & Astrophysics*, 658:A83, 2022. doi:10.1051/0004-6361/202142275.

[167] J. Holder, R.W. Atkins, H.M. Badran, G. Blaylock, S.M. Bradbury, J.H. Buckley, K.L. Byrum, et al. The first VERITAS telescope. *Astroparticle Physics*, 25(6):391–401, 2006. ISSN 0927-6505. doi:https://doi.org/10.1016/j.astropartphys.2006.04.002. URL https://www.sciencedirect.com/science/article/pii/S092765050600051X.

[168] Martin Ester, Hans-Peter Kriegel, Jörg Sander, and Xiaowei Xu. A density-based algorithm for discovering clusters in large spatial databases with noise. In *Proceedings of the Second International Conference on Knowledge Discovery and Data Mining*, KDD'96, page 226–231. AAAI Press, 1996.

[169] Jeong-Hun Kim, Jong-Hyeok Choi, Kwan-Hee Yoo, and Aziz Nasridinov. AA-DBSCAN: an approximate adaptive DBSCAN for finding clusters with varying densities. *The Journal of Supercomputing*, 75(1):142–169, 2019. doi:https://doi.org/10.1007/s11227-018-2380-z.

[170] Andraž Mehle, Boštjan Likar, and Dejan Tomaževič. In-line recognition of agglomerated pharmaceutical pellets with density-based clustering and convolutional neural network. In *2017 Fifteenth IAPR International Conference on Machine Vision Applications (MVA)*, pages 9–12, 2017. doi:10.23919/MVA.2017.7986760.

[171] Yukiho Kobayashi, Akira Okumura, Franca Cassol, Hideaki Katagiri, Julian Sitarek, Pawel Gliwny, et al. Camera Calibration of the CTA-LST prototype. In *Proceedings of 37th International Cosmic Ray Conference — PoS(ICRC2021)*, ICRC2021, page 720. Sissa Medialab, July 2021. doi:10.22323/1.395.0720. URL http://dx.doi.org/10.22323/1.395.0720.

[172] Ricardo JGB Campello, Davoud Moulavi, and Jörg Sander. Density-based clustering based on hierarchical density estimates. In *Pacific-Asia conference on knowledge discovery and data mining*, pages 160–172. Springer, 2013.

[173] Mihael Ankerst, Markus M Breunig, Hans-Peter Kriegel, and Jörg Sander. OPTICS: Ordering points to identify the clustering structure. *ACM Sigmod record*, 28(2):49–60, 1999. doi:10.1145/304182.304187.

[174] Python Software Foundation. Python language reference, version 3.11, 2023. URL https://www.python.org/.

[175] Travis E. Oliphant. Python for scientific computing. *Computing in Science 'I&' Engineering*, 9 (3):10–20, 2007. doi:10.1109/MCSE.2007.58.

[176] Jelena Ćelić, Rodrigo Guedes Lang, Simon Steinmassl, Jim Hinton, and Stefan Funk. A novel approach to optimizing the image cleaning performance of Imaging Atmospheric Cherenkov Telescopes: Application to a time-based cleaning for HESS. *Astronomy & Astrophysics*, 699: A96, 2025. doi:10.1051/0004-6361/202554824.

[177] Jodi Christiansen and VERITAS Collaboration. Improving VERITAS sensitivity by fitting 2D Gaussian image parameters. In *AIP Conference Proceedings*, volume 1505, pages 709–712. American Institute of Physics, 2012. doi:https://doi.org/10.1063/1.4772358.

[178] Mathieu De Naurois. Analysis methods for atmospheric cerenkov telescopes. *arXiv preprint astro-ph/0607247*, 2006. doi:https://doi.org/10.48550/arXiv.astro-ph/0607247.

[179] G Verna, F Cassol, H Costantini, T Armstrong, EO Anguner, et al. Reconstruction of truncated images for pevatron searches with the cherenkov telescope array. *IL NUOVO CIMENTO C*, 44(2-3), 2021. doi:10.1393/ncc/i2021-21104-8.

[180] Gaia Verna. *Study of the PeVatron candidate SNR G106.3+2.7 and optimization of the CTA-North sensitivity at high energies*. PhD thesis, École Doctorale Physique et sciences de la matière (Marseille), 2022. URL http://www.theses.fr/2022AIXM0388.

[181] Gaia Verna. Estimation of CTA potentiality in the search of galactic cosmic rays accelerators. Seminar, Thésards 3ème année, CPPM, Aix-Marseille Univ., CNRS/IN2P3, November 2020. URL https://indico.in2p3.fr/event/22599/. Talk presented at IN2P3 Seminar event 22599.

[182] clara-escanuela. Add algorithm to compute image parameters via fitting the light distribution, 2023. URL https://github.com/cta-observatory/ctapipe/pull/2275. GitHub Pull Request #2275, cta-observatory/ctapipe.

[183] Samir K Ashour and Mahmood A Abdel-hameed. Approximate skew normal distribution. *Journal of Advanced Research*, 1(4):341–350, 2010. doi:https://doi.org/10.1016/j.jare.2010.06.004.

[184] Wikipedia contributors. Skew normal distribution, 2025. URL https://en.wikipedia.org/wiki/Skew_normal_distribution. Wikipedia, The Free Encyclopedia; accessed 2025-12-28.

[185] SciPy Community. SciPy documentation: `scipy.stats.skewnorm`, 2025. URL https://docs.scipy.org/doc/scipy/reference/generated/scipy.stats.skewnorm.html. Accessed: 2025-12-28.

[186] Mathieu De Naurois and Loïc Rolland. A high performance likelihood reconstruction of γ-rays for imaging atmospheric Cherenkov telescopes. *Astroparticle Physics*, 32(5):231–252, 2009. doi:10.1016/j.astropartphys.2009.09.001.

[187] K Abe, S Abe, A Abhishek, F Acero, A Aguasca-Cabot, I Agudo, C Alispach, N Alvarez Crespo, D Ambrosino, LA Antonelli, et al. A new method of reconstructing images of gamma-ray telescopes applied to the LST-1 of CTAO. *Astronomy & astrophysics*, 691:A328, 2024. doi:10.1051/0004-6361/202450889.

[188] Fred James and Matts Roos. MINUIT: a system for function minimization and analysis of the parameter errors and corrections. *Comput. Phys. Commun.*, 10(CERN-DD-75-20):343–67, 1975. doi:https://doi.org/10.1016/0010-4655(75)90039-9. URL https://www.sciencedirect.com/science/article/pii/0010465575900399.

[189] Hans Dembinski, Piti Ongmongkolkul, Christoph Deil, Henry Schreiner, Matthew Feickert, Chris Burr, Jason Watson, Fabian Rost, Alex Pearce, Lukas Geiger, et al. scikit-hep/iminuit: v. *Zenodo*, 2020. doi:10.5281/zenodo.8249703.

[190] Cyril Trichard. Searching for PeVatrons in the CTA Galactic Plane Survey. *arXiv preprint arXiv:1709.01311*, 2017.

[191] Werner, Felix. Pdp module, 2024. URL https://git.mpi-hd.mpg.de/FlashCam/fc-pdp.

[192] F. Werner, C. Bauer, S. Bernhard, M. Capasso, S. Diebold, F. Eisenkolb, S. Eschbach, et al. Performance verification of the FlashCam prototype camera for the Cherenkov Telescope Array. *Nuclear Instruments and Methods in Physics Research Section A: Accelerators, Spectrometers, Detectors and Associated Equipment*, 876:31–34, December 2017. ISSN 0168-9002. doi:10.1016/j.nima.2016.12.056. URL http://dx.doi.org/10.1016/j.nima.2016.12.056.

[193] M. K. Daniel, M. Gaug, and P. Majumdar. The Camera Calibration Strategy of the Cherenkov Telescope Array. In *Proceedings of the 34th International Cosmic Ray Conference (ICRC2015)*, The Hague, The Netherlands, 2015.

[194] Markus Gaug, Steven Fegan, AMW Mitchell, Maria-Concetta Maccarone, Teresa Mineo, and Akira Okumura. Using muon rings for the calibration of the Cherenkov telescope array: a systematic review of the method and its potential accuracy. *The Astrophysical Journal Supplement Series*, 243(1):11, 2019. doi:10.3847/1538-4365/ab2123.

[195] Alison Mairi Wallace Mitchell. *Optical Efficiency Calibration for Inhomogeneous IACT Arrays and a Detailed Study of the Highly Extended Pulsar Wind Nebula HESS J1825-137*. PhD thesis, Ruprecht-Karls-Universität Heidelberg, 2016.

[196] C. Alispach, A. Araudo, M. Balbo, V. Beshley, A. Biland, J. Blažek, J. Borkowski, et al. The sst-1m imaging atmospheric cherenkov telescope for gamma-ray astrophysics. *Journal of Cosmology and Astroparticle Physics*, 2025(02):047, feb 2025. doi:10.1088/1475-7516/2025/02/047. URL https://doi.org/10.1088/1475-7516/2025/02/047.

[197] Generated by Doxygen, Konrad Bernlöhr. *HESSIO Objects Reference Manual*. Max-Planck-Institut für Kernphysik (MPIK), Heidelberg, 2023-05-31. URL https://www.mpi-hd.mpg.de/hfm/~bernlohr/sim_telarray/Documentation/hessio_refman.pdf. Documentation for the hessio I/O libraries used in sim_telarray, available at https://www.mpi-hd.mpg.de/hfm/b̃ernlohr/sim_telarray/Documentation/hessio_refman.pdf.

[198] Felix Werner. Fast, software-based muon tagging with FlashCam, 2021. URL https://www.mpi-hd.mpg.de/personalhomes/fwerner/research/2021/08/fast-muon-tagging-flashcam/. MPI-Heidelberg research page; accessed 2025-12-28.

[199] Andrii Neronov. Science talk: Cherenkov Telescope Array Observatory. Presented at the Spring 2025 Workshop on CSCS Alps IT infrastructure, CERN Indico, 2025. URL https://indico.cern.ch/event/1477299/contributions/6408894/attachments/3042291/5374595/Hepix_neronov.pdf.

[200] Escañuela Nieves, Clara, Barcelo, Miquel, Bauer, Christian, Bi, Baiyang, et al. FlashCam: A high-performance camera for IACTs. *EPJ Web Conf.*, 319:12006, 2025. doi:10.1051/epjconf/202531912006. URL https://doi.org/10.1051/epjconf/202531912006.

[201] cta-observatory. pyeventio: Python read-only implementation for the eventio data format used by the corsika iact extension and sim_telarray, 2025. URL https://github.com/cta-observatory/pyeventio. GitHub repository; accessed 2025-12-28.

[202] Charles R. Harris, K. Jarrod Millman, St'efan J. van der Walt, Ralf Gommers, Pauli Virtanen, et al. Array programming with NumPy. *Nature*, 585(7825):357–362, 2020. doi:10.1038/s41586-020-2649-2.

[203] NumPy Developers. numpy.clip — numpy manual, 2026. URL https://numpy.org/devdocs/reference/generated/numpy.clip.html. Accessed: 2026-01-03.

[204] The Gammapy Developers. Gammapy: Smooth broken power law spectral model example, 2025. URL https://docs.gammapy.org/2.0/user-guide/model-gallery/spectral/plot_smooth_broken_powerlaw.html. Accessed: 2026-01-03.

[205] Anne Timmermans, Miquel Barcelo, Christian Bauer, Baiyang Bi, Sebastian Diebold, Clara Escañuela Nieves, et al. Development and Performance of FlashCam. *PoS*, ICRC2025:865, 2025. doi:10.22323/1.501.0865.

[206] Fabian Leuschner, Johannes Schäfer, Simon Steinmassl, Tim Lukas Holch, Konrad Bernlöhr, Stefan Funk, Jim Hinton, Stefan Ohm, and Gerd Pühlhofer. Validating Monte Carlo simulations for an analysis chain in HESS. *arXiv preprint arXiv:2303.00412*, 2023. doi:10.22323/1.417.0231.

[207] Johannes Schäfer. *Simulation of IceACT with Target Validation of the HESS Simulation Chain and a New HESS 3D Analysis of the Crab Using the Abrir Method for Improved Background Rejection*. Friedrich-Alexander-Universitaet Erlangen-Nuernberg (Germany), 2023.

[208] J. Hahn, R. de los Reyes, K. Bernlöhr, P. Krüger, Y.T.E. Lo, P.M. Chadwick, M.K. Daniel, C. Deil, H. Gast, K. Kosack, and V. Marandon. Impact of aerosols and adverse atmospheric conditions on the data quality for spectral analysis of the H.E.S.S. telescopes. *Astroparticle Physics*, 54: 25–32, 2014. ISSN 0927-6505. doi:https://doi.org/10.1016/j.astropartphys.2013.10.003. URL https://www.sciencedirect.com/science/article/pii/S0927650513001540.

[209] J. Hahn, R. de los Reyes, K. Bernlöhr, P. Krüger, Y.T.E. Lo, P.M. Chadwick, M.K. Daniel, C. Deil, H. Gast, K. Kosack, and V. Marandon. Impact of aerosols and adverse atmospheric conditions on the data quality for spectral analysis of the H.E.S.S. telescopes. *Astroparticle Physics*, 54: 25–32, 2014. ISSN 0927-6505. doi:https://doi.org/10.1016/j.astropartphys.2013.10.003. URL https://www.sciencedirect.com/science/article/pii/S0927650513001540.

[210] B.N. Holben, T.F. Eck, I. Slutsker, D. Tanré, J.P. Buis, A. Setzer, E. Vermote, J.A. Reagan, Y.J. Kaufman, T. Nakajima, F. Lavenu, I. Jankowiak, and A. Smirnov. AERONET—A Federated Instrument Network and Data Archive for Aerosol Characterization. *Remote Sensing of Environment*, 66(1):1–16, 1998. ISSN 0034-4257. doi:https://doi.org/10.1016/S0034-4257(98)00031-5. URL https://www.sciencedirect.com/science/article/pii/S0034425798000315.

[211] S. Funk, G. Hermann, J. Hinton, D. Berge, K. Bernlöhr, W. Hofmann, P. Nayman, F. Toussenel, and P. Vincent. The trigger system of the H.E.S.S. telescope array. *Astroparticle Physics*, 22(3): 285–296, 2004. ISSN 0927-6505. doi:https://doi.org/10.1016/j.astropartphys.2004.08.001. URL https://www.sciencedirect.com/science/article/pii/S0927650504001422.

[212] Hans Dembinski, Ralph Engel, Anatoli Fedynitch, Thomas Gaisser, Felix Riehn, and Todor Stanev. Data-driven model of the cosmic-ray flux and mass composition from 10 GeV to 10^{11} GeV. *arXiv preprint arXiv:1711.11432*, 2017. doi:https://doi.org/10.48550/arXiv.1711.11432.

[213] T Sanuki, M Motoki, H Matsumoto, ES Seo, JZ Wang, K Abe, K Anraku, Y Asaoka, M Fujikawa, M Imori, et al. Precise Measurement of Cosmic-Ray Proton and Helium Spectra with the BESS Spectrometer. *The Astrophysical Journal*, 545(2):1135, 2000. doi:10.1086/317873.

[214] Laura Olivera-Nieto, Helena X Ren, Alison MW Mitchell, Vincent Marandon, and JA Hinton. Background rejection using image residuals from large telescopes in imaging atmospheric Cherenkov telescope arrays. *The European Physical Journal C*, 82(12):1118, 2022. doi:10.1140/epjc/s10052-022-11067-5.

[215] Fabian Leuschner. *Advancements in the Calibration of the FlashCam Camera for Imaging Air Cherenkov Telescopes and a New Analysis of HESS J1729-345*. PhD thesis, Dissertation, Tübingen, Universität Tübingen, 2024, 2024. URL http://dx.doi.org/10.15496/publikation-103309.

[216] Quentin Remy. Towards the second HESS Galactic plane catalogue. *arXiv preprint arXiv:2308.08969*, 2023. doi:https://doi.org/10.48550/arXiv.2308.08969.

[217] Andrej Dundovic, Carmelo Evoli, Daniele Gaggero, and Dario Grasso. Simulating the Galactic multi-messenger emissions with HERMES. *Astronomy & Astrophysics*, 653:A18, 2021. doi:10.1051/0004-6361/202140801.

[218] Soheila Abdollahi, Fabio Acero, M Ackermann, M Ajello, WB Atwood, Magnus Axelsson, L Baldini, J Ballet, G Barbiellini, D Bastieri, et al. Fermi large area telescope fourth source catalog. *The Astrophysical Journal Supplement Series*, 247(1):33, 2020. doi:10.3847/1538-4365/ab6bcb.

[219] NASA Goddard Space Flight Center. Lat 14-year source catalog (4fgl-dr4), 2025. URL https://fermi.gsfc.nasa.gov/ssc/data/access/lat/14yr_catalog/. Accessed: 2026-01-18.

[220] NASA Goddard Space Flight Center. Lat background models, 2025. URL https://fermi.gsfc.nasa.gov/ssc/data/access/lat/BackgroundModels.html. Accessed: 2026-01-18.

[221] Fabio Acero, M Ackermann, M Ajello, A Albert, Luca Baldini, J Ballet, G Barbiellini, Denis Bastieri, R Bellazzini, E Bissaldi, et al. Development of the model of galactic interstellar emission for standard point-source analysis of Fermi Large Area Telescope data. *The Astrophysical Journal Supplement Series*, 223(2):26, 2016. doi:10.3847/0067-0049/223/2/26.

[222] Fermi-LAT Collaboration. Galactic Interstellar Emission Model for the 4FGL Catalog Analysis. Fermi Science Support Center Technical Note, February 2019. URL https://fermi.gsfc.nasa.gov/ssc/data/analysis/software/aux/4fgl/Galactic_Diffuse_Emission_Model_for_the_4FGL_Catalog_Analysis.pdf. Draft version February 25, 2019.

[223] V. Zabalza. naima: a Python package for inference of relativistic particle energy distributions from observed nonthermal spectra. *Proc. of International Cosmic Ray Conference 2015*, page 922, 2015.

[224] Fabio Acero, Roberto Aloisio, J Amans, Elena Amato, Lucio Angelo Antonelli, Carla Aramo, T Armstrong, F Arqueros, Katsuaki Asano, Michael Ashley, et al. Prospects for Cherenkov Telescope Array Observations of the Young Supernova Remnant RX J1713. 7- 3946. *The Astrophysical Journal*, 840(2):74, 2017. doi:10.3847/1538-4357/aa6d67.

[225] Yasunobu Uchiyama, Felix A Aharonian, Takaaki Tanaka, Tadayuki Takahashi, and Yoshitomo Maeda. Extremely fast acceleration of cosmic rays in a supernova remnant. *Nature*, 449 (7162):576–578, 2007. doi:10.1038/nature06210.

[226] Evgeni G Berezhko and Heinrich J Völk. Theory of cosmic ray production in the supernova remnant RX J1713. 7-3946. *Astronomy & Astrophysics*, 451(3):981–990, 2006. doi:10.1051/0004-6361:20054595.

[227] Attila Abramowski, F Aharonian, F Ait Benkhali, AG Akhperjanian, EO Angüner, M Backes, Agnès Balzer, Yvonne Becherini, J Becker Tjus, David Berge, et al. Detailed spectral and morphological analysis of the shell type supernova remnant RCW 86. *Astronomy & Astrophysics*, 612:A4, 2018. doi:10.1051/0004-6361/201526545.

[228] H Abdalla, A Abramowski, F Aharonian, Faical Ait Benkhali, AG Akhperjanian, EO Angüner, M Arakawa, M Arrieta, P Aubert, M Backes, et al. Deeper HESS observations of Vela Junior (RX J0852. 0- 4622): Morphology studies and resolved spectroscopy. *Astronomy & Astrophysics*, 612:A7, 2018. doi:10.1051/0004-6361/201630002.

[229] VN Zirakashvili and FA Aharonian. Nonthermal Radiation of Young Supernova Remnants: The Case of RX J1713. 7- 3946. *The Astrophysical Journal*, 708(2):965–980, 2010. doi:10.1088/0004-637X/708/2/965.

[230] AA Abdo, Markus Ackermann, Marco Ajello, A Allafort, Luca Baldini, Jean Ballet, Guido Barbiellini, MG Baring, Denis Bastieri, R Bellazzini, et al. Observations of the young supernova remnant RX J1713. 7- 3946 with the Fermi Large Area Telescope. *The Astrophysical Journal*, 734(1):28, 2011. doi:10.1088/0004-637X/734/1/28.

[231] KO Cubuk, MG Burton, C Braiding, GF Wong, G Rowell, NI Maxted, D Eden, RZE Alsaberi, R Blackwell, R Enokiya, et al. The Mopra Southern Galactic Plane CO Survey–data release 4–complete survey. *Publications of the Astronomical Society of Australia*, 40:e047, 2023. doi:10.1017/pasa.2023.44.

[232] Burton, Michael , Cubuk, Kerem , Braiding, Catherine , Rebolledo, David , Rowell, Gavin , Maxted, Nigel , Wong, Graeme , Blackwell, Rebecca , Voisin, Fabian , Tothill, Nick . The Mopra Southern Galactic Plane Carbon Monoxide (CO) Survey. Dataset from CSIRO Data Access Portal: csiro:60463, 07 Dec 2023. URL https://data.csiro.au/collection/csiro:60463. Accessed: 2026-01-12.

[233] Lara Nava, Stefano Gabici, Alexandre Marcowith, Giovanni Morlino, and Vladimir S Ptuskin. Non-linear diffusion of cosmic rays escaping from supernova remnants–i. the effect of neutrals. *Monthly Notices of the Royal Astronomical Society*, 461(4):3552–3562, 2016. doi:10.1093/mnras/stw1592.

[234] JR Jokipii and EN Parker. Stochastic aspects of magnetic lines of force with application to cosmic-ray propagation. *Astrophysical Journal*, 155:777, 1969. doi:10.1086/149909.

LABELING OF AI TOOLS

To produce the results of this thesis, the following AI tools were used in agreement with the AI Guideline of Heidelberg University and the supervisor:

- ChatGPT: advice on language and coding, and an assistant for literature search.
- grammarly: for language checks and advice on the use of the English language.

The author declares that:

- She assumes full responsibility for the scholarly quality and content of the submitted work, the chosen methodology, the production process, and the cited literature.
- She confirms that the work was prepared in compliance with the principles of good academic practice (see guidelines on good academic practice).
- She confirms that the use of AI tools was agreed in advance with the instructor or examiner and that the agreed-upon rules were followed.

A

EFFECT OF TRIGGER TIME ON MUON TAGGING

Fig. A.1 shows a FlashCam camera where each point no longer represents a pixel of the camera, but a patch. Each patch is centred at the centre of gravity (COG) of the positions of the pixels that form it. The top layer illustrates a muon ring. On the right, the patches that trigger for a single muon ring are shown when the trigger is computed over the full trigger time window. On the left, the triggered patches are highlighted for the same event when the number of trigger patches is calculated within a time window that is limited to the first 2 samples after the first trigger. It is observed that the same patches trigger in both plots. All Cherenkov light emitted by muons is detected by the camera almost simultaneously.
On the other hand, the bottom layer of Fig. A.1 shows a highly energetic proton-initiated shower that exhibits a time gradient along the longitudinal axis of the shower. The left plot, which considers only two time samples, shows an apparent reduction in the number of triggered patches relative to the right plot. Therefore, the number of patches is significantly reduced by accounting for the trigger times. This is key for background rejection in the muon tagging method, as explained in Section 4.2.

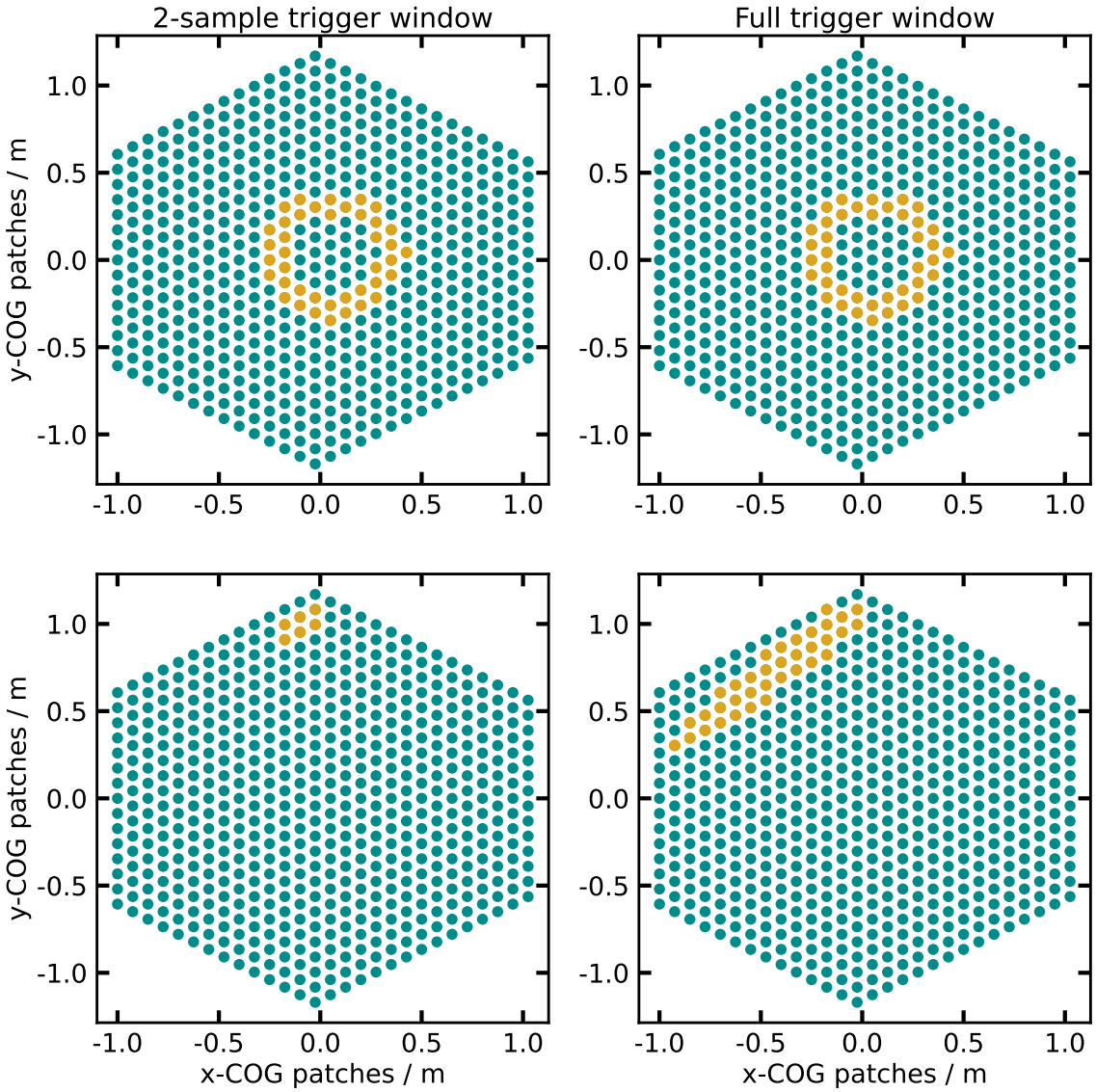

Figure A.1: Projected positions of all patches of a FlashCam and those that triggered for two events: a muon ring (upper) and a proton shower (lower). The position of each patch is the average position of the pixels that formed it. The triggered patches are highlighted. The top layer shows the patches triggered by a muon ring in a limited 2-sample time window (left) and over the full time window (right). The same is shown for a proton shower.

B

GEOMETRY OF PARANAL ARRAYS

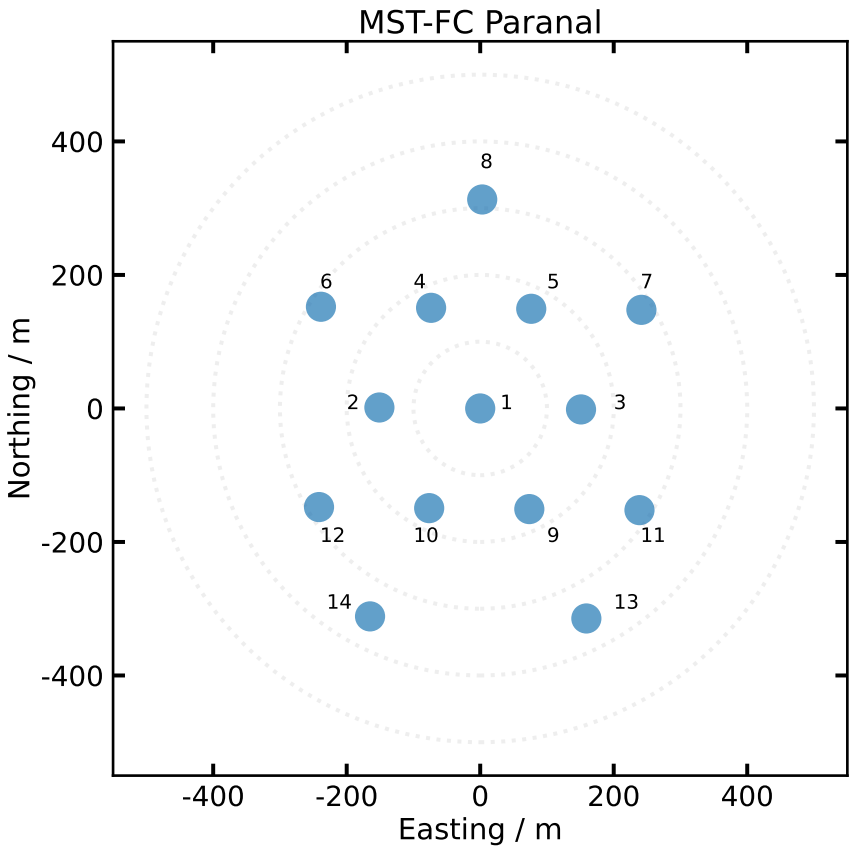

Figure B.1: The alpha configuration of the array of 14 MSTs in the Southern array of the CTAO. Made using ctapipe from sim_telarray simulations.

Fig. B.1 shows the subarray of 14 MSTs at Paranal. This is the array used in simulations based on the official alpha configuration of the CTAO. The fraction of monoscopic and stereoscopic events detected by each telescope strongly depends on the position of the telescope in the array. The energy distribution of monoscopic

and stereoscopic events detected by any of the telescopes in the array is shown in Fig. B.2. The energy distributions for two individual telescopes are shown in Fig. B.3. Telescope 1 is positioned at the centre of the array and is surrounded by six telescopes, each at a distance comparable to the size of a Cherenkov light pool on the ground. Therefore, telescope 1 can detect only low-energy monoscopic events. An event can be easily triggered by more than one telescope, as it is located between multiple telescopes. However, telescopes located outside the array, in the outer layers, such as telescope 14, trigger on more monoscopic events and at higher energies because there are fewer nearby telescopes.

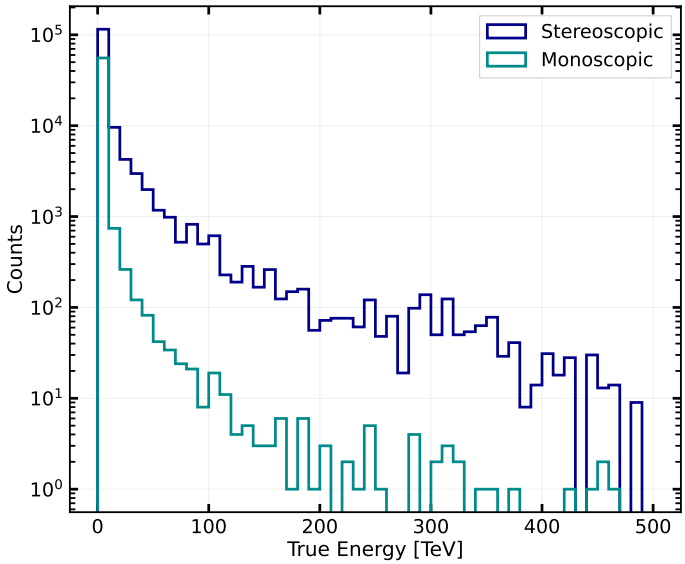

Figure B.2: Energy distribution of all stereoscopic and monoscopic events from any telescope from the simulated 14 MSTs subarray in Paranal.

The previous distributions, however, do not account for the other SST and LST telescopes inside the array, as they were not simulated. The full array of telescopes in the Southern array in the alpha configuration is shown in Fig. B.4. The array shows the four LSTs, which are an option for the Southern array.

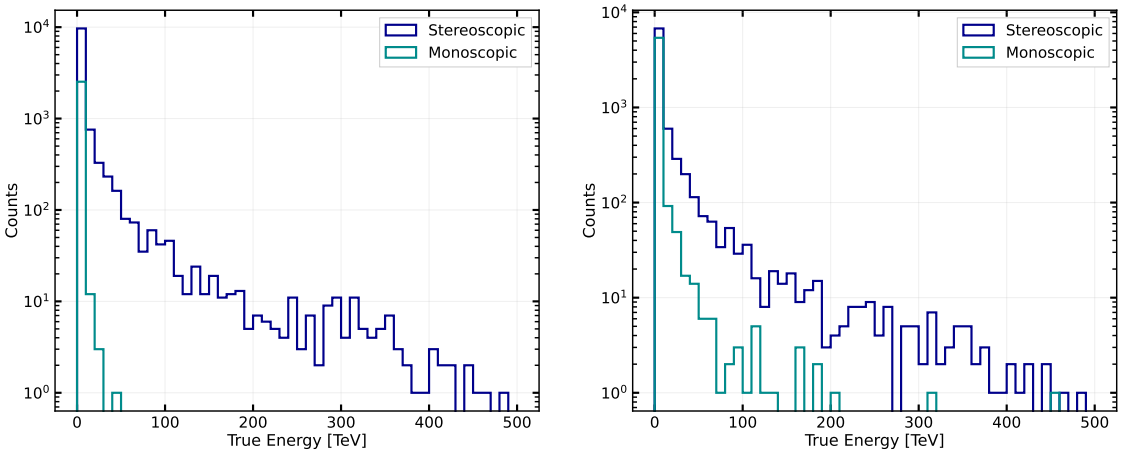

(a) Telescope 1 **(b)** Telescope 14

Figure B.3: Energy distribution of monoscopic and stereoscopic events from telescope 1 (located at the centre of the array) and telescope 14 (at the outer edge of the array). The different positions of the telescopes in the array significantly alter the distribution of monoscopic events.

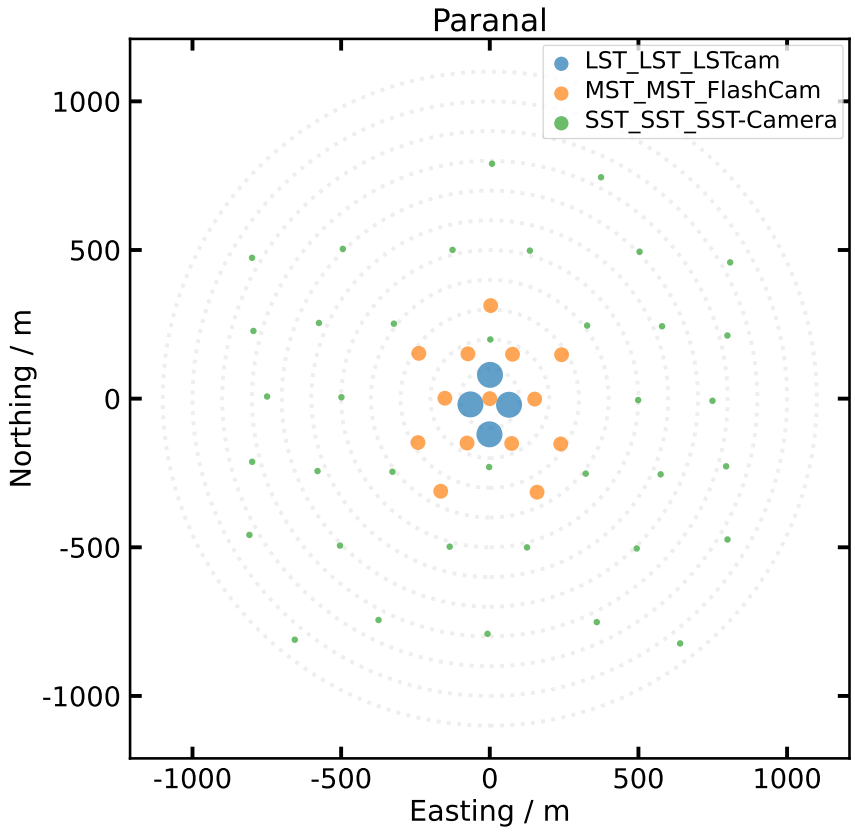

Figure B.4: Alpha configuration of the full array of telescopes in the Southern hemisphere in Paranal.

C

MODELS OF THE SNR RX J1713.7-3946

C.1 The remnant's interior

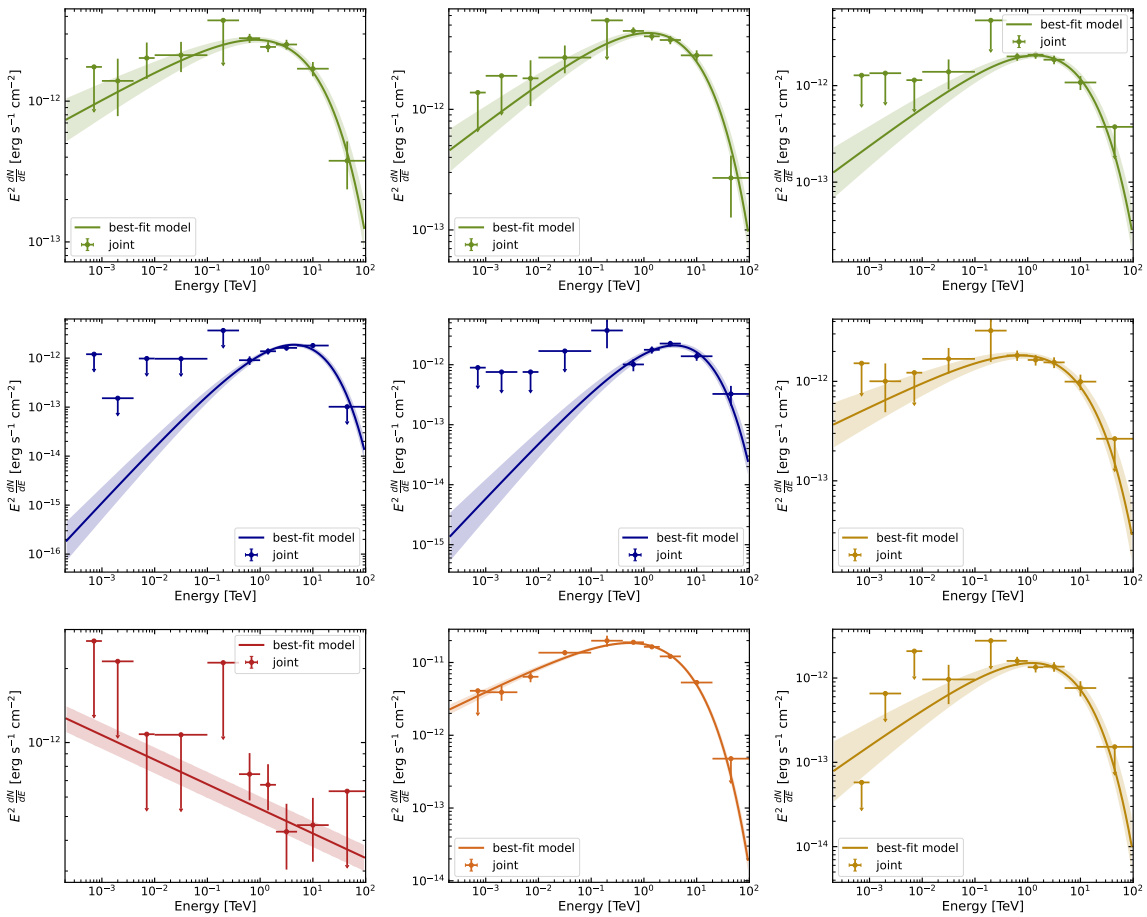

Figure C.1: Models and flux points for each region inside the remnant RX J1713.7-3946. Solid lines represent the best-fit models, and shaded areas indicate uncertainties. Flux points are superimposed.

The flux points and corresponding best-fit models have been shown in Fig. C.1. The red region is fitted with a hadronic and leptonic power-law model with naima and is shown in Fig. C.2. The hadronic fit (left) gives a power-law particle distribution with an index of 2.125 ± 0.05, and the leptonic fit (right) gives a power-law index of 2.834 ± 0.10. This region shows a spectrum similar to that of the leak outside the remnant.

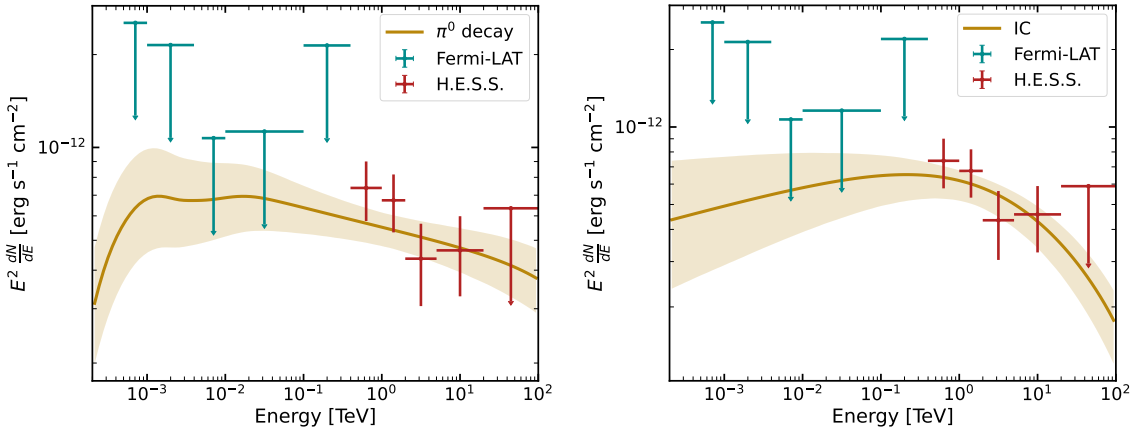

Figure C.2: Gamma-ray spectrum of the outer red region of the remnant using naima fits of hadronic (left) and leptonic (right) power-law models. The left panel shows the gamma-ray spectrum from a fitted π^0 spectrum with a power-law proton spectrum, and the corresponding flux points superimposed. The right panel shows the inverse-Compton spectrum from a power-law electron distribution. The best-fit spectral indices are 2.125 ± 0.05 (hadronic) and 2.834 ± 0.10 (leptonic).

C.2 Particle escape

The gamma-ray emission of the leak of particles using the full spatial template shown in Fig. 6.11 (left) is modelled with a proton distribution following an exponential cutoff power law and compared to the model of a simple power-law proton distribution. The results of the fit are shown in Table C.1 and the spectral shapes and flux points in Fig. C.3. The error in the energy cutoff is larger than its value; therefore, an exponential cutoff power law cannot be discriminated from a simple power law with only the H.E.S.S. data in the high energy regime.

	index	E_{cutoff}	beta
ExponentialCutoffPowerLaw	2.28 ± 0.10	64.05 ± 95.82	1.00 ± 0.17
PowerLaw	2.37 ± 0.05	-	-

Table C.1: Results of fitting a power-law spectral model with an exponential cutoff to the leak of the remnant in the full half-ring spatial template described in Fig. 6.11 (left). The corresponding power-law fit is also shown.

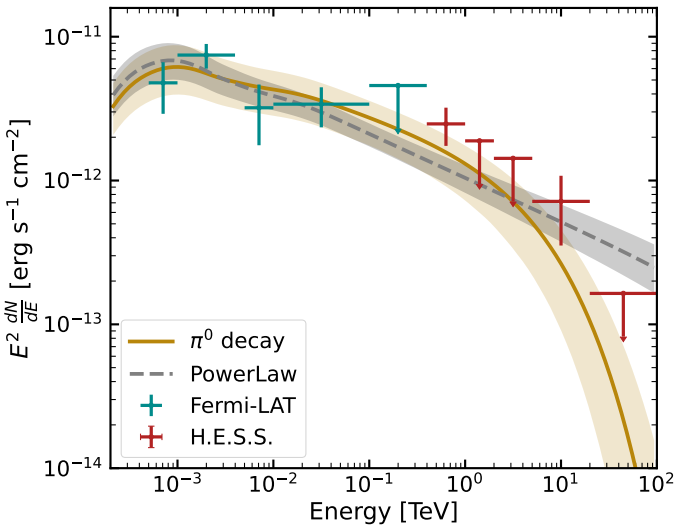

Figure C.3: Fit of the leakage region within the full half-ring shown in Figure 6.11 (left panel) using a π^0 model with an exponential cutoff power-law proton distribution, compared with a simple power law (grey). The flux points are also shown and computed on the exponential cutoff power-law model.

List of figures

List of tables

LIST OF ABBREVIATIONS

CR Cosmic Ray

SNR Supernova Remnant

CMB Cosmic Microwave Background

CTAO Cherenkov Telescope Array Observatory

LAT Large Area Telescope

H.E.S.S. High Energy Stereoscopic System

HAWC High-Altitude Water Cherenkov Observatory

DSA Diffusive Shock Acceleration

IC Inverse Compton

EAS Extensive Air Shower

EM Electromagnetic

IACT Imaging Atmospheric Cherenkov Telescope

PMT Photomultiplier tube

NSB Night Sky Background

ADC Analog-to-Digital Converter

FWHM Full Width Half Maximum

TTS Transit Time Spread

ENF Excess Noise Factor

FoV field-of-view

MAGIC Major Atmospheric Gamma Imaging Cherenkov

VERITAS Very Energetic Radiation Imaging Telescope Array System

MST Medium-Sized Telescope

SST Small-Sized Telescopes

LST Large-Sized Telescopes

ACADA Array Control and Data Acquisition

DPPS Data Processing and Preservation System

ADH Array Data Handler

SWAT Software Array Trigger

PB Petabyte

DVR Data Volume Reduction

SAG Science Alert Generation

SUSS Science User Support System

SOSS Science Operations Support System

ICT Information and Communications Technology

PE Photoelectron

LSB least significant bit

CORSIKA COsmic Ray SImulations for KAscade

COG centre of gravity

RMS root-mean-square

ImPACT Image Pixel-wise fit for Atmospheric Cherenkov Telescopes

IRF Instrument Response Function

PSF Point Spread Function

GLAST Gamma-Ray Large-Area Space Telescope

GBM Gamma-ray Burst

ACD Anti-coincidence detector

FITS Flexible Image Transport System

NPWS Neighbour Peak Window Sum

pz Pole-zero

DBSCAN Density-Based Spatial Clustering of Applications with Noise

HDBSCAN Hierarchical DBSCAN

OPTICS Ordering points to identify the clustering structure

PDP Photon-detector plane

DAQ Data acquisition

ROS Readout electronics system

MPIK Max Planck Institut für Kernphysik

FADC Flash Analog-to-Digital Converter

FPGA Field-Programmable Gate Array

ATC Atmospheric Transparency Coefficient

2HGPS Second H.E.S.S. Galactic Plane Survey

IEM Interstellar emission model

4FGL Fermi-LAT fourth source catalog

ACKNOWLEDGEMENTS

First and foremost, I would like to thank my supervisor, Prof. Dr. Jim Hinton, for his constant support and trust throughout this journey. I would also like to thank Prof. Dr. Andreas Quirrenbach for agreeing to read and evaluate this work and for being part of my committee. Thanks to Prof. Dr. Hans-Christian Schultz-Coulon and Prof. Dr. Tilman Plehn for serving on my thesis examination committee.
Many people helped throughout this journey, and I will not be able to mention all of them, but here is a try.
A special mention to Felix Werner, who was my co-supervisor during these years and consistently answered all my questions and helped me understand and develop my projects. I would also like to mention Quentin Remy for his unwavering support from day one, especially over the past year, and for proofreading part of this thesis. Thanks to Simon Steinmassl for his extensive help with H.E.S.S. and for proofreading part of this thesis. From my work on RXJ1713, I express my gratitude to Jim, Marianne Lemoine-Goumard, for the constant communication, great ideas, and help with Fermi; Brian Reville for helping with the analysis and interpretation; and Quentin for the catalogue that helped us understand the source. I would also like to acknowledge Konrad Bernlöhr for the many emails and conversations that helped me understand how sim_telarray works. From the FlashCam team, huge thanks to German Hermann, Felix Werner, Simon Steinmassl, and Baiyang Bi. Also, a special mention to the ctapipe team for their suggestions to improve the implementation of parts of the code.
I want to mention the Gamma Gang: Georg, Florian, Fredy, and Cormac, for the laughs and for sharing this journey from the beginning. Special thanks to Georg, who was extremely supportive both scientifically and personally, especially during the first two years of my PhD. I am happy to have shared the office with him during that time. A big mention to Fredy for reading this thesis, for his daily support and understanding, and for being there through both the good and the bad days. Thanks to Florian and Cormac for the good time, the joint discussions and learnings, and for organising a nice environment.

Acknowledgements

Many other people from MPIK made my stay better; thanks to all my colleagues for creating such a great environment, and to everyone who proofread parts of this thesis.

Por último, quiero agradecer a mi familia por todo el apoyo recibido. A mis hermanas, por estar siempre ahí. Y especialmente a mi padre, por su respaldo incondicional en todos los aspectos de mi vida. Sin él, esta tesis no habría sido posible.